NUEVOS MATERIALES DE CONSTRUCCIÓN ECOSOSTENIBLES POR SU ACCIÓN SUPERHIDROFUGANTE

Autor: Luis Antonio Martínez Carrascosa

Departamento de Química-Física
Universidad de Cádiz

Cádiz, 2019

NUEVOS MATERIALES DE CONSTRUCCIÓN ECOSOSTENIBLES POR SU ACCIÓN SUPERHIDROFUGANTE

Memoria presentada para optar al título de doctor

Fdo. Luis Antonio Martínez Carrascosa

Directora

Directora

Fdo. María Jesús Mosquera Díaz, Catedrática de la Universidad de Cádiz

Fdo. M. L. Almoraima Gil Montero, Profesora Titular de la Universidad de Cádiz

Agradecimientos

La presente memoria de Tesis Doctoral es el resultado de cinco años de trabajo durante los cuales he tenido el tiempo y la oportunidad de madurar, como persona y también como investigador. Desde mi incorporación al *Grupo de Investigación* TEP-243, he experimentado un continuo proceso de aprendizaje, el cual ha ido mucho más allá de los simples conocimientos teóricos, sino que también he podido experimentar de primera mano el trabajo en un grupo de investigación.

En primer lugar, me gustaría agradecer mis directoras de Tesis, María Jesús Mosquera y Almoraima Gil, por su constante dedicación e interés, sin los cuales esta Tesis no habría salido adelante.

También quiero agradecer a mis compañeros veteranos (Dario, Farid y Luís) por su ayuda para integrarme en el grupo de investigación.

Al doctor Rafael Zarzuela y al próximamente doctor Manuel Luna, con los que llevo desde que empecé la licenciatura en química diez años atrás. Quiero en especial agradecer a Rafa por su ayuda en la última etapa de la Tesis. Además, quiero agradecer su apoyo a todos los miembros más recientes del grupo. Por supuesto no puedo dejar de recordar a mis ayudantes particulares Alejandro y Nabil, sin cuya ayuda en el trabajo experimental el trabajo de esta Tesis habría sido más arduo.

A las empresas con las que he tenido la oportunidad de trabajar: COSENTINO y TINO, por ofrecerme una visión del mundo laboral fuera de los muros de la Universidad.

A mi familia: mi madre, mi padre y mis hermanos, sin cuyo apoyo moral no habría sido capaz de realizar esta proeza.

Y por último, pero no menos importante, a Carmen, mi compañera de viaje y de vida. Muchas gracias por todo lo que me aportas cada día. Gracias a ti la etapa final y más dura de esta tesis ha sido más llevadera. Gracias por estar siempre ahí apoyándome y haciéndome cada vez mejor persona.

A todos vosotros, gracias.

Resumen

La protección de materiales de construcción frente a la acción del agua, el principal vehículo de los agentes de degradación, es un factor clave para aumentar la vida útil de los edificios. Además de los tratamientos hidrofóbicos clásicos, en la actualidad existen materiales de construcción superhidrofugantes, los cuales poseen una elevada hidrofobicidad (dada por una baja energía superficial) que evita la penetración de agua, y una alta repelencia (debido a una rugosidad característica de un estado Cassie-Baxter) que dota a los materiales de propiedades auto-limpiantes. Sin embargo, estos materiales presentan dos inconvenientes principales: (1) su baja durabilidad, y (2) su escasa resistencia a contaminantes de naturaleza oleosa.

En la presente Tesis Doctoral, se plantean soluciones a estos inconvenientes mediante el desarrollo productos, obtenidos por ruta sol-gel, que dotan a los materiales de construcción de propiedades innovadoras. Para ello, se han seguido dos líneas de investigación:

1. <u>Materiales de construcción superhidrofugantes de elevada durabilidad.</u>: La primera estrategia ha sido desarrollar un producto superhidrofugante que contiene nanopartículas hidrófobas, unidas por un oligómero de sílice, lo que le confiere una elevada adhesión al sustrato. En la segunda aproximación, la superhidrofobicidad es obtenida mediante la combinación de la aplicación de un producto hidrofugante y la posterior ablación láser de la superficie

2<u>. Materiales de construcción con resistencia a contaminantes de naturaleza oleosa</u>. En una primera aproximación se ha diseñado un producto que contiene nanopartículas de sílice y un fluoroalquilsilano, el cual dota a los materiales de propiedades oleofugantes. La siguiente estrategia consiste en producir materiales de construcción que presenten superoleofobicidad bajo agua, como consecuencia de la superhidrofilia foto-inducida en su superficie, mientras el interior del material mantiene su hidrofobicidad. Para ello se emplea un producto que contiene nanopartículas de TiO_2 integradas en un ORMOSIL.

Abstract

The protection of building materials against water action, the main vehicle for most of the decay agents, is a key factor for increasing the self-life of buildings. In addition to classical hydrophobic treatments, nowadays, there are superhydrophobic building materials, which show a high hydrophobicity (given by their low surface energy) preventing water ingress, and repellence (due to the roughness promoting a Cassie-Baxter state) that gives rise to self-cleaning abilities. However, these materials present two main drawbacks: (1) low durability, and (2) low resistance to oil-based contaminants.

In the current Doctoral Thesis, we propose solutions for these drawbacks by the development of products, obtained by sol-gel route, which provide the building materials with innovative properties. To achieve this, we have follow two research lines:

1. <u>Long-lasting superhydrophobic building materials</u>. The first strategy has been the development of a superhydrophobic product that contains hydrophobic nanoparticles, joined by a silica oligomer, providing a high adhesion to the substrate. In the second approach, the superhydrophobicity is achieved by the combination of applying a hydrophobic product and the posterior laser ablation of the surface.

2. <u>Oil-resistance building materials</u>. In a first approach, a product that contains silica nanoparticles and a fluoroalkylsilane, which promote oleophobic performance, has been designed. The next strategy is the creation of building materials that present underwater superoleophobicity, due to the superhydrophilicity induced in their surface whereas the inner part of the materials remains as hydrophobic. To this end, we have employed a product that contains TiO_2 nanoparticles integrated into an ORMOSIL.

Índice

Capítulo 1

Introducción

Los materiales de construcción generalmente están sometidos al ataque del medio ambiente. Con el paso del tiempo, este ataque continuado puede producir alteraciones que transforman tanto sus propiedades mecánicas como su aspecto. Los factores que provocan estas alteraciones pueden actuar por mecanismos físicos, químicos o biológicos, siendo el agua, debido a las propiedades de disolvente universal, que le confiere la polaridad de su molécula, el vehículo principal de dichas alteraciones. Dependiendo de la porosidad del material, el agua puede penetrar a través de diversas vías difusión, transporte por capilaridad, condensación del vapor y evaporación del agua líquida. Esta capacidad de penetración le permite actuar como agente de deterioro mediante diferentes mecanismos, destacando entre ellos por ser los más generalizados la disolución de sales, los ciclos de congelación y descongelación o el biodeterioro [1–6]. Debido al coste de la reparación de los daños causados por dichas alteraciones, a lo largo de los últimos años, el desarrollo de métodos preventivos que requieran poco mantenimiento son el objetivo de numerosas investigaciones [7,8].

En este capítulo, se presenta un breve resumen de los mecanismos de degradación de los materiales de construcción debidos a la acción del agua, para a continuación, introducir los fundamentos de la hidrofugación, superhidrofugación y superhidrofilia como estrategias de protección contra este ataque, realizando para finalizar, una breve revisión de los productos empleados para la obtención de superficies hidrofugantes, superhidrofugantes y superhidrofílicas, destacando la importancia de la durabilidad de sus propiedades.

1.1. Mecanismos de degradación de los materiales de construcción bajo la acción del agua.

La penetración y transporte del agua en el interior de un material, tiene lugar mediante diferentes mecanismos. Los fenómenos de **difusión y condensación del vapor de agua,** dependen de la humedad relativa y la temperatura del ambiente. Cuando un material seco se encuentra en un ambiente húmedo, el agua que contiene el aire difunde rápidamente en los poros del material hasta que se alcanza la concentración de equilibrio a una determinada temperatura. En estas condiciones, la condensación del agua líquida

tendrá lugar cuando el vapor entre en contacto con una superficie con una temperatura igual o menor que el punto de rocío. En el interior del material, el **transporte de agua líquida por capilaridad** es un fenómeno complejo que depende de diversos factores relacionados por un lado con la estructura porosa del material y el diámetro de poro, (los poros más pequeños ejercen una presión de succión mayor acelerando el transporte del agua en su interior) y por otro lado tanto, de sus propiedades hidrófilas, como de la humedad presente en el suelo las condiciones microclimáticas. Finalmente, la **evaporación del agua** tiene lugar cuando un material saturado de humedad se expone a un flujo de aire con menor humedad relativa y mayor temperatura. La velocidad de evaporación se incrementa con el aumento de la temperatura y disminuye al disminuir la humedad relativa y la velocidad del flujo de aire.

Cuando mediante estos mecanismos, un material retiene agua o humedad en el interior de sus poros por un largo periodo de tiempo, el agua en poros cercanos a la superficie se evapora rápidamente, pero en los poros más profundos queda atrapada. Adicionalmente en los poros más pequeños, las fuerzas atractivas entre las moléculas de agua y las paredes del poro son mayores lo que ralentiza la evaporación. El agua atrapada en los poros da lugar a fenómenos químicos, físicos y biológicos que deterioran el material progresivamente. Entre las causas más comunes de degradación se incluyen (1) cristalización de sales solubles, (2) ciclos de hielo-deshielo (3) deterioro biológico [6,9].

(1) CRISTALIZACION DE SALES: El agua en su recorrido a través de los poros del material solubiliza y transporta las sales presentes (cloruros, sulfatos, nitratos...) provenientes de diversas fuentes, compuestos originales del material, materiales asociados, suelo, atmosfera, etc. depositándolas en forma de eflorescencia en la superficie, donde se produce la evaporación del agua [1]. En determinadas condiciones, puede tener lugar una evaporación más rápida produciéndose el fenómeno de subeflorescencia. Produciéndose la cristalización de sales dentro de la estructura porosa, lo que provoca expansiones que terminan causando la fractura y hasta la desintegración del material.

(2) CICLOS DE HIELO-DESHIELO: Cuando las diferencias de temperatura, entre estaciones o ciclos diarios son extremas, el agua contenida en los poros del material sufre ciclos de congelación-descongelación. Estas fluctuaciones producen dilataciones y

contracciones cíclicas del material destruyendo su estructura interna. La extensión y el patrón de los daños causados por este mecanismo están relacionados con la estructura porosa, el agua absorbida en el interior del material (grado de saturación) y el gradiente de temperatura. La presencia de sales solubles influye en este fenómeno al reducir el punto de congelación del agua [9].

   (3) DETERIORO BIOLÓGICO: Sobre la superficie de los materiales expuestos a la intemperie, suele existir una variedad de estructuras biológicas que predominan en el ambiente y que generalmente se encuentran en una forma inactiva como esporas y células vegetativas. La colonización biológica y la intensidad del biodeterioro están fuertemente influenciadas por la disponibilidad de agua y nutrientes que hacen prosperar los microorganismos haciendo evidentes sus estructuras. La intensidad y la velocidad de los procesos de degradación biológica depende de una combinación de factores ambientales, parámetros específicos del material (porosidad, absorción de agua...) y condiciones arquitectónicas (orientación, capacidad de drenaje del agua...). El biodeterioro es uno de los principales procesos de degradación de los materiales de construcción expuestos al aire libre, incluyendo alteraciones estéticas por liberación de pigmentos y formación de costras por acumulación de contaminantes atmosféricos en el "biofilm" [10,11].

1.2. Hidrofugantes y superhidrofugantes en materiales de construcción.

1.2.1. Superficies hidrofugantes.

Debido a la degradación producida por el agua en los materiales de construcción, la investigación de superficies hidrofugantes es una solución muy popular para evitar la penetración de agua en la estructura porosa del material de construcción. Estas superficies poseen una baja energía superficial, lo que da lugar a ángulos de contacto superiores a 90° [12], tal como se deduce de la ecuación de Young [13] mostrada en la Figura 1.
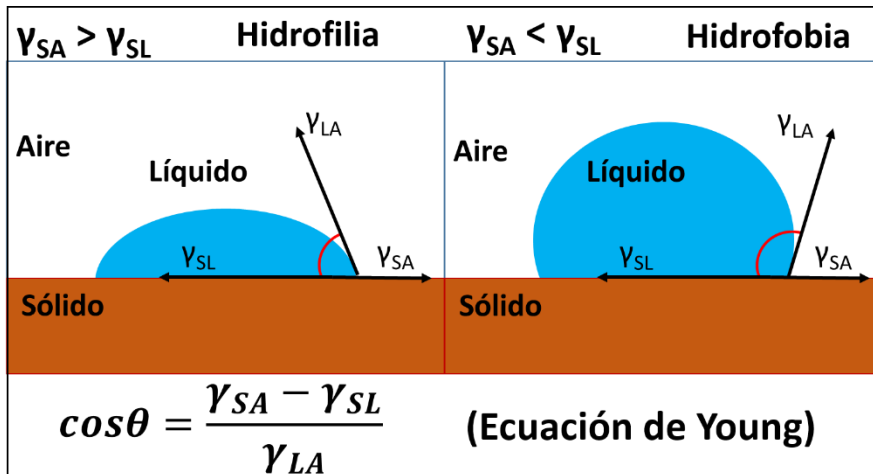
Figura 1. Deducción de la ecuación de Young.

La ecuación de Young muestra que el ángulo de contacto (θ) de un líquido depositado sobre una superficie ideal (homogénea y totalmente lisa) depende del balance de las tres tensiones interfaciales sólido-aire (γ_{SA}), sólido-líquido (γ_{SL}) y líquido-aire (γ_{LA}). De acuerdo a esta ecuación se puede deducir que valores de γ_{SA} superiores a γ_{SL} producirán superficies hidrofílicas (ángulo de contacto inferior a 90°), mientras que el caso contrario dará lugar a superficies hidrófobas (ángulo de contacto superior a 90°).

Es importante, sin embargo, aclarar que las superficies reales no son ideales, ya que presentan irregularidades. Para definir el comportamiento de un líquido sobre superficies reales se emplean típicamente dos teorías referentes a dos estados de humectación: el estado de Wenzel [14], y el de Cassie-Baxter [15].
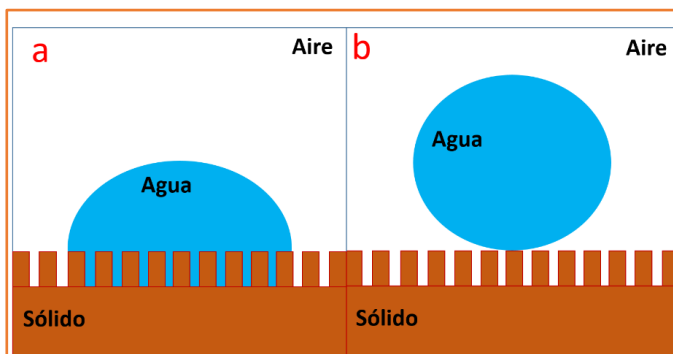
Figura 2. Modelos teóricos que describen los fenómenos de mojado de superficies. rugosas. (a) Modelo de Wenzel y (b) Modelo de Cassie-Baxter.

En el estado de Wenzel, el líquido penetra en los valles de rugosidad produciéndose un contacto total entre la superficie sólida y el líquido (Fig. 2a). Por lo tanto, el carácter hidrofílico o hidrofóbico se verá incrementado por la rugosidad, tal como se deduce de la **Ecuación 1**.

$$\cos \theta_w = r \cos \theta \qquad\qquad (\text{Ecuación 1})$$

Donde θ_W es el ángulo de contacto en una superficie rugosa, θ es el ángulo de contacto de Young en una superficie lisa similar, y r es el factor de rugosidad superficial, que se define como la proporción entre el área superficial real y la proyectada ($r=1$ para una superficie perfectamente lisa, y $r>1$ para una superficie con rugosidad).

Por otro lado, en el estado de Cassie-Baxter, la formación de bolsas de aire en los valles de rugosidad evita que el líquido penetre en estos, quedándose depositado sobre los picos de rugosidad (**Fig. 2b**) El comportamiento de un líquido sobre este tipo de superficie puede definirse según la **Ecuación 2**.

$$\cos \theta_{CB} = f(\cos \theta + 1) - 1 \qquad\qquad (\textit{Ecuación 2})$$

Donde θ_{CB} y θ son los ángulos de contacto en superficies Cassie-Baxter e ideal, respectivamente; y f es la fracción de líquido en contacto con el sólido, y toma valores entre 0 y 1. Para $f=0$ la gota no tocaría la superficie y para $f=1$ la superficie estaría completamente mojada, siendo este último el comportamiento característico de superficie plana. Para valores bajos de f (estado Cassie-Baxter) la interfase líquido-sólido es reducida, favoreciendo que las gotas de líquido rueden sobre la superficie produciéndose la repelencia.

Basados en las teorías de humectación previamente descritas, se han desarrollado diversos tratamientos con el fin de dotar de propiedades hidrófobas a materiales de construcción, empleando para ello productos basados en resinas epoxi, acrílicas y de poliuretano, así como alquilsilanos y alquilsiloxanos. Todos ellos empleados para reducir la energía superficial mediante el uso de grupos alifáticos [16–19].

Nuestro grupo de investigación ha desarrollado rutas para proteger los materiales de construcción de la acción del agua. En una primera aproximación [20], se preparó un producto hidrofugante mediante una ruta sol-gel en la cual se mezcló un oligómero de

sílice con un polidimetilsiloxano (PDMS), en presencia del surfactante no-iónico *n*-octilamina. El papel de la *n*-octilamina es catalizar la reacción sol-gel, además de prevenir la fractura del gel gracias a la creación de un material mesoporoso, como se describirá en un epígrafe posterior. Adicionalmente, la *n*-octilamina también favorece la co-condensación entre la matriz de sílice, produciendo un ORMOSIL. Respecto a la efectividad en materiales de construcción, el producto fue aplicado como un sol en una piedra calcárea, dotándola de propiedades hidrofugantes (ángulo de contacto alrededor de 130°) debido al papel del PDMS reduciendo la energía superficial.

La síntesis previa fue modificada añadiendo cantidades crecientes de PDMS con objeto de incrementar la resistencia a manchado [21]. Los soles obtenidos fueron aplicados sobre una caliza pura, dando lugar a propiedades hidrofugantes, las cuales se vieron incrementadas con la cantidad de PDMS (140° para la concentración más alta). La elevada hidrofobicidad se debe al efecto combinado del PDMS reduciendo la energía superficial y la rugosidad superficial que produce un estado Wenzel, el cual incrementa el valor de ángulo de contacto [14]. La eficacia hidrofugante fue comparada con un producto comercial, el cual dotó a las muestras calizas de ángulos alrededor de 90°, demostrando la efectividad de nuestro producto frente a los existentes en el mercado.

En un trabajo posterior [22] (**Fig. 3**)se aplicó un producto similar con proporciones de PDMS entre el 2 y 10 %v/v sobre una piedra calcárea dotándola de propiedades hidrofugantes (ángulo alrededor de 110° para la concentración más alta de PDMS).
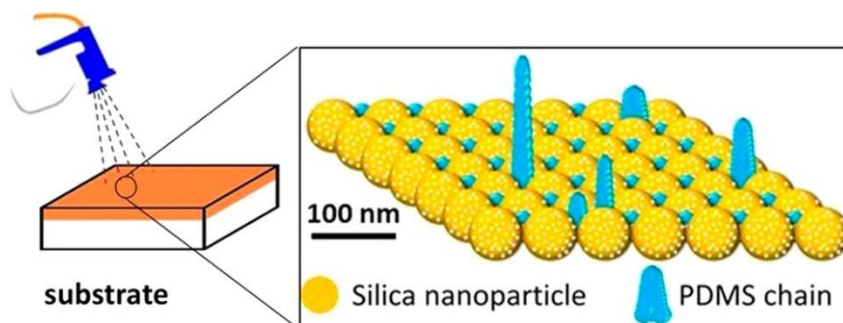
Figura 3. Aplicación de un producto que contiene un oligómero de silicio y PDMS sobre un material de construcción para dotarlo de propiedades hidrofugantes. Imagen tomada de [21].

Este mismo producto fue aplicado sobre muestras calizas [23] y areniscas [24], las

cuales fueron colocadas en yacimientos arqueológicos en condiciones de montaña y costa (**Fig. 4**), respectivamente, durante 3 años. Las muestras tratadas con el producto desarrollado en nuestro laboratorio demostraron una elevada efectividad, así como una gran durabilidad comparados con la aplicación de un producto comercial, el cual perdió rápidamente sus propiedades. La mayor durabilidad de nuestro producto puede ser explicada principalmente por la mayor penetración en la estructura porosa del material pétreo, al no usarse ningún disolvente volátil para su aplicación.

Figura 4. Evaluación de la durabilidad *in-situ* de un producto hidrofugante. Imagen tomada de [24].

1.2.2. Superficies superhidrofugantes.

Una superficie superhidrofugante es aquella que posee una elevada hidrofobicidad y una alta repelencia al agua, con de ángulo de contacto superiores a 150° y valores de histéresis inferiores a 10° [12,25,26]. Se define la histéresis del ángulo de contacto como la diferencia entre el mayor valor de ángulo alcanzado en una superficie (ángulo de avance, ACA) y el menor ángulo de esa misma superficie (ángulo de retroceso, RCA). Si la diferencia entre ambos es nula (histéresis igual a 0), no se requerirá fuerza alguna para mover una gota de líquido sobre esta superficie, mostrando repelencia [27,28].

Las superficies superhidrofugantes han sido observadas en la naturaleza en las hojas de algunas plantas, como la hoja de loto (**Fig. 5a**) [29]; y algunos animales, como la cigarra común [30]. La investigación de estas superficies naturales mostró que estaban compuestas por estructuras nano- y micro-rugosas, además de compuestos tales como ceras que les confieren una baja energía superficial.

La elevada repelencia de estas superficies las dota de propiedades auto-limpiantes

[31,32]. El agua es capaz de capturar las partículas contaminantes presentes en estas superficies y rodar fuera de ellas, limpiándolas. Este efecto puede ser observado en la hoja de loto, la cual es capaz de mantenerse limpia gracias a su superhidrofobicidad [29] (**Fig. 5b**).

Figura 5. (a) Gotas depositadas sobre la hoja de loto mostrando superhidrofobicidad. (b) Habilidad auto-limpiante de la hoja de loto.

Con objeto de obtener una superficie superhidrofugante es necesario combinar dos estrategias: (1) reducir la energía superficial para producir una superficie hidrofugante, y (2) crear una rugosidad superficial que dé lugar a un estado de Cassie-Baxter, tal como se ha definido previamente [33,34].

Con el fin de obtener dicha rugosidad se emplean dos estrategias diferentes: (1) los métodos bottom-up, en los cuales la rugosidad es obtenida creando una nueva superficie sobre el sustrato de partida; y (2) los métodos top-down, en los que la rugosidad es creada eliminando parte del material de la superficie original.

En el caso de los materiales de construcción, la metodología típicamente usada es la bottom-up. Una simple aproximación para obtener estas superficies consiste en la aplicación de una dispersión de NPs hidrófobas en un disolvente. Cuando el disolvente se evapora, las NPs producen una superficie Cassie-Baxter con propiedades superhidrofugantes. Algunas de estas dispersiones están incluso comercializadas (p. ej. AquaShield Ultimate, de Tecnan) para su aplicación en materiales de construcción. Sin embargo, esta estrategia presenta un importante inconveniente relacionado con su escasa penetración y su baja adherencia a los sustratos, lo que promueve una baja durabilidad del recubrimiento [35].

Se han investigado diferentes métodos para mejorar la durabilidad de las superficies

superhidrofugantes [26,36–38]. La estrategia más comúnmente empleada, en el caso de los materiales de construcción, es integrar las NPs en una matriz de sílice que le confiere adherencia al sustrato [39–44]. Sin embargo, cuando las NPs situadas en la superficie de la matriz son eliminadas por los agentes de degradación (agua, viento, etc.), se pierden las propiedades superhidrofugantes.

Nuestro grupo de investigación ha desarrollado distintos productos superhidrofugantes con aplicación en el campo de la construcción en los últimos años. Se integraron NPs de sílice de 40 nm en un ORMOSIL desarrollado en un trabajo previo [22], y el sol obtenido se aplicó sobre una arenisca [45] (**Fig. 6**). Las imágenes obtenidas por Microscopía de Fuerza Atómica (AFM) y Microscopía Electrónica de Barrido (SEM) demostraron la formación de un recubrimiento compuesto de partículas densamente empaquetadas. la evaluación de la eficacia superhidrofugante mostró ángulos de contacto superiores a 150° y valores de histéresis inferiores a 10°. Este efecto es debido al papel del PMDS reduciendo la energía superficial, como se ha descrito previamente, y a las NPs de sílice induciendo una rugosidad típica de un estado Cassie-Baxter.
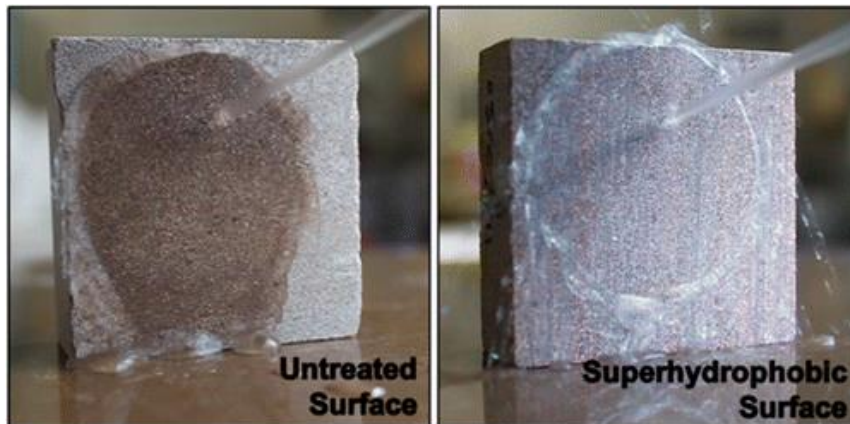
Figura 6. Demostración de las propiedades repelentes de un material de construcción tratado con un producto superhidrofugante, en comparación con el mismo sin tratar. Imagen tomada de [45].

El producto anterior fue también aplicado sobre muestras de teja cerámica, dotándolas de propiedades superhidrofugantes [40]. La durabilidad de las muestras tratadas fue evaluada empleando una cámara climática de envejecimiento. Tras finalizar el ensayo de degradación, las muestras tratadas preservaron valores elevados de ángulo de contacto.

11

Sin embargo, se observó la pérdida de las propiedades repelentes como consecuencia de la alteración de la rugosidad y, en consecuencia, la pérdida del estado Cassie-Baxter.

Por otro lado, los métodos top-down no han sido aplicado en materiales de construcción, con excepción de algún artículo que reporta el uso de ataque químico con clohídrico para obtener la rugosidad necesaria sobre muestras de mármol.

Entre los métodos "top-down", la texturización láser ha ganado especial importancia. Específicamente, en los últimos años, se han publicado varios trabajos en los cuales se emplea la texturización láser para obtener superficie superhidrofugantes [33,46–51].

En 1965, Birnbaun fue el primero en obtener estructuras superficiales periódicas inducidas por láser (LIPSS, del inglés *laser-induced periodic surface structures*) utilizando pulso de láser de rubí para irradiar semiconductores [52], lo que dio lugar a una nuevo campo de investigación. Cuando se produce la irradiación de una superficie con una energía por unidad de área (fluencia) cercana al límite de ablación del material, se producen cambios en la superficie como consecuencia del fundido del material superficial [53,54]. Esta técnica se emplea generalmente en sustratos tales como metales, semiconductores o polímeros [55].

1.3. Oleofugantes y superoleofugantes en materiales de construcción.

Aunque se han conseguido soluciones efectivas para fabricar materiales de construcción con superficies superhidrofugantes, la obtención de superficies superoleofóbicas aún es un reto por dos razones fundamentales. (1) la mayoría de la suciedad en fachadas es causada por contaminantes basados en aceites, tales como polución atmosférica y grafitis, (2) la durabilidad de las superficies superhidrofugantes está completamente comprometida por la contaminación con aceites, dando lugar a la pérdida de las propiedades auto-limpiantes [56]. La obtención de materiales anfifóbicos puede ayudar a solventar este problema; sin embargo, cuenta con ciertas limitaciones que dificultan su uso en el campo de la construcción.

Una superficie oleofugante es aquella que presenta ángulos de contacto con gotas de aceite superiores a 90°, mientras que una superoleofugantes posee ángulos de contacto

mayores de 150° y un valor de histéresis inferior a 10° [57–59].

Teniendo en cuenta la baja tensión superficial de los aceites (18-32 mN·m^{-1}) [60], es necesario el uso de compuestos con grupos fluorados con el fin de reducir la tensión superficial sólido-aire y obtener ángulos superiores a 90° [61,62], cumpliendo la ecuación de Young [13].

Siguiendo esta estrategia nuestro grupo de investigación ha desarrollado tratamientos con propiedades oleofugantes en materiales de construcción [39] (**Fig. 7**). Específicamente, un sol que contenía NPs de sílice se aplicó sobre una arenisca. Después de completarse la transición sol-gel, se obtuvo un nanocomposite formado por partículas densamente empaquetadas, dando lugar a un estado Cassie-Baxter. Posteriormente, se aplicó un fluoroalcoxisilano sobre el nanocomposite previo, con objeto de reducir la energía superficial. Las superficies tratadas mostraron propiedades superhidrofugantes y oleofugantes debido a la reducción de energía superficial dada por el compuesto fluorado.
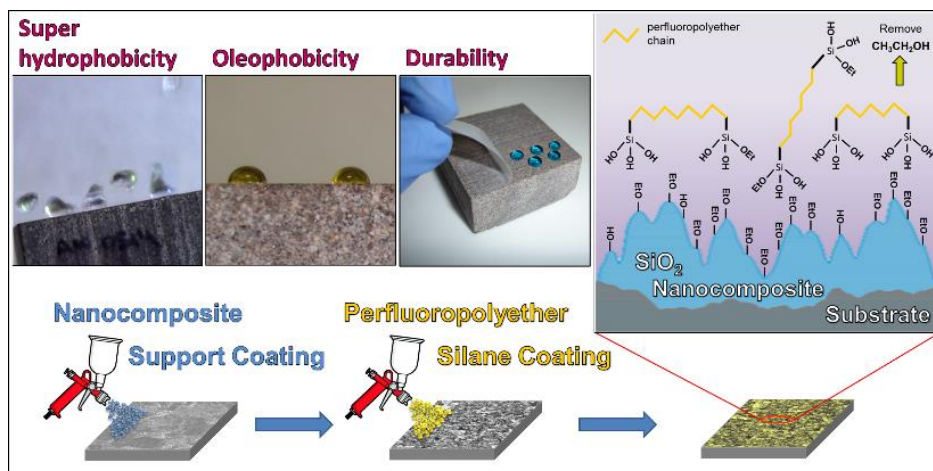
Figura 7. Obtención de materiales de construcción superhidrofugantes y oleofugantes empleando un procedimiento de dos aplicaciones. Imagen tomada de [39].

Por otro lado, la formación de estructuras rugosas típicamente empleadas para la obtención de superficies superhidrofugantes, no es suficiente para la creación de un estado Cassie-Baxter en el caso de aceites. Para ello es necesario el uso de estructuras re-entrantes con "forma de T o de hongo" (ver **Fig. 8**), en las cuales las gotas de aceite

13

son capaces de depositarse, formándose bolsas de aire entre el líquido y la superficie sólida [57,60,63].
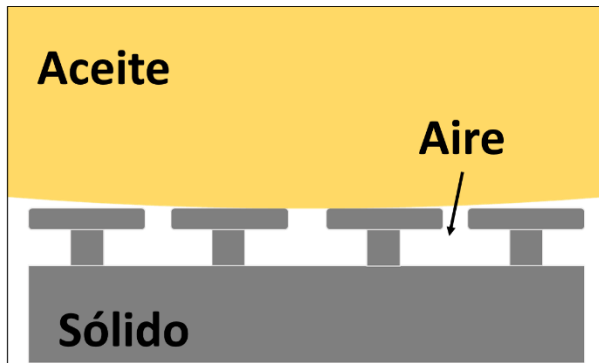
Figura 8. Estructuras re-entrantes produciendo un estado Cassie-Baxter sobre una gota de aceite.

1.4. Superhidrofilia: superoleofobicidad bajo agua.

Una reciente aproximación biomimética para producir superficies auto-limpiantes está basada en la habilidad de los peces para permanecer limpios, incluso en medio acuosos contaminados, debido a su superoleofobicidad bajo agua [64,65]. La combinación de compuestos hidrofílicos con la presencia de micropapilas, que promueven un micro/nano-estructura jerárquica, en las escamas de los peces da lugar a un estado Cassie-Baxter, en el cual una capa de agua se sitúa entre la superficie y el aceite [15,66].

Una gota de aceite sobre una superficie lisa ideal se ajusta al modelo desarrollado por Young. La **Fig. 9** muestra que el ángulo de contacto viene dado por el balance de las tensiones interfaciales sólido-aceite (γ_{SO}), sólido-agua (γ_{SW}) y aceite-agua (γ_{OW}) [64,67]. Por tanto, el ángulo de Young bajo agua (θ_{ow}) viene dado por la **Ecuación 3**.

$$cos\theta_{OW} = \frac{\gamma_{SO} - \gamma_{SW}}{\gamma_{OW}} \qquad (\textbf{\textit{Ecuación 3}})$$

Considerando el caso de gotas de agua o aceite en aire, sus ecuaciones de Young serían las siguientes:

$$cos\theta_{W} = \frac{\gamma_{SW} - \gamma_{SA}}{\gamma_{WA}} \qquad (\textbf{\textit{Ecuación 4}})$$

$$cos\theta_{O} = \frac{\gamma_{SO} - \gamma_{SA}}{\gamma_{OA}} \qquad (\textbf{\textit{Ecuación 5}})$$

Donde γ_{SA}, γ_{WA} y γ_{OA} son las tensiones interfaciales sólido-aire, agua-aire y aceite-aire,

respectivamente. Sustituyendo γ_{SW} y γ_{SO}, de las **Ecuaciones 4 y 5** respectivamente, en la **Ecuación 3**, se obtiene:

$$cos\theta_{OW} = \frac{\gamma_{OA}cos\theta_O - \gamma_{WA}cos\theta_W}{\gamma_{OW}}$$ (***Ecuación 6***)
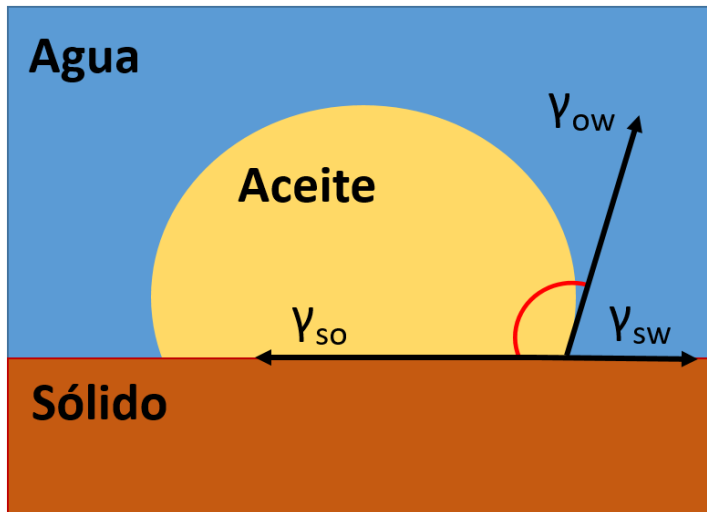
Figura 9. Balance de tensiones interfaciales de una gota de aceite bajo agua.

Para una superficie hidrofugante (θ_W>90°) y oleofílica (θ_O<90°) en aire, los valores de $cos\theta_W$ y $cos\theta_O$ serán negativo y positivo, respectivamente. Por lo tanto, el valor de $cos\theta_{OW}$ será positivo, y en consecuencia la superficie mostrará comportamiento oleofílico bajo agua (θ_{OW}<90°). Por el contrario, una superficie hidrofílica (θ_W<90°) y oleofílica (θ_O<90°) presentará valores positivos de $cos\theta_W$ y $cos\theta_O$. Teniendo en cuenta que el valor de γ_{OA} es significativamente inferior a γ_{WA}, el valor de $cos\theta_{OW}$ será negativo y, por lo tanto, la superficie mostrará oleofobicidad bajo agua (θ_{OW}>90°) [63,64,68].

Para los estados Wenzel y Cassie-Baxter bajo agua, se produce una inversión con respecto a estos mismo estados en aire, tal como se puede observar en la **Fig. 10**.
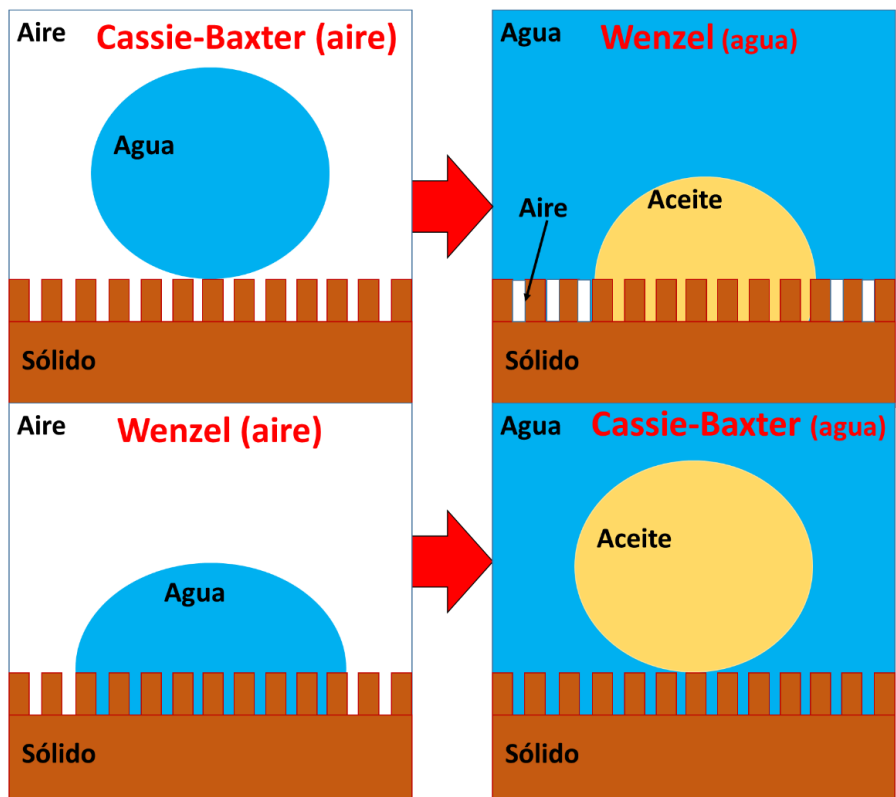
Figura 10. Estados de humectación (Wenzel y Cassie-Baxter) en aire y bajo agua.

Cuando una superficie que muestra superhidrofobicidad en aire es sumergida en agua, se observa un efecto espejo debido al aire que queda atrapado en los valles de rugosidad, como consecuencia del estado de Cassie-Baxter [69]. Cuando una gota de aceite es depositada sobre esta superficie, se extenderá rápidamente a lo largo del aire atrapado entre el agua y la superficie sólida, debido a la presión capilar. Por lo tanto, la superficie será completamente mojada por el aceite, dando lugar a un estado Wenzel bajo agua.

Por otro lado, una superficie superhidrófila en medio acuso mostrará los valles de rugosidad completamente cubierto por el agua, debido al estado de Wenzel obtenido [60,64,67]. Cuando una gota de aceite es depositada sobre esta superficie, la capa de agua situada en los valles de rugosidad evita el contacto del aceite con la superficie sólida, observándose un estado de Cassie-Baxter bajo agua y, en consecuencia, una superficie superoleofugante bajo agua.

La creación de superficies superhidrófilas no ha sido empleada en materiales de

16

construcción, ya que el agua es el principal vehículo de los principales agentes de degradación que afectan a los materiales de construcción [70,71].

1.5. Durabilidad de las superficies superhidrofugantes.

A pesar de los muchos avances que se han obtenido en los últimos años en el desarrollo de superficies superhidrofugantes, la durabilidad de dichas superficies continúa siendo su principal problema. Como se ha explicado previamente, para obtener una superficie superhidrofugante es imprescindible reducir la energía superficial y crear rugosidad superficial. Cualquier alteración de dichos requisitos provocará la pérdida total o parcial de la superhidrofobicidad. Es por ello que la aplicación de recubrimientos superhidrofugantes en materiales de construcción, los cuales están expuestos a condiciones de degradación al aire libre, supone un reto [28].

Si el recubrimiento es eliminado completamente, o si se produce la degradación de los grupos

responsables de reducir la energía superficial, se obtendrá una superficie hidrofílica. Un ejemplo es la reacción de grupos alcoxi con agua para producir grupos hidroxilos [72], los cuales son hidrofílicos. Además, los recubrimientos basados en resinas pueden ser degradados por la acción de la luz solar [73], perdiendo sus propiedades.

Por otro lado, si se produce la pérdida de rugosidad creada, se perderán las propiedades repelentes

de la superficie, ya que ocurre el paso de un estado de Cassie-Baxter (superhidrofóbico) [15] a un estado de Wenzel (sólo hidrofóbico) [14]. Por tanto, es fundamental el desarrollo de recubrimientos con una elevada durabilidad mecánica. Este factor es determinante para la aplicación de dichos recubrimientos en materiales de construcción [74–77].

Aunque existen multitud de trabajos relacionados con la durabilidad de superficies superhidrofugantes, la investigación en materiales de construcción ha sido poco desarrollada, no existiendo evaluación de la durabilidad más allá de la medida de ángulos de contacto estáticos [78,79], siendo insuficiente para la medida real de la durabilidad de los tratamientos. Es necesaria la conservación de valores bajos de histéresis para

asegurar la durabilidad de las propiedades superhidrofugantes, lo cual no es evaluado en estos trabajos.

Los materiales previamente desarrollados por nuestro grupo de investigación presentan propiedades superhidrofugantes y oleofugantes. Sin embargo, presentan problemas relacionados con la durabilidad, así como la necesidad de emplear procesos que implican múltiples aplicaciones. Por ese motivo, en la presente Tesis Doctoral, se plantea el desarrollo de superficies superhidrofugantes y oleofugantes duraderas, así como la simplificación de los procesos de aplicación. Además, se desarrollan superficies superhidrofílicas que puedan ser aplicadas sobre materiales de construcción.

1.6. Referencias.

[1]   N. Lindström, T. Talreja, K. Linnow, A. Stahlbuhk, M. Steiger, Crystallization behavior of Na2SO4–MgSO4 salt mixtures in sandstone and comparison to single salt behavior, Appl. Geochemistry. 69 (2016) 50.

[2]   A.E. Charola, Acid rain effects on stone monuments, J. Chem. Educ. 64 (1987) 436.

[3]   M.C. Phillipson, R. Emmanuel, P.H. Baker, The durability of building materials under a changing climate, Wiley Interdiscip. Rev. Clim. Chang. 7 (2016) 590.

[4]   E. Zanardini, P. Abbruscato, N. Ghedini, M. Realini, C. Sorlini, Influence of atmospheric pollutants on the biodeterioration of stone, Int. Biodeterior. Biodegradation. 46 (2000) 8305.

[5]   P. Tiano, Biodegradation of Cultural Heritage: Decay Mechanisms and Control Methods, CNR-Centro Di Stud. Sulle Cause Deperimento e Metod. Conserv. Opere d'Arte. 9 (2001) 1.

[6]   D. Chang, J. Liu, Review of the influence of freeze-thaw cycles on the physical and mechanical properties of soil, Sci. Cold Arid Reg. 4 (2013) 457.

[7]   S. Eyssautier-Chuine, I. Calandra, N. Vaillant-Gaveau, G. Fronteau, C. Thomachot-Schneider, J. Hubert, J. Pleck, M. Gommeaux, A new preventive coating for building stones mixing a water repellent and an eco-friendly biocide, Prog. Org. Coatings. 120 (2018) 132.

[8]   C. Salazar-Hernández, J. Cervantes, M.J. Puy-Alquiza, R. Miranda, Conservation of building materials of historic monuments using a hybrid formulation, J. Cult. Herit. 16 (2015) 185.

[9]   M.A. El-Gohary, A holistic approach to the assessment of the groundwater destructive effects on stone decay in Edfu temple using AAS, SEM-EDX and XRD, Environ. Earth Sci. 75 (2016) 13.

[10]   P.S. Griffin, N. Indictor, R.J. Koestler, The biodeterioration of stone: a review of deterioration mechanisms, conservation case histories, and treatment, Int. Biodeterior. 28 (1991) 187.

[11] T. Warscheid, J. Braams, Biodeterioration of stone: a review, Int. Biodeterior. Biodegradation. 46 (2000) 343.

[12] D. Ahmad, I. van den Boogaert, J. Miller, R. Presswell, H. Jouhara, Hydrophilic and hydrophobic materials and their applications, Energy Sources, Part A Recover. Util. Environ. Eff. 40 (2018) 2686.

[13] T. Young, An Essay on the Cohesion of Fluids, Philos. Trans. R. Soc. London. 95 (1805) 65.

[14] R.N. Wenzel, Resistance of solid surfaces to wetting by water, Ind. Eng. Chem. 28 (1936) 988.

[15] A.B.D. Cassie, S. Baxter, Wettability of porous surfaces, Trans. Faraday Soc. 40 (1944) 546.

[16] T. Hop, Z. Miodyński, Polymer-mineral mixtures as new building materials, Build. Sci. 2 (1967) 147.

[17] L. Concrete, Epoxy resins in the building industry - 25 years of experience, Int. J. Cem. Compos. Light. Concr. 7 (1985) 253.

[18] R. Zandi-Zand, A. Ershad-Langroudi, A. Rahimi, Silica based organic-inorganic hybrid nanocomposite coatings for corrosion protection, Prog. Org. Coatings. 53 (2005) 286.

[19] D.K. Chattopadhyay, K.V.S.N. Raju, Structural engineering of polyurethane coatings for high performance applications, Prog. Polym. Sci. 32 (2007) 352.

[20] M.J. Mosquera, D.M. de los Santos, T. Rivas, Surfactant-synthesized ormosils with application to stone restoration., Langmuir. 26 (2010) 6737.

[21] J.F. Illescas, M.J. Mosquera, Surfactant-Synthesized PDMS/Silica Nanomaterials Improve Robustness and Stain Resistance of Carbonate Stone, J. Phys. Chem. C. 115 (2011) 14624.

[22] J.F. Illescas, M.J. Mosquera, Producing surfactant-synthesized nanomaterials in situ on a building substrate, without volatile organic compounds., ACS Appl. Mater. Interfaces. 4 (2012) 4259.

[23] F. Elhaddad, L.A. Carrascosa, M.J. Mosquera, Long-Term Effectiveness, under a Mountain Environment, of a Novel Conservation Nanomaterial Applied on Limestone from a Roman Archaeological Site, Materials (Basel). 11 (2018) 694.

[24] F. Elhaddad, L.A.M. Carrascosa, M.J. Mosquera, Long-term effectiveness, under a coastal environment, of a novel conservation nanomaterial applied on sandstone from a Roman archaeological site, J. Cult. Herit. 34 (2018) 208.

[25] X.-M. Li, D. Reinhoudt, M. Crego-Calama, What do we need for a superhydrophobic surface? A review on the recent progress in the preparation of superhydrophobic surfaces., Chem. Soc. Rev. 36 (2007) 1350.

[26] S. Das, S. Kumar, S.K. Samal, S. Mohanty, S.K. Nayak, A Review on Superhydrophobic Polymer

Nanocoatings: Recent Development and Applications, Ind. Eng. Chem. Res. 57 (2018) 2727.

[27]   L. Gao, T.J. McCarthy, Contact angle hysteresis explained., Langmuir. 22 (2006) 6234.

[28]   M. Callies, D. Quéré, D. Quere, On water repellency, Soft Matter. 1 (2005) 55.

[29]   W. Barthlott, C. Neinhuis, H. Verlot, C.L. Schott, Purity of the sacred lotus , or escape from contamination in biological surfaces, Planta. 202 (1997) 1.

[30]   G. Zhang, J. Zhang, G. Xie, Z. Liu, H. Shao, Cicada wings: A stamp from nature for nanoimprint lithography, Small. 2 (2006) 1440.

[31]   M. Liu, Y. Hou, J. Li, L. Tie, Z. Guo, An all-water-based system for robust superhydrophobic surfaces, J. Colloid Interface Sci. 519 (2018) 130.

[32]   T. Darmanin, F. Guittard, Recent advances in the potential applications of bioinspired superhydrophobic materials, J. Mater. Chem. A. 2 (2014) 16319.

[33]   S.H. Anastasiadis, Development of functional polymer surfaces with controlled wettability, Langmuir. 29 (2013) 9277.

[34]   L. Gao, T.J. McCarthy, Wetting 101° †, Langmuir. 25 (2009) 14105.

[35]   L. De Ferri, P.P. Lottici, A. Lorenzi, A. Montenero, E. Salvioli-Mariani, Study of silica nanoparticles - polysiloxane hydrophobic treatments for stone-based monument protection, J. Cult. Herit. 12 (2011) 356.

[36]   C. Hu, W. Chen, T. Li, Y. Ding, H. Yang, S. Zhao, E.A. Tsiwah, X. Zhao, Y. Xie, Constructing non-fluorinated porous superhydrophobic SiO2-based films with robust mechanical properties, Colloids Surfaces A Physicochem. Eng. Asp. 551 (2018) 65.

[37]   Y. Liu, Q. Xu, A.M. Lyons, Durable, optically transparent, superhydrophobic polymer films, Appl. Surf. Sci. 470 (2019) 187.

[38]   M. Manca, A. Cannavale, L. De Marco, A.S. Aric??, R. Cingolani, G. Gigli, Durable superhydrophobic and antireflective surfaces by trimethylsilanized silica nanoparticles-based sol-gel processing, Langmuir. 25 (2009) 6357.

[39]   D.S. Facio, L.A.M. Carrascosa, M.J. Mosquera, Producing lasting amphiphobic building surfaces with self-cleaning properties, Nanotechnology. 28 (2017) 265601.

[40]   L.A.M. Carrascosa, D.S. Facio, M.J. Mosquera, Producing superhydrophobic roof tiles, Nanotechnology. 27 (2016) 095604.

[41]   M.J. Mosquera, L.A.M. Carrascosa, N. Badreldin, Producing superhydrophobic/oleophobic coatings on Cultural Heritage building materials, Pure Appl. Chem. 90 (2018) 551.

[42]   P.N. Manoudis, A. Tsakalof, I. Karapanagiotis, I. Zuburtikudis, C. Panayiotou, Fabrication of

super-hydrophobic surfaces for enhanced stone protection, Surf. Coatings Technol. 203 (2009) 1322.

[43]   D. Aslanidou, I. Karapanagiotis, D. Lampakis, Waterborne superhydrophobic and superoleophobic coatings for the protection of marble and sandstone, Materials (Basel). 11 (2018) 585.

[44]   P.N. Manoudis, S. Papadopoulou, I. Karapanagiotis, A. Tsakalof, I. Zuburtikudis, C. Panayiotou, Polymer-Silica nanoparticles composite films as protective coatings for stone-based monuments, J. Phys. Conf. Ser. 61 (2007) 1361.

[45]   D.S. Facio, M.J. Mosquera, Simple strategy for producing superhydrophobic nanocomposite coatings in situ on a building substrate., ACS Appl. Mater. Interfaces. 5 (2013) 7517.

[46]   P. Gregorčič, B. Šetina-Batič, M. Hočevar, Controlling the stainless steel surface wettability by nanosecond direct laser texturing at high fluences, Appl. Phys. A Mater. Sci. Process. 123 (2017) 1.

[47]   Q. Ma, Z. Tong, W. Wang, G. Dong, Fabricating robust and repairable superhydrophobic surface on carbon steel by nanosecond laser texturing for corrosion protection, Appl. Surf. Sci. 455 (2018) 748.

[48]   J. Huo, Q. Yang, F. Chen, J. Yong, Y. Fang, J. Zhang, L. Liu, X. Hou, Underwater Transparent Miniature "Mechanical Hand" Based on Femtosecond Laser-Induced Controllable Oil-Adhesive Patterned Glass for Oil Droplet Manipulation, Langmuir. 33 (2017) 3659.

[49]   C. Liu, H. Zhan, J. Yu, R. Liu, Q. Zhang, Y. Liu, X. Li, Design of superhydrophobic pillars with robustness, Surf. Coatings Technol. 361 (2019) 342.

[50]   J. Yong, Q. Yang, F. Chen, D. Zhang, U. Farooq, G. Du, X. Hou, A simple way to achieve superhydrophobicity, controllable water adhesion, anisotropic sliding, and anisotropic wetting based on femtosecond-laser-induced line-patterned surfaces, J. Mater. Chem. A. 2 (2014) 5499.

[51]   B. Farshchian, J.R. Gatabi, S.M. Bernick, S. Park, G.-H. Lee, R. Droopad, N. Kim, Laser-induced superhydrophobic grid patterns on PDMS for droplet arrays formation, Appl. Surf. Sci. 396 (2017) 359.

[52]   M. Birnbaum, Semiconductor Surface Damage Produced by Ruby Lasers, J. Appl. Phys. 36 (1965) 3688.

[53]   F. Chu, S. Yan, J. Zheng, L. Zhang, H. Zhang, K. Yu, X. Sun, A. Liu, Y. Huang, A Simple Laser Ablation-Assisted Method for Fabrication of Superhydrophobic SERS Substrate on Teflon Film, Nanoscale Res. Lett. 13 (2018).

[54]   F. Müller, C. Kunz, S. Gräf, Bio-Inspired Functional Surfaces Based on Laser-Induced Periodic

21

Surface Structures, Materials (Basel). 9 (2016) 476.

[55]   A.Y. Vorobyev, C. Guo, Direct femtosecond laser surface nano/microstructuring and its applications, Laser Photonics Rev. 7 (2013) 385.

[56]   L. Li, J. Zhang, A. Wang, Removal of Organic Pollutants from Water Using Superwetting Materials, Chem. Rec. (2017) 118.

[57]   T. Darmanin, F.F. Guittard, Superhydrophobic and superoleophobic properties in nature, Mater. Today. 18 (2015) 273.

[58]   M.S. Hosseini, M.T. Sadeghi, M. Khazaei, Improving oleophobicity and hydrophilicity of superhydrophobic surface by TiO2-based coatings, Mater. Res. Express. 5 (2018).

[59]   T. Jiang, Z. Guo, W. Liu, Biomimetic superoleophobic surfaces: Focusing on their fabrication and applications, J. Mater. Chem. A. 3 (2015) 1811.

[60]   J. Yong, F. Chen, Q. Yang, J. Huo, X. Hou, Superoleophobic surfaces, Chem. Soc. Rev. 46 (2017) 4168.

[61]   T. Nishino, M. Meguro, K. Nakamae, M. Matsushita, Y. Ueda, The Lowest Surface Free Energy Based on −CF3 Alignment, Langmuir. 15 (1999) 4321.

[62]   J. Liang, L. Wang, J. Bao, L. He, SiO2-g-PS/fluoroalkylsilane composites for superhydrophobic and highly oleophobic coatings, Colloids Surfaces A Physicochem. Eng. Asp. 507 (2016) 26.

[63]   Z. Xue, M. Liu, L. Jiang, Recent developments in polymeric superoleophobic surfaces, J. Polym. Sci. Part B Polym. Phys. 50 (2012) 1209.

[64]   M. Liu, S. Wang, Z. Wei, Y. Song, L. Jiang, Bioinspired Design of a Superoleophobic and Low Adhesive Water/Solid Interface, Adv. Mater. 21 (2009) 665.

[65]   Y. Wang, X. Gong, Special oleophobic and hydrophilic surfaces: approaches, mechanisms, and applications, J. Mater. Chem. A. 5 (2017) 3759.

[66]   J. Yong, F. Chen, M. Li, Q. Yang, Y. Fang, J. Huo, X. Hou, Remarkably Simple Achievement of Superhydrophobicity, Superhydrophilicity, Underwater Superoleophobicity, Underwater Superoleophilicity, Underwater Superaerophobicity, and Underwater Superaerophilicity on Femtosecond Laser Ablated PDMS Surfaces, J. Mater. Chem. A. 5 (2017) 25249.

[67]   J. Yong, F. Chen, Q. Yang, D. Zhang, U. Farooq, G. Du, X. Hou, Bioinspired underwater superoleophobic surface with ultralow oil-adhesion achieved by femtosecond laser microfabrication, J. Mater. Chem. A. 2 (2014) 8790.

[68]   J. Yong, Q. Yang, F. Chen, G. Du, C. Shan, U. Farooq, J. Wang, X. Hou, Using an "underwater superoleophobic pattern" to make a liquid lens array, RSC Adv. 5 (2015) 40907.

[69]   W. Barthlott, T. Schimmel, S. Wiersch, K. Koch, M. Brede, M. Barczewski, S. Walheim, A. Weis,

22

A. Kaltenmaier, A. Leder, H.F. Bohn, The Salvinia Paradox: Superhydrophobic Surfaces with Hydrophilic Pins for Air Retention Under Water, Adv. Mater. 22 (2010) 2325.

[70]   D. Jacques, L. Wang, E. Martens, D. Mallants, Modelling chemical degradation of concrete during leaching with rain and soil water types, Cem. Concr. Res. 40 (2010) 1306.

[71]   P. Romano, P.S.D. Brito, L. Rodrigues, Monitoring of the degradation of concrete structures in environments containing chloride ions, Constr. Build. Mater. 47 (2013) 827.

[72]   S.-D. Wang, Y.-S. Jiang, The durability of superhydrophobic films, Appl. Surf. Sci. 357 (2015) 1647.

[73]   A. Pedna, G. Giuntoli, M. Frediani, P. Frediani, L. Rosi, Synthesis of functionalized polyolefins with novel applications as protective coatings for stone Cultural Heritage, Prog. Org. Coatings. 76 (2013) 1600.

[74]   A. Milionis, E. Loth, I.S. Bayer, Recent advances in the mechanical durability of superhydrophobic materials, Adv. Colloid Interface Sci. 229 (2016) 57.

[75]   K. Ellinas, A. Tserepi, E. Gogolides, Durable superhydrophobic and superamphiphobic polymeric surfaces and their applications: A review, Adv. Colloid Interface Sci. 250 (2017) 132.

[76]   T. Verho, C. Bower, P. Andrew, S. Franssila, O. Ikkala, R.H.A. Ras, Mechanically Durable Superhydrophobic Surfaces, Adv. Mater. 23 (2011) 673.

[77]   B.P. Dyett, A.H. Wu, R.N. Lamb, Mechanical Stability of Surface Architecture—Consequences for Superhydrophobicity, ACS Appl. Mater. Interfaces. 6 (2014) 18380.

[78]   I. Karapanagiotis, A. Pavlou, P.N. Manoudis, K.E. Aifantis, Water repellent ORMOSIL films for the protection of stone and other materials, Mater. Lett. 131 (2014) 276.

[79]   D. Aslanidou, I. Karapanagiotis, C. Panayiotou, Tuning the wetting properties of siloxane-nanoparticle coatings to induce superhydrophobicity and superoleophobicity for stone protection, Mater. Des. 108 (2016) 736.

Capítulo 2

Objetivos

La presente Tesis Doctoral se ha desarrollado en el marco de los proyectos de investigación "Materiales de construcción ecosostenibles por su acción superhidrofugante, autolimpiante, descontaminante y biocida (Ref. MAT2013-42934)" y "Hormigón y otros materiales de construcción innovadores por su acción autolimpiante, secuestrante de contaminantes, repelente y biocida (Ref. MAT2017-84228R)", financiados por el Ministerio de Economía y Competitividad en la convocatoria de proyectos orientados a los retos de la sociedad. Asimismo, esta esis Doctoral se ha desarrollado dentro del marco del proyecto europeo "InnnovaConcrete (Ref. 760858)", perteneciente al programa H2020. De acuerdo a esto, el objetivo de esta Tesis Doctoral es **obtener materiales de construcción que posean propiedades de humectación especiales, lo que permita incrementar su vida útil**. Este objetivo general se puede desglosar en los siguientes objetivos específicos:

1. Diseño de un producto superhidrofugante que contenga nanopartículas hidrófobas (capaces de reducir la energía superficial y crear una rugosidad característica de un estado Cassie-Baxter), un oligómero que polimeriza para formar puentes de sílice entre las nanopartículas, y el tensioactivo n-octilamina, el cual cataliza la reacción sol-gel y favorece la formación de un gel mesoporoso. Además, se añade un disolvente (hexano) para favorecer la agregación de las nanopartículas. Este objetivo puede desglosarse en los siguientes objetivos:

- Estudio del efecto de la proporción oligómero de sílice/nanopartículas, así como la función del hexano promoviendo la agregación, en las estructuras de los nanomateriales obtenidos, empleando para ello Microscopía Electrónica de Trasmisión (TEM).

- Aplicación de los productos obtenidos sobre piedra caliza y evaluación de su eficacia superhidrofugante.

- Relación entre las estructuras formadas por las diferentes proporciones de nanopartículas con la rugosidad obtenida sobre el sustrato aplicado, y relación de la topografía con la eficacia superhidrofugante.

- Evaluación de la adhesión de los productos al sustrato, y relación con las diferentes estructuras obtenidas.

2. Obtención de superficies de mármol superhidrofugantes combinando la aplicación de un sol que contiene un oligómero de sílice y PDMS, para producir un ORMOSIL que reduzca la energía superficial, y posterior uso de la ablación láser para crear una rugosidad característica de un estado Cassie-Baxter. Este objetivo específico puede además dividirse en los siguientes:

- Aplicación del sol sobre mármol para producir superficies hidrofugantes.
- Ablación de la superficie previamente aplicada con un láser UV empleando diferentes valores de fluencia (energía por unidad de área).
- Estudio de la dependencia de la rugosidad (y en consecuencia de la efectividad superhidrofugante) con la fluencia.
- Evaluación de la adhesión de las superficies obtenidas.

3. Diseño de un producto superhidrofugante y oleofugante empleando para ello un sol consistente dispersión acuosa de nanopartículas (capaces de crear rugosidad) y un fluoroalquilsilano (capaz de reducir la energía superficial). Este objetivo principal se divide en los siguientes.

- Aplicación del producto obtenido sobre diferentes materiales de construcción (caliza, granito, hormigón y madera).
- Evaluación de la eficacia superhidrofugante y oleofugante.
- Estudio topográfico de las superficies obtenidas y relación con las propiedades de humectación.
- Evaluación de la durabilidad de las superficies tratadas mediante un ensayo de adhesión y un ensayo de simulación de lluvia.

4. Diseño de un producto para protección de hormigón, consistente en un oligómero de sílice y PDMS, capaz de reducir la energía superficial, y nanopartículas de TiO_2, las cuales promueven un estado Cassie-Baxter, y además son capaces de producir superhidrofilia en la superficie gracias al efecto fotocatalítico del TiO_2, mientras que el interior del material que no está expuesto a la luz preserva su hidrofobicidad, protegiendo al hormigón de la penetración de agua. Los siguientes objetivos específicos pueden desglosarse:

- Aplicación del producto obtenido sobre hormigón para producir superficies superhidrofugantes.

- Estudio de la influencia de la radiación UV-Vis en el paso de comportamiento superhidrófobo a superhidrofílico.

- Estudio topográfico de las superficies y relación con las propiedades de humectación.

- Evaluación de la eficacia superoleofugante bajo agua de las superficies superhidrofílicas, y de su consecuente habilidad auto-limpiante frente a manchas oleosas.

- Evaluación de la capacidad de las muestras tratadas para evitar la penetración de agua, usando para ello un ensayo de absorción por capilaridad. Con esto se pretende demostrar que las muestras superhidrofílicas mantienen la hidrofobicidad en el interior de la estructura porosa del material.

- Evaluación de la durabilidad de las muestras tratadas mediante diversos ensayos: adhesión, simulación de lluvia y exposición al exterior.
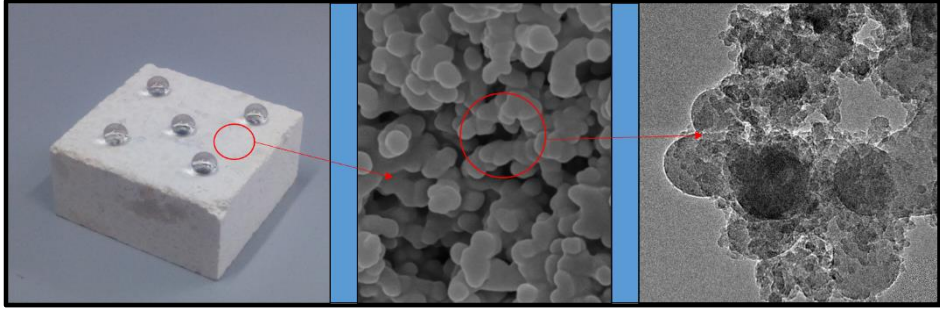
Capítulo 3

Long-lasting superhydrophobic coatings with application on building materials.

3.1. Abstract.

The use of hydrophobic nanoparticles to provide superhydrophobic performance to building materials finds important drawbacks due to the low adhesion of the nanoparticles to the treated surface, and the formation of aggregates promoting cracking, which promotes a low durability. A common strategy for enhance the durability is to integrate the hydrophobic nanoparticles into matrix. However, when the nanoparticles situated on the top of the matrix are removed the superhydrophobicity is lost. In this work, we reported a novel strategy for producing long-lasting superhydrophobic surfaces on building materials. Specifically, a coating mainly composed by hydrophobic silica nanoparticles aggregates, where the silica matrix only acts as a binder between the nanoparticles due to its low proportion, was applied. The obtained surfaces showed extremely high superhydrophobic performance due to the formation of aggregates, which promote double scale roughness. In addition, an adhesion test demonstrated the long-lasting superhydrophobic performance of the obtained coating, as a consequence of the role of the silica matrix joining the aggregates.

3.2. Introduction.

Water is the agent of decay which more aggressively attacks building materials, through different mechanisms, such as salt crystallization, biodecay or ice swelling [1–5].

For this reason, the research on superhydrophobic surfaces, which present static contact angle (SCA) value over 150° and contact angle hysteresis (CAH) value lower than 10° [6,7]. This kind of surfaces are obtained by the combined action of a low surface energy and a surface roughness able to create a Cassie-Baxter state [8,9].

The use of hydrophobic nanoparticles (NPs) to produce superhydrophobic surfaces has been investigated because they are able to lowering surface energy (due to their functionalization) and produce the Cassie-Baxter state (because of the creation of nano-roughness) [10]. This strategy is typically employed in some commercial products such as Aquashield, from Tecnan. However, the hydrophobic NPs are usually applied into a solvent, which is quickly evaporated leaving a coating of the NPs on the surface, producing an aggregation of the NPs and, therefore, a cracking of the coating [11]. In addition, the NPs on the surface present weak adhesion to the substrate due to the absence of any link between the NPs and the substrate [12]. It is obvious that the use of superhydrophobic surfaces with low durability are not adequate for employing on building materials, which are exposed to outdoor conditions.

According to the previously exposed, different methods has been investigated to improve the durability of the superhydrophobic surfaces [10,12–14]. The most typically strategy in the case of building materials is to integrate the NPs into a silica matrix that confers adherence to the substrate [15–20]. However, the NPs are situated on the silica matrix surface and after being removed by the degradation agents (wind, rain, etc.) the surfaces lose the superhydrophobic performance. In addition, the matrix present hydrophilic behaviour, which decrease the superhydrophobic performance.

The target of this work is the creation of long-lasting superhydrophobic surfaces on building materials by using a coating mainly composed by hydrophobic silica NPs, where the silica matrix is only acting as a binder due to its low proportion respect to

the NPs. A coating that presents superhydrophobic performance in the whole bulk, instead of only on the surface, is obtained. Thus, if the upper layer of NPs is removed, another layer will remain preserving the superhydrophobicity. In order to find the optimum proportion of hydrophobic NPs, different ratios hydrophobic NPs/silica matrix were studied. In addition, the effect of a non-polar solvent inducing the NPs aggregation was investigated.

The obtained nanomaterials were characterized by TEM in order to observe the changes in the morphological structure. The prepared products were applied, as sols, on limestone samples with application on building materials. The superhydrophobic performance as well as the durability of the treated samples was evaluated, and the obtained results were discussed in basis to the acquired SEM and AFM images of the samples surfaces under study.

3.3. Materials and methods.

3.3.1. Synthesis of the nanomaterials.

The following reactant were employed. Wacker TES40 (purchased by Wacker Chemie) is a mixture of oligomeric ethoxysiloxanes with an average chain length of 5 Si-O units. Aerosil NAX50 (hereinafter HSi-NPs, supplied by Evonik) are fumed silica NPs with a size of around 40 nm and an average surface area of 40 $m^2 \cdot g^{-1}$. They are functionalised with HMDS, which provides them hydrophobic properties. n-octylamine (purchased by Sigma-Aldrich) was employed as catalyst.

The superhydrophobic nanomaterials were prepared according the following synthesis route: (1) a starting silica sol was prepared by ultrasonic mixing of Wacker TES40, n-octylamine and deionized water. The relation of TES40, n-octylamine and water was 98.82, 0.36 and 0.82 % v/v, respectively. The sol was homogenized, with an ultrasonic probe (Bandelin Ultrasonic HD3200, from Sonopuls), during 10 minutes with a power of 2.5 $W \cdot mL^{-1}$. (2) Then, HSi-NPs were added to the prepared sol in three different proportions: 7, 10 and 20 %wt, respect to the total volume of the starting sol. The HSi-NPs were dispersed in hexane (0.25 g/mL), before mixing them with the

previously prepared sol. Thus, the amount of hexane was increased with the proportion of NPs. The obtained sols were homogenized with the ultrasonic probe for 2 minutes, with a power of 1 W·mL^{-1}. In addition, a product without HSi-NPs was also synthesized in order to study the sol-gel properties of the silica matrix. **Table 1** shows the composition of each product respect to the silica sol.

Table 1. Percentage values of the HSi-NPs respect to the silica sol.

Product	HSi-NP (%w/v)[a]	HSi-NPs/silica matrix ratio[b]
UCA	0	0.0
UCA7S	7	0.6
UCA10S	10	0.8
UCA20S	20	1.7

[a]Weight of NPs respect to the total volume of silica sol. [b]Volume ratio of the HSi-NPs respect to the silica matrix.

An important issue in this work is the space occupied by the HSi-NPs respect to the silica matrix where they are integrated. Thus, the apparent density of the silica matrix and the HSi-NPs was obtained by using a Mercury Intrusion Porosimeter (Poremaster, from QuantaChrome Instruments). Apparent density values of 0.8863 and 0.2632 g·cm^{-3} were obtained for UCA nanomaterial and HSi-NPs, respectively. The volume of the silica matrix was calculated taking into account that 100 g of TES40 turn into 40 g of silica after complete hydrolysis (according to manufacturer). The volume ratio of HSi-NPs/silica matrix is shown in **Table 1**.

3.3.2. Characterization of nanomaterials.

Immediately after being synthesized, the sols were subjected to a rheological study by means of a concentric cylinder viscometer DV-II with an UL/L adapter, from Brookfield Engineering Laboratories Inc. The measurements were carried out at constant temperature of 25 °C by means of recirculated water from a thermostatic bath. The shear rate vs. shear stress curve was represented and the viscosity was calculated as the slope of the lineal part of the curve (Newtonian threshold).

In order to study the sol-gel process of the products, 3 mL of each sol was casted in open Petri dishes, and they were let to gel. The obtained xerogels were studied after 4

months, when constant weight was reached. The rest volume of the sols was storage in closed vessel to test their stability.

A morphological study of the xerogels was performed by using a Transmission Electron Microscope (TEM) (JEOL 2010F).

The textural properties of the obtained xerogels were studied by means of Nitrogen Physisorption isotherms, acquired with an Autosorb IQ equipment, from Quantachrome. Total pore volume, pore size distribution and surface BET area were calculated. Pore size distribution was obtained from the adsorption branches by using NL-DFT (Non-Local Density Functional Theory) [21].

3.3.3. Evaluation of effectiveness and surface characterization.

The products under study were applied onto samples (4x4x2 cm) of a pure limestone (95 % $CaCO_3$ in composition, with impurities of SiO_2) with low open porosity (around 4 %). The products were sprayed with a pressure of 2 bars, and the excess of product was removed with an air flow (same pressure). Additionally, in order to stablish a comparison, a solution of HSi-NPs in hexane (0.25 g/mL) was applied in order to test the effectiveness and durability of the NPs without a silica oligomer. UCA product, which does not contain HSi-NPs, was not applied to evaluate effectiveness.

The samples were weighed before and immediately after being applied, in order to calculate their uptake value. Then, they were re-weighed after 4 months and the dry-matter value was calculated. All the tests described in the next paragraphs were carried out 4 months after application.

The topography of untreated samples and their treated counterparts was examined by Scanning Electron Microscopy (SEM), by using a Nova NanoSEM 450 from FEI. An elemental analysis of the surfaces was carried out with an EDS (Energy Dispersive of X-ray Spectroscopy) detector attached to the SEM.

Additionally, the roughness surface of the stones was evaluated by using an Atomic Force Microscope (AFM) Dulcinea, from Nanotec Electrónica.S.L., operating in tapping mode. Surface areas of 2.5 x 2.5 µm were acquired.

The wetting properties of untreated and treated samples were characterized by measuring water contact angle test (sessile drop method), using a commercial video-based, software-controlled contact angle analyzer, model OCA 15plus, from Dataphysics Instruments. Static (SCA) and dynamic (advancing and receding, ACA and RCA respectively) contact angle values were determined by following the procedure describe in a previous work [17]. Five water droplets were measured on each surface and the average values and standard deviation were calculated. The contact angle hysteresis value (CAH) was calculated as the difference between ACA and RCA, as a measure of water repellence.

In order to test the water repellent properties of treated stone surface, we performed a simple experiment. A treated sample was slightly tilted (15°) and water droplets of about 50 μL were directly poured onto the surface under study. In order to stablish comparisons, the experiment was also performed on an untreated sample. The test was recorded by a digital compact camera (Sony Cyber-Shot model DSC- P200) at 30 frames/s.

3.3.5. Evaluation of the durability.

In order to evaluate the durability of the different treatments, the adhesion of the coatings on the stone surfaces was tested by means of a tape test [15,17]. For each sample, a Magic Scott Tape from 3M was applied on the treated surface and removed. The process was repeated for 1, 2, 5, 10, 15 and 20 attach/detach cycles, and the CA values were measured after each one. In addition, SEM images of the treated surfaces were acquired after the tape test.

3.3.6. Evaluation of the negative effects.

The possible negative effect were evaluated. First, the changes in colour of the building material induced by the application of the products were tested. Total colour difference (ΔE*) was calculated by using a solid reflection spectrophotometer, Colorflex model, from Hunterlab. Illuminant D65 and observer CIE 10° were stablished at parameters. CIE L*a*b* scale was used, and variations in colour were evaluated. In

addition, the changes water vapour diffusivity were evaluated by using an automatic apparatus designed in our group [22].

3.4. Results and discussion.

3.4.1. Characterization of nanomaterials.

The sol-gel properties of the products under study are shown in **Table S1** in Supporting Information. All the sols showed a Newtonian behaviour with coefficient regression values over 0.99. Thus, the viscosity values were calculated as the slopes of the represented curves. UCA sol showed a viscosity value similar to the obtained in previous works using a similar synthesis route [23–25]. In the case of the products containing hexane (UCA7S, UCA10S and UCA20S), a gradual decrease in viscosity as the hexane content increases is observed. All the obtained viscosity values were low enough to guarantee their applicability by common procedures (spraying or brushing) [24].

The **Table S1** also shows the gel times for the synthesized products. All of them spontaneously gelled (gel time<24 h) because of the role played by n-8, which acts as a basic catalyst [26]. This spontaneous gelation confirms the applicability of all the products in situ, on buildings. By comparing the products, a gradual decrease of gel time was observed as HSi-NPs content was increased with significantly short time values for the highest HSi-NPs content (2 and 1 hour for UCA10S and UCA20S, respectively). As explained in a previous work [27], the presence of n-octylamine in the starting sol promotes the formation of silica seeds inside of inverse micelles, and posterior growth of these seeds until create the xerogel. We hypothesize that the HSi-NPs can play as preformed seeds, which accelerate the formation of the xerogel. Moreover, the use of a non-polar solvent, as previously demonstrated [28], promotes the aggregation of the HSi-NPs, decreasing the gel time.

Regarding to the stability in closed vessels (**Table S1**), all the products remained as sols for time above 6 months. Thus, the products can be storage during long periods, being susceptible of commercialization.

In order to test the morphology of the synthesized nanomaterials, TEM images were obtained. **Figure 1** shows representative images of the nanomaterials under study. In addition, TEM images of the silica matrix (UCA) and the HSi-NPs can be observed in Supporting Information (**Fig. S1**).
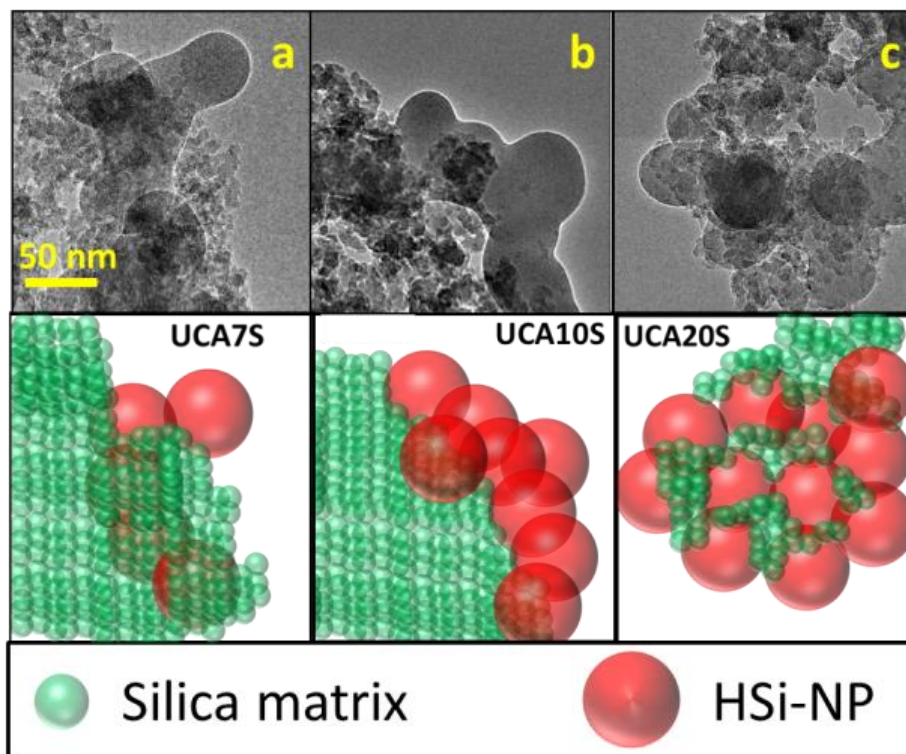
Figure 1. TEM images of the materials under study. (a)UCA7S, (b) UCA10S, (f) UCA20S. An schematic representation of the xerogel structures is also included.

The silica matrix (UCA, **Fig. S1a**) is composed of uniform NPs with an average size of 10 nm. As previously reported [27], the formation of this uniform NPs is due to the role of the surfactant n-octylamine involved in the synthesis. The micelles created by the surfactant act as nano-reactors, producing a xerogel composed of nearly uniform silica NPs with sizes ranging 8-20 nm in function of the surfactant content. The HSi-NPs (**Fig. S1b**) were homogeneous with an average diameter of 45 nm. The rest of nanomaterials showed a structure composed by the HSi-NPs integrated into the nanoparticulate silica matrix previously described. UCA7S and UCA10S (with ratios of 0.6 and 0.8, respectively) showed some of the hydrophobic NPs in the silica matrix surface (**Fig. 1a**

and 1b). On the other hand, UCA20S, with a significantly higher volume of HSi-NPs than that associated to the silica matrix (ratio of 1.7), showed a completely different structure (see **Fig. 1c**). HSi-NPs seem to be forming aggregates, which are joined by the silica matrix. **Figure 1** also shows schematic representations of the main structures formed for the UCA products.

The formation of the different structures can be explained according to: (i) the role played by the solvent polarity [28], (ii) the volumetric percentage of HSi-NPs respect to the silica matrix (see **Table 1**), and (iii) the differences in density of HSi-NPs and silica matrix. First, UCA7S showed evidences of a partial HSi-NPs aggregation (Fig. 1a). It is explained as a consequence of the presence of hexane in the sol. The non-polar solvent promotes the HSi-NPs aggregation as previously described [28]. As dispersion of the HSi-NPs in hexane was increases (UCA10S), a total aggregation of the NPs was observed. In addition, HSi-NPs were located on the xerogel surface due to the significant differences in apparent density values between the HSi-NPs and the silica matrix (0.3 and 0.9 g/cm^3, respectively). Finally, for UCA20S, the HSi-NPs/silica matrix ratio was 1.7. Thus, the significant higher proportion of HSi-NPs promotes the creation of xerogel mainly composed of HSi-NPs. In this case, the silica NPs does not produces a matrix due to their lower proportion. They are exclusively binding the HSi-NPs.

In order to study the textural properties of the nanomaterials under study, an analysis by Nitrogen Physisorption was carried out. The **Figure 2** shows the obtained adsorption-desorption isotherms (left) and pore size distribution (right), obtained by NL-DFT. In addition, the table inset in the Figure includes the textural parameters data. All our materials presented type IV isotherm according to IUPAC classification, which is characteristic of mesoporous materials [21]. Regarding to the hysteresis between the adsorption and the desorption branches, the products UCA and UCA7S showed a type H2(b) hysteresis, characterized by a triangular shape and a step in the desorption branch. As previously discussed [24], this kind of hysteresis indicates that mesoporous materials composed by uniform size particles, confirming the TEM results. On the other

hand, UCA10S and UCA20S presented H1 hysteresis, characteristic of mesoporous materials with a higher connectivity between pores [21].
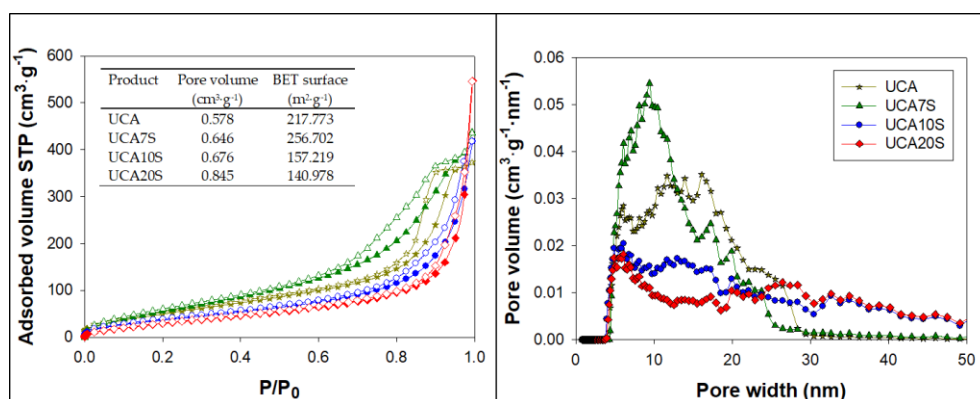

Figure 2. Adsorption-desorption isotherms (left) and pore size distributions obtained by the NL-DFT method (right) of the nanomaterials under study. The textural properties of the nanomaterials under study are included in an inset.

The pore size distribution (**Fig. 2**, right) was obtained from the adsorption branches of the isotherms. The NL-DFT method was employed. The obtained distributions demonstrated the formation of nanomaterials with uniform pore size, centred on 13 nm. For the product with the lowest proportion of solvent and NPs (UCA7S), the distribution was slightly narrower, with smaller pores (around 9 nm). Finally, in the case of the products with the highest concentrations of solvent and NPs (UCA10S and UCA20S), an increase of pore size, as well as a wider distribution (ranging from 6 to 25 nm), was observed, being this one highest for UCA20S.

Regarding to pore volume, the inset of **Fig. 2** shows that this one initially decreases when HSi-NPs, without solvent (UCA5S), is added to the sol. For the products with solvent, an increase of pore volume with NPs concentration was experimented.

In the case of the obtained values for BET surface area (also shown in the inset of **Fig. 2**), a decrease of the value of the pure silica matrix (UCA) was experimented when HSi-NPs were added (UCA5S), which can be due to the low surface area of these NPs (around 40 $m^2 \cdot g^{-1}$). An increase of this value was measured when solvent was added without a significant increase of NPs concentration (UCA7S). From this one, a decrease is observed for further increases in NPs concentration (UCA10S and UCA20S).

3.4.2 Evaluation of effectiveness and surface characterization.

All the UCA products containing HSi-NPs were applied onto a low-porous limestone and evaluated after 4 months. In addition, HSi-NPs dispersed in hexane were also applied. Both uptake and dry-matter percentage values were calculated. In all the cases, the uptake values were about 0.03 %w/w and dry-matter values about 0.01 %w/w, due to the low porosity of the stone.

The surface morphology of the surfaces under study was evaluated by means of SEM and AFM. **Figure 3** shows the obtained results for the untreated sample and its treated counterparts.

The first column of the **Fig. 3** shows the SEM images of the untreated surface and its treated counterparts. In addition, the Ca/Si ratio obtained by EDS analysis are included into the images. The untreated sample showed a heterogeneous surface mainly composed of calcite, as demonstrated by the high Ca/Si ratio. All the products formed a coating over the surface reducing the Ca/Si ratio (values around 0.05), demonstrating that a continuous coating was created by all the products [29]. The sample treated with the HSi-NPs presented a surface composed by dense aggregates of hydrophobic NPs heterogeneously distributed. As previously reported [28], the dispersion of HSi-NPs into a non-polar media (such as hexane) promotes the aggregation of the NPs.

In the case of UCA7S and UCA10S, the HSi-NPs could be clearly observed on the sample surface. We previously discussed the effect of solvent producing the accumulation of the HSi-NPs (see **Fig. 1a and b**). In addition, due to the low density of the HSi-NPs compared with the silica matrix, they were situated on the surface. Finally, the coating generated by the treatment with UCA20S showed bigger NPs than those observed for UCA7S and UCA10S. As explained according to TEM (see **Fig. 1c**), the dispersion of the HSi-NPs in hexane promotes aggregation, and the silica matrix acts as a binder, due to the high HSi-NPs/silica matrix ratio (1.7).
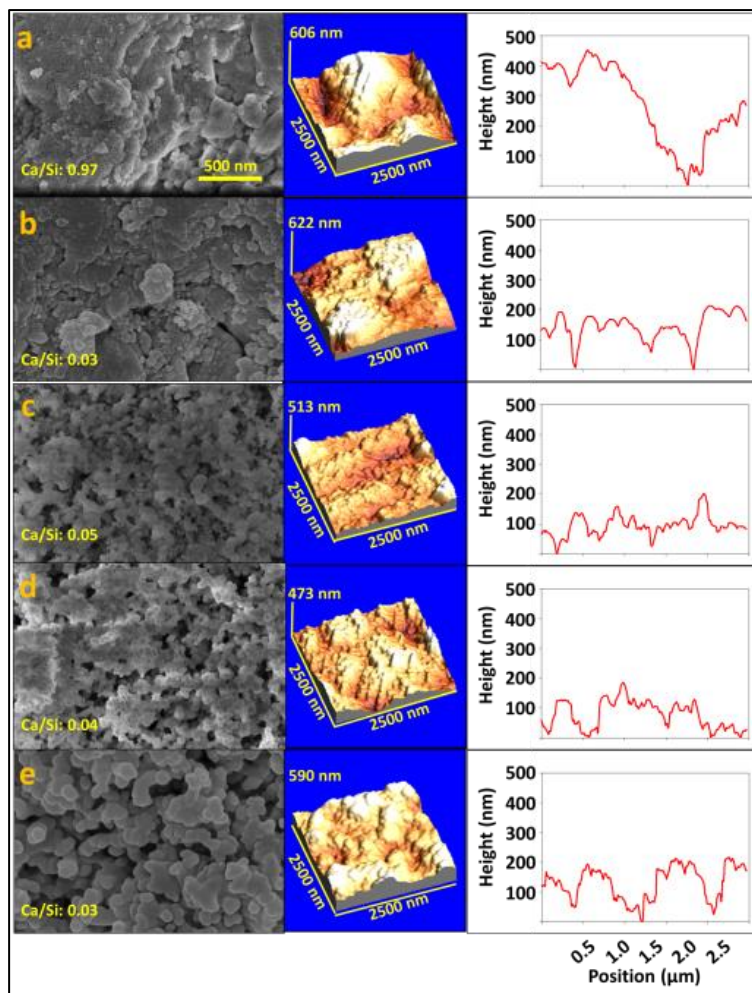
Figure 3. SEM images (first column), 3D AFM surface images (second column), and 2D roughness profiles (third column) of the surfaces under study. (a) Untreated, (b) HSi-NPs, (c) UCA7S, (d) UCA10S, (e) UCA20S.

The roughness of the surfaces under study was evaluated by acquiring AFM images. **Fig. 3** (second column) shows 3D AFM images of the untreated surface and its treated counterparts. The untreated stone showed a random roughness surface, which was covered for all the applied products, as previously observed in SEM. HSi-NPs and UCA products formed a surface composed of densely-packed NPs. As previously observed in SEM images, HSi-NPs (**Fig. 3b**) presented a high aggregation of the NPs due to the effect of the solvent, whereas UCA7S and UCA10S presented a surface with the HSi-NPs homogeneously distributed. Regarding to the sample treated with UCA20S, a surface

composed by great NPs was observed, because of the formation of aggregates previously described in TEM (**Fig. 1c**).

The 2D roughness profiles (**Fig. 3** third column) showed that the untreated surface (Fig. 3a) produced a profile with great valleys. As previously reported [24], the presence of great valley (combined with a high surface energy) promotes the adhesion of water droplets to the surface, giving rise to hydrophilic behaviour. On the other hand, all the treated surfaces presented profiles composed of uniformly separated peaks. Regarding to differences, samples treated with UCA7S and UCA10S showed similar profiles, with peaks spaced around 100 nm, whereas the samples treated with the HSi-NPs and UCA20S produced profiles with bigger peaks due to formation of aggregates, in which smaller peaks can be observed. Lee et al. [28] reported the creation of double roughness due to the aggregation of NPs by the effect of a non-polar solvent.

The results of contact angle measurements are shown in **Fig. 4a**. In addition, the numerical values are included in Supporting Information (**Table S2**).
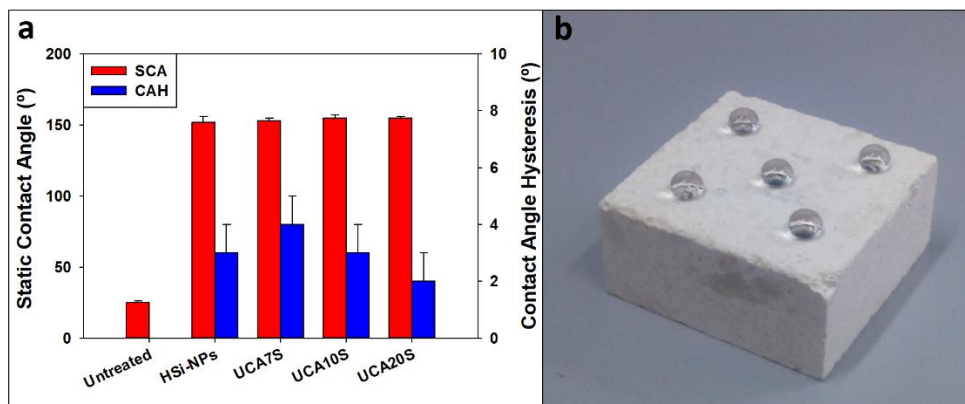
Figure 4. (a) SCA and CAH values of the untreated surfaces and their treated counterparts. (b) Photograph of water droplets on a sample treated with UCA20S.

The untreated surface presented a hydrophilic behaviour due to its composition (calcite), showing SCA values around 25°. All the treated samples showed SCA values higher than 150°, which negligible differences between them, and CAH values lower than 10°, demonstrating the superhydrophobic performance of all the products. In addition, **Fig. 4b** shows a photograph of water droplets deposited on a sample treated

with UCA20S. The droplets shows spherical shape due to the superhydrophobic performance of the surface.

Interestingly, the samples treated with HSi-NPs and UCA20S presented similar CAH values (around 3°), which were higher than those measured for UCA7S and UCA10S (around 6°). As previously demonstrated according to SEM and AFM (see **Fig. 3**), the coatings formed by HSi-NPs and UCA20S presented a high NPs aggregation, which promoted the formation of a double roughness structure. As reported in the literature [28,30,31], the creation of a double roughness structure gives rise to extremely high superhydrophobic performance.

In order to confirm the water repellent properties of the samples treated with our products, a simple test was carried out. A sample treated with UCA20S was slightly tilted (around 15°). Then, water droplets were deposited on the surface. The droplets rapidly rolled off the surface, demonstrating the water repellence given by our treatment. The video of this experiment can be found in the supporting information (**video S1**).

3.4.3. Evaluation of the durability.

The long-lasting superhydrophobic performance of the treated samples under study were evaluated by means of a tape test. The obtained results are shown in **Figure 5**.
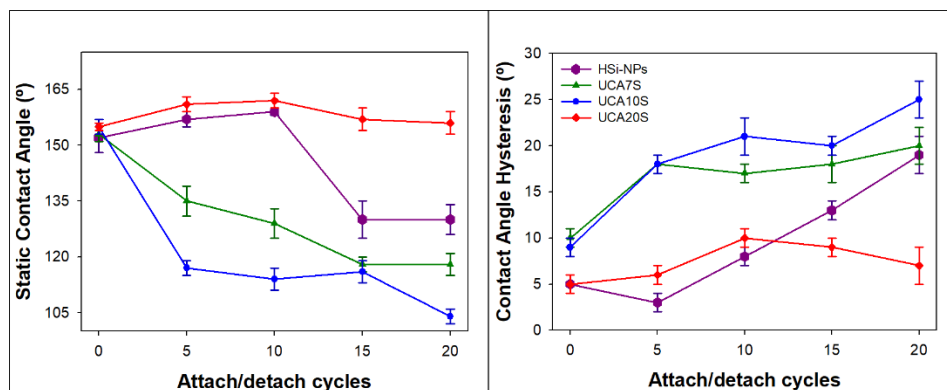

Figure 5. SCA (left) and CAH (right) values variation of the treated samples with the attach/detach cycles.

All the treatments, apart from UCA20S, suffered a rapid decrease of SCA and increase of CAH values. HSi-NPs were able to resist until 10 cycles, but after that, the superhydrophobic properties were quickly lost.

In order to explain the loss of the properties, a study of the surfaces by SEM images, after the 20 attach/detach cycles, were acquired and the results are shown in **Fig. 6**.

The obtained images showed that the surface treated with the HSi-NPs (**Fig. 6a**) was totally changed. The HSi-NPs were partially removed, exposing the untreated surface, which was confirmed by the increase of the Ca/Si ratio compared to the one before the tape test.

In the case of UCA7S and UCA10S (**Fig. 6b and c**, respectively), SEM images showed that the HSi-NPs were removed from the surface, leaving the exposed silica matrix. The Ca/Si ratio was hardly unmodified respect to the one before tape test, demonstrating that the silica matrix remains as a coating for these treatments.

Finally, the surfaces treated with UCA20S (**Fig. 6d**) did not present significant changes in SEM images, demonstrating that the created surface was maintained after the tape test.

As previously reported [28], the dispersion of the HSi-NPs in a non-polar media (hexane) promotes the aggregation between the NPs increasing the durability of the coatings, as observed for the samples treated with HSi-NPs, which resisted until 10 attach/detach cycles. Similar behaviour was reported by Latthe and co-workers [32] who applied an hexane dispersion of HDMS functionalized silica NPs on various substrates. The treated surfaces demonstrated moderated durability against tape test due to the aggregation of the NPs and the creation of several layers of coating. However, after the forth attach/detach cycle, the superhydrophobic performance were lost.
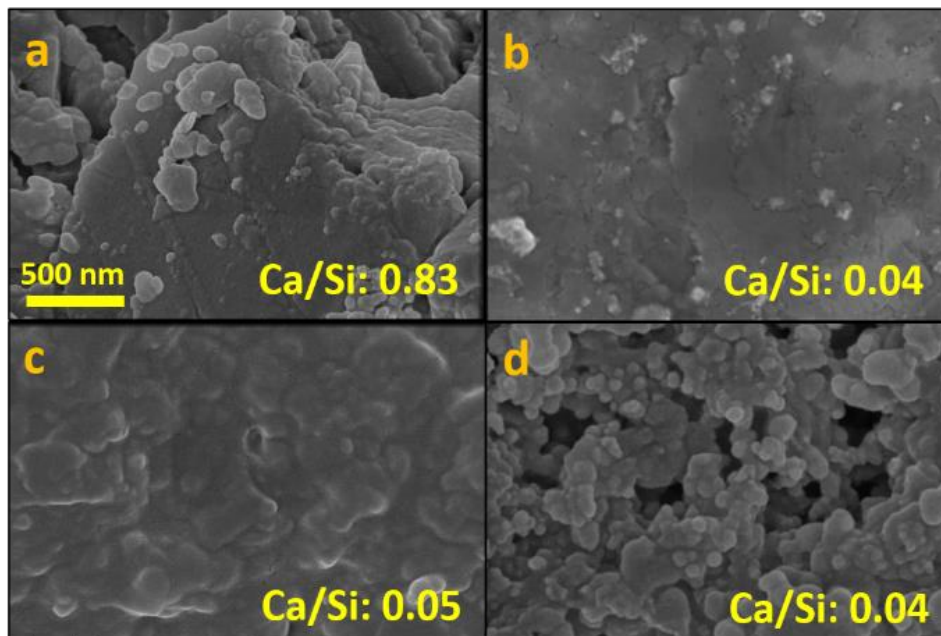
Figure 6. SEM images of the treated surfaces under study after 20 attach/detach cycles. (a) HSi-NPs, (b) UCA7S, (c) UCA10S, (d) UCA20S. Ca/Si ratio obtained by EDS analysis is also included.

On the other hand, the silica matrix produced by our sol-gel route is firmly attached to the stone substrate, as demonstrated in the current work for UCA7S and UCA10S, and in previous works [15,25]. In the case of UCA20S, the aggregation of the HSi-NPs (due to the solvent) is combined with the linking properties of the silica matrix, which acts as a binder between HSi-NPs increasing the durability of the formed aggregates. In addition, the silica matrix also assure the adhesion of the HSi-NPs aggregates to the sample surfaces, giving rise to long-lasting performance [33].

Hu and co-workers [12] reported the creation of long-lasting superhydrophobic surfaces by integrating hydrophobic silica NPs into an acrylic resin, which increased the adhesion to the substrate. However, a decrease of the SCA value was observed respect to the one measured for the hydrophobic NPs without the resin. The authors discussed that the hydrophilic behaviour of the acrylic resin reduce the superhydrophobicity obtained by the hydrophobic NPs. In the specific case of this work, the use an adequate HSi-NPs/silica matrix ratio allows to increase the durability of the coating without decrease the superhydrophobic performance.

3.4.5. Evaluation of the negative effects.

Regarding to the colour measurement, the results are shown in Supplementary Information (**Table S1**). All the treated samples showed values of ΔE* lower than 5 (or even 3), being below the human threshold perception. Thus, the colour change was totally negligible [34].

In the case of water vapour diffusivity measurement (**Table S1**), a value of 1.07±0.30 $m^2 \cdot s^{-1}$ was obtained for the untreated sample, which is due to its low porosity. All the treatments produced decrease in diffusivity lower than 11 %, which is consider an optimum value for building materials [34].

3.5. Conclusions.

The obtained results demonstrated the creation of superhydrophobic coatings by incorporating HSi-NPs to a silica matrix, obtained by a simple sol-gel synthesis. Different proportions of the HSi-NPs respect to the silica matrix were employed, and the influence of the volume occupied by the HSi-NPs in the effectiveness and durability was studied. For the product with the highest proportion of HSi-NPs (UCA20S), TEM results demonstrated the formation of aggregates of HSi-NPs joined by means of the silica matrix. These aggregates produced a double roughness on the treated surfaces, promoting superhydrophobic properties. In addition, the aggregates are joined each other and to the substrate by means of the silica matrix, increasing their adhesion, as demonstrated by tape test. Moreover, the creation of multilayers increased the durability by assuring the presence of undamaged layers of aggregates.

3.6. References.

[1]   A.E. Charola, Acid rain effects on stone monuments, J. Chem. Educ. 64 (1987) 436.

[2]   M.C. Phillipson, R. Emmanuel, P.H. Baker, The durability of building materials under a changing climate, Wiley Interdiscip. Rev. Clim. Chang. 7 (2016) 590–599.

[3]   E. Zanardini, P. Abbruscato, N. Ghedini, M. Realini, C. Sorlini, Influence of atmospheric pollutants on the biodeterioration of stone, Int. Biodeterior. Biodegradation. 46 (2000) 8305–8305.

[4]   P. Tiano, Biodegradation of Cultural Heritage: Decay Mechanisms and Control Methods, CNR-Centro Di Stud. Sulle Cause Deperimento e Metod. Conserv. Opere d'Arte. 9 (2001) 1–37.

[5]   D. Chang, J. Liu, Review of the influence of freeze-thaw cycles on the physical and mechanical properties of soil, Sci. Cold Arid Reg. 4 (2013) 457–460.

[6]   L. Gao, T.J. McCarthy, Wetting 101 degrees., Langmuir. 25 (2009) 14105–15.

[7]   L. Gao, T.J. McCarthy, Wetting 101° †, Langmuir. 25 (2009) 14105–14115.

[8]   J.B. Boreyko, C.H. Baker, C.R. Poley, C.H. Chen, Wetting and dewetting transitions on hierarchical superhydrophobic surfaces, Langmuir. 27 (2011) 7502–7509.

[9]   A.B.D. Cassie, S. Baxter, Wettability of porous surfaces, Trans. Faraday Soc. 40 (1944) 546–551.

[10]   S. Das, S. Kumar, S.K. Samal, S. Mohanty, S.K. Nayak, A Review on Superhydrophobic Polymer Nanocoatings: Recent Development and Applications, Ind. Eng. Chem. Res. 57 (2018) 2727–2745.

[11]   L. De Ferri, P.P. Lottici, A. Lorenzi, A. Montenero, E. Salvioli-Mariani, Study of silica nanoparticles - polysiloxane hydrophobic treatments for stone-based monument protection, J. Cult. Herit. 12 (2011) 356–363.

[12]   C. Hu, W. Chen, T. Li, Y. Ding, H. Yang, S. Zhao, E.A. Tsiwah, X. Zhao, Y. Xie, Constructing non-fluorinated porous superhydrophobic SiO2-based films with robust mechanical properties, Colloids Surfaces A Physicochem. Eng. Asp. 551 (2018) 65–73.

[13]   Y. Liu, Q. Xu, A.M. Lyons, Durable, optically transparent, superhydrophobic polymer films, Appl. Surf. Sci. 470 (2019) 187–195.

[14]   M. Manca, A. Cannavale, L. De Marco, A.S. Aric??, R. Cingolani, G. Gigli, Durable superhydrophobic and antireflective surfaces by trimethylsilanized silica nanoparticles-based sol-gel processing, Langmuir. 25 (2009) 6357–6362.

[15]   D.S. Facio, L.A.M. Carrascosa, M.J. Mosquera, Producing lasting amphiphobic building surfaces with self-cleaning properties, Nanotechnology. 28 (2017) 265601.

[16]   L.A.M. Carrascosa, D.S. Facio, M.J. Mosquera, Producing superhydrophobic roof tiles, Nanotechnology. 27 (2016) 095604.

[17]   M.J. Mosquera, L.A.M. Carrascosa, N. Badreldin, Producing superhydrophobic/oleophobic coatings on Cultural Heritage building materials, Pure Appl. Chem. 90 (2018) 551–561.

[18]   P.N. Manoudis, A. Tsakalof, I. Karapanagiotis, I. Zuburtikudis, C. Panayiotou, Fabrication of super-hydrophobic surfaces for enhanced stone protection, Surf. Coatings Technol. 203 (2009) 1322–1328.

[19]   D. Aslanidou, I. Karapanagiotis, D. Lampakis, Waterborne superhydrophobic and superoleophobic coatings for the protection of marble and sandstone, Materials (Basel). 11 (2018).

[20]   P.N. Manoudis, S. Papadopoulou, I. Karapanagiotis, A. Tsakalof, I. Zuburtikudis, C. Panayiotou, Polymer-Silica nanoparticles composite films as protective coatings for stone-based monuments, J. Phys. Conf. Ser. 61 (2007) 1361–1365.

[21]   M. Thommes, K. Kaneko, A. V. Neimark, J.P. Olivier, F. Rodriguez-Reinoso, J. Rouquerol, K.S.W. Sing, Physisorption of gases, with special reference to the evaluation of surface area and pore size distribution (IUPAC Technical Report), Pure Appl. Chem. 87 (2015) 1051–1069.

[22]   M.J. Mosquera, D. Benítez, S.H. Perry, Pore structure in mortars applied on restoration: Effect on properties relevant to decay of granite buildings, Cem. Concr. Res. 32 (2002) 1883–1888.

[23]   J.F. Illescas, M.J. Mosquera, Surfactant-Synthesized PDMS/Silica Nanomaterials Improve Robustness and Stain Resistance of Carbonate Stone, J. Phys. Chem. C. 115 (2011) 14624–14634.

[24]   D.S. Facio, M.J. Mosquera, Simple strategy for producing superhydrophobic nanocomposite coatings in situ on a building substrate., ACS Appl. Mater. Interfaces. 5 (2013) 7517–26.

[25]   L. Pinho, M.J. Mosquera, Titania-Silica Nanocomposite Photocatalysts with Application in Stone Self-Cleaning, J. Phys. Chem. C. 115 (2011) 22851–22862.

[26]   M.J. Mosquera, D.M. de los Santos, L. Valdez-Castro, L. Esquivias, New route for producing crack-free xerogels: Obtaining uniform pore size, J. Non. Cryst. Solids. 354 (2008) 645–650.

[27]   D.S. Facio, M. Luna, M.J. Mosquera, Facile preparation of mesoporous silica monoliths by an inverse micelle mechanism, Microporous Mesoporous Mater. 247 (2017) 166–176.

[28]   D.H. Lee, J. Jeong, S.W. Han, D.P. Kang, Superhydrophobic surfaces with near-zero sliding angles realized from solvent relative permittivity mediated silica nanoparticle aggregation, J. Mater. Chem. A. 2 (2014) 17165–17173.

[29]   F. Elhaddad, L. Carrascosa, M. Mosquera, Long-Term Effectiveness, under a Mountain Environment, of a Novel Conservation Nanomaterial Applied on Limestone from a Roman Archaeological Site, Materials (Basel). 11 (2018) 694.

[30]   M. Nosonovsky, B. Bhushan, Hierarchical roughness optimization for biomimetic superhydrophobic surfaces, Ultramicroscopy. 107 (2007) 969–979.

[31]   L. Passoni, G. Bonvini, A. Luzio, A. Facibeni, C.E. Bottani, F. Di Fonzo, Multiscale Effect of Hierarchical Self-Assembled Nanostructures on Superhydrophobic Surface, Langmuir. 30

(2014) 13581–13587.

[32]   S.S. Latthe, R.S. Sutar, V.S. Kodag, A.K. Bhosale, A.M. Kumar, K. Kumar Sadasivuni, R. Xing, S. Liu, Self – cleaning superhydrophobic coatings: Potential industrial applications, Prog. Org. Coatings. 128 (2019) 52–58.

[33]   X. Jing, Z. Guo, Biomimetic super durable and stable surfaces with superhydrophobicity, J. Mater. Chem. A. 6 (2018) 16731–16768.

[34]   J.D. Rodrigues, A. Grossi, Indicators and ratings for the compatibility assessment of conservation actions, J. Cult. Herit. 8 (2007) 32–43.

3.7. Supplementary information.

Table S1. Viscosity, gel time and stability of the prepared nanomaterials.

Product	Viscosity (mPa·s)	Gel time (hours)	Stability (months)
UCA	4.87	24	>6
UCA7S	2.95	8	>6
UCA10S	1.79	2	>6
UCA20S	1.02	1	>6
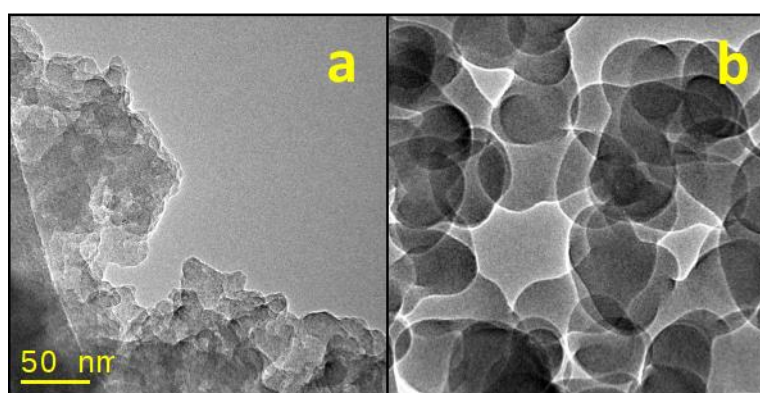
Figure S1. TEM images of (a) UCA xerogel and (b) HSi-NPs.

Table S2. Contact angle of water droplet (5 μL) placed on treated and untreated stone surfaces.

Product	SCA (°)	CAH (°)	ΔE*	VD (x10^{-6}, m^2·s^{-1})
Untreated	25±1	---	---	1.07±1.01
HSi-NPs	152±4	3.2±0.5	4.15±0.42	0.99±0.50
UCA7S	153±2	6.1±0.7	3.25±0.53	1.06±0.78
UCA10S	155±2	6.4±0.8	2.42±0.25	1.01±0.85
UCA20S	155±1	2.7±0.3	2.50±0.50	0.95±0.74

SCA: static contact angle, CAH: contact angle hysteresis (difference between advancing and receding CA). ΔE*: total colour difference. VD: vapour diffusivity.
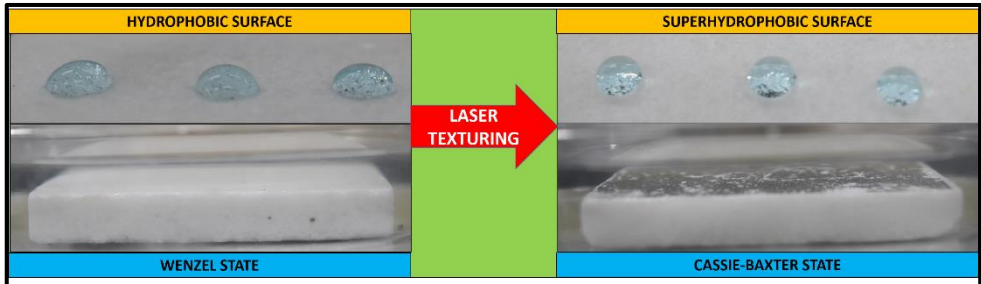
Capítulo 4

Producing Superhydrophobic Building Material by Laser Ablation.

4.1. Abstract.

4.2. Introduction.

4.3. Materials and methods.

4.4. Results and discussion.

4.5. Conclusions.

4.6. References.

4.1. Abstract.

The development of superhydrophobic surfaces, defined by static contact angle values higher than 150° and contact angle hysteresis lower than 10°, has gained significant interest in recent years due to their multiple applications for the protection of building materials against water-related decay, or their self-cleaning action. These surfaces, obtained by the combination of reducing surface energy (by chemical modification) and the creation of a micro- or nanoroughness, have been obtained in building materials by bottom-up approaches, but the use of top-down methods still remains unexplored.

In this work, we employ a versatile laser-based top-down approach that allows to create superhydrophobic surfaces on marble samples by laser ablation. The samples were pre-treated with a hydrophobic primer coating to decrease the surface energy and the texture was modified by laser ablation with a nanosecond-pulse laser. A clear correlation between the laser fluence (energy per unity of area), surface roughness and hydrophobic performance was observed, demonstrating that this strategy enables to have a proper control over the surface properties. Fluence values over the ablation threshold promoted a Cassie-Baxter state (superhydrophobic) due to melting of the material and its deposition on the surface as sub-micrometric particles, whereas the lower fluences gave rise to a random micro-roughness due to deformation of the material, which promotes a Wenzel wetting state (without water repellence).

4.2. Introduction.

Nowadays, the construction sector, which constitutes one of the fastest-growing markets, is facing significant challenges related with the service life of building materials under the increasingly aggressive environments (i.e. pollution, climate conditions…) and the associated repair and maintenance costs. Among the decay agents that compromise the durability of our buildings, water is often considered the most aggressive one due to its involvement in a wide variety of degradation processes [1,2], either by direct action (e.g. freeze-thaw cycles, lixiviation…) or as a vehicle for other decay agents (e.g. soluble salts, biological deteriogens, acid rain…). Calcium-rich materials, such as limestone, marble or concrete are especially susceptible to acid rain [1,3], commonplace in urban and industrial environments, which causes their solubilization by the formation of calcium sulphate (gypsum) and is involved in the formation of black crusts.

Because of the aforementioned reasons, there has been a growing interest for the development of hydrophobic protective treatments, which decrease the water ingress, and, more recently, superhydrophobic ones, with the ability to repel water and provide self-cleaning properties. Superhydrophobic surfaces are characterized by water static contact angle (SCA) values above 150° and contact angle hysteresis (CAH) values lower than 10° [4–6]. CAH is defined as the difference between advancing and receding contact angle (ACA and RCA, respectively) values, and it is measurement of the repellence [7]. In order to obtain superhydrophobic surfaces, it is necessary to decrease the surface free energy and to create a surface with regular micro- or nano-roughness [6,8–10]. Under these conditions, the surface reaches a Cassie-Baxter wetting state, characterized by a low interaction of water with the surface due to the entrapment of air pockets between its roughness features.

In order to produce the required surface roughness, several approaches have been reported in literature. These can be divided in two categories [11]: (1) bottom-up methods, where the roughness is created from smaller units (monomers, oligomers, nanoparticles…) by polymerization, aggregation or self-assembly processes. (2) Top-down methods, in which the surface roughness is created by the controlled removal of

material from the bulk. Examples of top-down methods include lithography, plasma etching, and laser ablation.

In the specific case of building materials, most efforts have been focused on the use bottom-up methods [12–15], mainly through the use of nanoparticles assemblages [16,17] and their combination with sol-gel strategies (e.g. organic modified silica gels, fluoroalkylsilanes) [12,18–21], due to their simplicity and suitability for *on site* applications. The top-down strategies, however, have not been exploited in this field despite their potential advantages regarding the control of the final structure, time requirements or the reduced use of reagents. Although these strategies have been usually considered too cumbersome for their practical use on building materials, the development of portable technologies with lower costs may place them as a viable alternative to the more traditional methods.

Among the top-down methods, laser texturing has gained special attention during the last years for a wide variety of applications [22–25]. This strategy have been successfully applied for controlling the roughness of substrates such as metals, semiconductors or polymers, with applications in nano/microfluidics, optofluidics, lab-on-chip technology, fluidic microreactors, biochemical sensors, biomedicine, and thermal management [26] among others. In spite of their versatility, as far as we are aware, laser treatments have not been used in order to achieve superhydrophobic surfaces for building materials. Nevertheless, the use of portable laser systems has been reported for the removal of stains and biological patinas on building materials [27–29], thus highlighting the feasibility of designing laser equipment for other applications on these materials.

In this work, we studied the application of the laser ablation method to promote superhydrophobic surfaces on building materials with self-cleaning performance and a high adhesion to the substrate. The Cassie Baxter state was achieved by the application of a ormosil primer coating [30], which reduces surface free energy, and its subsequent ablation by a nanosecond laser in order to control the surface roughness (by modifying the laser fluence). We found a high correlation between the laser fluence, the obtained surface roughness and the SCA and hysteresis values, indicating that this strategy can be potentially used to customize the surface properties of different substrates.

4.3. Materials and methods.

4.3.1. Synthesis and application of the hydrophobic primer coating.

The hydrophobic primer coating was prepared by a sol-gel according to a procedure developed in a previous work [30]. Specifically, a silica oligomer (TES40 WN, from Wacker Chemie AG), polydimethylsiloxane (PDMS from ABCR) were mixed, under ultrasound stirring, with an aqueous dispersion of n-octylamine (89.67 TES40, 10.00 PDMS, 0.08 n-oct. and 0.25 H_2O %v/v).

The prepared sol was sprayed on marble slabs by using an air-gun (pressure 3 bar) ($10x10x1$ cm^3) and removing the excess of product was removed with an airflow (pressure 2 bar). Afterwards, the samples were stored for one month in room conditions (20°C, 40% RH), until polymerization and dying of the gel were complete.

4.3.2. Texture modification by laser ablation.

Laser ablation of the surfaces (in 2.5 x 2.5 cm^2 areas) was carried out using a Nd:YAG solid state tripled-frequency laser of wavelength of 355 nm and 11 ns of pulse duration, model TruMark6350 from Trumpf. At 33 kHz, the nominal power reached is 5 W, resulting in a pulse energy of 0.15 mJ and pulse power of 13.6 kW. Considering that the beam diameter at the focal length is approximately 10 μm, the maximum fluence of the laser was calculated as 193 $J \cdot cm^{-2}$. All the experiments were carried out with a pulse repetition rate of 20 kHz, and the scanning speed was maintained at 50 $mm \cdot s^{-1}$. Different experiments were performed by varying the laser power between 60 and 100 %, for a fluence interval between 115.81 and 193.0 $J \cdot cm^{-2}$ (see Table 1).

Table 1. Values pulse power percentage and fluence for each percentage of nominal laser power (5 W).

%Power	Fluence ($J \cdot cm^{-2}$)
60	115.81
70	135.11
80	154.41
90	173.71
100	193.01

4.3.3. Evaluation of superhydrophobic performance and surface characterization.

The wetting properties of the marble surfaces were characterized by measuring the SCA and CAH values of 5 μl water droplets with a commercial video-based, software-controlled contact-angle analyzer (model OCA 15plus, from Dataphysics Instruments). Details of the experiment are reported in a previous paper [31].

The self-cleaning performance of the superhydrophobic surfaces was evaluated by registering a video of their ability to remove an staining agent under a low pressure water stream [14,32]. An untreated marble sample and its treated counterpart were stained with roof tile powder, in order to simulate dust. Then, water was dropped onto both samples to remove the powder.

The modifications on the surface topography caused by the laser treatment were evaluated by mean of two techniques.

First, the surface roughness was evaluated by using confocal optical profilometry. A 3D optical profilometer, model Z-300 from Zeta Instruments was employed. S_a (arithmetic mean surface roughness) were calculated from 2.0 x 2.5 cm^2 areas for each treatment.

The morphology of the surfaces under study was visualized by Scanning Electron Microscopy (SEM), using a Quanta200 equipment, from FEI. Prior to the measurement the samples were gold-sputtered with a 5 nm layer.

4.3.4. Evaluation of durability.

The durability of the treated marble surface exhibiting the best performance was evaluated by means of a tape test, according to a previously reported procedure [14,31]. The procedure was carried out by applying Scotch® MagicTM tape (3M) on the surface and swiftly detaching the tape in a vertical angle for repeated cycles. SCA and CAH values were evaluated at regular attach/detach intervals.

4.4. Results and discussion.

4.4.1. Evaluation of the superhydrophobic performance and surface characterization.

In order to test the relationship between the wetting behavior of the textured surfaces and the applied laser fluence, SCA and CAH values were evaluated (see **Fig. 1a**).
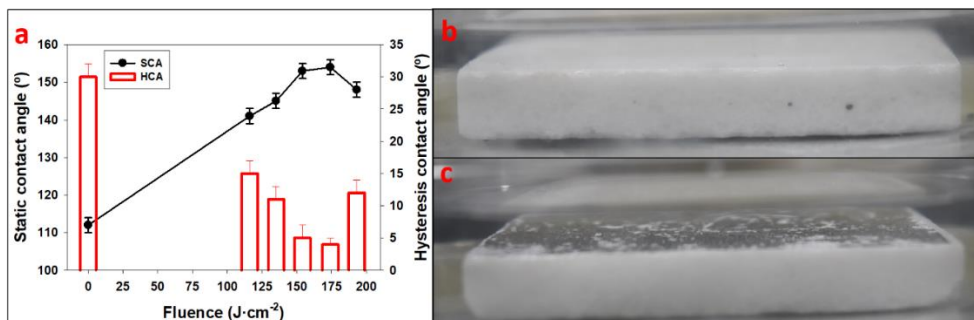

Figure 1. (a) Evolution of SCA and CAH values with laser fluence value. Photographs of (b) hydrophobic and (c) superhydrophobic samples soaked in water.

Prior to the laser ablation, the surface displayed a SCA value of 112°, due to the presence of the hydrophobic primer coating [30] reducing the surface free energy. The effect of the roughness induced by the laser treatment can be clearly seen by a significant increase in the SCA values up to 135-155°. Furthermore, a positive linear trend ($R^2 > 0.9$) was observed between the SCA values and the laser fluence up to 173.71 J/cm^{-2}, with superhydrophobic angles (> 150°) obtained at 150 and 173 J/cm^{-2}. This trend, however, changes at higher fluence values (193.01 J·cm^{-2}), where a slight decrease of the SCA was observed, suggesting that the high energy causes damages to the structure.

A similar trend could be observed for the repellence of the surfaces, indicated by the CAH value. Non-texturized surface showed a high CAH value (c.a. 30°), with no repellent properties, and a linear decrease of the CAH value as laser fluence increased was observed. The most effective treatments were obtained for laser fluences of 154.41 and 173.71 J·cm^{-2}, which displayed CAH below 10° that, along with their high (>150°) SCA values, confirmed the superhydrophobic nature of these surfaces [7,33]. A further increase of laser fluence caused the loss of the repellent properties, manifested by the CAH change from 4° (173.71 J·cm^{-2}) to 12° (193.01 J·cm^{-2}), which is characteristic of the

phenomenon known as petal rose effect [34], where water partially penetrates into the grooves of a highly hydrophobic surface, causing it to get pinned to the surface.

The transformation from Wenzel to Cassie-Baxter wetting states due to the laser treatment was assessed by visually observing the entrapment of air pockets between the roughness peaks [35] after submerging the samples in water. For this purpose, a comparison was made between two marble samples, an untexturized one and the other texturized with a fluence of 173.71 J·cm^{-2}. The first sample (**Fig. 1b**), which presented a hydrophobic behaviour with SCA around 120° and no repellence, showed that the surface was totally covered by the water, evidencing a Wenzel state. In this state, water penetrates the into the roughness valleys, and a total contact of water with the solid surface is achieved [36]. In contrast with this behaviour, the sample (**Fig. 1c**) presenting superhydrophobic performance (SCA above 150°), showed a mirror-like surface after immersion in water due to the presence of an air interlayer between water and the surface. This behaviour can be attributed with a Cassie-Baxter state, where water is deposited over the roughness peaks and air-pockets get trapped between the valleys [10].

The self-cleaning performance, achieved as a consequence of the superhydrophobic properties [37], was evaluated for the surfaces of the sample texturized with a fluence of 173.71 J·cm^{-2}, which showed the highest SCA and repellence. Specifically, an untreated sample and the treated one were soiled with roof tile powder and cleaned with a low-pressure water stream (A video recording of the experiment is available in Supporting Information, **Video S1**). For the untreated sample, the water extended over the non-repellent surface, spreading the powder over it and leaving a visible trail. On the other hand, in the case of the superhydrophobic sample, the low interaction causes the water to easily roll off the surface while carrying the powder with it, thus resulting in an effective removal of the stain.

As explained above, the differences in the wetting properties of the studied surfaces can be explained consider not only considering the effect of the hydrophobic primer coating, but also the influence of their topography (i.e. roughness and morphology) [6,12,13,38,39]. The results of the his study are presented in **Fig. 2** and **Fig. 3,** that show

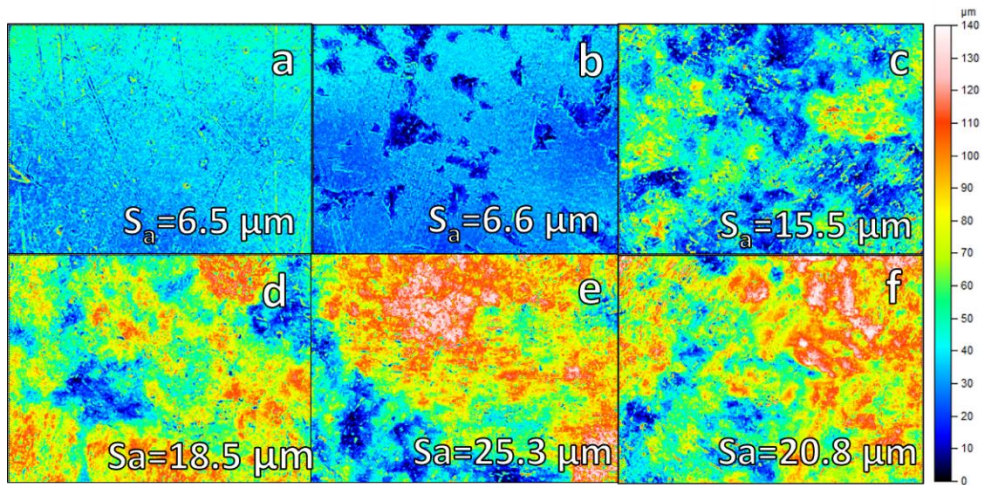surface roughness maps and SEM images, respectively, of the surfaces texturized at different laser fluence values.

Figure 2. Profilometry images of the marble surfaces texturized at different laser fluences: a) Non-texturized, b) 115.81 J·cm^{-2}, c) 135.11 J·cm^{-2}, d) 154.11 J·cm^{-2}, e) 173.71 J·cm^{-2}, 193.01 J·cm^{-2}. The measured surface was in all cases 2.0x2.5 cm.

The ability of the laser treatment to texturize the primer coating become evident by the profilometry maps and S_a values **(Figure 2),** which showed an evident increase of the roughness respect to the non-texturized surfaces. The non-texturized surface presented a smooth profile ($S_a = 6.5$ µm), practically without any defining topographical features, which is consistent with the typical morphology of the primer coating applied observed in other works [12]. At the lower laser fluence (115.81 J·cm^{-2}) values, the average roughness barely changed ($S_a = 6.6$ µm), but the surface presented a profile defined by plateaus and shallow valleys, indicating that the laser caused a mild ablation of the material. As laser fluence increases, the height differences became more pronounced (higher S_a) and the surfaces presented an aspect characterized by the presence of more tightly packed peaks and valleys, evidencing that a higher energy was necessary to promote effective changes to the material. A closer analysis of the S_a values showed a linear trend ($R^2 > 0.95$) correlating the fluence values (in the 115-173 J·cm^{-2} range) with the roughness, which explains the, also linear, trend observed for the contact angle (SCA, CAH) values (**Fig. 1a**). Also in agreement with the observed decreased in the contact angle values, at a higher fluence (193.01 J·cm^{-2}), the laser caused apparent damages in

the surface features, resulting in a similar profile but with a lower S_a value. In general, these results demonstrate that it is possible to have a control over the roughness by modifying the laser parameters, a versatility that could be potentially exploited for adapting this methodology to different substrates.

This almost linear dependence of SCA value with roughness is in good agreement with the Wenzel model, which stablishes that, for an inherently hydrophobic material (i.e. SCA >90° on an ideal flat surface), the contact angle will increase proportionally to a factor defined by the surface roughness [36]. Although roughness values can be related with SCA value, the S_a parameter and the Wenzel model by themselves, however, are not enough to explain the superhydrophobic performance (high SCA and low hysteresis) showed by the surfaces texturized with the highest fluence values. An explanation for this kind of behaviour has to account for the surface morphology, whose relation with the wetting properties is defined by the Cassie-Baxter model [10] (see **Fig. 1c**).

Thus, the surfaces under study were characterized by SEM in order to observe their morphology. **Figure 3** shows the micrographs of the texturized and non-texturized surfaces at different fluence values.

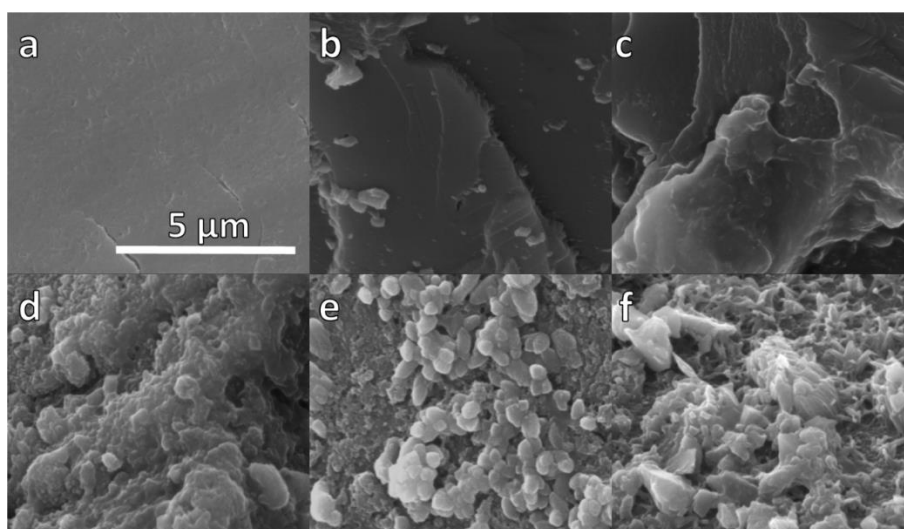**Figure 3**. SEM images of the marble surfaces texturized at different laser fluences: a) Non-texturized surface, b) 115.81 J·cm^{-2}, c) 135.11 J·cm^{-2}, d) 154.11 J·cm^{-2}, e) 173.71 J·cm^{-2}, 193.01 J·cm^{-2}.

For the non-texturized surface (**Fig. 3a**), a complete smooth surface was observed, which matches with the low roughness value obtained (see Fig. 3a), as well as the low

SCA value (112°). As reported in the literature [6,9], the maximum SCA value achievable in an ideal smooth surfaces would be 120° [40]. Regarding to the texturized surfaces, those irradiated with fluence values of 115.81 and 135.11 $J \cdot cm^{-2}$ (**Fig. 3b and c**, respectively) showed a heterogeneous rough surface, where the laser ablation have caused delamination-like removal of the material. An increase of surface roughness with the increase of laser fluence value, as well as the appearance of some (poorly defined) sub-micrometric bumps can be observed, which is in agreement with the data obtained from profilometry measurements. This situation fits the definition of a Wenzel surface, characterized by the presence of roughness features separated by large distances and following random arrangements.

The aspect of the samples ablated with higher fluence values, on the other hand, showed a hierarchical structure, characterized by the presence of submicron-scale ellipsoid particles of similar size on top of to the micron-scale alterations observed at lower fluence. These micrometric particles likely originated from melting of the material under the heat provoked by the laser pulse and its subsequent re-deposition on the surface, similarly to the observations made by different authors [41,42]. As explained in the previous sections, this hierarchical roughness promotes the creation of a Cassie-Baxter state [43–45], giving rise to superhydrophobic properties. In the case of the surface treated with the maximum fluence (193.01 $J \cdot cm^{-2}$, **Fig.3f**), the excessive energy caused a destruction of the previously created roughness, manifested by decreasing number of particles, irregular size and the loss of their ellipsoid shape. This irregular roughness profile promotes a switch from the Cassie-Baxter to the Wenzel state, which matches with the reduction of the SCA and increase of CAH (**Fig. 1a**).

According to the scientific literature, the effect of the laser ablation over the surface depends on three main factors: (1) The number of pulses per area [41] (depending of pulse repetition ratio, spot laser diameter and scanning speed). (2) The ablation threshold [46], which depends on the surface composition. (3) The fluence value of the laser radiation, which is the energy per unity of area. In our study, two of these variables can be considered constant. The pulse repetition ratio (20 kHz), spot laser diameter (10 μm) and scanning speed (50 $mm \cdot s^{-1}$) were maintained constant for all the texturized

surfaces, which means that 4 consecutive laser pulses were given on the same area. Thus, an accumulative effect due to the overlapping of laser pulses is produced [35,41,47]. On the other hand, the surface composition of the primer coating was also maintained constant (ormosil xerogel), and therefore, the ablation threshold is the same for all the texturized surfaces.

The effects on topography due to surface ablation at different laser fluences have been reported in several papers. According to the literature [43,48], fluence values slightly below the ablation threshold produce deformations and holes on the surface, which is responsible of the increase in roughness. This matches with the results obtained in this work for the lowest fluence values, where an increase in the surface roughness is observed for profilometry (**Fig. 2b and c**) and SEM (**Fig. 3b and c**) images. On the other hand, for fluence values exceeding this threshold, the generated heat causes the melting and rapid re-solidification of the surface material, which produce its deposition in the form of particles, as observed in the **Figure 3d and e**. Finally, for extreme fluence values over the threshold ablation, the heat is unable dissipate fast enough and causes the destruction of the previously formed surface (including the deposited nanoparticles) [49], in line with the changes observed in **Fig. 3f**.

Comparable observations to the results obtained in our work have been reported for different materials texturized by laser, highlighting the viability of adopting this strategy for its application on building materials. In a previous work [50], Yoon et al. reported the fabrication of superhydrophobic PDMS sheet by using laser texturing by employing a femtosecond laser (150fs) with a constant pulse repetition ratio of 1kHz. The increase in fluence value (from 3.4 to 4.9 J·cm^{-2}) promoted the deposition of nanoparticles onto the ablated surface, giving rise to a Cassie-Baxter surface topography with superhydrophobic performance. In another work [51], Farshchian et al. produced superhydrophobic grid patterns on PDMS sheets by using laser texturing with a nanosecond laser (25 ns) with a constant pulse repetition rate of 10 Hz and fluence value (5 J·cm^{-2}), also resulting in the deposition of nanoparticles and susequent superhydrophobic performance.

It should be noted that, although the conclusions are similar, a direct comparison of the values may prove difficult to establish due to the different laser and material

parameters. In the aforementioned works, PDMS sheets were employed as substrate for produce the superhydrophobic surfaces. Specifically, a 10:1 mixture by weight of PDMS base/curing agent (tetraethoxysilane) was prepared. Although these components are similar to the primer coating used in our work, the lower PDMS/silica oligomer we employed (c.a. 1:10) produces a highly reticulated silica backbone, unlike the mostly linear structure of PDMS sheets. This difference in the network reticulation explain the higher fluence required to surpass the ablation threshold (between 115 and 150 $J \cdot cm^{-2}$) compared to that used in the aforementioned works (around 5 $J \cdot cm^{-2}$).

4.4.3. Evaluation of durability.

The durability of the superhydrophobic surfaces and their adhesion to the substrate is an important requirement for their application to building materials, which are often exposed to aggressive environments. In order to test this factor, the sample texturized with a fluence value of 173 $J \cdot cm^{-2}$, which presented the best superhydrophobic performance, was evaluated by an adhesive tape test. The evolution of SCA and CAH values with the attach/detach cycles is shown in **Fig. 4**.
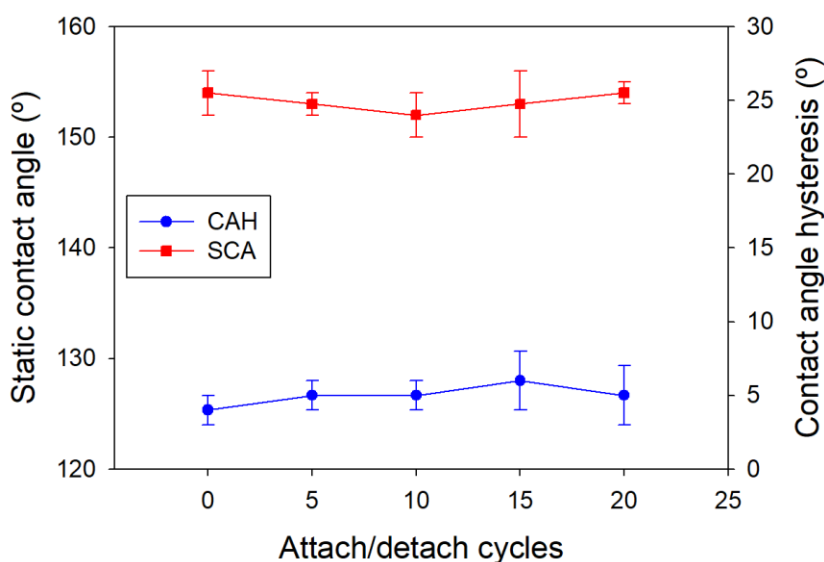

Figure 4. Evolution of SCA and CAH value with the attach/detach cycles.

The superhydrophobic long-lasting performance was evidenced by the lack of significant changes in SCA and CAH values after the attach/detach cycles, confirming a high adhesion of the primer coating to the marble surface and the sub-microparticles generated by laser ablation, meaning that the Cassie-Baxter topography was maintained [52–54]. This result is in line with previous works of our group [55,56], which confirmed the high adhesion of the xerogel prepared according to our synthesis route to different stone substrates (both sandstone and limestone).

4.5. Conclusions.

Superhydrophobic properties were successfully achieved on marble surfaces by a top-down laser texturization method based on two steps: (1) pre-conditioning of the surface by the application of a hydrophobic primer coating (ormosil). (2) Creation of a surface roughness by laser ablation with a nanosecond laser. By modifying the laser fluence, it is possible to regulate the textural properties (i.e. roughness and morphology) and, therefore, the wetting properties of the surfaces, highlighting the versatility of this approach and the possibility for customizable applications to other building materials.

The obtained results showed a high positive correlation between the laser fluence and the hydrophobic performance, with the highest superhydrophobic properties being reached at 150-170 J/cm^{-2} values (over the ablation threshold). At these values, the profilometry and SEM images showed the maximum roughness and the presence of sub-micrometric on the surface, generated by the melting and rapid deposition of the material, which promotes a Cassie-Baxter wetting state. Fluence values below the ablation threshold improved the hydrophobic performance to a lesser degree, mainly because the changes, limited to holes and deformations, promoted a Wenzel state instead. A lower performance was also observed after treatment with the highest fluence values due to the destruction of the sub-micro structures under the high energy conditions.

In addition, the results from the tape test proved a long-lasting durability of the best-performing superhydrophobic sample due to an adequate adhesion of the primer coating to the marble surface and to the preservation of the Cassie-Baxter state.

4.6. References.

[1]   A.E. Charola, Acid rain effects on stone monuments, J. Chem. Educ. 64 (1987) 436.

[2]   M.O. Figueiredo, T.P. Silva, J.P. Veiga, Analysis of degradation phenomena in ancient, traditional and improved building materials of historical monuments, Appl. Phys. A Mater. Sci. Process. 92 (2008) 151–154.

[3]   H. Bravo A., R. Soto A., R. Sosa E., P. Sanchez A., A.L. Alarcon J., J. Kahl, J. Ruiz B., Effect of acid rain on building material of the El Tajín archaeological zone in Veracruz, Mexico, Environ. Pollut. 144 (2006) 655–660.

[4]   R. Fürstner, W. Barthlott, C. Neinhuis, P. Walzel, Wetting and self-cleaning properties of artificial superhydrophobic surfaces, Langmuir. 21 (2005) 956–961.

[5]   W. Barthlott, C. Neinhuis, H. Verlot, C.L. Schott, Purity of the sacred lotus , or escape from contamination in biological surfaces, Planta. 202 (1997) 1–8.

[6]   L. Gao, T.J. McCarthy, Wetting 101 degrees., Langmuir. 25 (2009) 14105–15.

[7]   L. Gao, T.J. McCarthy, Contact angle hysteresis explained., Langmuir. 22 (2006) 6234–7.

[8]   L. Gao, T.J. McCarthy, A Perfectly Hydrophobic Surface (θ A /θ R = 180°/180°), J. Am. Chem. Soc. 128 (2006) 9052–9053.

[9]   A. Lafuma, D. Quéré, Superhydrophobic states., Nat. Mater. 2 (2003) 457–60.

[10]   A.B.D. Cassie, S. Baxter, Wettability of porous surfaces, Trans. Faraday Soc. 40 (1944) 546–551.

[11]   X.-M. Li, D. Reinhoudt, M. Crego-Calama, What do we need for a superhydrophobic surface? A review on the recent progress in the preparation of superhydrophobic surfaces., Chem. Soc. Rev. 36 (2007) 1350–1368.

[12]   D.S. Facio, M.J. Mosquera, Simple strategy for producing superhydrophobic nanocomposite coatings in situ on a building substrate., ACS Appl. Mater. Interfaces. 5 (2013) 7517–26.

[13]   L.A.M. Carrascosa, D.S. Facio, M.J. Mosquera, Producing superhydrophobic roof tiles, Nanotechnology. 27 (2016) 095604.

[14]   D.S. Facio, L.A.M. Carrascosa, M.J. Mosquera, Producing lasting amphiphobic building surfaces with self-cleaning properties, Nanotechnology. 28 (2017) 265601.

[15]   I. Karapanagiotis, A. Pavlou, P.N. Manoudis, K.E. Aifantis, Water repellent ORMOSIL films for the protection of stone and other materials, Mater. Lett. 131 (2014) 276–279.

[16]   I. Karapanagiotis, P.N. Manoudis, A. Savva, C. Panayiotou, Superhydrophobic polymer-particle composite films produced using various particle sizes, Surf. Interface Anal. 44 (2012) 870–875.

[17]   D. Aslanidou, I. Karapanagiotis, D. Lampakis, Waterborne superhydrophobic and

superoleophobic coatings for the protection of marble and sandstone, Materials (Basel). 11 (2018) 585.

[18] M.J. Mosquera, D.M. de los Santos, A. Montes, L. Valdez-Castro, New nanomaterials for consolidating stone., Langmuir. 24 (2008) 2772–8.

[19] J.F. Illescas, M.J. Mosquera, Surfactant-Synthesized PDMS/Silica Nanomaterials Improve Robustness and Stain Resistance of Carbonate Stone, J. Phys. Chem. C. 115 (2011) 14624–14634.

[20] L. Pinho, F. Elhaddad, D.S. Facio, M.J. Mosquera, A novel TiO2–SiO2 nanocomposite converts a very friable stone into a self-cleaning building material, Appl. Surf. Sci. 275 (2013) 389–396.

[21] R. Zarzuela, M. Carbú, M.L.A. Gil, J.M. Cantoral, M.J. Mosquera, CuO/SiO2 nanocomposites: A multifunctional coating for application on building stone, Mater. Des. 114 (2017) 364–372.

[22] P. Gregorčič, B. Šetina-Batič, M. Hočevar, Controlling the stainless steel surface wettability by nanosecond direct laser texturing at high fluences, Appl. Phys. A Mater. Sci. Process. 123 (2017) 1–8.

[23] Q. Ma, Z. Tong, W. Wang, G. Dong, Fabricating robust and repairable superhydrophobic surface on carbon steel by nanosecond laser texturing for corrosion protection, Appl. Surf. Sci. 455 (2018) 748–757.

[24] J. Huo, Q. Yang, F. Chen, J. Yong, Y. Fang, J. Zhang, L. Liu, X. Hou, Underwater Transparent Miniature "Mechanical Hand" Based on Femtosecond Laser-Induced Controllable Oil-Adhesive Patterned Glass for Oil Droplet Manipulation, Langmuir. 33 (2017) 3659–3665.

[25] S.H. Anastasiadis, Development of functional polymer surfaces with controlled wettability, Langmuir. 29 (2013) 9277–9290.

[26] A.Y. Vorobyev, C. Guo, Direct femtosecond laser surface nano/microstructuring and its applications, Laser Photonics Rev. 7 (2013) 385–407.

[27] P. Pouli, M. Oujja, M. Castillejo, Practical issues in laser cleaning of stone and painted artefacts: optimisation procedures and side effects, Appl. Phys. A. 106 (2012) 447–464.

[28] P. Pouli, C. Fotakis, B. Hermosin, C. Saiz-Jimenez, C. Domingo, M. Oujja, M. Castillejo, The laser-induced discoloration of stonework; a comparative study on its origins and remedies, Spectrochim. Acta Part A Mol. Biomol. Spectrosc. 71 (2008) 932–945.

[29] M. Sanz, M. Oujja, C. Ascaso, S. Pérez-Ortega, V. Souza-Egipsy, R. Fort, A. de los Rios, J. Wierzchos, M. V. Cañamares, M. Castillejo, Influence of wavelength on the laser removal of lichens colonizing heritage stone, Appl. Surf. Sci. 399 (2017) 758–768.

[30] J.F. Illescas, M.J. Mosquera, Producing surfactant-synthesized nanomaterials in situ on a

building substrate, without volatile organic compounds., ACS Appl. Mater. Interfaces. 4 (2012) 4259–69.

[31]   M.J. Mosquera, L.A.M. Carrascosa, N. Badreldin, Producing superhydrophobic/oleophobic coatings on Cultural Heritage building materials, Pure Appl. Chem. 90 (2018) 551–561.

[32]   J.Y. Huang, S.H. Li, M.Z. Ge, L.N. Wang, T.L. Xing, G.Q. Chen, X.F. Liu, S.S. Al-Deyab, K.Q. Zhang, T. Chen, Y.K. Lai, Robust superhydrophobic TiO_2 @fabrics for UV shielding, self-cleaning and oil–water separation, J. Mater. Chem. A. 3 (2015) 2825–2832.

[33]   S. Moradi, P. Englezos, S.G. Hatzikiriakos, Contact angle hysteresis: surface morphology effects, Colloid Polym. Sci. 291 (2013) 317–328.

[34]   L. Feng, Y. Zhang, J. Xi, Y. Zhu, N.N. Wang, F. Xia, L. Jiang, Petal effect: A superhydrophobic state with high adhesive force, Langmuir. 24 (2008) 4114–4119.

[35]   J. Yong, F. Chen, M. Li, Q. Yang, Y. Fang, J. Huo, X. Hou, Remarkably Simple Achievement of Superhydrophobicity, Superhydrophilicity, Underwater Superoleophobicity, Underwater Superoleophilicity, Underwater Superaerophobicity, and Underwater Superaerophilicity on Femtosecond Laser Ablated PDMS Surfaces, J. Mater. Chem. A. 5 (2017) 25249–25257.

[36]   R.N. Wenzel, Resistance of solid surfaces to wetting by water, Ind. Eng. Chem. 28 (1936) 988–994.

[37]   A. Nakajima, K. Hashimoto, T. Watanabe, K. Takai, G. Yamauchi, A. Fujishima, Transparent superhydrophobic thin films with self-cleaning properties, Langmuir. 16 (2000) 7044–7047.

[38]   D. Öner, T.J. McCarthy, Ultrahydrophobic Surfaces. Effects of Topography Length Scales on Wettability, Langmuir. 16 (2000) 7777–7782.

[39]   B. Bhushan, E.K. Her, Fabrication of superhydrophobic surfaces with high and low adhesion inspired from rose petal., Langmuir. 26 (2010) 8207–17.

[40]   T. Nishino, M. Meguro, K. Nakamae, M. Matsushita, Y. Ueda, The Lowest Surface Free Energy Based on −CF3 Alignment, Langmuir. 15 (1999) 4321–4323.

[41]   J. Yong, F. Chen, Q. Yang, D. Zhang, H. Bian, G. Du, J. Si, X. Meng, X. Hou, Controllable adhesive superhydrophobic surfaces based on PDMS microwell arrays., Langmuir. 29 (2013) 3274–3279.

[42]   B.N. Chichkov, C. Momma, S. Nolte, F. von Alversleben, A. Tünnermann, Femtosecond, picosecond and nanosecond laser ablation of solids, 63 (1996) 109–115.

[43]   F. Chen, D. Zhang, Q. Yang, J. Yong, G. Du, J. Si, F. Yun, X. Hou, Bioinspired wetting surface via laser microfabrication, ACS Appl. Mater. Interfaces. 5 (2013) 6777–6792.

[44]   C. Kosak Söz, E. Yilgör, I. Yilgör, Influence of the average surface roughness on the formation of superhydrophobic polymer surfaces through spin-coating with hydrophobic fumed silica,

Polym. (United Kingdom). 62 (2015) 118–128.

[45]   E. Huovinen, J. Hirvi, M. Suvanto, T. a. Pakkanen, Micro-micro hierarchy replacing micro-nano hierarchy: A precisely controlled way to produce wear-resistant superhydrophobic polymer surfaces, Langmuir. 28 (2012) 14747–14755.

[46]   M. Grehn, T. Seuthe, M. Höfner, N. Griga, C. Theiss, A. Mermillod-Blondin, M. Eberstein, H. Eichler, J. Bonse, Femtosecond-laser induced ablation of silicate glasses and the intrinsic dissociation energy, Opt. Mater. Express. 4 (2014) 689.

[47]   R. Jagdheesh, B. Pathiraj, E. Karatay, G.R.B.E. Römer, a. J. Huis In'T Veld, Laser-induced nanoscale superhydrophobic structures on metal surfaces, Langmuir. 27 (2011) 8464–8469.

[48]   X. Li, L. Chang, R. Qiu, C. Wen, Z. Li, S. Hu, Microstructuring and doping of silicon with nanosecond laser pulses, Appl. Surf. Sci. 258 (2012) 8002–8007.

[49]   A. V. Kabashin, P. Delaporte, A. Pereira, D. Grojo, R. Torres, T. Sarnet, M. Sentis, Nanofabrication with Pulsed Lasers, Nanoscale Res. Lett. 5 (2010) 454–463.

[50]   T.O. Yoon, H.J. Shin, S.C. Jeoung, Y.-I. Park, Formation of superhydrophobic poly(dimethysiloxane) by ultrafast laser-induced surface modification, Opt. Express. 16 (2008) 12715.

[51]   B. Farshchian, J.R. Gatabi, S.M. Bernick, S. Park, G.-H. Lee, R. Droopad, N. Kim, Laser-induced superhydrophobic grid patterns on PDMS for droplet arrays formation, Appl. Surf. Sci. 396 (2017) 359–365.

[52]   B.P. Dyett, A.H. Wu, R.N. Lamb, Mechanical Stability of Surface Architecture - Consequences for Superhydrophobicity, ACS Appl Mater Interfaces. 6 (2014) 18380–18394.

[53]   J.-H. Zhi, L.-Z. Zhang, Y. Yan, J. Zhu, Mechanical durability of superhydrophobic surfaces: The role of surface modification technologies, Appl. Surf. Sci. 392 (2017) 286–296.

[54]   L. Wang, J. Yang, Y. Zhu, Z. Li, T. Sheng, Y.M. Hu, D.Q. Yang, A study of the mechanical and chemical durability of Ultra-Ever Dry Superhydrophobic coating on low carbon steel surface, Colloids Surfaces A Physicochem. Eng. Asp. 497 (2016) 16–27.

[55]   D.S. Facio, L.A.M. Carrascosa, M.J. Mosquera, Producing lasting amphiphobic building surfaces with self-cleaning properties, Nanotechnology. 28 (2017).

[56]   L. Pinho, M.J. Mosquera, Titania-Silica Nanocomposite Photocatalysts with Application in Stone Self-Cleaning, J. Phys. Chem. C. 115 (2011) 22851–22862.

SUPERHYDROHOBICITY   SELF-CLEANING   OLEOPHOBICITY
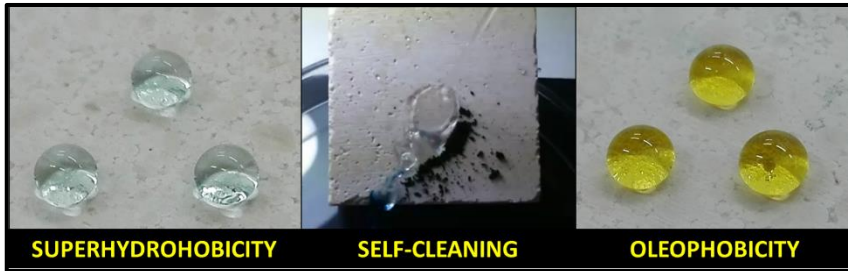
Capítulo 5

Producing Superhydrophobic/oleophobic Coatings on Cultural Heritage Building Materials.

5.1. Abstract.

Water is the main vehicle of decay agents in Cultural Heritage building materials exposed to weathering. In this work, a simple method to produce superhydrophobic/oleophobic coatings building materials, including under outdoors conditions, has been developed. In addition, a study of the behaviour of the developed coatings on different substrates (limestone, granite, concrete and wood) is reported.

The addition of 40 nm-SiO_2 nanoparticles to a fluoroalkylsilane reduces surface energy and produces a Cassie-Baxter surface in all the materials evaluated. It promotes high static contact angle values of around 160º, and a contact angle hysteresis of around 3º, giving rise to repellence. The building surfaces also demonstrate an excellent self-cleaning performance. The coatings maintain the building materials aesthetics as required in the Cultural Heritage field. Finally, the coating presents a long-lasting performance due to condensation reactions producing effective grafting to the four building materials evaluated.

5.2. Introduction.

A surface is considered as superhydrophobic when it presents high hydrophobicity and water repellence. These kinds of surfaces have to fulfil two requirements: (1) Static Contact Angle (SCA) values over 150° (2) Contact Angle Hysteresis (CAH, which is the difference between Advancing and Receding Contact Angles) values lower than 10°. As previously explained [1], the hysteresis controls the movement of water droplets on the surface and, therefore, it characterizes the repellence.

Nature has developed numerous species of plants, insects and other animals, which have had surfaces with superhydrophobic properties for millennia. The most well-known example is the lotus leaf [2], whose structure includes waxes with hierarchical micro- and nano-roughness. Thus, waxes reduce surface energy, giving rise to hydrophobic properties on the surface, and the roughness produces repellence [2,3]. In order to promote repellence, the roughness has to produce a Cassie-Baxter surface [4] where air-pockets are created between liquid droplets and the solid surface, thus assisting the water droplets to roll off the surface.

Superhydrophobic materials find applications in the field of building due to their interesting properties, such as self-cleaning, anti-fouling, stain-resistance and ice-repellence [5], and especially in Cultural Heritage materials in which their preservation is crucial. In the specific case of treatments applied on Cultural Heritage elements, their requirements are even more restrictive, being required to evaluate compatibility between substrates and treatments associated to physical-chemical, environmental, operational and socio-cultural issues [6]. However, most approaches found in the literature [7–10] require expensive and multi-stage processes and subsequently, they cannot be applied on building facades [11]. Other drawback for building application is associated to the low durability of these strategies [12]. Surface roughness is induced by top down or bottom up procedures. This surface architecture of roughness in the coating contributes significantly to low durability [13]. Thus, fabrication of durable superhydrophobic surfaces exposed to the weather under outdoor conditions still remains a challenge.

Producing Superhydrophobic/oleophobic Coatings on Cultural Heritage Building Materials

In recent years, specific approaches for producing superhydrophobic coatings on building materials have been developed [14–18], although most of them do not consider the durability of the treatments, a critical requirement stemming from their exposure to outdoor conditions. Regarding previous papers which consider durability in superhydrophobic building materials, Aslanidou et al. [19] applied a commercial water soluble hydrophobic siloxane emulsion enriched with silica nanoparticles (NPs) onto white marble and sandstone. These coatings demonstrated chemical resistance by measuring SCA values of water drops with different pH values. In addition, the coatings maintained high SCA (around 150°) after a tape test.

Manoudis et al. [20] produced superhydrophobic coatings by applying dispersions of silica NPs in a polysiloxane onto white marble. In order to evaluate the durability, the treated samples were exposed outdoors during 5 months, maintaining a SCA of around 150°.

Finally, de Ferri et al. [21] produced superhydrophobic coatings by mixing hydrophobic silica NPs with a glycidoxypropyltrimethoxysilane. The obtained products were applied on three different kinds of stone: marble, sandstone and granite. Specifically, the treated samples were placed outdoors for four months, with a significant decrease in SCA values being produced. In addition, the samples were also subjected to a test of water absorption by capillarity. After five days in continuous contact with water, the superhydrophobic, and even hydrophobic, properties of the coatings were completely lost.

In the above works, the SCA values were used to evaluate the durability of superhydrophobic products, but parameters regarding repellence, such as CAH were not evaluated. As we previously described [22], roughness, producing repellence, is more susceptible to decay and it cannot be evaluated by SCA values.

Our research group have developed specific materials for building conservation by using a simple sol-gel route [23], which allows application over large-areas, as well as application in situ under outdoor conditions. This product was evaluated in different Cultural Heritage elements [24,25]. Specifically, a surfactant and a silica oligomer are mixed by ultrasonic agitation [26]. An inverse micelle mechanism permit to obtain

crack-free coatings with high adhesion to the substrates [27]. The addition of an organic silica oligomer gives rise to hydrophobic properties [26]. To promote superhydrophobicity, we have added silica NPs to a mixture of organic-inorganic silica oligomers. Finally, we have also produced lasting amphiphobic (superhydrophobic and oleophobic) coatings by the application of two successive coatings: (1) a silica nanocomposite containing silica NPs and (2) a fluorinated alcoxysilane [28].

In this work, a superhydrophobic product was prepared by a simple mixture of a water soluble fluoroalkylsilane and silica NPs. We employed a halogen compound in order to confer additional oleophobic properties to the coating. This product was applied on four different building materials of interest in the Cultural Heritage field (limestone, granite, concrete and wood), and superhydrophobicity was evaluated. In addition, the durability was evaluated by two different procedures (tape test and rain simulation test). Finally, since a possible application of this product is the Cultural Heritage conservation, aesthetic changes induced by the treatment were evaluated by measuring colour variations of the treated materials. However, we want to remark that other compatibility parameters, including long term incompatibility, will require evaluation previous to its application in specific Cultural Heritage materials.

5.3. Materials and methods.

5.3.1. Preparation of superhydrophobic product.

The reagents employed were: (1) Aerosil OX50 (hereinafter SiNPs), which consists of fumed silica NPs (primary size of 40 nm and surface area of 50 $m^2 \cdot g^{-1}$) supplied by Evonik. (2) Dynasylan F8815 (hereinafter F8815) is a water-soluble fluoroalkylsilane. It has a fluoroalkyl chain, which provides hydrophobic and oleophobic properties, an aminoalkyl chain which confers solubility in water, and two hydroxyl groups for siloxane polymerization.

The superhydrophobic product was prepared by means of a simple method: (1) SiNPs were dispersed in deionized water (2 % w/v), and the dispersion was ultrasonically agitated for 10 minutes. (2) 2 % v/v of F8815 was added dropwise, and the product was magnetically stirred for 30 minutes. The product was always applied one hour after its

preparation in order to maintain reproducibility of the results. The product showed stability in closed vessel for one month. After this time, a slight precipitate, which can be re-dispersed by mechanical agitation, was observed.

5.3.2. Application of superhydrophobic product.

The sol was applied on four different building materials: limestone, granite, concrete and wood. The samples size was 4 x 4x 4 cm for granite and limestone, 3.5 x 3.5 x 3.5 cm for the concrete and 3.5 x 3.5x 0.5 cm for the wood. The four materials under study are commonly employed in modern buildings. The selected limestone (commercially available as Capri Limestone) has an open porosity around 9%, and it presents a homogeneous structure, composed of micritic matrix containing oolites and oncolites, having a 90% of calcite and a 10% of silicate minerals. The granite (White Pearl Granite) is a biotitic granite with an open porosity around 0.5%, and the main components are SiO_2 (64 %) and Al_2O_3 (19 %). The rest of components (Fe_2O_3, MgO, Na_2O and K_2O) are found in percentage lower than 10 %. A type I white Portland cement and a calcareous sand (ϕ 1-6 mm) were employed to fabricate the concrete samples. The water:cement ratio and the cement:sand ratio (w/w) were 1:2 and 1:5 (w/w), respectively. The specimens were cured under water at 21 ± 2º C for 28 days, according with standard UNE-EN 12390-2 [29], being their open porosity around 10%. Finally, the pine wood samples (hereinafter Wood) present an open porosity around 58 % and it is composed of cellulose (50 %), hemicellulose (25 %) and lignin (25 %). All the surfaces were used as received without any modification. The sol was applied by brushing on all the substrates, except wood. Specifically, three applications, with an elapsed time between applications of 30 seconds were performed. The wood samples were immersed into the sol for five minutes. After application, the samples were let overnight in laboratory conditions (20 °C and 40 % RH), to allow the sol-gel transition. Then, the samples were heated into an oven at 100 °C, for 1 hour, in order to remove the solvent (water). Once the treated samples were dried and cold, the following experiments were carried out on two replicates for each surface under study. In order to calculate the uptake of product, the samples were weight before and immediately after being treated. After drying, the samples were re-weight to calculate the dry matter. The penetration depth

of the product inside the building materials under study was evaluated. Specifically, the samples were cut in order to obtain cross-sections. Then, water was dropped on the cross-sections, corresponding the non-wetted area to the penetration depth of the product.

5.3.3. Characterization of the treated surfaces and effectiveness.

Static and dynamic CAs were evaluated by using OCA15 Plus video-measuring equipment, from DataPhysics Instruments, according to the following method: droplets of distilled water (5 µL) were applied with a syringe at 5 different points on each surface under study, and SCA values were evaluated. Then, 2.5 µL were added, obtaining the advancing CA (ACA) values. Finally, 2.5 µL were removed and the receding CA (RCA) values were measured. In addition, the oleophobic properties of the coatings were evaluated by placing 5 µL droplets of olive oil at 5 different points on each surface and measuring the SCA values.

As an additional experimental test of the water-repellent behaviour, a water jet was projected onto each treated surface under study from a distance of 20 cm. The experiment was recorded by a digital camera (Sony Cyber-shot model DSCP200) at 30 frames/s.

The self-cleaning properties of the treated surfaces and their untreated counterparts were tested according to a previously described procedure [30]. Specifically, methylene blue powder was applied to the surfaces of the samples. Next, the samples were placed under a water column in order to simulate the effect of rain. The water column fell over the surface of the samples from a height of 50 cm, with a flow of 45 mL·s^{-1}. These experiments were registered with the previously described camera. In order to evaluate the self-cleaning effectiveness, the colour of the samples was measured before and after the test by using a ColorFlex spectrophotometer from HunterLab. Illuminant D65 and observer CIE10° were selected as measurement parameters. The CIE L*a*b* scale was employed [31].These experiments were registered with the previously described camera.

In order to evaluate the changes produced in the topography of the treated samples, Atomic Force Microscopy (AFM) images of the surfaces were obtained by using an AFM Dulcinea model from Nanotec Electrónica, operating in tapping mode. The root mean square (RMS) roughness values were evaluated from 5 μm x 5 μm images. Measurements were recorded in five points on the surface.

Finally, the colour change caused by the application of the product was evaluated by means of a ColorFlex spectrophotometer from HunterLab. Illuminant D65 and observer CIE10° were selected as measurement parameters. The CIE L*a*b* scale was employed [31].

5.3.4. Evaluation of durability.

The lasting properties of the treated samples were tested by performing two different tests. The adhesion between coating and substrate is an important issue that determines the lasting properties of the treatment, since a coating with poor adhesion will be easily removed due to environmental conditions (rain, wind). Thus, the adhesion of the coatings to the surface samples was evaluated according to a previous test developed of our group [28]. Specifically, an adhesive tape was applied on the treated surfaces and it was subsequently removed. Static and dynamic CAs for water were measured after 1, 2, 5, 10, 15 and 20 attachment-detachment cycles.

The resistance to water impact was evaluated by placing the treated samples under a water column in order to simulate the effect of rain. The water column fell over the surfaces of the samples from a height of 50 cm with a flow of 45 mL·s^{-1}. The total amount of water falling onto the treated surfaces was 2500 L·m^{-2}. After the test, the samples were dried in an oven at 60 °C and the static and dynamic CA values for water were evaluated.

5.4. Results and discussion.

5.4.1. Application of superhydrophobic product.

Table 1 shows the average uptake, dry-matter and penetration depth values for the applied samples.

Table 1. Uptake, dry-matter and penetration depth average values for the treated samples.

Sample	Uptake (%)	Dry-matter (%)	Penetration depth (mm)
Limestone	0.51±0.02	0.11±0.02	2.6±0.1
Granite	0.21±0.02	0.05±0.01	0.5±0.2
Concrete	0.53±0.04	0.12±0.02	3.1±0.2
Wood	73.98±0.06	0.19±0.04	---

As observed in **Table 1**, all the substrates showed product uptake values with a clear relation with their open porosity values. In the case of wood, this value was significantly higher than the other substrates due to the application method (immersion). After solvent evaporation all the samples showed a significant loss of weight due to the solvent evaporation. Regarding to penetration depth, the measured value was also related with the porosity of the substrates. In the case of wood, this value could not be measured because the product was applied by immersion.

5.4.2. Characterization of the treated surfaces and effectiveness.

Figure 1 shows the SCA, ACA and RCA values for the treated samples under study (left), and images of 25 µL water droplets on the building materials surfaces under study are shown on the right. The untreated surfaces were hydrophilic, showing SCA values of 35°, 60° and 10° for limestone, granite and concrete samples, respectively. In the case of the wood samples, the water droplet was quickly absorbed and thus, the SCA could not be evaluated. All the treated surfaces showed superhydrophobic properties with SCA values of around 160°. Moreover, ACA and RCA presented very close values, the CAH value being around 3° in all cases. As previously discussed [11,22], 40 nm-SiO_2 NPs are able to produce a surface roughness typical of a Cassie-Baxter regime, providing repellent properties [32–34]. In addition, the fluoroalkylsilane is able to decrease surface energy due to the action of fluoroalkyl chains [35–37]. The combination of both effects (roughness and low surface energy) gives rise to superhydrophobic properties. In order to demonstrate the water repellent properties of the treated surfaces, a video was recorded (see Supplementary Information, **Video S1**). The video shows a water jet impacting on the four treated surfaces. The water jet is completely repelled for all the building material surfaces evaluated.
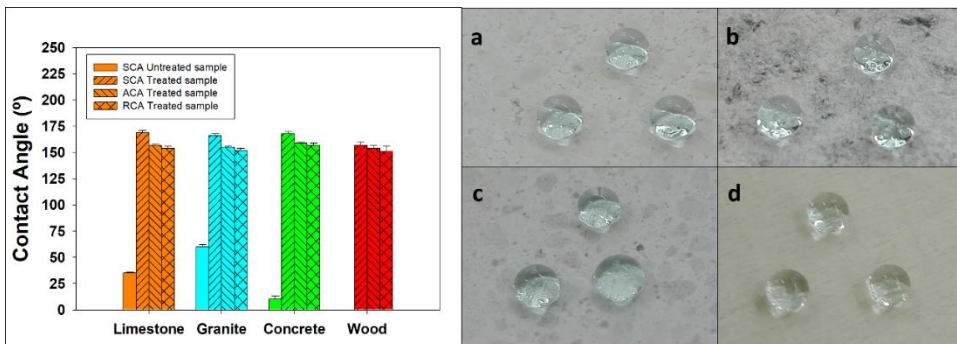
Figure 1. Static (SCA), Advancing (ACA) and Receding (RCA) Contact Angle values obtained on the surface of the treated building material samples under study. In order to stablish a comparison, SCA of the untreated samples were also included. Photographs of water droplets on the treated building material surfaces evaluated are included: (a) limestone, (b) granite, (c) concrete, and, (d) wood. The water droplets were dyed with methylene blue to have a better contrast.

Alfieri et al. [38] also employed fluoroalkylsilane in order to produce hydrophobic coatings, but they added TiO_2 NPs with a size of around 4 nm in order to confer photoactive properties. In this case, repellence was not evaluated, and the SCA values were lower than those obtained in the present work. This different behaviour is associated with the size of NPs integrated into the fluoroalkylsilica gel. The 4 nm-size NPs (ten times less than the 40 nm-size NPs employed in the present synthesis) cannot produce the required roughness to promote a Cassie-Baxter regime and an SCA above 150°.

In our work, the superhydrophobic behaviour observed suggests that a self-cleaning effect can be induced in these surfaces [19,39]. Thus, a test was carried out as previously described in the experimental section. Results are shown in **Table 2**.

Table 2. Total colour difference (ΔE*) values for the untreated and treated samples after self-cleaning test.

Sample	ΔE* (untreated sample)	ΔE* (treated sample)
Limestone	35.33±0.34	0.51±0.18
Granite	22.48±0.21	0.37±0.15
Concrete	33.19±0.18	0.43±0.21
Wood	34.87±0.24	0.42±0.13

In the case of the untreated samples, the dye was dissolved by the water droplets, and the hydrophilic nature of the surfaces promoted the absorption of the solution by

the pores of the different substrates. Thus, a blue stain was permanently maintained on the building materials under study. Thus, significant ΔE^* values were obtained for all the untreated samples, as observed in **Table 2**. On the other hand, the dye was completely removed from the treated surfaces by the droplets rolling off. This behaviour was confirmed by the colorimetric test, being all the ΔE^* values lower than 0.6. As an example, a video showing this self-cleaning effect on the limestone samples is shown in the Supplementary Information (**Video S2**).

The addition of a fluorinated compound reduces the surface energy to values lower than those produced by organic components, giving rise to oleophobic properties. The surface tension of olive oil (32 mN·m^{-1}, at 25 ºC) [40] is significantly lower than that of water (72 mN·m^{-1}). Thus, it is necessary to use halogen compounds in order to decrease the coating surface energy below the surface energy in the olive oil-coating interphase [35,37,41,42]. Therefore, the oleophobic behaviour of the treated surfaces under study was evaluated by measuring the SCA values of olive oil droplets. **Fig. 2** shows the SCA values of oil droplets deposited on the untreated substrates and their treated counterparts. In addition, photographs of the olive oil droplets on the treated surfaces are included. The untreated surfaces showed oleophilic behaviour with SCA values of 10, 15 and 21° for limestone, granite and concrete, respectively. In the case of wood, oil droplets were rapidly absorbed and, therefore, they could not be measured. Regarding to the treated substrates, all of them showed highly oleophobic properties, with SCA values above 100°. Photographs of the olive oil droplets on the treated surfaces, along with the SCA values, can be seen in **Fig. 2**. All the surfaces showed highly oleophobic properties, with SCA values above 100°.
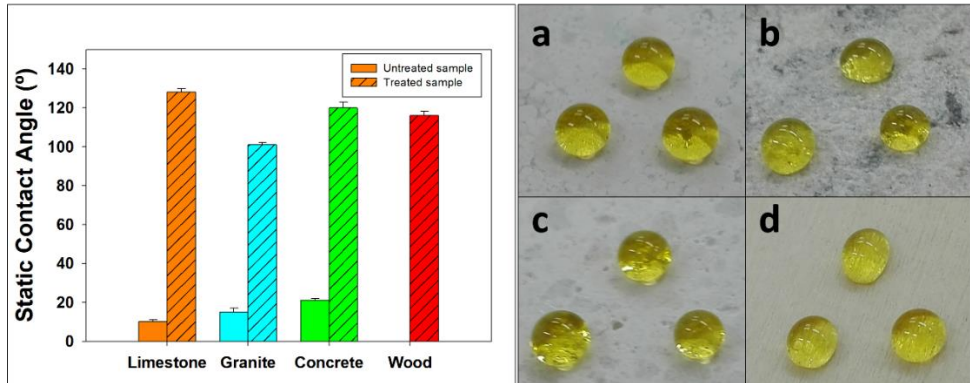
Figure 2. SCA values of the oil droplets deposited on the untreated substrates and their treated counterparts. Photographs of the olive oil droplets deposited on the surfaces of the treated building material samples under study: (a) limestone, (b) granite, (c) concrete, and, (d) wood.

Since the superhydrophobicity is a combination of decreasing surface energy and creating a roughness characteristic of a Cassie-Baxter regime, a study of the topography modification of the surfaces under study was carried out by AFM measurements. **Fig. 3** shows AFM results for the treated samples under study and their untreated counterparts.

Figure 3. 3D AFM images for the untreated (top) and treated (middle) surfaces. (a) limestone, (b) granite, (c) concrete, (d) wood. The Root Mean Square (RMS) Roughness values are also included. 2D roughness profiles are included below.

All the untreated samples showed completely heterogeneous surfaces with a random roughness (high RMS values are observed). On the contrary, the treated substrates showed homogeneous surfaces composed by densely-packed, uniform, NPs aggregation. It confirms that SiO_2 NPs were integrated into the fluorinate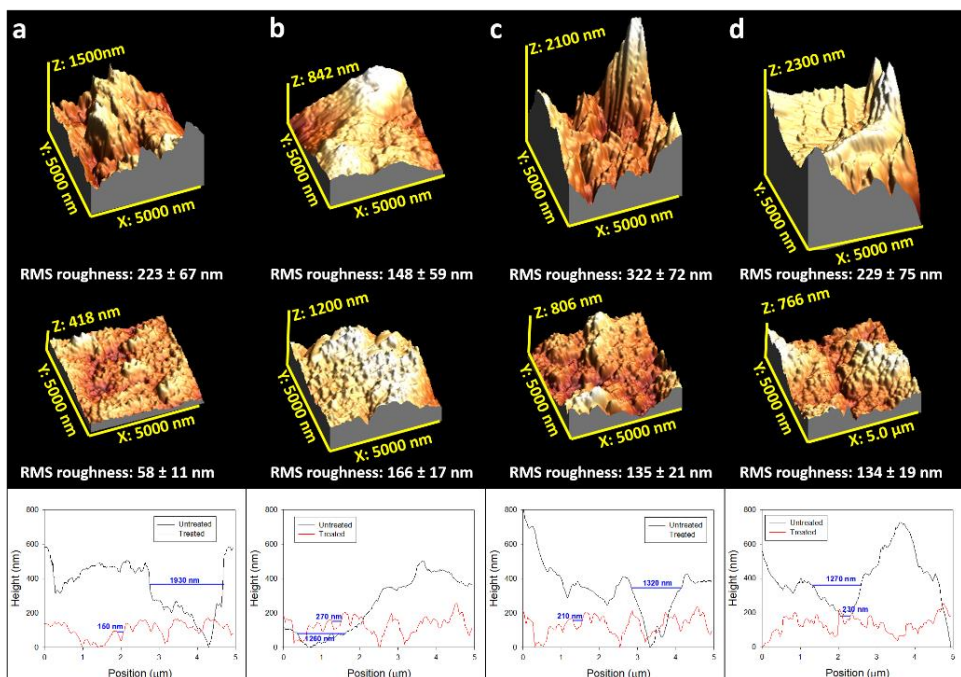d silica gel, producing the uniform packing observed by AFM. All the surfaces showed a significant decrease in the RMS values after being treated because the coating is able to cover the irregularities of the surfaces excepting the granite samples. In this case RMS value is increased after the application of the coating. This can be due to the low porosity of granite (0.5 %), which promotes the accumulation of product on the surface. This can be explained as a consequence of the low product penetration in granite (see **Table 1**).

Figure 3 (bottom) presents the 2D AFM roughness profiles. As previously discussed by Bhushan et al. [43], the space between peaks is important in order to trap air pockets, producing a Cassie-Baxter regime. The treated surfaces show, for all the substrates, distance between peaks with fairly uniform values between 150 and 250 nm, whereas the untreated surfaces showed heterogeneous distances between peaks, bigger than 1000 nm. These results suggest that the water droplets will be less able to penetrate into the treated surfaces, hence the contact area between droplet and surface will be minimized. This promotes high contact angle values and repellence behaviour, as previously suggested [11,22,43,44]. In the case of the oleophobic behaviour, a mushroom-like roughness is required to produce superoleophobicity [42,45]. Thus, our product promotes high SCA, but it cannot produce oil repellence.

A practical limitation of the superhydrophobic products to be applied in Cultural Heritage will be encountered if a change in the colour of the building material is produced (physical-chemical compatibility). Therefore, the variations in the colorimetric coordinates (ΔL^*, Δa^* and Δb^*) of the substrates induced by the product were obtained, and total colour difference (ΔE^*) was calculated. The results are shown in **Table 3** and photographs of the untreated building materials and their treated counterparts are shown in **Fig. 4**.

Table 3. Colour variation of the samples after application of the products.

Sample	ΔL*	Δa*	Δb*	ΔE*
Limestone	2.03±0.22	0.97±0.28	0.87±0.24	2.38±0.30
Granite	2.75±0.31	0.95±0.44	-0.91±0.33	3.05±0.45
Concrete	2.41±0.28	0.93±0.51	0.94±0.46	2.75±0.65
Wood	1.96±0.24	0.88±0.54	-0.89±0.34	2.33±0.77

As observed in **Table 2**, the application of the superhydrophobic product on the building materials under study caused negligible colour modification, as can be demonstrated by ΔE* values lower than or equal to 3. According with Delgado-Rodrigues and Grossi [6], colour variation lower than 3 are perfectly acceptable in Cultural Heritage field. Regarding to the changes produced in the individual colour coordinates (ΔL*, Δa* and Δb*), it was observed that the values obtained for Δa* and Δb* were negligible. In the case of ΔL*, a slight increase to positive values was observed, which indicates a slight lighter than that observed for the untreated surfaces. This value was slightly higher in the case of granite due to their lower porosity that allows the accumulation of the product on the surface, as previously discussed.
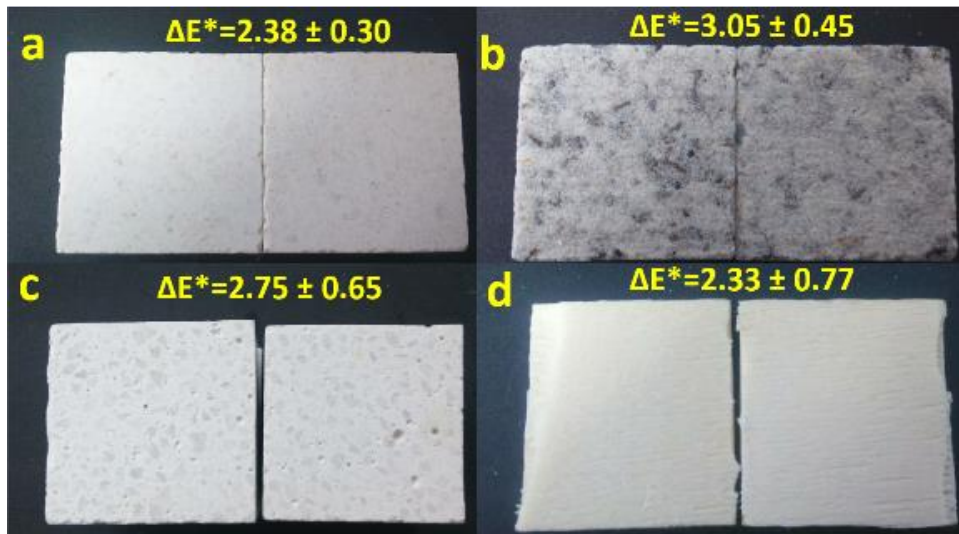

Figure 4. Photographs of untreated (left) and treated (right) substrates, together with the calculated values of total colour difference. (a) limestone, (b) granite, (c) concrete, (d) wood.

5.4.3. Evaluation of durability.

The durability of the superhydrophobic surfaces is a critical requirement for their application on building materials which are exposed to outdoor conditions. Thus, the lasting-effectiveness of the coatings is an important parameter to evaluate. Adhesion of the coatings to the substrates was evaluated by a tape test. **Figure 5** shows evolution of the SCA and CAH values through attachment-detachment cycles for the building material surfaces under study.
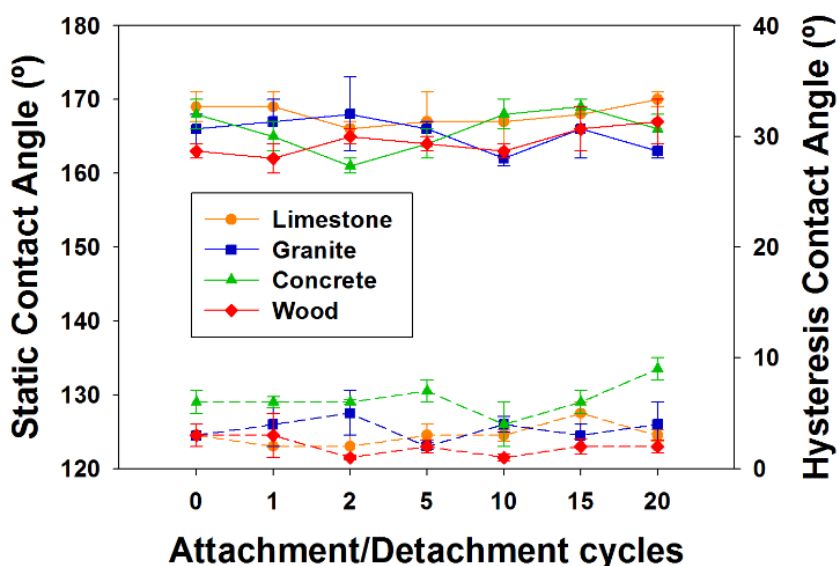
Figure 5. Evolution of the SCA (solid lines) and CAH (dashed lines) values with the tape test for the surfaces under study.

The obtained results showed that all the treated surfaces presented long-lasting mechanical properties. The superhydrophobic behaviour was maintained in all the building materials under study during the 20 attachment-detachment cycles tested. Only small fluctuations in the SCA and CAH values were observed, and they can be related to measurement errors.

Finally, a durability test associated with rain resistance was performed (see **Fig. 6**). The obtained results did not show significant changes in the SCA values of the treated samples. In the case of the CAH values, a slight increase can be observed in the surfaces, except for the granite samples. However, the hysteresis is always maintained below 5°

(required value to maintain superhydrophobic properties). Thus, we can conclude that all the treated building materials present long-lasting performance against rain water, demonstrating its possible application for outdoor conditions.
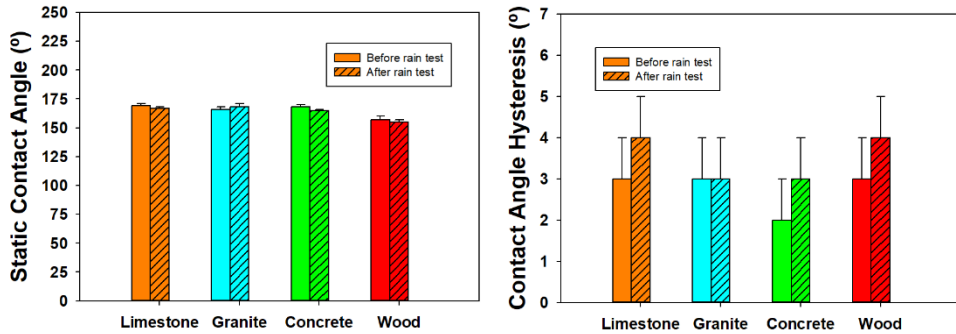
Figure 6. SCA (left) and CAH (right) values of water droplets on the treated surfaces, before and after the rain test.

The long-lasting properties presented by our coating can be explained as a consequence of its effective grafting to the four building materials evaluated, produced by condensation reactions between silanol groups (Si-OH) present in the fluoroalkylsilane, which allow it to polymerize and, moreover, to condense with Si-OH present in the SiO_2 NPs, giving rise to a durable nano-particulate coating [11,22]. These silanol groups can condense with the silanol groups of the quartz minerals present in high and low proportion in the granite and the limestone, respectively. The Si-OH can also condense with the silanol groups of the concrete, and with the hydroxyl groups (OH) of the cellulose of wood. In addition, the high penetration of the product into the pore structure of the substrates (see **Table 1**) contributes significantly to improve the durability of the superhydrophobic materials because in case of removing the superficial coating, the product into the building material can preserve the superhydrophobic properties. Additionally, the product polymerizing inside the pores structure can improve the attachment of the coating with the substrate.

In addition, the high resistance to rain water demonstrate the high stability of the obtained Cassie-Baxter regime. On a Cassie-Baxter surface the water droplets are placed on the top of roughness peaks, and air-pockets are created between water and solid surface [4]. However, if a critical pressure is reached, the water droplets

eventually touch the roughness valleys [46] and thus, the surface can be transformed to a Wenzel regime [47]. In this regime, the repellence properties are lost. In the specific resistance rain simulation (see **Fig. 6**) carried out in this work, repellence is maintained, confirming the high resistance of the coatings under study.

5.6. Conclusions.

Superhydrophobic and oleophobic surfaces were created, by means of a simple procedure, on four common building materials employed in Cultural Heritage. The product, synthesized by an aqueous media sol-gel route, was able to decrease surface energy (by the action of alkyl fluorinated chains), giving rise to hydrophobic and oleophobic properties. In addition, the creation of Cassie-Baxter roughness by adding 40-nm SiO_2 NPs into the starting sol, gave rise to surfaces with repellence and self-cleaning properties.

Finally, the lasting properties of the coatings were tested by means of a mechanical test and a resistance to rain evaluation. All the building surfaces under study maintained superhydrophobic properties, demonstrating that an effective grafting between the substrates and the coating was achieved. In addition, the product penetration of the product into the pores of the substrates is a critical parameter promoting durability.

Since this product can find application in Cultural Heritage, changes in colour induced by the treatment were evaluated, being negligible the colour change observed for all the substrates. Future compatibility studies will be carried out in order to assure its correct application in this field.

5.6. References.

[1]   L. Gao, T.J. McCarthy, Wetting 101º, Langmuir. 25 (2009) 14105.

[2]   W. Barthlott, C. Neinhuis, H. Verlot, C.L. Schott, Purity of the sacred lotus , or escape from contamination in biological surfaces, Planta. 202 (1997) 1.

[3]   K. Koch, B. Bhushan, Y.C. Jung, W. Barthlott, Fabrication of artificial Lotus leaves and significance of hierarchical structure for superhydrophobicity and low adhesion, Soft Matter. 5 (2009) 1386.

[4]   A.B.D. Cassie, S. Baxter, Wettability of porous surfaces, Trans. Faraday Soc. 40 (1944) 546.

[5]   C. Kosak Söz, E. Yilgör, I. Yilgör, Influence of the average surface roughness on the formation of superhydrophobic polymer surfaces through spin-coating with hydrophobic fumed silica, Polym. (United Kingdom). 62 (2015) 118.

[6]   J.D. Rodrigues, A. Grossi, Indicators and ratings for the compatibility assessment of conservation actions, J. Cult. Herit. 8 (2007) 32.

[7]   D. Öner, T.J. McCarthy, Ultrahydrophobic Surfaces. Effects of Topography Length Scales on Wettability, Langmuir. 16 (2000) 7777.

[8]   G. McHale, S. Aqil, N.J. Shirtcliffe, M.I. Newton, H.Y. Erbil, Analysis of droplet evaporation on a superhydrophobic surface, Langmuir. 21 (2005) 11053.

[9]   M. Hikita, K. Tanaka, T. Nakamura, T. Kajiyama, A. Takahara, Super-liquid-repellent surfaces prepared by colloidal silica nanoparticles covered with fluoroalkyl groups., Langmuir. 21 (2005) 7299.

[10]   S.S. Latthe, H. Imai, V. Ganesan, A. Venkateswara Rao, Porous superhydrophobic silica films by sol–gel process, Microporous Mesoporous Mater. 130 (2010) 115.

[11]   D.S. Facio, M.J. Mosquera, Simple strategy for producing superhydrophobic nanocomposite coatings in situ on a building substrate., ACS Appl. Mater. Interfaces. 5 (2013) 7517.

[12]   M. Callies, D. Quéré, D. Quere, On water repellency, Soft Matter. 1 (2005) 55.

[13]   B.P. Dyett, A.H. Wu, R.N. Lamb, Mechanical Stability of Surface Architecture—Consequences for Superhydrophobicity, ACS Appl. Mater. Interfaces. 6 (2014) 18380.

[14]   A. Chatzigrigoriou, P.N. Manoudis, I. Karapanagiotis, Fabrication of water repellent coatings using waterborne resins for the protection of the cultural heritage, Macromol. Symp. 331–332 (2013) 158.

[15]   J. MacMullen, J. Radulovic, Z. Zhang, H.N. Dhakal, L. Daniels, J. Elford, M.A. Leost, N. Bennett, Masonry remediation and protection by aqueous silane/siloxane macroemulsions incorporating colloidal titanium dioxide and zinc oxide nanoparticulates: Mechanisms, performance and benefits, Constr. Build. Mater. 49 (2013) 93.

[16]   P.N. Manoudis, S. Papadopoulou, I. Karapanagiotis, A. Tsakalof, I. Zuburtikudis, C. Panayiotou, Polymer-Silica nanoparticles composite films as protective coatings for stone-based monuments, J. Phys. Conf. Ser. 61 (2007) 1361.

[17]   P.N. Manoudis, I. Karapanagiotis, A. Tsakalof, I. Zuburtikudis, C. Panayiotou, Superhydrophobic composite films produced on various substrates., Langmuir. 24 (2008) 11225.

[18]   C.-H. Xue, S.-T. Jia, J. Zhang, J.-Z. Ma, Large-area fabrication of superhydrophobic surfaces for practical applications: an overview, Sci. Technol. Adv. Mater. 11 (2010) 033002.

[19]   D. Aslanidou, I. Karapanagiotis, C. Panayiotou, Tuning the wetting properties of siloxane-nanoparticle coatings to induce superhydrophobicity and superoleophobicity for stone protection, Mater. Des. 108 (2016) 736.

[20]   P.N. Manoudis, A. Tsakalof, I. Karapanagiotis, I. Zuburtikudis, C. Panayiotou, Fabrication of super-hydrophobic surfaces for enhanced stone protection, Surf. Coatings Technol. 203 (2009) 1322.

[21]   L. De Ferri, P.P. Lottici, A. Lorenzi, A. Montenero, E. Salvioli-Mariani, Study of silica nanoparticles - polysiloxane hydrophobic treatments for stone-based monument protection, J. Cult. Herit. 12 (2011) 356.

[22]   L.A.M. Carrascosa, D.S. Facio, M.J. Mosquera, Producing superhydrophobic roof tiles, Nanotechnology. 27 (2016) 095604.

[23]   M.J. Mosquera, D.M. de los Santos, T. Rivas, P. Sanmartín, B. Silva, New Nanomaterials for Protecting and Consolidating Stone, J. Nano Res. 8 (2009) 1.

[24]   I. De Rosario, T. Rivas, G. Buceta, J. Feijoo, M.J. Mosquera, Surfactant-Synthesized Consolidants Applied To A Granitic Medieval Necropolis In NW Spain. Laboratory And In Situ Effectiveness Evaluation, Int. J. Archit. Herit. 11 (2017) 1166.

[25]   I. De Rosario, F. Elhaddad, A. Pan, R. Benavides, T. Rivas, M.J. Mosquera, Effectiveness of a novel consolidant on granite: Laboratory and in situ results, Constr. Build. Mater. 76 (2015) 140.

[26]   J.F. Illescas, M.J. Mosquera, Producing surfactant-synthesized nanomaterials in situ on a building substrate, without volatile organic compounds., ACS Appl. Mater. Interfaces. 4 (2012) 4259.

[27]   D.S. Facio, M. Luna, M.J. Mosquera, Facile preparation of mesoporous silica monoliths by an inverse micelle mechanism, Microporous Mesoporous Mater. 247 (2017) 166.

[28]   D.S. Facio, L.A.M. Carrascosa, M.J. Mosquera, Producing lasting amphiphobic building surfaces with self-cleaning properties, Nanotechnology. 28 (2017) 265601.

[29]   UNE-EN 12390-2. Ensayo de hormigón endurecido. Parte 2: Fabricación y curado de hormigón para ensayo de resistencia, 2009.

[30]   J.Y. Huang, S.H. Li, M.Z. Ge, L.N. Wang, T.L. Xing, G.Q. Chen, X.F. Liu, S.S. Al-Deyab, K.Q. Zhang, T. Chen, Y.K. Lai, Robust superhydrophobic TiO_2@fabrics for UV shielding, self-cleaning and oil–water separation, J. Mater. Chem. A. 3 (2015) 2825.

[31]   R.S. Berns, Billmeyer and Saltzman's Principles of Color Technology, 3rd ed., New York, 2000.

[32]   T. Sun, L.I.N. Feng, X. Gao, L. Jiang, Bioinspired Surfaces with Special Wettability, Acc. Chem. Res. 38 (2005) 644.

[33]   B. Cortese, S. D'Amone, M. Manca, I. Viola, R. Cingolani, G. Gigli, Superhydrophobicity due to the hierarchical scale roughness of PDMS surfaces, Langmuir. 24 (2008) 2712.

[34]   R.M. Wagterveld, C.W.J. Berendsen, S. Bouaidat, J. Jonsmann, Ultralow Hysteresis Superhydrophobic Surfaces by Excimer Laser Modification of SU-8, Langmuir. 22 (2006) 10904.

[35]   J.D. Brassard, D.K. Sarkar, J. Perron, Synthesis of monodisperse fluorinated silica nanoparticles and their superhydrophobic thin films, ACS Appl. Mater. Interfaces. 3 (2011) 3583.

[36]   J. Li, Y. Lu, Z. Wu, Y. Bao, R. Xiao, H. Yu, Y. Chen, Durable, self-cleaning and superhydrophobic bamboo timber surfaces based on TiO_2 films combined with fluoroalkylsilane, Ceram. Int. 42 (2016) 9621.

[37]   S. Zhou, X. Ding, L. Wu, Fabrication of ambient-curable superhydrophobic fluoropolysiloxane/TiO_2 nanocomposite coatings with good mechanical properties and durability, Prog. Org. Coatings. 76 (2013) 563.

[38]   I. Alfieri, A. Lorenzi, L. Ranzenigo, L. Lazzarini, G. Predieri, P.P. Lottici, Synthesis and characterization of photocatalytic hydrophobic hybrid TiO_2-SiO_2 coatings for building applications, Build. Environ. 111 (2017) 72.

[39]   Y. Li, X. Men, X. Zhu, B. Ge, F. Chu, Z. Zhang, One-step spraying to fabricate nonfluorinated superhydrophobic coatings with high transparency, J. Mater. Sci. 51 (2016) 2411.

[40]   L.D. a. Chumpitaz, L.F. Coutinho, A.J. a. Meirelles, Surface tension of fatty acids and triglycerides, J. Am. Oil Chem. Soc. 76 (1999) 379.

[41]   R.A. Hayn, J.R. Owens, S.A. Boyer, R.S. McDonald, H.J. Lee, Preparation of highly hydrophobic and oleophobic textile surfaces using microwave-promoted silane coupling, J. Mater. Sci. 46 (2011) 2503.

[42]   T. Darmanin, F.F. Guittard, Superhydrophobic and superoleophobic properties in nature, Mater. Today. 18 (2015) 273.

[43]   B. Bhushan, E.K. Her, Fabrication of superhydrophobic surfaces with high and low adhesion inspired from rose petal., Langmuir. 26 (2010) 8207.

[44]   L. Xu, R.G. Karunakaran, J. Guo, S. Yang, Transparent, Superhydrophobic Surfaces from One-Step Spin Coating of Hydrophobic Nanoparticles, ACS Appl. Mater. Interfaces. 4 (2012) 1118.

[45]   H. Bellanger, T. Darmanin, E. Taffin de Givenchy, F. Guittard, Chemical and Physical Pathways for the Preparation of Superoleophobic Surfaces and Related Wetting Theories, Chem. Rev. 114 (2014) 2694.

[46]   E. Bormashenko, Progress in understanding wetting transitions on rough surfaces, Adv. Colloid Interface Sci. 222 (2015) 92.

[47]   R.N. Wenzel, Resistance of solid surfaces to wetting by water, Ind. Eng. Chem. 28 (1936) 988.

5.7. Supplementary information.

Table S1. Average Contact Angle values of water droplets on the different substrates.

Substrate	Static CA (°)	Advancing CA (°)	Receding CA (°)	Hysteresis CA (°)
Limestone	169±2	157±1	154±2	3±1
Granite	166±2	155±1	152±2	3±1
Concrete	168±2	159±1	157±2	2±1
Wood	157±3	154±3	151±5	3±1

Capítulo 6

Producing Hydrophobic Concrete with Photo-induced Superhydrophilic surface: Detergent-Free Cleaning Performance.

6.1. Abstract.

6.2. Introduction.

6.3. Materials and methods.

6.4. Results and discussion.

6.5. Conclusions.

6.6. References.

6.7. Supplementary information.

Producing Hydrophobic Concrete with Photo-induced Superhydrophilic surface: Detergent-Free Cleaning Performance

6.1. Abstract.

In spite of the promising abilities of superhydrophobic surfaces, such as the self-cleaning performance promoted by their high water repellence, these surfaces may lose their properties when contaminated with oils. An alternative solution to this problem is the use of superhydrophilic surfaces, which present underwater superoleophobic behavior. In this work, a photo-induced superhydrophilic surface was produced on concrete samples. Specifically, a superhydrophobic product was prepared by adding TiO_2 NPs, to create a Cassie-Baxter state, to a sol containing a silica oligomer and polydimethylsiloxane. After being exposed to sunlight, the treated surfaces switched from superhydrophobic to superhydrophilic because of the photo-induced hydrophilic behavior of TiO_2. The superhydrophilic surfaces displayed underwater superoleophobicity, as well the ability to remove oil contaminants without the need of employing detergents. In addition, a water absorption by capillarity test demonstrated that the superhydrophilicity was only produced on the surface, whereas the bulk of the treated material prevented the penetration of water. Finally, the durability of the treated samples was evaluated by means of different tests, demonstrating the long-lasting performance of the product against degradation.

6.2. Introduction.

Nowadays, cement-based materials are second only to water in terms of the materials that are most commonly used by humankind. Thus, the development of innovative solutions for their conservation is a significant challenge for the current society and it opens the doors to an immense global market. In addition, it is remarkable that repairing and conservation activities in the construction sector promote even more employment than that generated by new construction.

Water is involved in most of degradation processes produced in concrete and other building materials, including frost action, chloride aggression, leaching and biological decay [1–3]. Thus, hydrophobic products with application in concrete have been commercially available for a long time. Such products have been traditionally employed for increasing concrete service-life in bridges and other structures in contact with water [3,4]. Most of these products are based on oligomeric alkylsiloxanes (eg. Silres BS290, from Wacker Chemie), which penetrate into the concrete pores due to their low viscosity and are able to polymerize spontaneously via a sol-gel process while reducing the surface energy due to the organic moieties, preventing water ingress into the structure.

In the last years, a new generation of surface bioinspired treatment agents, has emerged. Learning from natural structures, such as lotus leaves or water strider legs, the combination of a hierarchical micro/nano roughness promoting a Cassie-Baxter state and a low surface energy produces surfaces with superhydrophobic performance [5–7]. In these surfaces, air-pockets are created between water and solid surface, producing high hydrophobicity and repellence [8–10], which can be exploited to obtain self-cleaning surfaces [10–12] among other uses. A simple approach to obtain these surfaces consists on the use of hydrophobic nanoparticles (NPs) dispersions into a solvent. As the solvent is evaporated, the NPs self-assembly produces a Cassie-Baxter surface with superhydrophobic performance. Some of this solutions have even launched to the market (i.e. AquaShield Ultimate, from Tecnan) for application in building materials. However, this strategy has a significant drawback related to their poor penetration and low adherence to substrates, promoting a low durability of the

coating. In order to increase durability, NPs have been integrated in organosilanes sols with low viscosity [11,13–18]. These sols can be sprayed, dipped or brushed on building materials, penetrating into their pore structure to produce, through a sol-gel route, a silica matrix in which the NPs are integrated. This approach increases the adhesion to the substrate, and subsequently their durability. Our group used this approach to produce superhydrophobic building materials such as stones and roof tiles[13,14]. In recent years, similar approaches have been employed to produce superhydrophobic concretes [19–22].

Even though effective solutions to fabricate superhydrophobic concrete surfaces have been attained, the obtention of superoleophobic surfaces still remains as a key challenge for two significant reasons: (i) most of facades staining is caused by oil-based contaminants, including atmospheric pollutants and graffiti; (ii) durability of superhydrophobic surfaces is completely compromised by surface contamination with oils, promoting loss of their self-cleaning performance [23]. The obtention of amphiphobic materials can help to circumvent this problem, but it requires the use of fluorinated materials [12,18], with all the environmental limitations involved in their applications. In the case of superoleophobic surfaces, the surface structures typically employed for obtaining Cassie-Baxter state for superhydrophobic surfaces are not enough for promoting oil-repellence. Thus, it is necessary the creation of roughness with re-entrant structures (T-shape or mushroom-like) [24–26].

A recent biomimetic approach to produce self-cleaning surfaces is based on the fishes ability to stay clean, even in polluted water media, due to its underwater superoleophobicity [27,28]. The combination of hydrophilic compounds with the presence of micropapillaes, promoting a hierarchical micro/nano-structure, in the fish scales promotes a Cassie-Baxter state, in which a layer of water is situated between the surface and the oil contaminant [8,29].

In this work, we produce concrete surfaces with superolephobicity in contact with water, taking inspiration from fish scales behavior, promoting an effective self-cleaning performance of oil-based contaminants. According to the biomimetic approach employed, it is required to produce a superhydrophilic concrete surface in air. However,

since water is the main vehicle of most agents promoting decay in concrete [1,2], it is of utmost importance for the bulk structure to remain hydrophobic, preventing water ingress. According to these requirements, TiO_2 was chosen as a suitable candidate to produce hydrophilic behavior in building materials because its exposure to near UV-visible light in facades or other architectonic elements produces hydroxyl groups on its surface, giving rise to photo-induced hydrophilic properties [30]. Nevertheless, the TiO_2 located under concrete surface, without exposure to UV radiation, does not present induced-hydrophilicity and subsequently, it prevents water ingress.

According to this strategy, TiO_2NPs were added to a sol containing a silica oligomer and an organosilane (polydimethylsiloxane, PDMS). The oligomer spontaneously produces a silica matrix into the pore structure of concrete, assuring a long-lasting performance. The PDMS gives rise to low surface energy, giving rise to hydrophobic performance. TiO_2NPs were added to the sol with two objectives: (1) create a surface roughness promoting a Cassie-Baxter and (2) to induce superhydrophilicity in concrete surfaces as a consequence of the photocatalytic behavior of TiO_2. In addition, n-octylamine was added to the starting sol with two objectives [31]: (1) to catalyze the sol-gel process and (2) to prevent gel cracking during drying. The sol was sprayed on concrete samples and its performance was evaluated. A comparative study was performed between this material and two superhydrophobic products: (1) a similar material in which TiO_2NPs were replaced by SiO_2, in order to prevent induced-superhydrophilicity was also evaluated and (2) a typical commercial superhydrophobic product consisting on a dispersion of hydrophobic NPs into a solvent.

6.3. Materials and methods.

6.3.1. Synthesis.

The following reagents were employed: Wacker TES40 WN (hereafter TES40, from Wacker Chemie AG) is a mixture of ethoxysilane oligomers with an average polymerization degree of 5 Si-O units. A hydroxyl-terminated polydimethylsiloxane (PDMS, from ABCR) with a polymerization degree of 12 and a molecular mass between 400 and 600 and a 5 to 6 %w/w OH percentage. n-octylamine (n-8, from Sigma Aldrich).

Aerosil OX50 fumed silica nanoparticles (from Evonik), with an average size of 40 nm and a BET surface of 50 m^2/g. Aeroxide P25 TiO_2 NPs (from Evonik), with an average size of 21 nm and surface BET area of 50 m^2/g. The commercial superhydrophobic product (AQUASHIELD Ultimate from TECNAN®) was used as-received, According to its technical data sheet, this product consists of an isopropanol-based dispersion of NPs treated with a low surface energy agent.

The materials under study were synthetized through a sol-gel route, by mixing TES40, PDMS, n-octylamine, water (89.67, 10.00, 0.08 and 0.25 %v/v, respectively) and the TiO_2NPs (5 %w/v) or, alternatively, SiO_2NPs. The mixture was sonicated for 10 minutes in an ultrasonic probe (Sonopuls, HD3200 from Bandelin) with a power of 1 $W·mL^{-1}$. The sols were named as UCA-T and UCA-S (containing TiO_2 NPs or SiO_2NPs, respectively).

6.3.2. Sol-gel characterization.

The viscosity properties of the sols was measured at 25 °C by using a concentric cylinder viscometer (model DV-II+ with UL/Y adapter) from Brookfield Engineering Laboratories Inc.

Gel time was studied by casting 3 mL of each sol in glass Ø90 mm Petri dishes and storing them at laboratory conditions (60 % RH, 20 °C) until complete gelation and drying.

6.3.3. Evaluation of the performance on concrete.

A type I white Portland cement and a calcareous sand (ϕ 1–6 mm) were employed to fabricate the concrete samples. The water:cement and the cement:sand weight ratios were 1:2 and 1:5, respectively. The specimens were cured under water at 21 ± 2 °C for 28 days, according with standard UNE-EN 12390-2, being their open porosity around 12 %. Prior to application, the samples were cut into 3.5x3.5x.3.5 cubes, washed with de-ionized water and dried into an oven at 60 °C until constant weight. Both of the synthetized sols and the commercial superhydrophobic product were applied on the concrete surface by spraying with an air gun (at 2 bars during 10 seconds). Product uptake and dry matter (after weight remained constant) were calculated by weight difference. After six months, the following tests were carried out:

The changes in color induced by the application of the products were evaluated, in the *CIE L*a*b** color space [32], by using a spectrophotometer colorimeter ColorFlex, from Hunterlab. The measurement conditions used were: Illuminant C and observer CIE 10°.

The changes in water diffusivity after the products application, was evaluated by using an automatized device designed in our laboratory. Details of the experiment are described in previous papers [33].

Penetration depth of the nanomaterials into the concrete substrate was evaluated by observing the hydrophobic regions of cross-sectional cuts and registering the images by a Nikon model SMZ800 stereoscopic microscope.

The topography of the surfaces was studied by Scanning Electron Microscopy (SEM) with a Nova Nano SEM 450 model from the FEI Company. The samples were gold-sputtered (4 nm thick) prior to observation.

Surface roughness was characterized by Atomic Force Microscopy (AFM, model Dulcinea from NanotecElectrónica S.L.), operating in tapping mode. The Root Mean Square (RMS) roughness values were obtained from 5x5 μm regions.

Static (SCA) and advancing and receding (ACA and RCA) contact angle values were determined by the sessile drop method, using a commercial video-based, software-controlled contact angle analyzer, model OCA 15Plus, from Dataphysics Instruments GmbH. Details of the measurement process are described in a previous paper [18]. The underwater superoleophobic behavior was evaluated by measuring SCA values of chloroform droplets on samples immersed in water. Chloroform was chosen as a model due to having a higher density than water and a surface tension similar to common oils (28 mN·m^{-1}).

The superhydrophilic behavior of the sample treated with UCA-T was induced by placing the treated samples into a climatic chamber model Solarbox 3000e RH from Cofomegra Srl, equipped with a solar spectrum lamp. The irradiation power was 500 W·m^{-2}, and the temperature and the relative humidity were maintained at 50 °C and

60 %, respectively. The water CA values were monitored during the first 12 hours of exposure.

The water absorption by capillarity of the samples, before and after inducing the superhydrophylic surface, was evaluated by a modification of European standard UNE-EN 1925. Each sample was placed on a petri dish containing a piece of cotton soaked in distilled water and the weight was monitored until it reached a constant value.

A qualitative assessment of the underwater oil repellence was performed by observing the rolling behavior of chloroform droplets (dyed with methylene blue) over the superhydrophobic and superhydrophilic samples immersed in water and tilted at 5°.

The self-cleaning properties the treatments were evaluated by observing the removal of model staining agents by a water stream. In the first experiment, dry roof tile powder was deposited on the concrete surface. For the second experiment, the powder was contaminated with oleic acid, in order to simulate greasy dust.

6.3.5. Evaluation of the durability.

The durability of the treatments in different conditions was evaluated by three different tests. For all the three tests, the CA values were monitored at different intervals during the tests and the alterations to the surface after the test were studied by registering SEM images with the equipment previously described.

The adhesion of the applied products to the concrete substrates was evaluated via an adhesive tape test [18,34]. The procedure was carried out by applying Scotch® MagicTM tape (3M) on the coated surface and swiftly detaching the tape in a vertical angle for repeated cycles.

In order to evaluate the stability of the treatments under rainy conditions, a simulated rain- test was performed [35]. For this purpose, the samples were placed under a water column falling form 50 cm, with a flow around 45 mL·s^{-1} in increasing steps of discharged volumes.

A field study of the durability of the products was carried out by exposing the treated samples to outdoor conditions for 3 months (April to June). Specifically, the samples were placed on a rooftop located in Puerto Real (Cádiz, Spain). Monthly meteorological

data (average on the April-June interval) according to Spanish State Meteorological Agency (AEMET): max. Temperature = 22.5 °C, min. temperature = 16.5 °C, Rainfall = 26.3 mm, Humidity = 69%, Hours of sunshine = 297.

6.4. Results and discussion.

6.4.1. Sol-gel characterization.

Regarding the rheological properties of UCA-T and UCA-S sols, both products displayed a Newtonian behavior, with respective viscosity values of 5.8 and 6.3 mPa·s^{-1}. These values are similar to the viscosity of other similar commercial product (5 mPa·s^{-1}), indicating that the products fulfil the requirement for application on building materials by conventional methods (i.e. brushing, spraying…) [36,37].

After casting the products in Petri dishes and allowing them to dry under laboratory conditions, sol-gel transition of UCA-T and UCA-S took place spontaneously within 24 hours, due to the role played by n-octylamine as a basic catalyst [38]. It is worth mentioning that this gelation time was short enough to ensure the *on site* applicability of the products [13] and, at the same time, long enough to allow the sol to penetrate into the porous structure of the concrete. When stored in closed vessels, the products remain stable (i.e. no gelation occurs) for over 12 months. Therefore, the results demonstrated the compatibility of our products with commercial requirements.

6.4.2 Evaluation of the performance on concrete.

After application, the treated concrete specimens showed uptake values ranging from 750 to 790 g·m^{-2}, with no significant differences for the three different products (see Table 1), likely as a consequence of their similar viscosity values. The dry-matter values, on the other hand, could not be determined with precision due to fluctuations caused by the hygroscopic behavior of the concrete.

Table 1. Uptake, depth of penetration, total color difference (ΔE*) and water diffusivity reduction (DR) values of the treated samples respect to the untreated one.

Product	Uptake (g·m^{-2})	Penetration (mm)	ΔE*	DR (%)
Commercial	790±21	1.0±0.2	0.28±0.08	25
UCA-S	766±14	4.3±0.6	0.22±0.09	51
UCA-T.	754±18	3.8±0.2	0.32±0.10	53

Penetration depth of the applied products into the concrete structure, determined by their hydrophobic behavior, is shown in **Table 1**. In addition, photographs of the cross-sections are shown in Supporting Information (**Fig. S1**). The commercial product showed the lowest penetration, likely as a result of its high content in VOC's. As reported by other authors [39], the products with lowest active matter tend to display poor penetration, because the solvent (which acts as a vehicle) is quickly evaporated before the active matter of the product has time to penetrate into the porous structure. On the opposite, UCA-T and UCA-S products, with a higher content of active matter (solvent-free), penetrated up to four times deeper than the commercial one.

A typical drawback associated with the application of products on building materials is the modification of the original aspect. Thus, the color change of the samples treated with our products and the commercial one was evaluated. The calculated total color difference values (ΔE*) are shown in **Table 1**. All the products produced color change lower than 2. According to Rodrigues and Grossi [40], color changes lower than 3 (below human perception threshold) are considered ideal value for application on building materials from cultural heritage, which are subjected to more restrictive requirements than standard building materials [32].

Regarding to water vapor diffusivity, superhydrophobic treatments must prevent the penetration of liquid water into the concrete porous structure. However, the treated samples have to allow the transport of water vapor through them (i.e. they must maintain their breathability).Thus, the water vapor diffusivity of the untreated samples and their treated counterparts were studied. A diffusivity value of $2.60 \cdot 10^{-6}$ m$^2 \cdot$s^{-1} was obtained for the untreated sample. As observed in Table 1, all the products reduced the vapor diffusivity. For the commercial product a decrease around 25 % was reached, whereas UCA products caused a reduction around 50 %. According to Rodrigues and Grossi [40], diffusivity reductions lower than 50 % is considered acceptable. On the other hand, some authors suggest that, in order to prevent specific concrete decay processes (mainly carbonation) [3], a reduction of air diffusivity around 60 % (close to the values of UCA-S and UCA-T) may be appropriate.

The surface topography of the treated concrete surfaces (and their untreated counterpart), which plays a crucial role on their wetting properties [9,41,42], was studied by using SEM and AFM (see **Fig. 1**)

SEM micrographs of the concrete surfaces, shown in **Fig. 1** (top row), show evident modifications of the surface morphology after the different treatments. The untreated surface presented an irregular aspect with clearly visible mineral grains, typical of heterogeneous materials such as concrete.
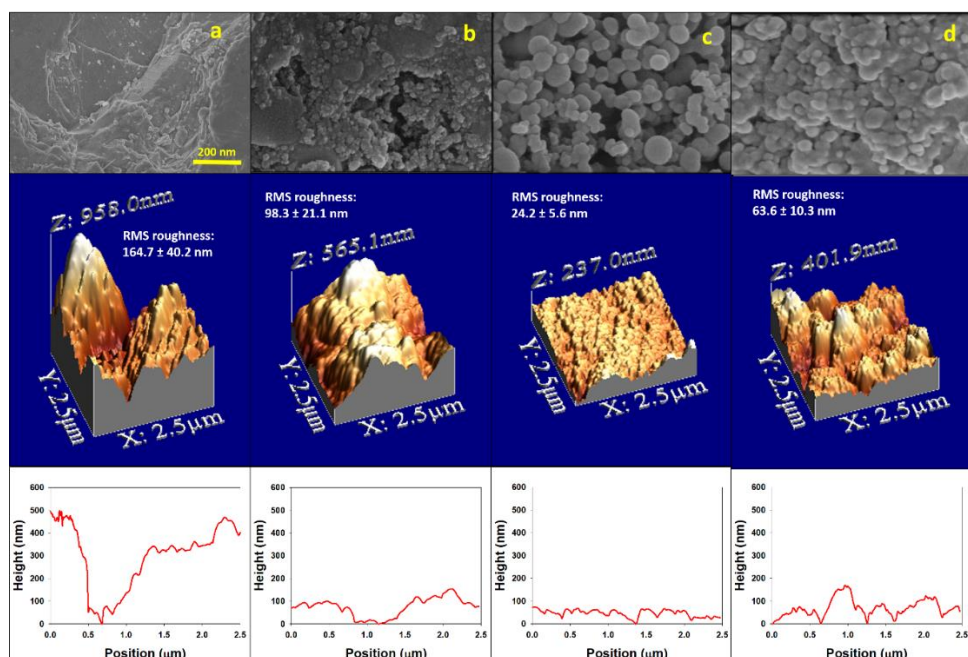

Figure 1. SEM images (first row), AFM 3D images (second row), and representative roughness 2D profiles (third row) of the untreated surface and the treated counterparts. RMS roughness value are also included. (a) Untreated, (b) Commercial, (c) UCA-S, (d) UCA-T.

The sample treated with the commercial product showed overall similar features in the micron range, with NPs aggregates heterogeneously distributed on the surface, instead of forming a continuous coating on the surface. This observation is consistent with previous works [43], which showed that products based on silica NPs dispersions may be unable to create a continuous and effective coating. In contrast with this behavior, the surfaces treated with UCA-S and UCA-T presented a compact structure composed of densely packed NPs, demonstrating the effective formation of a coating on the surface. This is a consequence of the reaction of the silica precursors used in

these products to form, after a sol-gel process, a SiO_2 backbone that fulfills two functions [44] (1) it bridges the mineral grains and covers the pores of substrate, increasing its compaction, (2) it acts as a matrix for the NPs, promoting a better adhesion and a more homogeneous distribution on the surface.

A more detailed textural study of the surfaces was obtained by analyzing the AFM maps. The 3D topographical maps, along with the RMS values (**Fig. 1**, middle row) demonstrated the roughness changes due to the presence of the xerogel matrix and the NPs. In agreement with the SEM images, the untreated sample presented an irregular topography, with tall roughness peaks separated by wide valleys, corresponding to mineral grains and grain borders respectively. This observation also manifested in a higher RMS value (165 nm), with a significant standard deviation (±40). The application of the commercial product significantly reduced the RMS value (98 nm). However, the irregular aspect of the 3D maps and the high standard deviation obtained for the RMS (±21) can be interpreted as an evidence that this product failed to produce an effective coating. As previously observed by SEM, the NPs formed clusters that randomly deposited over the surface, occupying a fraction of the spaces instead of forming a homogeneous layer over the untreated surface.

The surface treated with UCA-S, on the other hand, presented a more homogenous profile, with a lower roughness in the micrometric range and regularly spaced topographical features in the nanometric scale, which translates into smaller RMS values (24 nm) with low standard deviation (±6), confirming the formation of a homogenous coating on the surface. The size of the topographical features (~100 nm), slightly larger than the SiO_2NPs, can be attributed to the formation of clusters of the silica network around the 40 nm-SiO_2NPs, as observed by TEM in prior works [13].

The sample treated with UCA-T product displayed overall similar characteristics to UCA-S (i.e. reduced roughness in the micron scales and regularly spaced nanometric features) due to the formation of a compact layer with embedded TiO_2NPs. The distribution of the nanometric topographical features, however, was different than the surface treated with UCA-S. Specifically a raspberry-like hierarchical structure was formed, composed of larger sub-micrometric peaks and a secondary nanometric

structure, which explains the higher RMS values (64 ±10 nm) observed. The formation of these structures can be attributed to aggregation processes of the TiO_2NPs due to their smaller size compared to the SiO_2NPs.

The size differences of the roughness peaks are more clearly observed in the 2D roughness profiles, shown in **Fig. 1** (bottom row), extracted from the 3D topographical maps. In the case of the untreated substrate, the mineral grains generate an irregular profile with peaks and valleys separated by 0.5-3 µm distances. The commercial product decreased the peak height from ~500 nm to ~150 nm, although the width of said peaks and valleys was barely altered, indicating a tendency for the NPs clusters to deposit at the bottom of the valleys. The nano-roughness due to the NPs was present, albeit poorly defined because of the small particle size and their random distribution. In contrast with this structure, the products containing the silica gel matrix (UCA-T and UCA-S) created an effective layer and produced a roughness profile with regular peak height and width in the nano- and/or sub-micron scale. More specifically, the surface treated with UCA-T displayed 60-100 nm high peaks separated by similar distances, corresponding to the individual TiO_2NPs and the TiO_2NPs/silica matrix aggregates observed by SEM. The hierarchical roughness of the surface treated with UCA-T due to the formation of clusters was clearly observed by the presence of sub-micrometric peaks, separated by 150-300 nm distances, which were composed by evenly spaced 40-50 nm peaks, roughly the size of the individual TiO_2NPs.

The wetting behavior by water of the concrete samples under study, as evaluated by static and dynamic contact angle measurements, can be seen in **Fig. 2**.
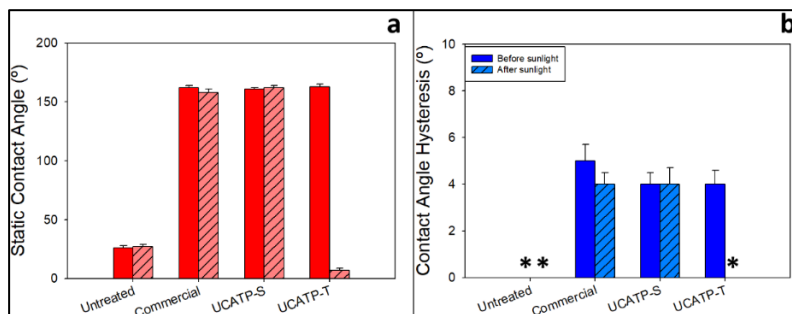

Figure 2. (a) SCA and (b) CAH values of the untreated samples and their treated counterparts, before and after sunlight exposure. *These values could not be measured due to the quick spreading of the water droplets over the surface.

Producing Hydrophobic Concrete with Photo-induced Superhydrophilic surface: Detergent-Free Cleaning Performance

The initial wetting behavior of all the three treatments was evidenced by the change from the hydrophilic character (SCA ~25°) of the untreated surface, due to the presence of polar groups (i.e. Si-OH, $CO_3^=$...), to a superhydrophobic surface with SCA around 160° and CAH values lower than 4°, which are related to water-repellence phenomena [45]. No significant differences could be detected between the three different treatments. This superhydrophobic behavior can be explained by the existence of a Cassie-Baxter wetting regime [8], which predicts that the combination of a low surface energy and a nano/micro-roughness can lead to water contact angles higher than those of an ideal flat surface due to the formation of air pockets between the topographical features. As observed by SEM and AFM (**Fig.1**), all of the treated surfaces presented different arrangements of the nanoparticles that generated nanometric structures capable of creating this state, as well as components containing aliphatic moieties that effectively decrease the surface energy [7,13,46].

After irradiation with simulated sunlight in a climatic chamber, the CA were evaluated in order to demonstrate the ability to activate photo-induced superhydrophilic properties of the concrete samples treated with UCA-T (see **Fig. 2**). For comparison purposes and to determine if the changes were actually due to the presence TiO_2, the samples treated with the commercial product and UCA-S were also subjected to the same conditions.

The obtained results showed an effective switch from superhydrophobic to superhydrophilic behavior for the samples treated with UCA-T, where SCA decreased down to values < 10° after 12 hours of sunlight exposure, whereas the CAH could not be evaluated due to the rapid spread of water on the surface. This behavior is in agreement with different TiO_2-based systems reported in the literature [47], where after TiO_2 is irradiated with UV light, oxygen vacancies are created, resulting the conversion of Ti^{4+} sites to Ti^{3+} sites, promoting a higher interaction with water due to dissociative water adsorption mechanisms [48]. This effect in turn leads to an increase in the number of polar hydroxide groups on the surface, which turns the surface into superhydrophilic [49,50]. As observed by the SEM images (**Fig. 1**), the TiO_2NPs were

effectively exposed on the surface of the treated specimens, thus reinforcing the explanation of the changes due to TiO$_2$-related phenomena.

Regarding the surfaces treated with the commercial product and UCA-S, no significant changes were observed for SCA and CAH values after irradiation, which confirmed that the matrix and the organic component of the products are stable under the test conditions. Therefore, the switch towards a superhydrophilic behavior of UCA-T treated samples can be solely attributed to the changes induced by the presence of TiO$_2$. For clarity sake, we will refer to the photo-activated superhydrophilic surface as UCA-T* in order to differentiate it from the initial superhydrophobic state (UCA-T).

Since the main objective of this work, which is exploiting the underwater superoleophobic properties promoted by the superhydrophilic surfaces, as demonstrated in other fields such as water-oil separation and self-cleaning systems [29,51], this property was evaluated. Specifically, the SCA values of chloroform droplets on samples immersed in water were compared for the superhydrophobic and the superhydrophilic surfaces (UCA-S and UCA-T*, respectively). Chloroform droplets were rapidly spread on the superhydrophobic surface, showing underwater oleophilic behavior, with SCA of 12°± 2° (see **Fig. 3a**). On the other hand, chloroform droplets showed spherical shape when they were deposited onto the UCA-T* treated samples, presenting a superoleophobic behavior, with SCA values of 152°±1° (see **Fig. 3b**).
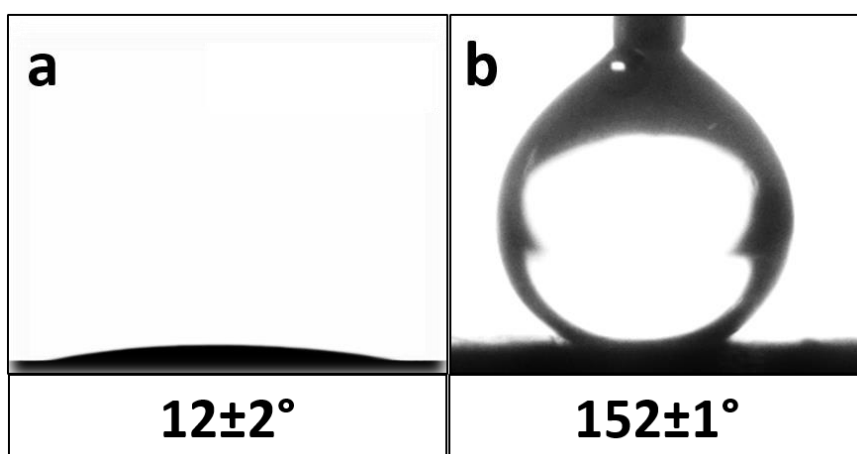

Figure 3. Underwater chloroform droplets placed on concrete samples surfaces treated with (a) UCA-S and (b) UCA-T*.

The oil repellent properties were evidenced through the qualitative test by dropping chloroform droplets (dyed with methylene blue) over concrete samples, tilted at 5°, immersed in water treated with UCA-S, and its counterpart treated with UCA-T*. **Figure 4** shows the snapshots of the test for each surface under study. In addition, a video of the chloroform droplets hitting the underwater surfaces under study is available in Supporting Information (**Video S1**). For the superhydrophobic surface (**Fig. 4, a-d**), it was observed that the chloroform droplets were rapidly spread, leaving a visible trail over the surface. In contrast, the chloroform droplets poured onto the superhydrophilic surface (**Fig. 4, e-h**), rapidly rolled off the tilted surface, thus fulfilling the requisites of an oil-repellent surface (i.e. sliding angle > 10°).
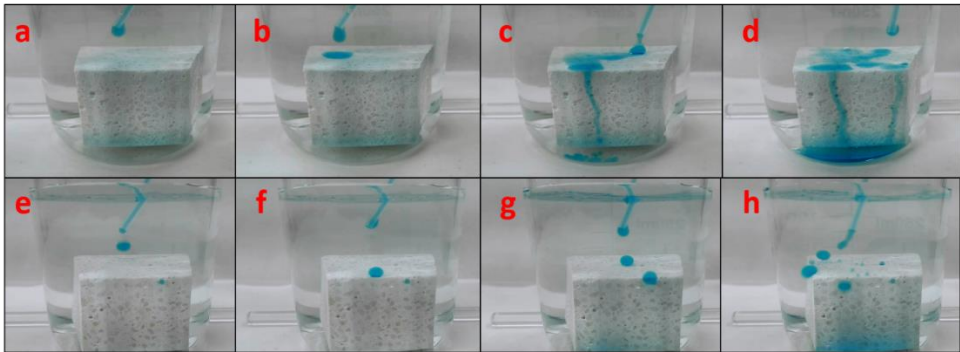

Figure 4. Time-lapse sequence of chloroform droplets hitting the surfaces under study. (a-d) superhydrophobic surface, and (e-h) superhydrophilic surface.

A partial explanation for the contrast between the water behavior in air and the oil behavior underwater can be derived from the surface tension balance by using a modified form of Young equation (equation 1) [27,52].

$$cos\theta_{OW} = \frac{\gamma_O cos\theta_O - \gamma_W cos\theta_W}{\gamma_{OW}} \qquad (1)$$

Where θ_{ow} is the contact angle of an underwater oil droplet on an ideal smooth surface; θ_o and θ_w are the contact angles (in air media) of oil and water droplets, respectively, and γ_o, γ_w and γ_{ow} are the surface tensions of oil and water, and the interfacial tension of oil in water, respectively.

In our specific case, the theoretical θ_{ow} values of the surfaces under study can be calculated by inserting in Equation 1 the surface tension values, obtained from literature: γ_o = 26.7, γ_w = 72.0 mN·m^{-1}, γ_{ow} = 31.6 mN·m^{-1}; and the experimental values

of the contact angles measured on xerogel pieces of UCA-S and UCA-T*, which can be considered close to ideal smooth surfaces: θ_w = 90° and 65° for UCATP-S and UCA-T*, θ_o = 55° for both UCA-S and UCA-T*. According to this equation the calculated θ_{ow} values are 61° and 118°, for chloroform droplets on UCA-S and UCA-T* surfaces respectively, which in general agrees with the underwater oleophilic and oleophobic character of these surfaces observed experimentally.

The exact value of these contact angles, however, differs from the experimental measurements, and fails to explain the underwater superoleophobic behavior of the superhydrophilic (UCA-T*) concrete sample under study. Such a discrepancy arises from the influence of surface roughness over the wettability of liquids on solid surfaces [41,42,53]. In accordance with the Cassie-Baxter wetting regime, when the superhydrophobic surface (treated w/ UCA-S) is immersed, air pockets get trapped between the roughness features(see **Fig. 5**) [8]. Under these conditions, the chloroform droplets are able to easily replace the position of the air pockets, penetrating into the roughness valleys and impregnating the whole surface, thus effectively switching the wetting state from a Cassie-Baxter to a Wenzel regime [29,51,54]. According to the model proposed by Wenzel [55] (for an intrinsically oleophilic material (i.e. SCA < 90 ° on an ideal flat surface), the contact angle value will decrease proportionally to a factor dependent on the surface roughness, which is in line with our experimental observations (θ_{ow} = 12° vs the theoretical 61°).

On the other hand, the behavior of the superhydrophilic concrete sample (UCA-T*) responds to a Cassie-Baxter state. After initially submerging the surface, water is able to penetrate the grooves of roughness and, therefore, fully wet the surface (Wenzel state) [55]. When the chloroform droplet is deposited onto this surface (see **Fig. 4, e-h**), the water layer in the roughness valleys gets between the chloroform and the solid surface, giving rise to a Cassie-Baxter where the air is substituted by water (see **Fig. 5**) [26,29,51,54]. As previously discussed, for a surface in this wetting regime, the value of the contact angle will increase (and the surface will present repellent behavior) with the presence of micro/nanometric roughness features, and this effect will be more

remarkable on surfaces with a hierarchical roughness, as observed by AFM images (**Fig. 1**), where the contact area between the surface and the chloroform will be minimized.
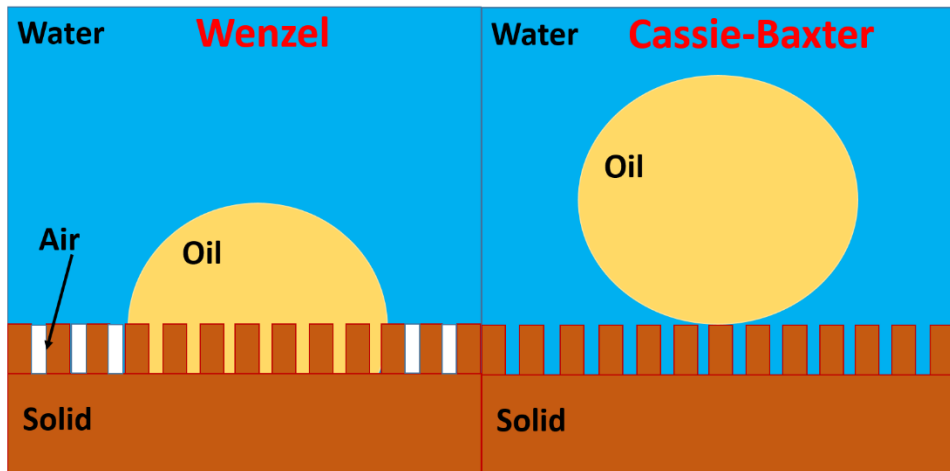

Figure 5. Underwater version of Wenzel and Cassie-Baxter states, describing the behaviour of UCA-S and UCA-T* respectively.

The self-cleaning properties of the treated concrete surfaces as a consequence of their wetting properties, evaluated in three different situations, can be seen in the snapshots from the different tests (**Figure 6**). In addition, a video showing the experiment is available in Supporting Information (**Video S2**). In the first experiment (**Fig. 6, a-d**), powdered brick was deposited over the concrete sample treated with the superhydrophobic treatment (UCA-S). As observed in previous works, water was able to easily remove the solid while barely interacting with the surface due to its high repellence, effectively promoting a self-cleaning performance [12,18]. In contrast with the previous situation, when the powder deposited over the sample with the superhydrophobic treatment was contaminated with oleic acid (**Fig. 6, e-h**), the water jet was not able to wash the surface due to the immiscibility of water and oil and the oleophilic nature of the surface (in line with the measurements with chloroform in **Figs. 3 & 4**), clearly manifesting one of the main drawbacks of self-cleaning superhydrophobic surfaces [24,26,28].
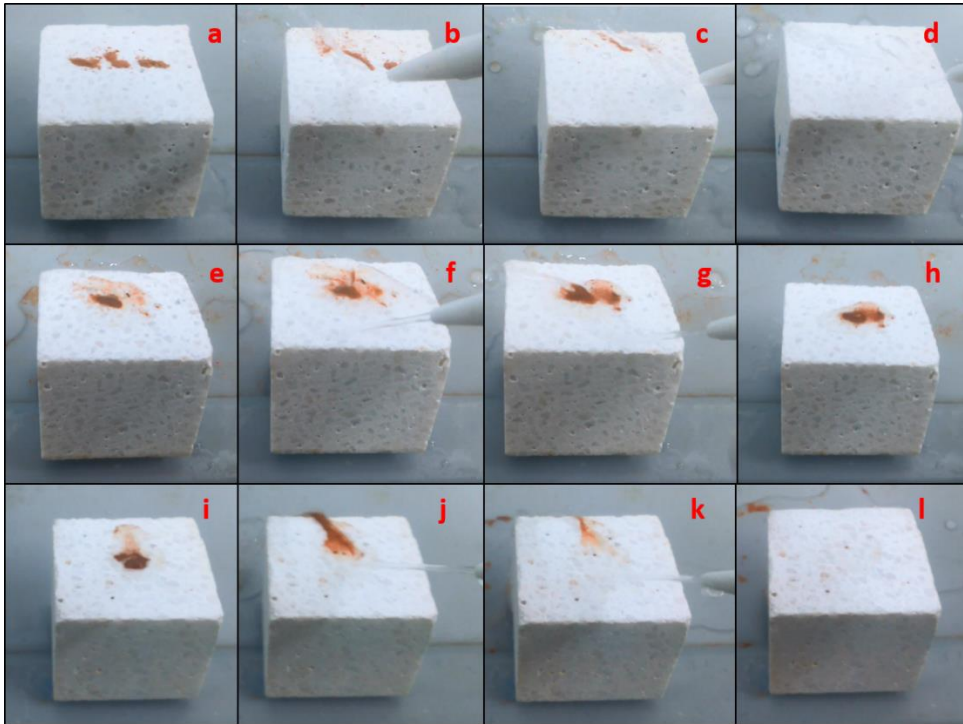
Figure 6. Time-lapse sequence of self-cleaning process for the different cases of study. (a-d) dry powder on superhydrophobic surface, (e-h) oil-contaminated powder on superhydrophobic surface, and (i-l) oil-contaminated powder on superhydrophilic surface.

In contrast with the previous situation, the water stream was able to easily remove the oil-contaminated powder from the superhydrophilic concrete sample (UCA-T*), as pictured in **Fig. 6, i-l** as a consequence of its underwater superoleophobic behavior. As previously discussed, the water from the stream can penetrate into the roughness groves of the surface due to its superhydrophilic character, decreasing the interaction with the oil and allowing the removal of oily contaminants just by the action of a low pressure water jet. These experiments demonstrate the applicability of this route for minimizing the main drawbacks of superhydrophobic protective treatments for buildings, which are associated with their inefficacy against facades staining caused by oil-based contaminants and the loss of its hydrophobic performance due to the contamination with said contaminants [23]. Furthermore, by using this strategy the detergent-free self-cleaning building surfaces are produced [28], which may constitute an eco-friendly alternative to the use of cleaning products that are classified as water contaminants.

Producing Hydrophobic Concrete with Photo-induced Superhydrophilic surface: Detergent-Free Cleaning Performance

Regarding the reduction of water absorption by capillarity (WAC), a crucial factor for the protection of concrete structures, the test was performed before and after inducing the superhydrophilic surface, in order to verify if the barrier effect against water was maintained. **Table S1** shows the capillary coefficient values and the total water uptake values for the treated samples and the untreated counterparts.

In general, all of the treatments decreased water absorption respect to the 3.5 % value measured for the untreated specimens. In the case of the commercial product, the protection against water absorption was limited, reaching a water uptake around 3.0 % (14% reduction). On the other hand, the treatment with UCA-S or UCA-T reduced the water absorption below 0.4 % (88% decrease). According to the literature [4], a hydrophobic treatment for concrete can be considered effective as long as the reduction in water absorption is higher than 75 %. The difference in the effectiveness of the treatments in preventing water absorption can be explained according to the low penetration (see **Table 1** and **Fig. S2**) and the discontinuous coating (**Fig. 1**) formed by the commercial product, compared to the higher penetration and compact structure created by the products with a silica matrix (UCA-T and UCA-S). The low effectiveness of the treatments without a matrix against water absorption is in line with other works [56] which demonstrated that the application of colloidal silica NPs hardly reduced the water absorption because they did not form a continuous coating on the surface.

Regarding to the samples after sunlight exposure, none of them showed noticeable changes in their absorption values, indicating that the organic component of the treatments is UV-resistant. This appreciation is especially noteworthy in the case of the samples treated with UCA-T*, where water uptake was decreased even after the surface became superhydrophilic, thus indicating its suitability as a protective treatment for concrete. This observation has two implications: (1) the induced superhydrophilicity phenomenon is limited to the changes on the TiO_2NPs on the surface, and (2) the organic component of the gel is resistant to the photo-oxidative degradation processes promoted by TiO_2.

6.4.3. Evaluation of the durability.

The previous results demonstrated that concrete surfaces with superhydrophobic and superhydrophilic performance has been obtained. However, the dependence on specific topographical features usually makes these surfaces sensitive to external agents, leading to the eventual loss of their properties. Thus, a series of tests were carried out in order to check the durability of the different treatments. Considering the difficulty of measuring quantitatively the superhydrophilic behavior (hysteresis cannot be evaluated), and that roughness was found to be the governing factor for both the water and oil repellence phenomena, all the tests have been carried out on the superhydrophobic surfaces (UCA-T, UCA-S). Since the photo-activation the superhydrophilic surface does not modify the topography, the results (related to damages to the surface) of the not activated samples can be assumed as extrapolative.

The adhesion of the applied products to the concrete substrate was evaluated by means of a tape test. **Fig. 7** shows the evolution of the static and dynamic contact angles after attachment/detachment cycles.
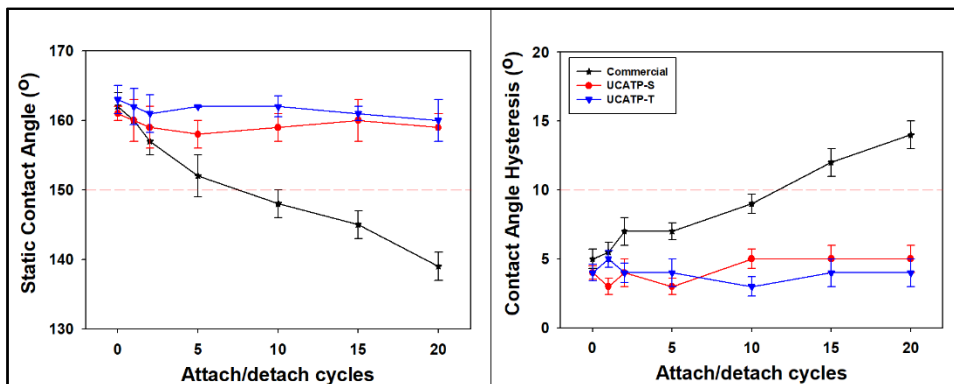
Figure 7. SCA (left) and CAH (right) values variation with attach/detach cycles.

The obtained results showed that the SCA value of the samples treated with the commercial product rapidly decreased down to 140°, whereas the CAH value increased over 10°, indicating the loos of their superhydrophobic performance. On the other hand, samples treated with UCA-S and UCA-T product maintained the SCA and CAH values without significant differences.

Similar trends were observed regarding the resistance of the different treatments to continuous water dropping by means of a rain simulation test [18], as pictured in **Fig. 8** showing the evolution of SCA (left) and CAH (right) value with the rainfall volume.
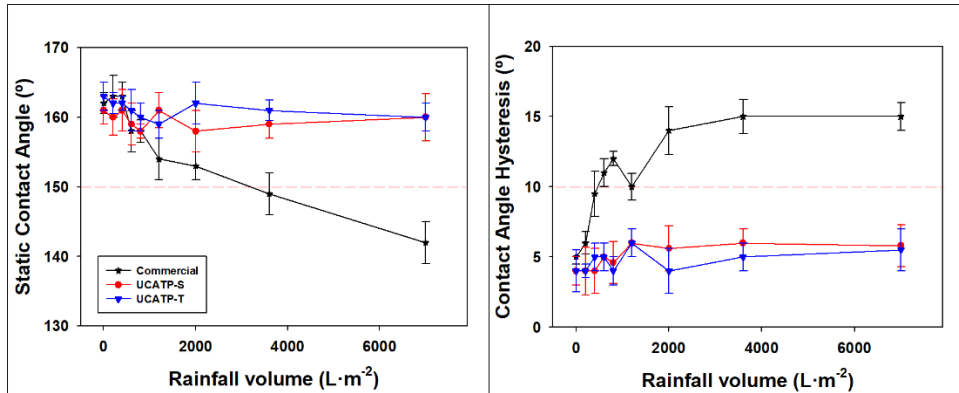
Figure 8. SCA (left) and CAH (right) values variation with rainfall volume.

Firstly, a rapid decrease in the SCA value and an increase of the CAH value were observed for the commercial product, as a consequence of the low adhesion of the commercial NPs as demonstrated in the previous tape test. In the case of UCA products, all of them maintained SCA values (higher than 150°) and CAH values (lower than 10°) during all the experiment.

In order to account for a more realistic durability scenario, the long-lasting performance of the treated samples was evaluated by exposing them to outdoor conditions. **Figure 9** shows the SCA and CAH values evolution of the treated samples during the outdoor exposure.
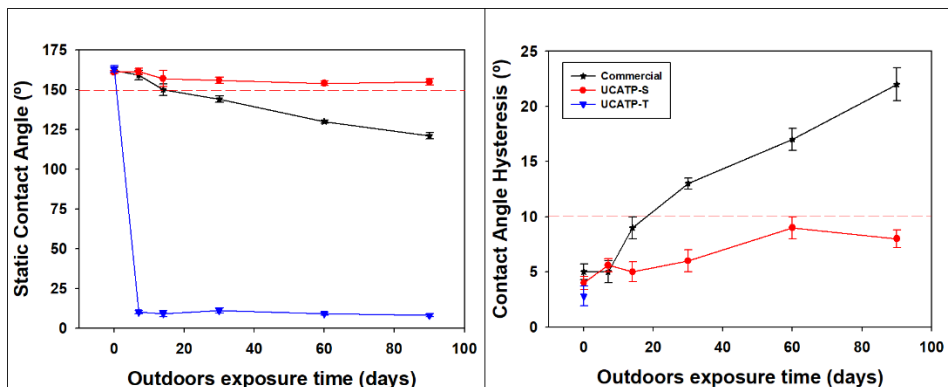
Figure 9. SCA (left) and CAH (right) values evolution with the time of outdoors exposure.

In a similar vein to the two previous tests, the samples treated with the commercial product quickly lost the superhydrophobic properties due to the action of the environmental agents (wind, rain, marine aerosol…). In the case of UCA-S treated samples, the superhydrophobic performance was maintained during the whole test, with slight fluctuations likely related with deposition of dirt or other external materials. Regarding to the product containing TiO_2 NPs in its composition (UCA-T), a rapid decrease in SCA value (CAH could not be measured due to the rapid spread of water droplets on the surface), down to < 10° values, was observed due to the photo-induced superhydrophilicity of titania, demonstrating that the superhydrophilic behavior can be induced by action of sunlight alone, without the need of previous conditioning with UV lamps. It should be noted that the SCA are similar to the ones previously obtained by photo-activation in laboratory conditions.

An explanation for the different durability of the commercial product respect the products with a silica matrix (UCA-S and UCA-T) can be found in the surface morphology changes, as observed by SEM images of the treated concrete surface before and after the three different tests (see **Fig. 10**).

In general, it became evident that the different behavior depends on whether the Cassie-Baxter state (reliant on the existence of a regular micro/nano-roughness) o is maintained or not under the aggressive conditions [57,58]. The obtained SEM images show that the surfaces treated with the commercial product were seriously damaged after being subjected to the different tests, with a decrease in the areas covered by the NPs and a loss of compaction, confirming that the SiO_2NPs tend to detach under the action of external forces due to a low interaction with the surface. In contrast, the modifications of the surfaces treated with UCA-S and UCA-T after the tests were minimal and the NPs were still homogeneously distributed over the surface in both cases, which explains with the results obtained for the CA measurements. It is worth mentioning that the fact that the surface treated with UCA-T kept its topography intact after the outdoor test, indicates that the underwater Cassie-Baxter state for oil drops is still achievable.

As discussed in previous sections, these differences in the adhesion to the substrate result from the use of a silica matrix for UCA-T and UCA-S. In the case of the commercial product, the SiO_2NPs barely interact with the substrate, leading to loosely attached clusters. This situation changes for the products containing a silica matrix, where the silanol groups generated during the sol-gel process can form covalent Si-O-Si bonds by reaction with the silanol in the surface of the concrete substrate, a process that is further favored by the basic character of concrete [59]. Previous works of our group have demonstrated the adhesion of the silica matrix to building materials such as sandstone and limestone [34,60]. This matrix in turn embeds the SiO_2 or TiO_2NPs, while interacting with them through the Si-OH or Ti-OH groups. The adherence of this matrix to the surface, combined with the formation of a compact structure, lead to an effective attachment of the NPs to the surface.
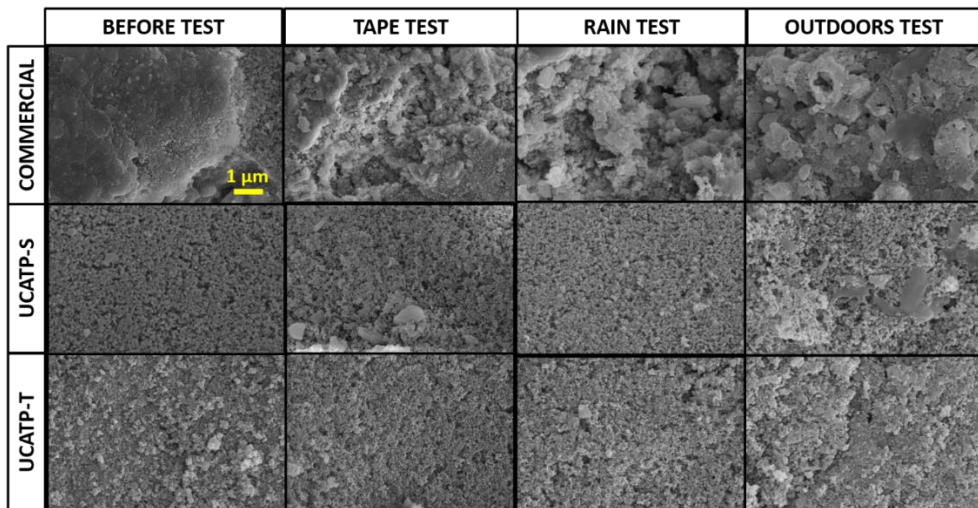
Figure 10. SEM images of the treated concrete surfaces before and after the different durability tests.

6.5. Conclusions.

In this work, we developed a product for the protection of concrete that combines a photo-induced superhydrophilic surface, with the creation of a hydrophobic matrix inside the pore structure. Specifically, the integration of TiO_2 into an ORMOSIL gives rise to two effects: (1) the creation of a nano-roughness, which promoted superhydrophobic/superhydrophilic performance; and (2) the capacity to turn from

superhydrophobic to superhydrophilic behavior, due to the photo-induced hydrophilicity of TiO_2. As a consequence of this effect, the treated concrete surfaces displayed underwater superoleophobic performance, an effect that can be exploited for overcoming the ineffectiveness of superhydrophobic surfaces against oily contaminants, in addition to the obtention of building materials surfaces with detergent-free self-cleaning performance, a promising solution to reduce the contamination caused by the excessive use of detergents.

Although the use of induced-superhydrophilic surfaces to promote underwater superoleophobicity phenomenon has already been investigated, as far as we are aware, the application of this strategy for building materials has not yet been reported, mainly because the water ingress inside building materials has to be avoided. In this paper, we report a work-around for the apparent disadvantage of using hydrophilic surfaces by incorporating a hydrophobic component in the sol that prevents water absorption inside the material, while the induced superhydrophilicity is limited to the photoactive component on the surface. Thus, a treatment showing the advantages of both a superhydrophilic surface, and a hydrophobic impregnation treatment was achieved.

Finally, the samples treated with this product demonstrated long-lasting performance against different durability tests, due to the effective penetration of the product in the porous structure of concrete and to the creation of a compact ormosil matrix coating on the surface.

6.6. References.

[1]   P. Romano, P.S.D. Brito, L. Rodrigues, Monitoring of the degradation of concrete structures in environments containing chloride ions, Constr. Build. Mater. 47 (2013) 827.

[2]   D. Jacques, L. Wang, E. Martens, D. Mallants, Modelling chemical degradation of concrete during leaching with rain and soil water types, Cem. Concr. Res. 40 (2010) 1306.

[3]   X. Pan, Z. Shi, C. Shi, T.C. Ling, N. Li, A review on concrete surface treatment Part I: Types and mechanisms, Constr. Build. Mater. 132 (2017) 578.

[4]   X. Pan, Z. Shi, C. Shi, T.C. Ling, N. Li, A review on surface treatment for concrete – Part 2: Performance, Constr. Build. Mater. 133 (2017) 81.

[5]   S. Moradi, P. Englezos, S.G. Hatzikiriakos, Contact angle hysteresis: surface morphology effects, Colloid Polym. Sci. 291 (2013) 317.

[6]   A. Lafuma, D. Quéré, Superhydrophobic states., Nat. Mater. 2 (2003) 457.

[7]   K. Koch, B. Bhushan, Y.C. Jung, W. Barthlott, Fabrication of artificial Lotus leaves and significance of hierarchical structure for superhydrophobicity and low adhesion, Soft Matter. 5 (2009) 1386.

[8]   A.B.D. Cassie, S. Baxter, Wettability of porous surfaces, Trans. Faraday Soc. 40 (1944) 546.

[9]   L. Gao, T.J. McCarthy, Wetting 101 degrees., Langmuir. 25 (2009) 14105.

[10]   R. Fürstner, W. Barthlott, C. Neinhuis, P. Walzel, Wetting and self-cleaning properties of artificial superhydrophobic surfaces, Langmuir. 21 (2005) 956.

[11]   P.N. Manoudis, A. Tsakalof, I. Karapanagiotis, I. Zuburtikudis, C. Panayiotou, Fabrication of super-hydrophobic surfaces for enhanced stone protection, Surf. Coatings Technol. 203 (2009) 1322.

[12]   D.S. Facio, L.A.M. Carrascosa, M.J. Mosquera, Producing lasting amphiphobic building surfaces with self-cleaning properties, Nanotechnology. 28 (2017).

[13]   D.S. Facio, M.J. Mosquera, Simple strategy for producing superhydrophobic nanocomposite coatings in situ on a building substrate., ACS Appl. Mater. Interfaces. 5 (2013) 7517.

[14]   L.A.M. Carrascosa, D.S. Facio, M.J. Mosquera, Producing superhydrophobic roof tiles, Nanotechnology. 27 (2016) 095604.

[15]   C.P. Panagiotis N. Manoudis, Ioannis Karapanagiotis, Andreas Tsakalof, Ioannis Zuburtikudis, Superhydrophobic Composite Films Produced on Various Substrates, Langmuir. 24 (2008) 11225.

[16]   P.N. Manoudis, S. Papadopoulou, I. Karapanagiotis, A. Tsakalof, I. Zuburtikudis, C. Panayiotou, Polymer-Silica nanoparticles composite films as protective coatings for stone-based monuments, J. Phys. Conf. Ser. 61 (2007) 1361.

[17]   D. Aslanidou, I. Karapanagiotis, C. Panayiotou, Superhydrophobic, superoleophobic coatings for the protection of silk textiles, Prog. Org. Coatings. 97 (2016) 44.

[18]   M.J. Mosquera, L.A.M. Carrascosa, N. Badreldin, Producing superhydrophobic/oleophobic coatings on Cultural Heritage building materials, Pure Appl. Chem. 90 (2018) 551.

[19]   A. Arabzadeh, H. Ceylan, S. Kim, K. Gopalakrishnan, A. Sassani, S. Sundararajan, P.C. Taylor, Superhydrophobic coatings on Portland cement concrete surfaces, Constr. Build. Mater. 141 (2017) 393.

[20]   Y. Zhao, Y. Liu, Q. Liu, W. Guo, L. Yang, D. Ge, Icephobicity studies of superhydrophobic coatings on concrete via spray method, Mater. Lett. 233 (2018) 263.

[21]   J. Song, Y. Li, W. Xu, H. Liu, Y. Lu, Inexpensive and non-fluorinated superhydrophobic concrete coating for anti-icing and anti-corrosion, J. Colloid Interface Sci. 541 (2019) 86.

[22]   Y. Li, L. Gou, H. Wang, Y. Wang, J. Zhang, N. Li, S. Hu, J. Yang, Fluorine-free superhydrophobic carbon-based coatings on the concrete, Mater. Lett. 244 (2019) 31.

[23]   L. Li, J. Zhang, A. Wang, Removal of Organic Pollutants from Water Using Superwetting Materials, Chem. Rec. (2017) 118.

[24]   T. Darmanin, F.F. Guittard, Superhydrophobic and superoleophobic properties in nature, Mater. Today. 18 (2015) 273.

[25]   Z. Xue, M. Liu, L. Jiang, Recent developments in polymeric superoleophobic surfaces, J. Polym. Sci. Part B Polym. Phys. 50 (2012) 1209.

[26]   J. Yong, F. Chen, Q. Yang, J. Huo, X. Hou, Superoleophobic surfaces, Chem. Soc. Rev. 46 (2017) 4168.

[27]   M. Liu, S. Wang, Z. Wei, Y. Song, L. Jiang, Bioinspired Design of a Superoleophobic and Low Adhesive Water/Solid Interface, Adv. Mater. 21 (2009) 665.

[28]   Y. Wang, X. Gong, Special oleophobic and hydrophilic surfaces: approaches, mechanisms, and applications, J. Mater. Chem. A. 5 (2017) 3759.

[29]   J. Yong, F. Chen, M. Li, Q. Yang, Y. Fang, J. Huo, X. Hou, Remarkably Simple Achievement of Superhydrophobicity, Superhydrophilicity, Underwater Superoleophobicity, Underwater Superoleophilicity, Underwater Superaerophobicity, and Underwater Superaerophilicity on Femtosecond Laser Ablated PDMS Surfaces, J. Mater. Chem. A. 5 (2017) 25249.

[30]   T. Watanabe, A. Nakajima, R. Wang, M. Minabe, S. Koizumi, A. Fujishima, K. Hashimoto, Photocatalytic activity and photoinduced hydrophilicity of titanium dioxide coated glass, Thin Solid Films. 351 (1999) 260.

[31]   D.S. Facio, M. Luna, M.J. Mosquera, Facile preparation of mesoporous silica monoliths by an inverse micelle mechanism, Microporous Mesoporous Mater. 247 (2017) 166.

[32]   Berns R S, Billmeyer and Saltzman's Principles of Color Technology, 3rd ed., Wiley-Interscience, New York, 2000.

[33]   M.J. Mosquera, D. Benítez, S.H. Perry, Pore structure in mortars applied on restoration: Effect on properties relevant to decay of granite buildings, Cem. Concr. Res. 32 (2002) 1883.

[34]   D.S. Facio, L.A.M. Carrascosa, M.J. Mosquera, Producing lasting amphiphobic building surfaces with self-cleaning properties, Nanotechnology. 28 (2017) 265601.

[35]   S.-D. Wang, Y.-S. Jiang, The durability of superhydrophobic films, Appl. Surf. Sci. 357 (2015) 1647.

[36]   L.A.M. Carrascosa, D.S. Facio, M.J. Mosquera, Producing superhydrophobic roof tiles, Nanotechnology. 27 (2016).

[37]   L. Pinho, M. Rojas, M.J. Mosquera, Ag–SiO2–TiO2 nanocomposite coatings with enhanced photoactivity for self-cleaning application on building materials, Appl. Catal. B Environ. 178 (2015) 144.

[38]   M.J. Mosquera, D.M. de los Santos, T. Rivas, Surfactant-synthesized ormosils with application to stone restoration., Langmuir. 26 (2010) 6737.

[39]   J.G. Dai, Y. Akira, F.H. Wittmann, H. Yokota, P. Zhang, Water repellent surface impregnation for extension of service life of reinforced concrete structures in marine environments: The role of cracks, Cem. Concr. Compos. 32 (2010) 101.

[40]   J.D. Rodrigues, A. Grossi, Indicators and ratings for the compatibility assessment of conservation actions, J. Cult. Herit. 8 (2007) 32.

[41]   C. Kosak Söz, E. Yilgör, I. Yilgör, Influence of the average surface roughness on the formation of superhydrophobic polymer surfaces through spin-coating with hydrophobic fumed silica, Polym. (United Kingdom). 62 (2015) 118.

[42]   M. Nosonovsky, B. Bhushan, Roughness optimization for biomimetic superhydrophobic surfaces, Microsyst. Technol. 11 (2005) 535.

[43]   L. De Ferri, P.P. Lottici, A. Lorenzi, A. Montenero, E. Salvioli-Mariani, Study of silica nanoparticles - polysiloxane hydrophobic treatments for stone-based monument protection,

J. Cult. Herit. 12 (2011) 356.

[44] L. Pinho, F. Elhaddad, D.S. Facio, M.J. Mosquera, A novel TiO2–SiO2 nanocomposite converts a very friable stone into a self-cleaning building material, Appl. Surf. Sci. 275 (2013) 389.

[45] J.T. Simpson, S.R. Hunter, T. Aytug, Superhydrophobic materials and coatings: a review, Reports Prog. Phys. 78 (2015) 086501.

[46] X.-M. Li, D. Reinhoudt, M. Crego-Calama, What do we need for a superhydrophobic surface? A review on the recent progress in the preparation of superhydrophobic surfaces., Chem. Soc. Rev. 36 (2007) 1350.

[47] J. Schneider, M. Matsuoka, M. Takeuchi, J. Zhang, Y. Horiuchi, M. Anpo, D.W. Bahnemann, Understanding TiO2 Photocatalysis: Mechanisms and Materials, Chem. Rev. 114 (2014) 9919.

[48] M.B. Hugenschmidt, L. Gamble, C.T. Campbell, The interaction of H2O with a TiO2(110) surface, Surf. Sci. 302 (1994) 329.

[49] A. Fujishima, T.N. Rao, D.A. Tryk, Titanium dioxide photocatalysis, J. Photochem. Photobiol. C Photochem. Rev. 1 (2000) 1.

[50] R. Wang, K. Hashimoto, A. Fujishima, M. Chikuni, E. Kojima, A. Kitamura, M. Shimohigoshi, T. Watanabe, Photogeneration of highly amphiphilic TiO2surfaces, Adv. Mater. 10 (1998) 135.

[51] G. Li, Y. Lu, P. Wu, Z. Zhang, J. Li, W. Zhu, Y. Hu, D. Wu, J. Chu, Fish scale inspired design of underwater superoleophobic microcone arrays by sucrose solution assisted femtosecond laser irradiation for multifunctional liquid manipulation, J. Mater. Chem. A. 3 (2015) 18675.

[52] H. Bellanger, T. Darmanin, E. Taffin de Givenchy, F. Guittard, Chemical and Physical Pathways for the Preparation of Superoleophobic Surfaces and Related Wetting Theories, Chem. Rev. 114 (2014) 2694.

[53] L. Gao, T.J. McCarthy, Wetting 101º, Langmuir. 25 (2009) 14105.

[54] Z. Lian, J. Xu, Y. Wan, Y. Li, Z. Yu, Q. Liu, H. Yu, Tribological properties of fish scale inspired underwater superoleophobic hierarchical structure in aqueous environment Tribological properties of fish scale inspired underwater superoleophobic hierarchical structure in aqueous environment, Mater. Res. Express. (2017) 3.

[55] R.N. Wenzel, Resistance of solid surfaces to wetting by water, Ind. Eng. Chem. 28 (1936) 988.

[56] P. Hou, X. Cheng, J. Qian, S.P. Shah, Effects and mechanisms of surface treatment of hardened cement-based materials with colloidal nanoSiO2and its precursor, Constr. Build. Mater. 53 (2014) 66.

[57] B.P. Dyett, A.H. Wu, R.N. Lamb, Mechanical Stability of Surface Architecture—Consequences for Superhydrophobicity, ACS Appl. Mater. Interfaces. 6 (2014) 18380.

[58] E. Bormashenko, Progress in understanding wetting transitions on rough surfaces, Adv. Colloid Interface Sci. 222 (2015) 92.

[59] R.S.C. Woo, H. Zhu, M.M.K. Chow, C.K.Y. Leung, J.K. Kim, Barrier performance of silane-clay nanocomposite coatings on concrete structure, Compos. Sci. Technol. 68 (2008) 2828.

[60] L. Pinho, M.J. Mosquera, Titania-Silica Nanocomposite Photocatalysts with Application in Stone Self-Cleaning, J. Phys. Chem. C. 115 (2011) 22851.

6.7. Supplementary information.
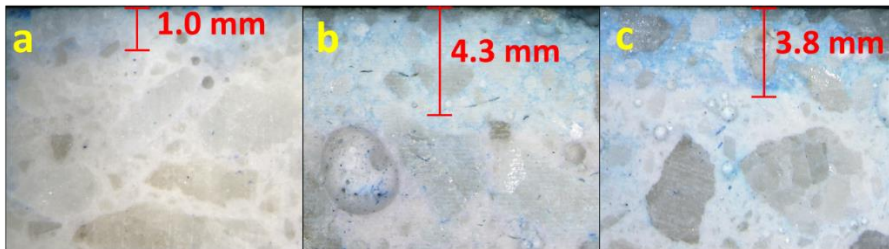
Figure S1. Cross-section of the samples treated with the different products under study. (a) Commercial, (b) UCA-S, (c) UCA-T.

Table S1. Water absorption by capillarity test results.

Product	Before irradiation (w/w%)	After irradiation (w/w%)
Untreated	3.49±0.17	3.45±0.21
Commercial	3.01±0.21	3.27±0.15
UCA-S	0.37±0.12	0.38±0.14
UCA-T	0.39±0.16	0.40±0.19

Capítulo 7

Discusión general

En la presente Tesis Doctoral se han desarrollado superficies, sobre materiales de construcción, con propiedades superhidrofugantes y oleofugantes. Además, se han preparado materiales de construcción con superficies que poseen superhidrofilia inducida, las cuales muestran superoleofobicidad cuando son sumergidas en agua.

En primer lugar, se prepararon recubrimientos superhidrofugantes sobre muestras de piedra caliza mediante la creación de un nanomaterial formado principalmente por agregados de NPs de sílice hidrofóbicas, unidas mediante una matriz de sílice que forma puentes entre las NPs. Este recubrimiento muestra una elevada durabilidad debido a: (1) la elevada agregación de las NPs por el uso de un disolvente apolar; (2) el papel del oligómero de sílice uniendo las NPs entre sí, y al sustrato aplicado; (3) la formación de un recubrimiento formado principalmente por NPs hidrofóbicas.

En segundo lugar, se empleó una estrategia alternativa para obtener superficies superhidrofugantes sobre muestras de mármol. Específicamente se combinó el efecto de un ORMOSIL (para reducir la energía superficial), y de ablación láser (para producir la rugosidad típica de un estado Cassie-Baxter). Los resultados demostraron la formación de partículas sub-micrométricas sobre la superficie, por efecto de la ablación, las cuales inducen las propiedades superhidrofugantes de éstas superficies.

En un siguiente paso, se crearon superficies con propiedades superhidrofugantes y oleofugantes sobre diversos materiales típicamente empleados en construcción (granito, caliza, hormigón y madera), empleando una fluoroalquilsilano y NPs de sílice. La elevada repelencia obtenida para los materiales de construcción tratados los dotó de propiedades auto-limpiantes. Además, se consiguió una elevada durabilidad debido a la formación de enlaces entre el fluoroalquilsilano, las NPs de sílice y los sustratos tratados.

Finalmente, se desarrollaron superficies de hormigón con propiedades superoleofugantes bajo agua, como consecuencia de la superhidrofilia foto-inducida en inducida en su superficie, debido a la acción de las NPs de TiO_2 integradas en un ORMOSIL. Sin embargo, el producto en el interior de la estructura porosa del hormigón, que no está expuesta a la luz, preserva sus propiedades hidrofugantes evitando la penetración de agua.

Capítulo 7

7.1. Materiales de Construcción Superhidrofugantes.

Inicialmente se sintetizó un sol de sílice mediante la mezcla, asistida por ultrasonidos, de un oligómero de sílice, el surfactante *n*-octilamina y agua. Como se discutió en un trabajo previo [1], esta ruta de síntesis permite obtener materiales nanoparticulados libres de fracturas. A este sol de sílice obtenido se le adicionaron distintas proporciones de una dispersión de NPs de sílice hidrófobas (en adelante HSi-NPs) en hexano. Específicamente se prepararon 3 proporciones de HSi-NPs distintas respecto del sol de sílice inicial: 7, 10 y 20 % p, respecto del volumen total del sol inicial (ver Capítulo 3-Tabla 1).

Los nanomateriales obtenidos, tras la gelificación y secado, fueron caracterizados mediante TEM. Los nanomateriales con proporciones de HSi-NPs de 7 y 10 % (en adelante UCA7S y UCA10S, respectivamente) mostraron algunas de las HSi-NPs en la superficie de la matriz de sílice (Capítulo 3-Fig. 1 a y b). Por otro lado, el nanomaterial con la proporción de HSi-NPs más alta (20 %, en adelante UCA20S) mostró una estructura completamente distinta. Las HSi-NPs formaron agregados unidos mediante puentes de sílice (Capítulo 3-Fig.1c). La formación de las distintas estructuras puede ser explicada de acuerdo a:

(1) El papel jugado por la polaridad del disolvente [2].

(2) El ratio volumétrico HSi-NPs/matriz de sílice tras la gelificación y secado (Capítulo 3-Tabla 1).

(3) Las diferencias en densidad entre las HSi-NPs (0.26 g·cm^{-3}) y la matriz de sílice 0.89 g·cm^{-3}).

UCA7S y UCA10S presentaron ratios HSi-NPs/matriz de sílice de 0.6 y 0.8, respectivamente), siendo la proporción volumétrica de la matriz de sílice superior a la de las HSi-NPs. UCA7S mostró evidencia de agregación parcial de las HSi-NPs, la cual se explica como consecuencia de la presencia de hexano en el sol. El disolvente apolar promueve la agregación de las HSi-NPs, tal como se ha descrito en trabajos previos [2]. Al incrementar la proporción de HSi-NPs (UCA10S), se observó una agregación total de las HSi-NPs. Además, las HSi-NPs se situaron en la superficie de la matriz de sílice

debido a las diferencias de densidad entre las HSi-NPs y la matriz de sílice (0.3 y 0.9 g/cm^3, respectivamente). Finalmente, para UCA20S, el ratio HSi-NPs/matriz de sílice fue de 1.7. Por lo tanto, la mayor proporción de HSi-NPs favoreció la creación de un xerogel compuesto por HSi-NPs. En este caso, las NPs generadas por el sol de sílice no produjeron una matriz debido a su baja proporción, sino que actuaron exclusivamente como unión entre las HSi-NPs.

Los tres productos preparados (UCA7S, UCA10S y UCA20S) fueron aplicados sobre muestras de piedra caliza (porosidad abierta alrededor de 10 %). Además, se aplicó una dispersión de HSi-NPs en hexano, con el fin de estudiar el efecto de las NPs sin integrarlas en una matriz de sílice. Todas las superficies mostraron propiedades superhidrofugantes con valores de ángulo de contacto estático (SCA) superiores a 150°, y valores de histéresis del ángulo de contacto (CAH) inferiores a 10° (Capítulo 3-Fig. 4 y Tabla S2). Los valores obtenidos pueden ser explicados en base a dos factores:

(1) La reducción de energía libre superficial debido al componente orgánico de las HSi-NPs (hexametildisilazano) [3,4].

(2) La rugosidad generada por las HSi-NPs, la cual produce una topografía propia de un estado Cassie-Baxter [3,5].

Respecto a diferencias entre los distintos tratamientos, se puede apreciar que los valores de CAH fueron similares para las muestras tratadas con UCA20S y las HSi-NPs sin matriz de sílice (alrededor de 3°), siendo inferiores a los medidos para las superficies tratadas con UCA7S y UCA20S (alrededor de 6°). Esta diferencia puede ser explicada de acuerdo a los resultados obtenidos para SEM y AFM (ver Capítulo 3-Fig. 3) de las superficies objeto de estudio.

En el caso de las muestras tratadas con UCA7S y UCA10S, las imágenes de SEM mostraron las HSi-NPs distribuidas homogéneamente sobre la superficie. Como se ha discutido previamente, las HSi-NPs se posicionaron en la superficie de la matriz de sílice debido a su menor densidad. Por otro lado, las superficies tratadas con HSi-NPs y UCA20S presentaron la formación de agregados de HSi-NPs en dichas superficies debido a la agregación favorecida por la adición de un disolvente apolar (hexano) [2], así como de la baja proporción del oligómero de sílice en el producto UCA20S, lo que

causa que forme puentes entre las NPs en lugar de una matriz. Los perfiles bidimensionales de rugosidad, obtenidos AFM, mostraron que las muestras tratadas con UCA7S y UCA10S presentaron perfiles compuestos por picos separados por alrededor de 100 nm. Como se ha discutido en trabajos previos [6–9], la creación de una rugosidad compuesta por picos separados uniformemente favorece la formación de bolsas de aire entre la superficie sólida y la gota de agua, promoviendo la repelencia. Sin embargo, las muestras tratadas con HSi-NPs y UCA20S mostraron perfiles que demuestran la formación de doble estructura nano- y submicro-métrica, como consecuencia de la formación de agregados[2]. La formación de una rugosidad con una doble estructura ha sido reportada por varios autores como una forma de obtener superficies con una elevada superhidrofobicidad, debido al incremento de superficie específica, lo que favorece la formación de un estado Cassie-Baxter [10–12].

La repelencia de las superficies obtenidas fue confirmada mediante un sencillo experimento (ver Capítulo 3-Vídeo S1). Específicamente, una muestra tratada con UCA20S fue colocada con una ligera inclinación (alrededor de 15°). A continuación, se depositaron gotas de agua, mediante una pipeta Pasteur, sobre la superficie. Las gotas rodaron rápidamente demostrando la repelencia dotada a la muestra por el tratamiento [13].

La durabilidad de las propiedades superhidrofugantes, dotadas a las muestras de piedra caliza objeto de estudio, fueron evaluadas por medio de un ensayo de adhesión de acuerdo al procedimiento previamente descrito previamente en la bibliografía [14–16]. Específicamente, se aplicó una tira adhesiva sobre las superficies tratadas y posteriormente se retiró. El proceso se repitió durante 20 ciclos, y la evolución de los valores de SCA y CAH fue estudiada (ver Capítulo 3-Fig. 5). Los resultados mostraron que las superficies tratadas con UCA7S y UCA10S perdieron rápidamente las propiedades superhidrofugantes en los primeros ciclos del test, mientras que las muestras tratadas con las HSi-NPs fueron capaces de resistir hasta 10 ciclos. Por el contrario, las superficies tratadas con UCA20S no mostraron variación en los valores de ángulo de contacto.

Con objeto de explicar las diferencias en durabilidad de los diferentes productos, se adquirieron imágenes de SEM de las superficies tratadas tras ser sometidas a 20 ciclos de ensayo de adhesión (ver Capítulo 3-Fig. 6). En primer lugar, se observó que las HSi-NPs fueron eliminadas dejando expuesta la superficie sin tratar (Capítulo 3-Fig. 6a). Por otro lado, las imágenes de SEM de las muestras tratadas con UCA7S y UCA10S mostraron que las HSi-NPs fueron eliminadas dejando la matriz de sílice (Capítulo 3-Fig. 6b y c, respectivamente). Finalmente, las superficies tratadas con UCA20S no presentaron cambios significativos, demostrando que el recubrimiento se mantuvo tras el ensayo de adhesión (Capítulo 3-Fig. 6d).

Tal como se ha discutido previamente [2], el disolvente apolar (hexano) promueve la agregación de las NPs. Esto explica que las HSi-NPs sin matriz de sílice sean capaces de resistir hasta 10 ciclos del ensayo de adhesión. Además, la presencia de varias capas de HSi-NPs incrementan moderadamente la durabilidad de los tratamientos, tal y como demostraron Latthe y colaboradores [17]. Por otro lado, trabajos previos han demostrado que la matriz de sílice generada por nuestra ruta sol-gel muestra una elevada adherencia a los substratos pétreos [14,18]. Debido a ello, la matriz de sílice se mantiene inalterada en el caso de las superficies tratadas con UCA7S y UCA10S, mientras que las HSi-NPs son eliminadas. Finalmente, en el caso de UCA20S, la agregación de las HSi-NPs (debido al disolvente) es combinado con las propiedades de adhesión de la matriz de sílice, que en este caso únicamente actúa como un nexo entre las HSi-NPs. Además, la matriz de sílice también asegura la adhesión de los agregados de HSi-NPs a la superficie de las muestras, dando lugar a una elevada durabilidad [19].

Finalmente se evaluaron los efectos negativos causados por la aplicación de los productos a los materiales de construcción (ver Capítulo 3-Tabla S2). En todos los casos, los cambios de color (ΔE^*) de las muestras tratadas respecto de las sin tratar fueron inferiores a 5, que es el valor límite de percepción del ojo humano [20]. Por otro lado, ninguno de los productos redujo la difusividad al vapor más del 11 %, permitiendo por tanto que el vapor de agua pueda pasar a través de las muestras tratadas. Ambos parámetros, cambio de color y difusividad al vapor, se encuentran dentro de valores óptimos para materiales de construcción [21].

En una segunda aproximación, se obtuvieron superficies superhidrofugantes sobre materiales de construcción empleando la ablación láser como método para crear la rugosidad típica del estado Cassie-Baxter (ver Capítulo 4).

Inicialmente, se trataron muestras de mármol con un ORMOSIL previamente desarrollado por nuestro grupo de investigación [22], con objeto de reducir la energía superficial [23], dando lugar a superficies hidrofugantes con valores de SCA alrededor de 112° (ver Capítulo 4-Fig. 1). Tras someter estas superficies hidrofugantes a ablación láser, se observó un incremento del valor de SCA y una disminución de CAH al aumentar la fluencia del láser (Capítulo 4-Fig. 1). Las medidas realizadas mediante perfilometría demostraron un incremento de la rugosidad con la fluencia empleada (ver Capítulo 4-Fig. 2). Esto demuestra la dependencia del valor de los ángulos de contacto con la rugosidad, tal como establece el estado de Wenzel [24]. Además, para las fluencias más altas se obtuvieron superficies superhidrofugantes, con valores de SCA superiores a 150° y CAH alrededor de 6°. Las imágenes de SEM de estas superficies (Capítulo 4-Fig. 3d y e) mostraron la deposición de material en forma de partículas sub-micrométricas (alrededor de 500 nm). De acuerdo a artículos encontrados en la literatura científica [25,26], el calor generado, por los pulsos de láser, funde en material en la superficie, el cual es posteriormente depositado en forma de partículas. Estas partículas contribuyen a crear una topografía superficial típica de un estado Cassie-Baxter, dando lugar a superficies superhidrofugantes.

La obtención de un estado Cassie-Baxter fue demostrada mediante un sencillo experimento [27]. Específicamente una muestra con propiedades hidrofugantes (sin ablación láser), y otra con superficie superhidrofugante (tras haber sido sometida a ablación), fueron sumergidas en agua. La muestra hidrofugante mostró un contacto total del agua con la superficie (ver Capítulo 4-Fig.a), demostrando la obtención de un estado de Wenzel, en el cual el agua penetra en los valles de rugosidad y, por tanto, el contacto entre el agua y la superficie es total. Por otro lado, la muestra superhidrofugante mostró una superficie con reflejos, debido a que el agua no es capaz de cubrir la superficie. Esto demuestra el estado de Cassie-Baxter, en el cual el agua se

sitúa sobre los picos de rugosidad, permitiendo que una capa de aire se forme entre la superficie sólida y el agua.

Las propiedades autolimpiantes dotadas a los materiales debido a la superhidrofobicidad también fueron evaluadas [28,29] (ver Capítulo 4-Vídeo S1). Una muestra sin tratar y otra superhidrofugante fueron manchadas con polvo de teja y, posteriormente, se dejaron caer gotas de agua sobre las superficies contaminadas. En el caso de la muestra sin tratar, el agua disolvió el polvo, y el carácter hidrofílico de la superficie favoreció que el agua se extendiera contaminado la superficie. Por el contrario, el agua cayendo sobre la muestra superhidrofugante también fue capaz de disolver el polvo. Sin embargo, la elevada repelencia presentada por esta superficie, permitió que el agua (junto con el contaminante) rodará fuera de la superficie, limpiándola.

Finalmente, la durabilidad de la superficie con la mayor eficacia fue evaluada mediante un test de adhesión, siguiendo el procedimiento empleado en el Capítulo 3. Los resultados obtenidos (Capítulo 4-Fig. 4) mostraron una elevada adhesión del recubrimiento al sustrato, coincidiendo con lo observado en trabajos previos del grupo para productos preparados siguiendo una ruta de síntesis similar [18,30].

7.2. Obtención de Materiales de Construcción Superhidrofugantes y Oleofugantes.

El siguiente paso en el marco de esta Tesis Doctoral fue el desarrollo de materiales de construcción con superficies superhidrofugantes y oleofugantes, tal como se describió en el Capítulo 5. Para ello se preparó un producto, consistente en una dispersión de nanopartículas de sílice en una disolución acuosa de un fluoroalquilsilano, el cual fue aplicado sobre distintos materiales de construcción: caliza, granito, hormigón y madera.

La evaluación de la eficacia superhidrofugante mostró que todas las superficies tratadas presentaron superhidrofobicidad, con valores de SCA y CAH alrededor de 160° y 3°, respectivamente (ver Capítulo 5-Fig. 1). Además, se evaluó la repelencia de las superficies tratadas mediante un sencillo experimento (ver Capítulo 5-Video S1). El

video muestra un chorro de agua impactando sobre las diferentes superficies tratadas, y siendo repelido debido a la superhidrofobicidad de las superficies.

La superhidrofobicidad dotada a los diferentes materiales de construcción sugiere que éstos pueden tener propiedades auto-limpiantes [28,29]. Con el fin de evaluar esta propiedad, muestras tratadas y sin tratar fueron manchadas con polvo de azul de metileno y colocadas bajo una columna de agua. La efectividad auto-limpiante fue evaluada midiendo el color de las muestras antes y después del ensayo (ver Capítulo 5-Tabla 2). En el caso de las muestras sin tratar, las gotas de agua disolvieron el azul de metileno, y el carácter hidrofílico de las muestras promovieron la absorción de la disolución, dando lugar a una mancha azul permanente sobre las superficies. Por lo tanto, un cambio de color elevado fue medido ($\Delta E^* > 20$). Por otro lado, en el caso de las muestras tratadas, las gotas de agua también disolvieron el azul de metileno. Sin embargo, debido a la repelencia dada a las superficies por el recubrimiento, las gotas de disolución rodaron fuera de las superficies superhidrofóbicas eliminando el agente contaminante. En consecuencia, cambios de color inferiores a 1 fueron medidos, confirmando la eficacia auto-limpiante de los materiales de construcción tratados. Un ejemplo de la auto-limpieza dotada por el producto aplicado puede observarse en la Información Suplementaria del capítulo (ver Capítulo 5-Video S2).

Las propiedades oleofugantes fueron evaluadas mediante medidas de ángulo de contacto de micro-gotas de aceite (ver Capítulo 5-Fig. 2). Todas las superficies tratadas mostraron valores de SCA superiores a 100° debido a la presencia de grupos fluoroalquilo [31–34] que son capaces de reducir la energía superficial por debajo de la del aceite (32 mN·m^{-1}, at 25 ºC) [35].

Las propiedades superhidrofugantes y oleofugantes obtenidas pueden ser explicadas en base a la combinación de baja energía superficial generada por las cadena fluoroalquilo [31,32,36], y la creación de un estado Cassie-Baxter debido a la rugosidad generada por las NPs de 40 nm [6,7]. El efecto de la rugosidad fue confirmado gracias a las medidas de AFM de las superficies objeto de estudio (Capítulo 5-Fig. 3), que mostraron la formación de agregados de NPs densamente empaquetados. Además, los perfiles bidimensionales de rugosidad mostraron que todas las superficies tratadas

presentaban picos uniformemente separados por 150-250 nm. Como se ha discutido previamente [6,7,9,37], la creación de una rugosidad compuesta por picos uniformemente separados favorece la creación de bolsas de aire entre la superficie sólida y la gota de agua, lo que da lugar a propiedades superhidrofugantes. En el caso de las propiedades oleofugantes, la rugosidad produce un incremento de los valores de SCA. Sin embargo no se obtuvieron superficies superolefugantes (valor de SCA superior a 150° e histéresis inferior a 10°), ya que es necesario obtener una rugosidad compuesta por estructuras re-entrantes (con forma de hongo) [34,38].

La durabilidad de las propiedades superhidrofugantes de las muestras bajo estudio fue evaluada por medio de dos ensayos. En el primer ensayo las muestras fueron sometidas a un ensayo de adhesión (ver Capítulo 5-Fig. 5) siguiendo el procedimiento empleado en el Capítulo 3, mientras que para el segundo ensayo las muestras fueron colocadas bajo una columna de agua con el fin de simular la lluvia (Capítulo 5-Fig. 6). Ambos ensayos demostraron la durabilidad de la superhidrofobicidad de todas las superficies, no observándose cambios significativos en los valores.

Esta elevada durabilidad puede ser explicada como consecuencia de una efectiva unión del recubrimiento a los diferentes materiales de construcción evaluados, producida por reacciones de condensación, entre los grupos silanol (Si-OH) presentes en el fluoroalquilsilano, los cuales le permiten polimerizar y, además, condensar con los grupos silanol presentes en la superficie de las NPs de sílice, dando lugar a un recubrimiento nanopartículado duradero [6,7]. Los grupos silanol también pueden condensar con los grupos hidroxilo presentes en los diferentes materiales de construcción. Además, la penetración de los productos en la estructura porosa de los sustratos (ver Capítulo 5-Tabla 1) contribuye significativamente a incrementar la durabilidad de los materiales superhidrofugantes porque en caso de eliminar la capa superficial de recubrimiento, el producto dentro del material de construcción puede mantener las propiedades superhidrofugantes. Adicionalmente, la polimerización del producto dentro de la estructura porosa puede contribuir a mejorar la adhesión del recubrimiento al sustrato.

Por otro lado, la elevada resistencia al agua de lluvia demuestra la alta estabilidad del estado de Cassie-Baxter obtenido para los diferentes materiales de construcción. Como es sabido, en una superficie Cassie-Baxter, las gotas de agua se colocan sobre los picos de rugosidad, formándose gotas de agua entre la superficie sólida y el agua [5]. Sin embargo, si se alcanza una presión crítica, las gotas de agua tocarán los valles de rugosidad [39] y, por tanto, la superficie pasará a tener un estado de Wenzel [24], el cual no posee propiedades repelentes.

Finalmente se evaluó el cambio de color provocado por la aplicación del producto sobre los diferentes sustratos (ver Capítulo 5-Fig. 4). Todas las superficies tratadas mostraron cambios de color (ΔE^*) iguales o inferiores a 3, el cual es un valor perfectamente aceptable en el campo de los materiales de construcción [20,21].

7.3. Obtención de Hormigón con Superoleofobicidad bajo agua

Como se ha descrito en el **Epígrafe 7.2** la obtención de superficies superoleofugantes, sobre materiales de construcción, presenta dificultades debido a la necesidad de combinar la acción de una energía superficial extremadamente baja y la generación de una rugosidad con estructuras re-entrantes [34,38].

Por esta razón se han desarrollado superficies de hormigón las cuales presentan superoleofobicidad bajo agua, debido a la superhidrofilia foto-inducida. Específicamente, se integraron NPs de TiO_2 en un ORMOSIL que contenía un oligómero de sílice y PDMS. La aplicación del producto obtenido (en adelante UCA-T) sobre muestras de hormigón dio lugar a superficie superhidrofugantes (ver Capítulo 6-Fig. 2a) como consecuencia de la reducción de energía superficial por la acción del PDMS y la obtención de una rugosidad característica de un estado Cassie-Baxter (ver Capítulo 6-Fig. 1) [6,11,40]. Cuando las muestras tratadas fueron expuestas a radiación solar, durante 12 horas, se observó la disminución de los ángulos de contacto hasta mostrar valores superhidrofílicos (SCA<10°, ver Capítulo 6-Fig. 2b). De acuerdo a la literatura científica [41–44], la exposición de TiO_2 a radiación UV-visible produce la generación de grupos hidroxilos en su superficie, contribuyendo a un aumento de la energía superficial. Además, la rugosidad generada sobre las muestras tratadas (ver Capítulo 6-

Fig. 1) promueve un estado de Wenzel, en el cual las propiedades de humectación (en este caso la hidrofilia) se ven incrementadas. El papel de las NPs de TiO_2 induciendo la superhidrofilia fue confirmado mediante la aplicación de un producto que contenía NPs de SiO_2 (en adelante UCA-S) en lugar de TiO_2. En este caso, las muestras tratadas con este producto preservaron sus propiedades superhidrofugantes tras la exposición a radiación solar.

Las propiedades superoleofugantes bajo agua fueron evaluadas mediante la medida de ángulos de contacto de gotas de cloroformo, el cual presenta una tensión superficial similar a la mayoría de aceites. Con fines comparativos, se evalúo una muestra que presentaba superhidrofobicidad en aire (tratadas con UCA-S), y otra con superhidrofilia (tratada con UCA-T). La muestra tratada con UCA-S mostró oleofilia bajo agua, con ángulos de contacto cercanos a 10° (ver Capítulo 6-Fig. 3a). Además, se observó que las gotas de cloroformo se extendían rápidamente sobre su superficie cuando eran depositadas (ver Capítulo 6-Fig. 4 y Video S1). Esto se debe a la generación de una capa de aire entre el agua y la superficie sólida, como consecuencia del estado Cassie-Baxter generado [5]. Por lo tanto, la gota de cloroformo depositada sobre esta superficie, se extenderá rápidamente a lo largo del aire atrapado entre el agua y la superficie sólida, debido a la presión capilar generada [45]. Por el contrario, la muestra tratada con UCA-T presentó ángulos de contacto superiores a 150° (ver Capítulo 6-Fig. 3b), confirmando su superoleofobicidad bajo agua. Además, la repelencia fue confirmada depositando gotas de cloroformo, sobre la superficie sumergida, las cuales rodaron fuera de ésta (ver Capítulo 6-Fig. 4 y Video S1). En este caso, el agua es capaz de cubrir totalmente los valles de rugosidad debido a la superhidrofilia de la superficie. Por lo tanto, una capa de agua es situada entre la superficie sólida y el cloroformo, dando lugar a un estado Cassie-Baxter bajo agua [45,46].

Las propiedades auto-limpiantes de las muestras tratadas también fueron evaluadas (ver Capítulo 6-Fig. 6 y Video S2). En primer lugar, se observó que la muestra superhidrofugante fue capaz de eliminar fácilmente polvo de teja depositado sobre ella, al rociarla con agua, debido a su elevada repelencia. Sin embargo, cuando el polvo fue contaminado con aceite, el agua no pudo eliminarlo debido a la inmiscibilidad agua-

aceite. Por el contrario, la muestra superhidrofílica fue capaz de eliminar fácilmente el polvo contaminado con aceite, empleando agua. Esto se debe a la superhidrofilia obtenida, la cual permite que el agua moje completamente la superficie. Además, la superoleofobicidad bajo agua obtenida facilita la eliminación del contaminante.

Ya que la penetración de agua en la estructura porosa del hormigón puede producir la degradación de éste [47,48], se llevó a cabo un ensayo de absorción de agua por capilaridad. Los resultados obtenidos (ver Capítulo 6-Tabla S1) demostraron que las muestras tratadas con UCA-T fueron capaces de evitar la penetración de agua incluso tras volverse superhidrofílicas. Esto confirma que la superhidrofilia sólo es inducida en la superficie, mientras que el producto en el interior de la estructura porosa del hormigón mantiene su hidrofobicidad. Esto se debe a que las NPs de TiO_2 que se encuentran en el interior de la estructura porosa del material no son alcanzadas por la luz solar, evitando de esta forma la inducción de hidrofilia.

Finalmente, la durabilidad de muestras tratadas con UCA-T y UCA-S, junto con un producto superhidrofugante comercial (una dispersión de NPs hidrófobas en un disolvente), fue evaluada mediante un ensayo de adhesión, un ensayo de simulación de lluvia, y finalmente mediante exposición en exterior durante 3 meses (ver Capítulo 6-Fig. 7, 8 y 9). Se observó que el producto comercial perdió sus propiedades superhidrofugantes al ser sometido a los distintos ensayos, debido a la baja adhesión y penetración (ver Capítulo 6-Tabla 1 y Fig. S1). Por el contrario, las muestras tratadas con UCA-S y UCA-T preservaron sus propiedades superhidrofugantes tras ser sometidas a los diferentes ensayos. En el caso del ensayo de exposición al exterior, las muestras tratadas con UCA-T mostraron superhidrofilia en la superficie como era de esperar.

Las imágenes obtenidas por SEM (ver Capítulo 6-Fig. 10) mostraron que las superficies tratadas con los productos desarrollados en nuestro laboratorio no mostraron alteraciones significativas tras los diferentes ensayos de durabilidad. Esto confirma la resistencia mecánica del estado Cassie-Baxter obtenido [49,50].

7.4. Referencias.

[1]   D.S. Facio, M. Luna, M.J. Mosquera, Facile preparation of mesoporous silica monoliths by an inverse micelle mechanism, Microporous Mesoporous Mater. 247 (2017) 166–176.

[2]   D.H. Lee, J. Jeong, S.W. Han, D.P. Kang, Superhydrophobic surfaces with near-zero sliding angles realized from solvent relative permittivity mediated silica nanoparticle aggregation, J. Mater. Chem. A. 2 (2014) 17165–17173.

[3]   C. Hu, W. Chen, T. Li, Y. Ding, H. Yang, S. Zhao, E.A. Tsiwah, X. Zhao, Y. Xie, Constructing non-fluorinated porous superhydrophobic SiO_2-based films with robust mechanical properties, Colloids Surfaces A Physicochem. Eng. Asp. 551 (2018) 65–73.

[4]   S. V. Slavov, A.R. Sanger, K.T. Chuang, Mechanism of Silation of Silica with Hexamethyldisilazane, J. Phys. Chem. B. 104 (2000) 983–989.

[5]   A.B.D. Cassie, S. Baxter, Wettability of porous surfaces, Trans. Faraday Soc. 40 (1944) 546–551.

[6]   D.S. Facio, M.J. Mosquera, Simple strategy for producing superhydrophobic nanocomposite coatings in situ on a building substrate., ACS Appl. Mater. Interfaces. 5 (2013) 7517–26.

[7]   L.A.M. Carrascosa, D.S. Facio, M.J. Mosquera, Producing superhydrophobic roof tiles, Nanotechnology. 27 (2016).

[8]   M. Nosonovsky, B. Bhushan, Roughness optimization for biomimetic superhydrophobic surfaces, Microsyst. Technol. 11 (2005) 535–549.

[9]   B. Bhushan, E.K. Her, Fabrication of superhydrophobic surfaces with high and low adhesion inspired from rose petal., Langmuir. 26 (2010) 8207–17.

[10]   M. Nosonovsky, B. Bhushan, Hierarchical roughness optimization for biomimetic superhydrophobic surfaces, Ultramicroscopy. 107 (2007) 969–979.

[11]   X.-M. Li, D. Reinhoudt, M. Crego-Calama, What do we need for a superhydrophobic surface? A review on the recent progress in the preparation of superhydrophobic surfaces., Chem. Soc. Rev. 36 (2007) 1350–1368.

[12]   B. Cortese, S. D'Amone, M. Manca, I. Viola, R. Cingolani, G. Gigli, Superhydrophobicity due to the hierarchical scale roughness of PDMS surfaces, Langmuir. 24 (2008) 2712–2718.

[13]   S. Das, S. Kumar, S.K. Samal, S. Mohanty, S.K. Nayak, A Review on Superhydrophobic Polymer Nanocoatings: Recent Development and Applications, Ind. Eng. Chem. Res. 57 (2018) 2727–2745.

[14]   D.S. Facio, L.A.M. Carrascosa, M.J. Mosquera, Producing lasting amphiphobic building

surfaces with self-cleaning properties, Nanotechnology. 28 (2017) 265601.

[15] J.Y. Huang, S.H. Li, M.Z. Ge, L.N. Wang, T.L. Xing, G.Q. Chen, X.F. Liu, S.S. Al-Deyab, K.Q. Zhang, T. Chen, Y.K. Lai, Robust superhydrophobic TiO2 @fabrics for UV shielding, self-cleaning and oil–water separation, J. Mater. Chem. A. 3 (2015) 2825–2832.

[16] X.Y. Ling, I.Y. Phang, G.J. Vancso, J. Huskens, D.N. Reinhoudt, Stable and transparent superhydrophobic nanoparticle films, Langmuir. 25 (2009) 3260–3263.

[17] S.S. Latthe, R.S. Sutar, V.S. Kodag, A.K. Bhosale, A.M. Kumar, K. Kumar Sadasivuni, R. Xing, S. Liu, Self − cleaning superhydrophobic coatings: Potential industrial applications, Prog. Org. Coatings. 128 (2019) 52–58.

[18] L. Pinho, M.J. Mosquera, Titania-Silica Nanocomposite Photocatalysts with Application in Stone Self-Cleaning, J. Phys. Chem. C. 115 (2011) 22851–22862.

[19] X. Jing, Z. Guo, Biomimetic super durable and stable surfaces with superhydrophobicity, J. Mater. Chem. A. 6 (2018) 16731–16768.

[20] R.S. Berns, Billmeyer and Saltzman's Principles of Color Technology, 3rd ed., New York, 2000.

[21] J.D. Rodrigues, A. Grossi, Indicators and ratings for the compatibility assessment of conservation actions, J. Cult. Herit. 8 (2007) 32–43.

[22] J.F. Illescas, M.J. Mosquera, Surfactant-Synthesized PDMS/Silica Nanomaterials Improve Robustness and Stain Resistance of Carbonate Stone, J. Phys. Chem. C. 115 (2011) 14624–14634.

[23] D. Ahmad, I. van den Boogaert, J. Miller, R. Presswell, H. Jouhara, Hydrophilic and hydrophobic materials and their applications, Energy Sources, Part A Recover. Util. Environ. Eff. 40 (2018) 2686–2725.

[24] R.N. Wenzel, Resistance of solid surfaces to wetting by water, Ind. Eng. Chem. 28 (1936) 988–994.

[25] J. Yong, F. Chen, Q. Yang, D. Zhang, H. Bian, G. Du, J. Si, X. Meng, X. Hou, Controllable adhesive superhydrophobic surfaces based on PDMS microwell arrays., Langmuir. 29 (2013) 3274–3279.

[26] B.N. Chichkov, C. Momma, S. Nolte, F. von Alversleben, A. Tünnermann, Femtosecond, picosecond and nanosecond laser ablation of solids, 63 (1996) 109–115.

[27] J. Yong, F. Chen, M. Li, Q. Yang, Y. Fang, J. Huo, X. Hou, Remarkably Simple Achievement of Superhydrophobicity, Superhydrophilicity, Underwater Superoleophobicity, Underwater Superoleophilicity, Underwater Superaerophobicity, and Underwater Superaerophilicity on Femtosecond Laser Ablated PDMS Surfaces, J. Mater. Chem. A. 5 (2017) 25249–25257.

[28]   D. Aslanidou, I. Karapanagiotis, C. Panayiotou, Tuning the wetting properties of siloxane-nanoparticle coatings to induce superhydrophobicity and superoleophobicity for stone protection, Mater. Des. 108 (2016) 736–744.

[29]   Y. Li, X. Men, X. Zhu, B. Ge, F. Chu, Z. Zhang, One-step spraying to fabricate nonfluorinated superhydrophobic coatings with high transparency, J. Mater. Sci. 51 (2016) 2411–2419.

[30]   D.S. Facio, L.A.M. Carrascosa, M.J. Mosquera, Producing lasting amphiphobic building surfaces with self-cleaning properties, Nanotechnology. 28 (2017).

[31]   J.D. Brassard, D.K. Sarkar, J. Perron, Synthesis of monodisperse fluorinated silica nanoparticles and their superhydrophobic thin films, ACS Appl. Mater. Interfaces. 3 (2011) 3583–3588.

[32]   S. Zhou, X. Ding, L. Wu, Fabrication of ambient-curable superhydrophobic fluoropolysiloxane/TiO 2 nanocomposite coatings with good mechanical properties and durability, Prog. Org. Coatings. 76 (2013) 563–570.

[33]   R.A. Hayn, J.R. Owens, S.A. Boyer, R.S. McDonald, H.J. Lee, Preparation of highly hydrophobic and oleophobic textile surfaces using microwave-promoted silane coupling, J. Mater. Sci. 46 (2011) 2503–2509.

[34]   T. Darmanin, F.F. Guittard, Superhydrophobic and superoleophobic properties in nature, Mater. Today. 18 (2015) 273–285.

[35]   L.D. a. Chumpitaz, L.F. Coutinho, A.J. a. Meirelles, Surface tension of fatty acids and triglycerides, J. Am. Oil Chem. Soc. 76 (1999) 379–382.

[36]   J. Li, Y. Lu, Z. Wu, Y. Bao, R. Xiao, H. Yu, Y. Chen, Durable, self-cleaning and superhydrophobic bamboo timber surfaces based on TiO2 films combined with fluoroalkylsilane, Ceram. Int. 42 (2016) 9621–9629.

[37]   L. Xu, R.G. Karunakaran, J. Guo, S. Yang, Transparent, Superhydrophobic Surfaces from One-Step Spin Coating of Hydrophobic Nanoparticles, ACS Appl. Mater. Interfaces. 4 (2012) 1118–1125.

[38]   H. Bellanger, T. Darmanin, E. Taffin de Givenchy, F. Guittard, Chemical and Physical Pathways for the Preparation of Superoleophobic Surfaces and Related Wetting Theories, Chem. Rev. 114 (2014) 2694–2716.

[39]   E. Bormashenko, Progress in understanding wetting transitions on rough surfaces, Adv. Colloid Interface Sci. 222 (2015) 92–103.

[40]   K. Koch, B. Bhushan, Y.C. Jung, W. Barthlott, Fabrication of artificial Lotus leaves and significance of hierarchical structure for superhydrophobicity and low adhesion, Soft Matter.

5 (2009) 1386.

[41]   J. Schneider, M. Matsuoka, M. Takeuchi, J. Zhang, Y. Horiuchi, M. Anpo, D.W. Bahnemann, Understanding TiO2 Photocatalysis: Mechanisms and Materials, Chem. Rev. 114 (2014) 9919–9986.

[42]   M.B. Hugenschmidt, L. Gamble, C.T. Campbell, The interaction of H2O with a TiO2(110) surface, Surf. Sci. 302 (1994) 329–340.

[43]   A. Fujishima, T.N. Rao, D.A. Tryk, Titanium dioxide photocatalysis, J. Photochem. Photobiol. C Photochem. Rev. 1 (2000) 1–21.

[44]   R. Wang, K. Hashimoto, A. Fujishima, M. Chikuni, E. Kojima, A. Kitamura, M. Shimohigoshi, T. Watanabe, Photogeneration of highly amphiphilic TiO2surfaces, Adv. Mater. 10 (1998) 135–138.

[45]   J. Yong, F. Chen, Q. Yang, J. Huo, X. Hou, Superoleophobic surfaces, Chem. Soc. Rev. 46 (2017) 4168–4217.

[46]   M. Liu, S. Wang, Z. Wei, Y. Song, L. Jiang, Bioinspired Design of a Superoleophobic and Low Adhesive Water/Solid Interface, Adv. Mater. 21 (2009) 665–669.

[47]   D. Jacques, L. Wang, E. Martens, D. Mallants, Modelling chemical degradation of concrete during leaching with rain and soil water types, Cem. Concr. Res. 40 (2010) 1306–1313.

[48]   X. Pan, Z. Shi, C. Shi, T.C. Ling, N. Li, A review on concrete surface treatment Part I: Types and mechanisms, Constr. Build. Mater. 132 (2017) 578–590.

[49]   A. Milionis, E. Loth, I.S. Bayer, Recent advances in the mechanical durability of superhydrophobic materials, Adv. Colloid Interface Sci. 229 (2016) 57–79.

[50]   B.P. Dyett, A.H. Wu, R.N. Lamb, Mechanical Stability of Surface Architecture—Consequences for Superhydrophobicity, ACS Appl. Mater. Interfaces. 6 (2014) 18380–18394.

Capítulo 8

Conclusiones

De acuerdo con los resultados obtenidos durante el desarrollo de esta Tesis Doctoral y de la discusión efectuada, se establecen la siguiente conclusión:

Se han desarrollado cuatro tipos de materiales, específicamente diseñados para aplicación en materiales de construcción, que evitan los daños causados por agua y/o sustancias oleosas. Los cuatros materiales cumplen los siguientes requisitos genéricos:

1. Han sido obtenidos mediante una ruta sol-gel que permite la aplicación sobre el sustrato de un sol con baja viscosidad que polimeriza de forma espontánea en su estructura porosa. Por tanto, es posible la aplicación de estos materiales, in situ, sobre las fachadas de los edificios. Además, la simplicidad de la ruta y su bajo coste permite su aplicación sobre grandes superficies.

2. La modificación superficial de la rugosidad mediante métodos *bottom-up* y *top-down* combinados con una reducción de la energía superficial ha permitido obtener un estado Cassi-Baxter en las superficies tratadas que promueven hidro-, y/o oleo-fobicidad y repelencia, dotando a los materiales de propiedades auto-limpiantes.

3. La penetración de los materiales en la estructura porosa de los sustratos y su similitud en cuanto a su naturaleza química ha permitido la adhesión producto/sustrato que garantiza su durabilidad.

4. Los productos desarrollados cumplen los requisitos para su aplicación en materiales de construcción, incluyendo las aplicaciones más restrictivas asociadas a los elementos del Patrimonio Cultural. En concreto, no inducen modificaciones en el color del sustrato superiores al umbral del ojo humano y la reducción de difusividad al vapor es inferior al 50%, garantizando la transpiración del material de construcción después del tratamiento.

Además, se han obtenido las siguientes conclusiones específicas relacionadas con cada uno de los materiales desarrollados:

1. Se ha desarrollado un producto superhidrofugante, para materiales de construcción, compuesto por nanopartículas hidrófobas (que reducen la energía superficial y crean rugosidad), agregadas por la acción de un disolvente apolar (hexano) y unidas entre sí por un oligómero que forma puentes de sílice. Esto permite incrementar la adhesión de las nanopartículas al sustrato, y entre sí.

2. Se han diseñado materiales de construcción superhidrofugantes empleando un procedimiento de dos pasos. (1) reducción de energía superficial aplicando un ORMOSIL que contiene un oligómero de sílice y PDMS, y (2) aumento de la rugosidad superficial empleando ablación láser. Se observó la formación de una rugosidad tipo Wenzel para valores de fluencia inferiores al umbral de ablación del material, incrementándose la hidrofobicidad con la rugosidad. Para valores de fluencia superiores a este umbral, se produce la deposición de sub-micropartículas sobre la superficie promoviendo un estado Cassie-Baxter y, en consecuencia, propiedades superhidrofugantes.

3. Se ha desarrollado un producto superhidrofugante y oleofugante, para materiales de construcción, consistente en una dispersión de nanopartículas de sílice, que crean una rugosidad típica de un estado Cassie-Baxter, en una disolución acuosa de un fluoroalquilsilano, el cual permite reducir la energía superficial dotando a los materiales de propiedades superhidrofugantes y oleofugantes, y en consecuencia auto-limpiantes.

4. Se ha desarrollado un producto para la protección de hormigón que combina la acción de una superficie superhidrofílica, con la creación de una matriz hidrófoba dentro de la estructura porosa. Específicamente, la integración de TiO_2 dentro de un ORMOSIL da lugar dos efectos: (1) la creación de una nano-rugosidad, que promueve superhidrofobicidad/superhidrofilia, y (2) la capacidad para cambiar de el comportamiento de superhidrofóbico a superhidrofílico, debido al carácter fotocatalítico del TiO_2. Como consecuencia, las superficies de hormigón muestran capacidad superoleofugante bajo agua, y este efecto puede ser explotado para solventar la ineficacia de las superficies superhidrofugantes frente a contaminantes oleosos, además de la obtención de superficies de materiales de construcción con capacidad auto-limpiante sin necesidad de emplear detergentes. Además, el comportamiento superhidrofílico es producido únicamente en la superficie del hormigón, mientras que el producto que penetra en la estructura porosa, y por tanto no está expuesto a la radiación solar, mantiene su hidrofobicidad evitando la penetración de agua.

Anexo I-Artículos pertenecientes a la Tesis

Conference paper

Maria J. Mosquera*, Luis A.M. Carrascosa and Nabil Badreldin

Producing superhydrophobic/oleophobic coatings on Cultural Heritage building materials

Abstract: Water is the main vehicle of decay agents in Cultural Heritage building materials exposed to weathering. In this work, a simple method to produce superhydrophobic/oleophobic coatings building materials, including under outdoors conditions, has been developed. In addition, a study of the behavior of the developed coatings on different substrates (limestone, granite, concrete and wood) is reported. The addition of 40 nm-SiO_2 nanoparticles to a fluoroalkylsilane reduces surface energy and produces a Cassie-Baxter surface in all the materials evaluated. It promotes high static contact angle values of around 160°, and a contact angle hysteresis of around 3°, giving rise to repellence. The building surfaces also demonstrate an excellent self-cleaning performance. The coatings maintain the building materials esthetics as required in the Cultural Heritage field. Finally, the coating presents a long-lasting performance due to condensation reactions producing effective grafting to the four building materials evaluated.

Keywords: 2016 ChemCutHerit; 40-nm silica particles; building material; Cultural Heritage; fluoroalkylsilane; long-lasting properties; oleophobicity; self-cleaning; superhydrophobicity.

Introduction

A surface is considered as superhydrophobic when it presents high hydrophobicity and water repellence. These kinds of surfaces have to fulfill two requirements: (1) static contact angle (SCA) values over 150° (2) contact angle hysteresis (CAH, which is the difference between advancing and receding contact angles) values lower than 10°. As previously explained [1], the hysteresis controls the movement of water droplets on the surface and, therefore, it characterizes the repellence.

Nature has developed numerous species of plants, insects and other animals, which have had surfaces with superhydrophobic properties for millennia. The most well-known example is the lotus leaf [2], whose structure includes waxes with hierarchical micro- and nano-roughness. Thus, waxes reduce surface energy, giving rise to hydrophobic properties on the surface, and the roughness produces repellence [2, 3]. In order to promote repellence, the roughness has to produce a Cassie-Baxter surface [4] where air-pockets are created between liquid droplets and the solid surface, thus assisting the water droplets to roll off the surface.

*Corresponding author: Maria J. Mosquera, Nanomaterials Group TEP-243, Departamento de Química-Física, Facultad de Ciencias, Universidad de Cádiz, Campus Río San Pedro, Puerto Real (Cádiz) 11510, Spain, e-mail: mariajesus.mosquera@uca.es
Luis A.M. Carrascosa and Nabil Badreldin: Nanomaterials Group TEP-243, Departamento de Química-Física, Facultad de Ciencias, Universidad de Cádiz, Campus Río San Pedro, Puerto Real (Cádiz) 11510, Spain

Superhydrophobic materials find applications in the field of building due to their interesting properties, such as self-cleaning, anti-fouling, stain-resistance and ice-repellence [5], and especially in Cultural Heritage materials in which their preservation is crucial. In the specific case of treatments applied on Cultural Heritage elements, their requirements are even more restrictive, being required to evaluate compatibility between substrates and treatments associated to physical-chemical, environmental, operational and socio-cultural issues [6]. However, most approaches found in the literature [7–10] require expensive and multi-stage processes and subsequently, they cannot be applied on building facades [11]. Other drawback for building application is associated to the low durability of these strategies [12]. Surface roughness is induced by top down or bottom up procedures. This surface architecture of roughness in the coating contributes significantly to to low durability [13]. Thus, fabrication of durable superhydrophobic surfaces exposed to the weather under outdoor conditions still remains a challenge.

In recent years, specific approaches for producing superhydrophobic coatings on building materials have been developed [14–18], although most of them do not consider the durability of the treatments, a critical requirement stemming from their exposure to outdoor conditions. Regarding previous papers which consider durability in superhydrophobic building materials, Aslanidou et al. [19] applied a commercial water soluble hydrophobic siloxane emulsion enriched with silica nanoparticles (NPs) onto white marble and sandstone. These coatings demonstrated chemical resistance by measuring SCA values of water drops with different pH values. In addition, the coatings maintained high SCA (around 150°) after a tape test.

Manoudis et al. [20] produced superhydrophobic coatings by applying dispersions of silica NPs in a polysiloxane onto white marble. In order to evaluate the durability, the treated samples were exposed outdoors during 5 months, maintaining a SCA of around 150°.

Finally, De Ferri et al. [21] produced superhydrophobic coatings by mixing hydrophobic silica NPs with a glycidoxypropyltrimethoxysilane. The obtained products were applied on three different kinds of stone: marble, sandstone and granite. Specifically, the treated samples were placed outdoors for 4 months, with a significant decrease in SCA values being produced. In addition, the samples were also subjected to a test of water absorption by capillarity. After 5 days in continuous contact with water, the superhydrophobic, and even hydrophobic, properties of the coatings were completely lost.

In the above works, the SCA values were used to evaluate the durability of superhydrophobic products, but parameters regarding repellence, such as CAH were not evaluated. As we previously described [22], roughness, producing repellence, is more susceptible to decay and it cannot be evaluated by SCA values.

Our research group have developed specific materials for building conservation by using a simple sol–gel route [23], which allows application over large-areas, as well as application *in situ* under outdoor conditions. This product was evaluated in different Cultural Heritage elements [24, 25]. Specifically, a surfactant and a silica oligomer are mixed by ultrasonic agitation [26]. An inverse micelle mechanism permits to obtain crack-free coatings with high adhesion to the substrates [27]. The addition of an organic silica oligomer gives rise to hydrophobic properties [26]. To promote superhydrophobicity, we have added silica NPs to a mixture of organic-inorganic silica oligomers [11, 22]. Finally, we have also produced lasting amphiphobic (superhydrophobic and oleophobic) coatings by the application of two successive coatings: (1) a silica nanocomposite containing silica NPs and (2) a fluorinated alcoxysilane [28].

In this work, a superhydrophobic product was prepared by a simple mixture of a water soluble fluoroalkylsilane and silica NPs. We employed a halogen compound in order to confer additional oleophobic properties to the coating. This product was applied on four different building materials of interest in the Cultural Heritage field (limestone, granite, concrete and wood), and superhydrophobicity was evaluated. In addition, the durability was evaluated by two different procedures (tape test and rain simulation test). Finally, since a possible application of this product is the Cultural Heritage conservation, esthetic changes induced by the treatment were evaluated by measuring color variations of the treated materials. However, we want to remark that other compatibility parameters, including long term incompatibility, will require evaluation previous to its application in specific Cultural Heritage materials.

Experimental section

Preparation of superhydrophobic product

The reagents employed were: (1) Aerosil OX50 (hereinafter SiNPs), which consists of fumed silica NPs (primary size of 40 nm and surface area of 50 $m^2 \cdot g^{-1}$) supplied by Evonik. (2) Dynasylan F8815 (hereinafter F8815) is a water-soluble fluoroalkylsilane. It has a fluoroalkyl chain, which provides hydrophobic and oleophobic properties, an aminoalkyl chain which confers solubility in water, and two hydroxyl groups for siloxane polymerization.

The superhydrophobic product was prepared by means of a simple method: (1) SiNPs were dispersed in deionized water (2 % w/v), and the dispersion was ultrasonically agitated for 10 min. (2) 2 % v/v of F8815 was added dropwise, and the product was magnetically stirred for 30 min. The product was always applied 1 h after its preparation in order to maintain reproducibility of the results. The product showed stability in closed vessel for 1 month. After this time, a slight precipitate, which can be re-dispersed by mechanical agitation, was observed.

Application of superhydrophobic product

The sol was applied on four different building materials: limestone, granite, concrete and wood. The samples size was $4 \times 4 \times 2$ cm for granite and limestone, $3.5 \times 3.5 \times 3.5$ cm for the concrete and $3.5 \times 3.5 \times 0.5$ cm for the wood. The four materials under study are commonly employed in modern buildings. The selected limestone (commercially available as Capri limestone) has an open porosity around 9 %, and it presents a homogeneous structure, composed of micritic matrix containing oolites and oncolites, having a 90 % of calcite and a 10 % of silicate minerals. The granite (white pearl granite) is a biotitic granite with an open porosity around 0.5 %, and the main components are SiO_2 (64 %) and Al_2O_3 (19 %). The rest of components (Fe_2O_3, MgO, Na_2O and K_2O) are found in percentage lower than 10 %. A type I white Portland cement and a calcareous sand (ϕ 1–6 mm) were employed to fabricate the concrete samples. The water:cement ratio and the cement:sand ratio (w/w) were 1:2 and 1:5 (w/w), respectively. The specimens were cured under water at $21 \pm 2\,°C$ for 28 days, according with standard UNE-EN 12390-2 [29], being their open porosity around 10 %. Finally, the pine wood samples (hereinafter Wood) present an open porosity around 58 % and it is composed of cellulose (50 %), hemicellulose (25 %) and lignin (25 %). All the surfaces were used as received without any modification. The sol was applied by brushing on all the substrates, except wood. Specifically, three applications, with an elapsed time between applications of 30 s were performed. The wood samples were immersed into the sol for 5 min. After application, the samples were let overnight in laboratory conditions (20 °C and 40 % RH), to allow the sol–gel transition. Then, the samples were heated into an oven at 100 °C, for 1 h, in order to remove the solvent (water). Once the treated samples were dried and cold, the following experiments were carried out on two replicates for each surface under study. In order to calculate the uptake of product, the samples were weighed before and immediately after being treated. After drying, the samples were re-weighed to calculate the dry matter. The penetration depth of the product inside the building materials under study was evaluated. Specifically, the samples were cut in order to obtain cross-sections. Then, water was dropped on the cross-sections, corresponding the non-wetted area to the penetration depth of the product.

Characterization of the treated surfaces and effectiveness

Static and dynamic CAs were evaluated by using OCA15 Plus video-measuring equipment, from DataPhysics Instruments, according to the following method: droplets of distilled water (5 µL) were applied with a syringe at five different points on each surface under study, and SCA values were evaluated. Then, 2.5 µL were added, obtaining the advancing CA (ACA) values. Finally, 2.5 µL were removed and the receding CA (RCA) values were measured. In addition, the oleophobic properties of the coatings were evaluated by placing 5 µL droplets of olive oil at five different points on each surface and measuring the SCA values.

As an additional experimental test of the water-repellent behavior, a water jet was projected onto each treated surface under study from a distance of 20 cm. The experiment was recorded by a digital camera (Sony Cyber-shot model DSCP200) at 30 frames/s.

The self-cleaning properties of the treated surfaces and their untreated counterparts were tested according to a previously described procedure [30]. Specifically, methylene blue powder was applied to the surfaces of the samples. Next, the samples were placed under a water column in order to simulate the effect of rain. The water column fell over the surface of the samples from a height of 50 cm, with a flow of 45 mL $\cdot$ s^{-1}. These experiments were registered with the previously described camera. In order to evaluate the self-cleaning effectiveness, the color of the samples was measured before and after the test by using a ColorFlex spectrophotometer from HunterLab. Illuminant D65 and observer CIE10° were selected as measurement parameters. The CIE L*a*b* scale was employed [31]. These experiments were registered with the previously described camera.

In order to evaluate the changes produced in the topography of the treated samples, atomic force microscopy (AFM) images of the surfaces were obtained by using an AFM Dulcinea model from Nanotec Electrónica, operating in tapping mode. The root mean square (RMS) roughness values were evaluated from 5 µm × 5 µm images. Measurements were recorded in five points on the surface.

Finally, the color change caused by the application of the product was evaluated by means of a Color-Flex spectrophotometer from HunterLab. Illuminant D65 and observer CIE10° were selected as measurement parameters. The CIE L*a*b* scale was employed [31].

Evaluation of durability

The lasting properties of the treated samples were tested by performing two different tests. The adhesion between coating and substrate is an important issue that determines the lasting properties of the treatment, since a coating with poor adhesion will be easily removed due to environmental conditions (rain, wind). Thus, the adhesion of the coatings to the surface samples was evaluated according to a previous test developed of our group [28]. Specifically, an adhesive tape was applied on the treated surfaces and it was subsequently removed. Static and dynamic CAs for water were measured after 1, 2, 5, 10, 15 and 20 attachment-detachment cycles.

The resistance to water impact was evaluated by placing the treated samples under a water column in order to simulate the effect of rain. The water column fell over the surfaces of the samples from a height of 50 cm with a flow of 45 mL $\cdot$ s^{-1}. The total amount of water falling onto the treated surfaces was 2500 L $\cdot$ m^{-2}. After the test, the samples were dried in an oven at 60 °C and the static and dynamic CA values for water were evaluated.

Results and discussion

Application of superhydrophobic product

Table 1 shows the average uptake, dry-matter and penetration depth values for the applied samples.

As observed in Table 1, all the substrates showed product uptake values with a clear relation with their open porosity values. In the case of wood, this value was significantly higher than the other substrates due

Table 1: Uptake, dry-matter and penetration depth average values for the treated samples.

Sample	Uptake (%)	Dry-matter (%)	Penetration depth (mm)
Limestone	0.51 ± 0.02	0.11 ± 0.02	2.6 ± 0.1
Granite	0.21 ± 0.02	0.05 ± 0.01	0.5 ± 0.2
Concrete	0.53 ± 0.04	0.12 ± 0.02	3.1 ± 0.2
Wood	73.98 ± 0.06	0.19 ± 0.04	−

to the application method (immersion). After drying, all the samples showed a significant loss of weight due to the solvent evaporation. Regarding to penetration depth, the measured value was also related with the porosity of the substrates. In the case of wood, this value could not be measured because the product was applied by immersion.

Characterization of the treated surfaces and effectiveness

Figure 1 shows the SCA, ACA and RCA values for the treated samples under study (left), and images of 25 µL water droplets on the building materials surfaces under study are shown on the right. The untreated surfaces were hydrophilic, showing SCA values of 35°, 60° and 10° for limestone, granite and concrete samples, respectively. In the case of the wood samples, the water droplet was quickly absorbed and thus, the SCA could not be evaluated. All the treated surfaces showed superhydrophobic properties with SCA values of around 160°. Moreover, ACA and RCA presented very close values, the CAH value being around 3° in all cases. As previously discussed [11, 22], 40 nm-SiO_2 NPs are able to produce a surface roughness typical of a Cassie-Baxter regime, providing repellent properties [32–34]. In addition, the fluoroalkylsilane is able to decrease surface energy due to the action of fluoroalkyl chains [35–37]. The combination of both effects (roughness and low surface energy) gives rise to superhydrophobic properties. In order to demonstrate the water repellent properties of the treated surfaces, a video was recorded (see Supplementary Information, Video S1). The video shows a water jet impacting on the four treated surfaces. The water jet is completely repelled for all the building material surfaces evaluated.

Alfieri et al. [38] also employed fluoroalkylsilane in order to produce hydrophobic coatings, but they added TiO_2 NPs with a size of around 4 nm in order to confer photoactive properties. In this case, repellence was not evaluated, and the SCA values were lower than those obtained in the present work. This different behavior is associated with the size of NPs integrated into the fluoroalkylsilica gel. The 4 nm-size NPs (ten times less than the 40 nm-size NPs employed in the present synthesis) cannot produce the required roughness to promote a Cassie-Baxter regime and an SCA above 150°.

In our work, the superhydrophobic behavior observed suggests that a self-cleaning effect can be induced in these surfaces [19, 39]. Thus, a test was carried out as previously described in the experimental section. Results are shown in Table 2.

In the case of the untreated samples, the dye was dissolved by the water droplets, and the hydrophilic nature of the surfaces promoted the absorption of the solution by the pores of the different substrates. Thus, a blue stain was permanently maintained on the building materials under study. Thus, significant ΔE* values
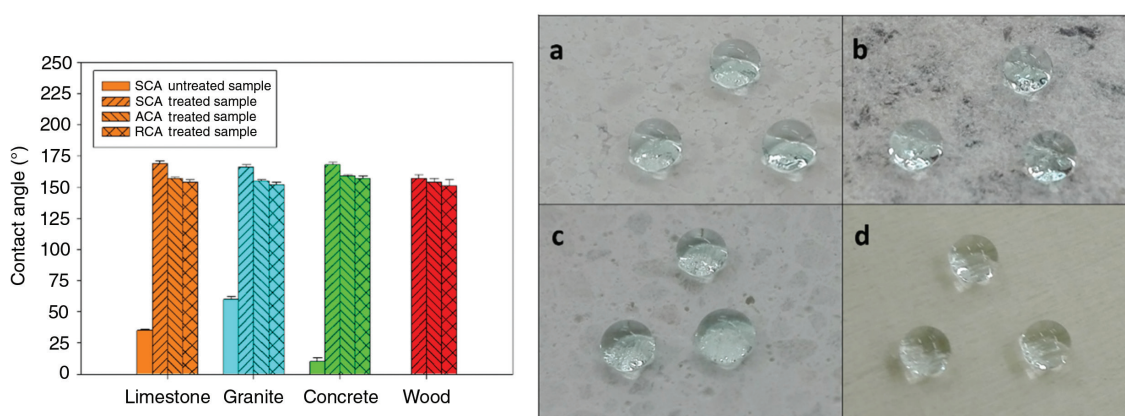

Fig. 1: Static (SCA), Advancing (ACA) and Receding (RCA) Contact Angle values obtained on the surface of the treated building material samples under study. In order to stablish a comparison, SCA of the untreated samples were also included. Photographs of water droplets on the treated building material surfaces evaluated are included: (a) limestone, (b) granite, (c) concrete, and (d) wood. The water droplets were dyed with methylene blue to have a better contrast.

Table 2: Total color difference (ΔE*) values for the untreated and treated samples after self-cleaning test.

Sample	ΔE* (untreated sample)	ΔE* (treated sample)
Limestone	35.33 ± 0.34	0.51 ± 0.18
Granite	22.48 ± 0.21	0.37 ± 0.15
Concrete	33.19 ± 0.18	0.43 ± 0.21
Wood	34.87 ± 0.24	0.42 ± 0.13

were obtained for all the untreated samples, as observed in Table 2. On the other hand, the dye was completely removed from the treated surfaces by the droplets rolling off. This behavior was confirmed by the colorimetric test, being all the ΔE* values lower than 0.6. As an example, a video showing this self-cleaning effect on the limestone samples is shown in the Supplementary Information (Video S2).

The addition of a fluorinated compound reduces the surface energy to values lower than those produced by organic components, giving rise to oleophobic properties. The surface tension of olive oil ($32 \, mN \cdot m^{-1}$, at $25 \, °C$) [40] is significantly lower than that of water ($72 \, mN \cdot m^{-1}$). Thus, it is necessary to use halogen compounds in order to decrease the coating surface energy below the surface energy in the olive oil-coating interphase [35, 37, 41, 42]. Therefore, the oleophobic behavior of the treated surfaces under study was evaluated by measuring the SCA values of olive oil droplets. Figure 2 shows the SCA values of oil droplets deposited on the untreated substrates and their treated counterparts. In addition, photographs of the olive oil droplets on the treated surfaces are included. The untreated surfaces showed oleophilic behavior with SCA values of 10, 15 and 21° for limestone, granite and concrete, respectively. In the case of wood, oil droplets were rapidly absorbed and, therefore, they could not be measured. Regarding to the treated substrates, all of them showed highly oleophobic properties, with SCA values above 100°. Photographs of the olive oil droplets on the treated surfaces, along with the SCA values, can be seen in Fig. 2. All the surfaces showed highly oleophobic properties, with SCA values above 100°.

Since the superhydrophobicity is a combination of decreasing surface energy and creating a roughness characteristic of a Cassie-Baxter regime, a study of the topography modification of the surfaces under study was carried out by AFM measurements. Figure 3 shows AFM results for the treated samples under study and their untreated counterparts.

All the untreated samples showed completely heterogeneous surfaces with a random roughness (high RMS values are observed). On the contrary, the treated substrates showed homogeneous surfaces composed by densely-packed, uniform, NPs aggregation. It confirms that SiO_2 NPs were integrated into the
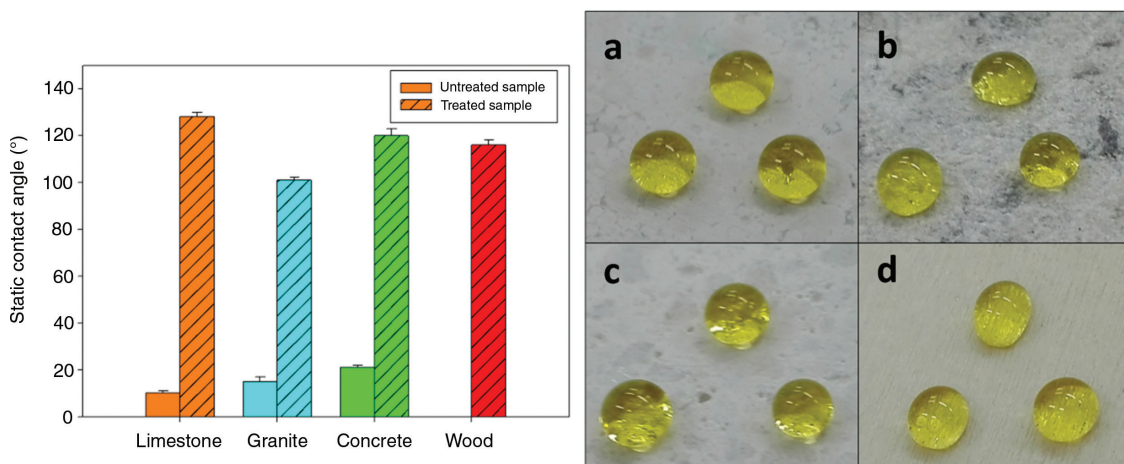

Fig. 2: SCA values of the oil droplets deposited on the untreated substrates and their treated counterparts. Photographs of the olive oil droplets deposited on the surfaces of the treated building material samples under study: (a) limestone, (b) granite, (c) concrete, and (d) wood.

fluorinated silica gel, producing the uniform packing observed by AFM. All the surfaces showed a significant decrease in the RMS values after being treated because the coating is able to cover the irregularities of the surfaces excepting the granite samples. In this case RMS value is increased after the application of the coating. This can be due to the low porosity of granite (0.5 %), which promotes the accumulation of product on the surface. This can be explained as a consequence of the low product penetration in granite (see Table 1).

Figure 3 (bottom) presents the 2D AFM roughness profiles. As previously discussed by Bhushan and Her [43], the space between peaks is important in order to trap air pockets, producing a Cassie-Baxter regime. The treated surfaces show, for all the subtrates, distance between peaks with fairly uniform values between 150 and 250 nm, whereas the untreated surfaces showed heterogeneous distances between peaks, bigger than 1000 nm. These results suggest that the water droplets will be less able to penetrate into the treated surfaces, hence the contact area between droplet and surface will be minimized. This promotes high contact angle values and repellence behavior, as previously suggested [11, 22, 43, 44]. In the case of the oleophobic behavior, a mushroom-like roughness is required to produce superoleophobicity [42, 45]. Thus, our product promotes high SCA, but it cannot produce oil repellence.

A practical limitation of the superhydrophobic products to be applied in Cultural Heritage will be encountered if a change in the color of the building material is produced (physical-chemical compatibility). Therefore, the variations in the colorimetric coordinates (ΔL^*, Δa^* and Δb^*) of the substrates induced by the product were obtained, and total color difference (ΔE^*) was calculated. The results are shown in Table 3 and photographs of the untreated building materials and their treated counterparts are shown in Fig. 4.

As observed in Table 3, the application of the superhydrophobic product on the building materials under study caused negligible color modification, as can be demonstrated by ΔE^* values lower than or equal to 3.
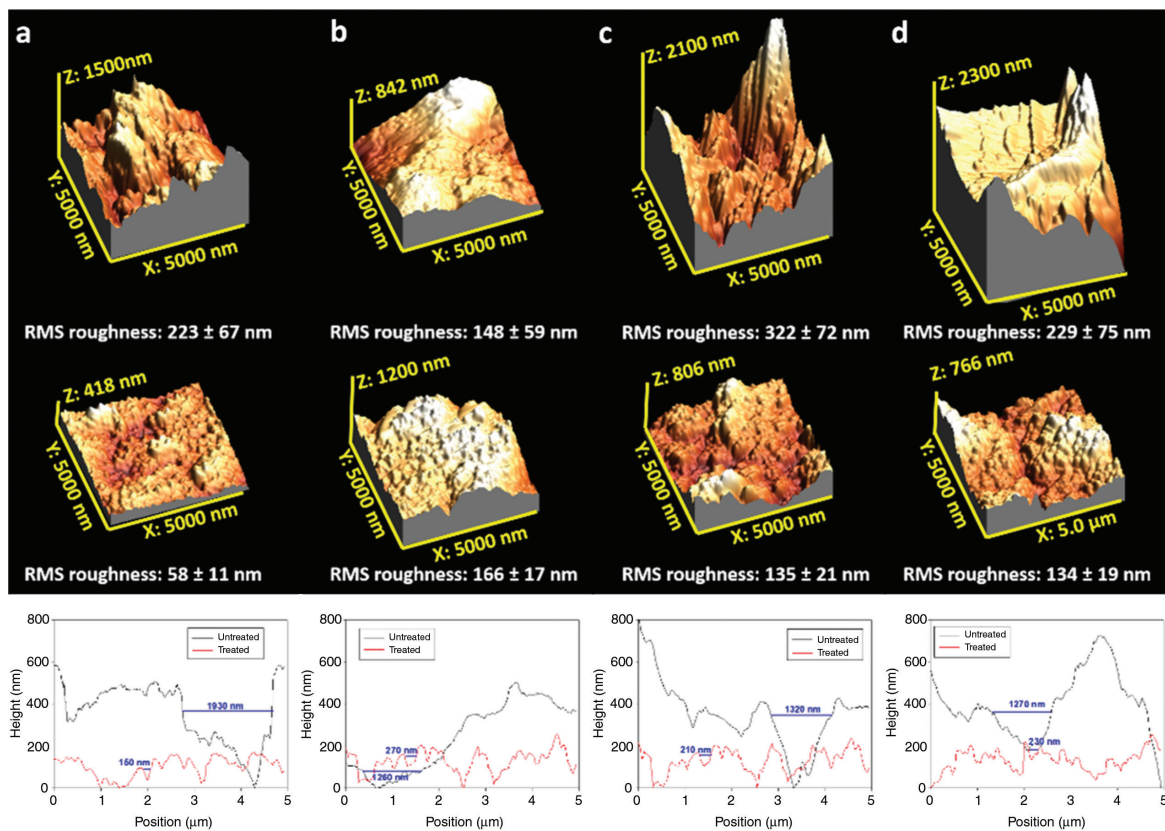

Fig. 3: 3D AFM images for the untreated (top) and treated (middle) surfaces. (a) limestone, (b) granite, (c) concrete, (d) wood. The root mean square (RMS) roughness values are also included. 2D roughness profiles are included below.

Table 3: Color variation of the samples after application of the products.

Sample	ΔL*	Δa*	Δb*	ΔE*
Limestone	2.03±0.22	0.97±0.28	0.87±0.24	2.38±0.30
Granite	2.75±0.31	0.95±0.44	−0.91±0.33	3.05±0.45
Concrete	2.41±0.28	0.93±0.51	0.94±0.46	2.75±0.65
Wood	1.96±0.24	0.88±0.54	−0.89±0.34	2.33±0.77
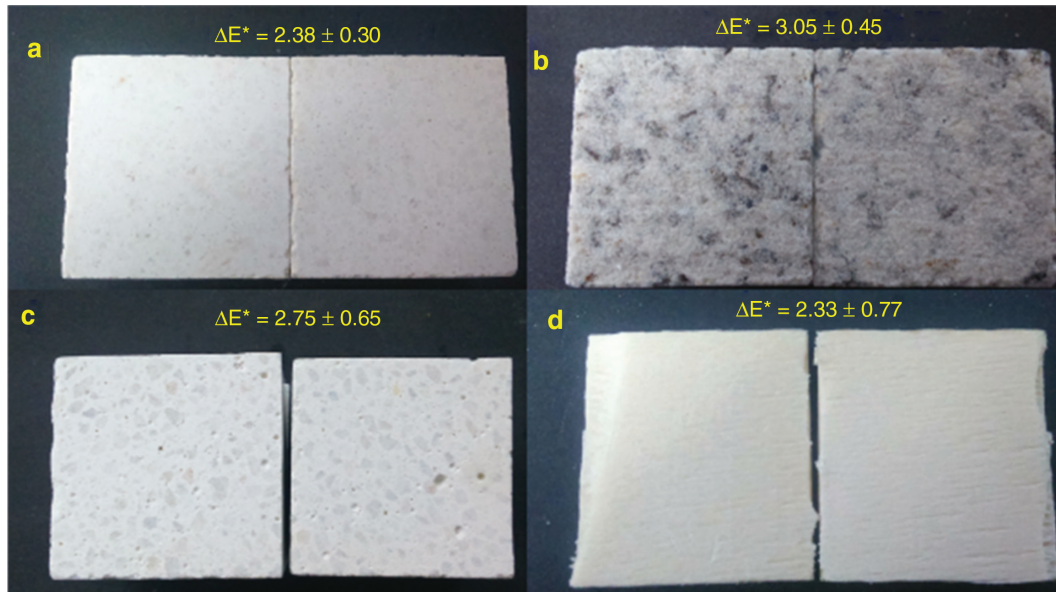
Fig. 4: Photographs of untreated (left) and treated (right) substrates, together with the calculated values of total color difference. (a) limestone, (b) granite, (c) concrete, (d) wood.

According with Delgado-Rodrigues and Grossi [6], color variation lower than 3 are perfectly acceptable in Cultural Heritage field. Regarding to the changes produced in the individual color coordinates (ΔL^*, Δa^* and Δb^*), it was observed that the values obtained for Δa^* and Δb^* were negligible. In the case of ΔL^*, a slight increase to positive values was observed, which indicates a slight lighter than that observed for the untreated surfaces. This value was slightly higher in the case of granite due to their lower porosity that allows the accumulation of the product on the surface, as previously discussed.

Evaluation of durability

The durability of the superhydrophobic surfaces is a critical requirement for their application on building materials which are exposed to outdoor conditions. Thus, the lasting-effectiveness of the coatings is an important parameter to evaluate. Adhesion of the coatings to the substrates was evaluated by a tape test. Figure 5 shows evolution of the SCA and CAH values through attachment-detachment cycles for the building material surfaces under study.

The obtained results showed that all the treated surfaces presented long-lasting mechanical properties. The superhydrophobic behavior was maintained in all the building materials under study during the 20 attachment-detachment cycles tested. Only small fluctuations in the SCA and CAH values were observed, and they can be related to measurement errors.

Finally, a durability test associated with rain resistance was performed (see Fig. 6). The obtained results did not show significant changes in the SCA values of the treated samples. In the case of the CAH values, a
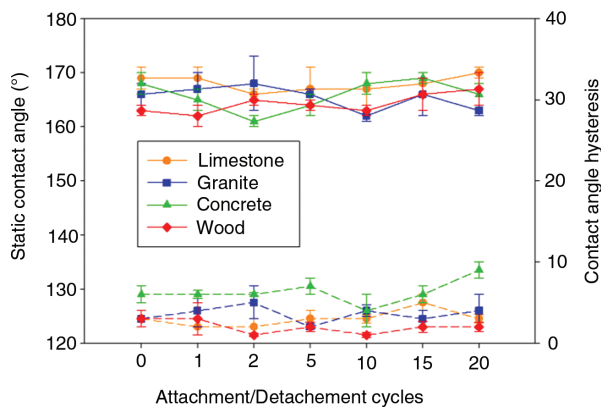
Fig. 5: Evolution of the SCA (solid lines) and CAH (dashed lines) values with the tape test for the surfaces under study.

slight increase can be observed in the surfaces, except for the granite samples. However, the hysteresis is always maintained below 5° (required value to maintain superhydrophobic properties). Thus, we can conclude that all the treated building materials present long-lasting performance against rain water, demonstrating its possible application for outdoor conditions.

The long-lasting properties presented by our coating can be explained as a consequence of its effective grafting to the four building materials evaluated, produced by condensation reactions between silanol groups (Si–OH) present in the fluoroalkylsilane, which allow it to polymerize and, moreover, to condense with Si–OH present in the SiO_2 NPs, giving rise to a durable nano-particulate coating [11, 22]. These silanol groups can condense with the silanol groups of the quartz minerals present in high and low proportion in the granite and the limestone, respectively. The Si–OH can also condense with the silanol groups of the concrete, and with the hydroxyl groups (OH) of the cellulose of wood. In addition, the high penetration of the product into the pore structure of the substrates (see Table 1) contributes significantly to improve the durability of the superhydrophobic materials because in case of removing the superficial coating, the product into the building material can preserve the superhydrophobic properties. Additionally, the polymerization inside the pore structure can take place between substrate and product in the case of the building materials containing hydroxyl groups (granite, concrete and wood). In the case of the limestone, the simple presence of the product inside the substrate can improve the durability.

In addition, the high resistance to rain water demonstrate the high stability of the obtained Cassie-Baxter regime. On a Cassie-Baxter surface the water droplets are placed on the top of roughness peaks, and air-pockets are created between water and solid surface [4]. However, if a critical pressure is reached, the water droplets eventually touch the roughness valleys [46] and thus, the surface can be transformed to a Wenzel regime
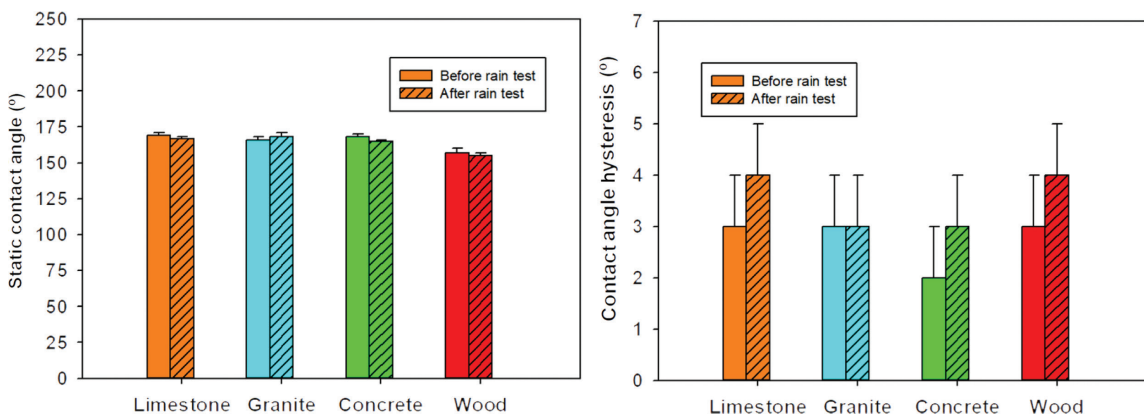

Fig. 6: SCA (left) and CAH (right) values of water droplets on the treated surfaces, before and after the rain test.

[47]. In this regime, the repellence properties are lost. In the specific resistance rain simulation (see Fig. 6) carried out in this work, repellence is maintained, confirming the high resistance of the coatings under study.

Conclusions

Superhydrophobic and oleophobic surfaces were created, by means of a simple procedure, on four common building materials employed in Cultural Heritage. The product, synthesized by an aqueous media sol–gel route, was able to decrease surface energy (by the action of alkyl fluorinated chains), giving rise to hydrophobic and oleophobic properties. In addition, the creation of Cassie-Baxter roughness by adding 40-nm SiO_2 NPs into the starting sol, gave rise to surfaces with repellence and self-cleaning properties.

The lasting properties of the coatings were tested by means of a mechanical test and a resistance to rain evaluation. All the building surfaces under study maintained superhydrophobic properties, demonstrating that an effective grafting between the substrates and the coating was achieved. In addition, we conclude that the suitable product penetration into the pores of the substrates is a critical parameter promoting durabilitiy.

Since this product can find application in Cultural Heritage, changes in color induced by the treatment were evaluated. A negligible change in color was observed for the four building materials under study. Future compatibility studies will be carried out in order to assure its correct application in the Cultural Heritage field.

References

[1]   L. Gao, T. J. McCarthy. *Langmuir* **25**, 14105 (2009).
[2]   W. Barthlott, C. Neinhuis, H. Verlot, C. L. Schott. *Planta* **202**, 1 (1997).
[3]   K. Koch, B. Bhushan, Y. C. Jung, W. Barthlott. *Soft Matter* **5**, 1386 (2009).
[4]   A. B. D. Cassie, S. Baxter. *Trans. Faraday Soc.* **40**, 546 (1944).
[5]   C. Kosak Söz, E. Yilgör, I. Yilgör. *Polym. (United Kingdom)* **62**, 118 (2015).
[6]   J. D. Rodrigues, A. Grossi. *J. Cult. Herit.* **8**, 32 (2007).
[7]   D. Öner, T. J. McCarthy. *Langmuir* **16**, 7777 (2000).
[8]   G. McHale, S. Aqil, N. J. Shirtcliffe, M. I. Newton, H. Y. Erbil. *Langmuir* **21**, 11053 (2005).
[9]   M. Hikita, K. Tanaka, T. Nakamura, T. Kajiyama, A. Takahara. *Langmuir* **21**, 7299 (2005).
[10] S. S. Latthe, H. Imai, V. Ganesan, A. Venkateswara Rao. *Microporous Mesoporous Mater.* **130**, 115 (2010).
[11] D. S. Facio, M. J. Mosquera. *ACS Appl. Mater. Interfaces* **5**, 7517 (2013).
[12] M. Callies, D. Quere. *Soft Matter* **1**, 55 (2005).
[13] B. P. Dyett, A. H. Wu, R. N. Lamb. *ACS Appl. Mater. Interfaces* **6**, 18380 (2014).
[14] A. Chatzigrigoriou, P. N. Manoudis, I. Karapanagiotis. *Macromol. Symp.* **331–332**, 158 (2013).
[15] J. MacMullen, J. Radulovic, Z. Zhang, H. N. Dhakal, L. Daniels, J. Elford, M. A. Leost, N. Bennett. *Constr. Build. Mater.* **49**, 93 (2013).
[16] P. Manoudis, S. Papadopoulou, I. Karapanagiotis, A. Tsakalof, I. Zuburtikudis, C. Panayiotou. *J. Phys. Conf. Ser.* **61**, 1361 (2007).
[17] P. N. Manoudis, I. Karapanagiotis, A. Tsakalof, I. Zuburtikudis, C. Panayiotou. *Langmuir* **24**, 11225 (2008).
[18] C.-H. Xue, S.-T. Jia, J. Zhang, J.-Z. Ma. *Sci. Technol. Adv. Mater.* **11**, 33002 (2010).
[19] D. Aslanidou, I. Karapanagiotis, C. Panayiotou. *Mater. Des.* **108**, 736 (2016).
[20] P. N. Manoudis, A. Tsakalof, I. Karapanagiotis, I. Zuburtikudis, C. Panayiotou. *Surf. Coatings Technol.* **203**, 1322 (2009).
[21] L. De Ferri, P. P. Lottici, A. Lorenzi, A. Montenero, E. Salvioli-Mariani. *J. Cult. Herit.* **12**, 356 (2011).
[22] L. A. M. Carrascosa, D. S. Facio, M. J. Mosquera. *Nanotechnology* **27**, 95604 (2016).
[23] M. J. Mosquera, D. M. de los Santos, T. Rivas, P. Sanmartín, B. Silva. *J. Nano Res.* **8**, 1 (2009).
[24] I. De Rosario, T. Rivas, G. Buceta, J. Feijoo, M. J. Mosquera. *Int. J. Archit. Herit.* **11**, 1166 (2017).
[25] I. De Rosario, F. Elhaddad, A. Pan, R. Benavides, T. Rivas, M. J. Mosquera. *Constr. Build. Mater.* **76**, 140 (2015).

[26] J. F. Illescas, M. J. Mosquera. *ACS Appl. Mater. Interfaces* **4**, 4259 (2012).

[27] D. S. Facio, M. Luna, M. J. Mosquera. *Microporous Mesoporous Mater.* **247**, 166 (2017).

[28] D. S. Facio, L. A. M. Carrascosa, M. J. Mosquera. *Nanotechnology* **28**, 265601 (2017).

[29] UNE-EN 12390-2. Testing hardened concrete. Part 2: making and curing specimens for strength tests, 2009.

[30] J. Y. Huang, S. H. Li, M. Z. Ge, L. N. Wang, T. L. Xing, G. Q. Chen, X. F. Liu, S. S. Al-Deyab, K. Q. Zhang, T. Chen, Y. K. Lai. *J. Mater. Chem. A* **3**, 2825 (2015).

[31] R. S. Berns. *Billmeyer and Saltzman's Principles of Color Technology*, 3rd ed., Jonh Wiley, New York, 2000.

[32] T. Sun, L. Feng, X. Gao, L. Jiang. *Acc. Chem. Res.* **38**, 644 (2005).

[33] B. Cortese, S. D'Amone, M. Manca, I. Viola, R. Cingolani, G. Gigli. *Langmuir* **24**, 2712 (2008).

[34] R. M. Wagterveld, C. W. J. Berendsen, S. Bouaidat, J. Jonsmann. *Langmuir* **22**, 10904 (2006).

[35] J. D. Brassard, D. K. Sarkar, J. Perron. *ACS Appl. Mater. Interfaces* **3**, 3583 (2011).

[36] J. Li, Y. Lu, Z. Wu, Y. Bao, R. Xiao, H. Yu, Y. Chen. *Ceram. Int.* **42**, 9621 (2016).

[37] S. Zhou, X. Ding, L. Wu. *Prog. Org. Coatings* **76**, 563 (2013).

[38] I. Alfieri, A. Lorenzi, L. Ranzenigo, L. Lazzarini, G. Predieri, P. P. Lottici. *Build. Environ.* **111**, 72 (2017).

[39] Y. Li, X. Men, X. Zhu, B. Ge, F. Chu, Z. Zhang. *J. Mater. Sci.* **51**, 2411 (2016).

[40] L. D. A. Chumpitaz, L. F. Coutinho, A. J. A. Meirelles. *J. Am. Oil Chem. Soc.* **76**, 379 (1999).

[41] R. A. Hayn, J. R. Owens, S. A. Boyer, R. S. McDonald, H. J. Lee. *J. Mater. Sci.* **46**, 2503 (2011).

[42] T. Darmanin, F. Guittard. *Mater. Today* **18**, 273 (2015).

[43] B. Bhushan, E. K. Her. *Langmuir* **26**, 8207 (2010).

[44] L. Xu, R. G. Karunakaran, J. Guo, S. Yang. *ACS Appl. Mater. Interfaces* **4**, 1118 (2012).

[45] H. Belanger, T. Darmanin, E. Taffin de Givenchy, F. Guittard. *Chem. Rev.* **114**, 2694 (2014).

[46] E. Bormashenko. *Adv. Colloid Interface Sci.* **222**, 92 (2015).

[47] R. N. Wenzel. *Ind. Eng. Chem.* **28**, 988 (1936).

Anexo II-Artículos ajenos a la Tesis

Modified Ethylsilicates as Efficient Innovative Consolidants for Sedimentary Rock

Monika Remzova [1,2], Luis A. M. Carrascosa [3], María J. Mosquera [3] and Jiri Rathousky [1,*]

[1]   J. Heyrovský Institute of Physical Chemistry of the CAS, Dolejskova 3, 18223 Prague, Czech Republic;
      monika.remzova@jh-inst.cas.cz
[2]   Department of Physical Chemistry, University of Chemistry and Technology Prague,
      16628 Prague, Czech Republic
[3]   TEP-243 Nanomaterials Group, Departamento de Química-Física, Facultad de Ciencias,
      Universidad de Cádiz, 11510 Puerto Real (Cádiz), Spain; luis.martinez@uca.es (L.A.M.C.);
      mariajesus.mosquera@uca.es (M.J.M.)
*   Correspondence: jiri.rathousky@jh-inst.cas.cz; Tel.: +420-26605-3945

Abstract: Although silicon alkoxides (especially ethylsilicates) have long been used as consolidants of weathered stone monuments, their physical properties are not ideal. In this study, an innovative procedure for the consolidation of sedimentary rocks was developed that combines the use of organometallic and alkylamine catalysts with the addition of well-defined nanoparticles exhibiting a narrow size distribution centered at ca. 10 nm. As a suitable test material, Pietra di Lecce limestone was selected because of its color and problematic physico-chemical properties, such as rather low hardness. Using the developed procedure, the mechanical and surface properties of the limestone were improved without the unwanted over-consolidation of the surface layers of the stone, and any significant deterioration in the pore size distribution, water vapor permeability, or the stone's appearance. The developed modified ethylsilicates penetrated deeper into the pore structure of the stone than the unmodified ones and increased the hardness of the treated material. The formed xerogels within the stone pores did not crack. Importantly, they did not significantly alter the natural characteristics of the stone.

Keywords: ethylsilicates; consolidation; nanoparticles; physico-chemical properties

1. Introduction

Historical stone artefacts are exposed to a wide range of outdoor conditions, including freeze-thaw cycles, humidity, irradiation, salt crystallization, and polluted air. As these weathering processes have a negative effect on the mechanical properties of stones, they must be conserved by suitable consolidants.

Alkoxides, especially ethylsilicates and their oligomers [1] are the most frequently used consolidants [2,3] but suffer from several major drawbacks. The syneresis and drying stress during the gelation process cause shrinkage and cracking of the formed xerogel, which reduces its mechanical strength [4]. Due to the presence of pores narrower than two nanometers, so-called micropores, within the consolidant xerogels, the capillary pressure, which is reciprocally proportional to the pore width according to the Young–Laplace equation, is very high [5]. The relatively brittle framework of the siliceous gel cannot resist such a high pressure and cracks. Furthermore, their physical properties, such as the hardness, porosity, and wettability, do not match those of the treated stone.

Because these drawbacks significantly reduce the performance of ethylsilicate consolidants, there has been a great deal of effort to overcome them. For example, gel shrinkage and cracking can be reduced by the formation of wider pores within the gels by suppressing the formation of micropores [6].

Using this approach, the addition of octylamine acting as a catalyst and probably also as a surface-active agent resulted in the formation of gels with an average pore size of approximately 10 nm [7]. Another approach involves improving the structural properties of xerogel by embedding nanoparticles. The modification of gels with nanoparticles has a substantial effect on the physico-chemical and especially mechanical [8] properties of stone. The incorporation of suitable metal oxide nanoparticles was shown to reduce the gel cracking [9]. The embedding of 10–20 nm nanoparticles increased the hardness and Young's modulus of sedimentary stones [10]. Moreover, consolidant xerogels with embedded nanoparticles more closely resemble the properties of natural stones than unmodified gels. Thus, by combining the above-described approaches, it might be possible to develop ethylsilicate consolidants with properties that better meet the requirements for the conservation and preservation of a specific type of stone than the standard ones.

In this study, we developed an innovative procedure for the consolidation of sedimentary rocks that combines the application of organometallic and alkylamine catalysts with the addition of well-defined nanoparticles exhibiting a narrow particle size distribution centered at ca. 10 nm. Using the developed procedure, the mechanical and surface properties of the selected sedimentary rock were improved without the unwanted over-consolidation of the surface layers of the stone, and any significant deterioration in pore size distribution, water vapor permeability, or the stone's appearance was avoided.

The Pietra di Lecce medium-fine grain limestone, selected for evaluating the effectiveness of the developed consolidant, has been a popular building material employed in the construction of historic monuments especially in the city of Lecce, which is therefore commonly nicknamed "The Florence of the South". The most important monuments, dating back to the Baroque era, are the Church of the Holy Cross (Basilica di Santa Croce) and the Lecce Cathedral (Duomo di Lecce).

This stone, already used as a substrate in numerous papers [10–13], shows a yellow-cream color, which enables to determine any changes in color easily. Regarding its composition, it is a Bioclastic limestone with a grain size distribution between 100 and 200 μm. The bioclasts are constituted prevalently by planctonic foraminifera and secondarily by shells. Rare are the quartz and feldspar grains. The binder is abundant and is constituted by microsparitic calcitic matrix. The macroporosity is relevant and due mainly to empty foraminifera chambers. Glauconite neoformation in form of tiny spherulae (80–100 μm) often filling the foraminifera chambers is frequent (5%). Its low hardness and high porosity (34% in total) are optimal for the consolidation and mechanical testing.

2. Materials and Methods

2.1. Materials

Following chemicals were used: Dynasylan®40 (Evonik, Essen, Germany, hereafter DYN40), hydroxyl-terminated polydimethylsiloxane (ABCR, Karlsruhe, Germany, hereafter PDMS), hydrophilic silica nanoparticles AEROSIL A200 (Evonik, hereafter A200), hydrophobic silica nanoparticles AEROSIL R805 (Evonik, hereafter R805), titania nanoparticles VP AEROPERL P25/20 (Evonik, hereafter VP), *n*-octylamine (Sigma-Aldrich, St. Louis, MO, USA), dioctyltin dilaurate (TIB Chemicals AG, Mannheim, Germany, hereafter DOTL), isopropanol (Sigma-Aldrich).

According to its technical data sheet, DYN40 is a mixture of monomeric and oligomeric ethoxysilanes, with an average chain length of approximately 5 Si–O units. PDMS has a polymerization degree of 12 with a molecular mass between 400 and 700, and an OH percentage ranging from 4 wt.% to 6 wt.%. A200 is a fumed silica with an average particle size of 12 nm and BET surface area of around 200 $m^2 \cdot g^{-1}$. R805 is a similar material, whose surface was treated with octylsilane to give it hydrophobic properties. VP is a micro-granulate with an average size of 20 μm, composed of TiO_2 NPs of around 20 nm in size.

2.2. Preparation of Consolidants

The sols were synthesized as follows:

- DYN40 was dissolved in isopropanol, in the presence of *n*-octylamine.
- Either PDMS, A200, R805, or VP was added.
- The sols were subjected to agitation in an ultrasonic bath for 30 min.

Alternatively, a sol containing the neutral catalyst DOTL instead of *n*-octylamine was prepared for comparative purposes. As most of the ethylsilicate consolidants in the market present a similar composition, this sample can be employed to compare the performance of the novel products with those available in the market.

All consolidants were prepared following the same procedure (an overview of their composition is given in Table 1).

Table 1. Composition of consolidant sols. DYN40 and isopropanol were mixed at 50 vol.%. The concentration of additives and catalysts is related to the volume of DYN40.

Sample	Additive	Additive Proportion	Catalyst	Catalyst Proportion
Dd	–	–	DOTL	1 vol.%
Do	–	–	*n*-octylamine	0.18 vol.%
DoP	PDMS	5 vol.%	*n*-octylamine	0.18 vol.%
DoA	A200	3 wt.%	*n*-octylamine	0.18 vol.%
DoR	R805	3 wt.%	*n*-octylamine	0.18 vol.%
DoV	VP	3 wt.%	*n*-octylamine	0.18 vol.%

2.3. Characterization of Sols and Xerogels

Immediately after being prepared, the rheological properties of the sols were determined using a Brookfield concentric cylinder viscosimeter (model DV-II+ with UL/Y adapter, Middleboro, MA, USA), the experiments being performed at a constant temperature of 25 °C. The test was performed in dynamic mode at a maximum of 60 rpm. The diameter of the spindle was 25 mm.

The size distribution of nanoparticles in the sols was determined using dynamic light scattering (DLS) carried out on a Malvern Zetasizer Nano ZS instrument (Malvern Instruments, Worcestershire, UK).

A morphological study of the sols was carried out by transmission electron microscopy using a JEOL 2010F TEM/STEM microscope (JEOL, Ltd., Tokyo, Japan), equipped with a JEOL high angle annular dark field (HAADF) detector, enabling the acquisition of STEM images.

In order to study the sol-gel transition, the sols were cast on Petri dishes. Gelation occurred spontaneously, and the gels were left to dry until xerogels were obtained.

Textural properties of the xerogels were determined by the analysis of adsorption isotherms of nitrogen at its boiling point (ca. 77 K) using a Micromeritics 3FLEX apparatus (Norcross, GA, USA). The pore width was described using the IUPAC nomenclature, namely micropores, mesopores, and macropores correspond to the width of less than 2 nm, 2–50 nm, and more than 50 nm, respectively.

Fourier transform infrared spectra (FTIR) in attenuated total reflection (ATR) mode were recorded for the xerogel powders using a Schimadzu FTIR-8400 spectrophotometer (Shimadzu Corp., Kyoto, Japan) in the region of 4000–650 cm^{-1} (resolution of 4 cm^{-1}). The samples were in contact with the zinc selenide (ZnSe) ATR crystal and the average of 64 scans was obtained for each.

2.4. Application on Stone and Evaluation of the Performance

The sols were sprayed for five seconds onto the 5 cm × 5 cm × 5 cm cubes of the Lecce stone using a pressure of 2×10^5 Pa. The spraying was repeated five times for each sample. Typically, 2.5 g of the sol was applied on the upper surface of the stone cube. With respect to application on larger area surfaces, the spray technique possesses substantial advantages in comparison with brushing or immersion.

Similar products have been previously applied on pure limestones [14]. The results obtained demonstrate adequate compatibility and adherence to the limestone, producing long-term effectiveness, homogeneity, and continuousness of the coating with a suitable depth of penetration. This compatibility can be explained in terms of the presence of effective interactions between *n*-octylamine integrated in the product and the carbonate substrate.

2.4.1. Stone–Product Interaction

The samples were weighed before and immediately after the application of the consolidant to calculate the uptake. In addition, they were re-weighed after complete drying (1 month after the consolidant application) to calculate the dry mass. All the experiments to determine the effectiveness of the products on the stone were carried out 1 month after the consolidant application.

Its penetration into the pore structure of the stone was determined by cutting the stones into thin slabs and dropping water on the cross-section. Dry and wet zones were observed, the latter corresponding to the depth of penetration.

The topography of the untreated and treated samples was studied by scanning electron microscopy, using a JEOL JSM-6510lv microscope.

2.4.2. Effectiveness of the Products on the Stone

The enhancement of the mechanical properties due to consolidation was analyzed by several techniques. A Drilling Resistant Measuring System (DRMS, from SINT Technology, Calenzano, Italy) was employed to test the effectiveness of the consolidation, with respect to the untreated sample. Drill bits of 4.8 mm diameter were used with a rotation speed of 200 rpm and penetration rate of 10 mm/min. Nine drillings were performed in three stone samples for each treatment.

By a peeling test [15], the increase in cohesion between the grains of the stone due to the treatment was determined. Furthermore, the adherence of the applied consolidant to the surface of the stone was measured by this method, which is determinant for the treatment durability. The test was carried out by attaching and detaching a Scotch® Magic™ Tape (3M, Maplewood, MN, USA). The process was repeated three times, the mass of material removed was determined by weighing.

Finally, the Vickers hardness test was performed using a Universal Centaur RB-2/200 hardness tester (Innovatest Europe BV Manufacturing, Maastricht, The Netherlands). The loading was 30 kg during 30 s, with a preloaded time of 15 s. For each sample, nine measurements were carried out.

The wettability of the untreated and treated samples was evaluated by measuring static and dynamic (advancing and receding) contact angles of water droplets, according to the procedure published in [16,17]. The water absorption by capillarity (WAC) was measured according to UNE-EN 1925:1999 [18]. After finishing the WAC test, the samples were dried at 60 °C for 24 h. Afterwards, the static and dynamic contact angles were measured again, in order to test the resistance of the treatments to a long-term contact with water.

2.4.3. Negative Effects Induced by the Applied Products

Water vapor permeability was determined using an automatic setup developed at the laboratory of the University of Cadiz Nanomaterials Group [19] based on the standard cup test (in accordance with a ASTM E96-90:1990 [20]) in 4 cm × 4 cm × 1 cm slabs. After drying at 60 °C until constant weight, the samples were placed as a cover over the cup, in which moisture saturated at ambient conditions (RH 98%) was maintained. The specimen cup perimeters were sealed with a silicone paste. The climatic chamber was maintained at 23 °C. At the start of tests, low relative humidity was achieved in the chamber by means of a desiccating agent (silica gel). Under these conditions, the humidity gradient across the specimen promoted water vapor flux. The monitoring of the cup mass decrease permitted the progress of vapor transport to be determined, with the temperature and relative humidity in the chamber being registered during the tests. After an initial increase, the relative humidity in the climatic chamber was stabilized at around 35%.

The changes in color were evaluated using a solid reflection spectrophotometer, Colorflex model, from Hunterlab (Reston, VA, USA), calibrated to a white tile standard surface, using Illuminant D65 and observer CIE 10°. Color variations in the CIE *L*a*b** color scale were evaluated using the total color difference (Δ*E**) [21]. Five measurements per sample were carried out.

3. Results and Discussion

The former part of this section is devoted to a detailed study into the properties of consolidant sols and xerogels obtained from these sols. The latter part deals with the performance of the sols as consolidants of the Pietra di Lecce limestone with a special attention devoted to the assessment of their suitability for the conservation praxis.

3.1. Characterization of the Consolidants

Immediately after being synthesized, the rheological properties of the sols were investigated. Shear stress vs. shear rate curves showed a Newtonian behavior (the regression linear coefficient higher than 0.99). The viscosities of the individual sols calculated from the slope of the curves are shown in Table 2.

Table 2. Properties of sols and gels.

Consolidant	Viscosity (mPa·s)	Gel Time (h)	Appearance	Stability (month)
Dd	2.75	60	Cracked	>18
Do	2.99	48	Monolithic	>18
DoP	3.59	48	Monolithic	=12
DoA	4.64	48	Monolithic	>18
DoR	4.41	48	Monolithic	>18
DoV	3.23	48	Phase separation	>18

All the sols presented viscosities lower than 5 mPa·s (value for DYN40). This is obviously due to the dissolution in isopropanol. Thus, all the sols are suitable for application on building materials. Previous papers used similar sols without solvents because the viscosity of the sols is enough low (around 5 mPa·s) to assure the product penetration [22]. In this case, we diluted the sol in isopropanol (50%) in order to obtain: (i) better penetration into the porous system in the stone; (ii) suppression of the over consolidation of the stone; (iii) faster hydrolysis due to miscibility of TEOS, water, and isopropanol.

The lowest viscosities were measured for the sols without additives (Dd and Do). They presented similar values, being slightly higher for Do. The addition of PDMS (DoP) increased the viscosity due to the starting co-condensation of PDMS and DYN40, as discussed in previous papers [21,22]. For sols containing NPs, the increase in the viscosity is explained by the presence of a particulate solid. As expected, the sols with the smaller NPs (DoA and DoR) showed the highest viscosities because their high specific surface area (about 200 $m^2 \cdot g^{-1}$) promoted a more extensive aggregation comparing to the product with titania NPs (DoV), whose surface area is around 50 $m^2 \cdot g^{-1}$.

Particle size distributions of the sols without and with added SiO_2 and TiO_2 nanoparticles measured by DLS are shown in Figure 1. Sols without added nanoparticles (i.e., Dd, Do, DoP) are characterized by the particle sizes in the range 1–10 nm together with some proportion of larger ones 0.1–1 μm in size (maybe dust particles). The nanoparticle-containing sols are characterized by much larger particles 0.06–6 μm in size, which are clearly agglomerates of the primary nanoparticles. The degree of agglomeration seems to depend on the nature of particles added. DoR and DoV exhibit similar particle size distributions in the range from 1 to 2 μm. They do not practically contain any substantially smaller particles. The particle size distribution of DoA containing hydrophilic silica NPs markedly differs, being characterized by a very broad range of particle size from 70 nm to several micrometers. Three distinct maxima were observed for this sample, centered at about 120, 500, and 5000 nm.
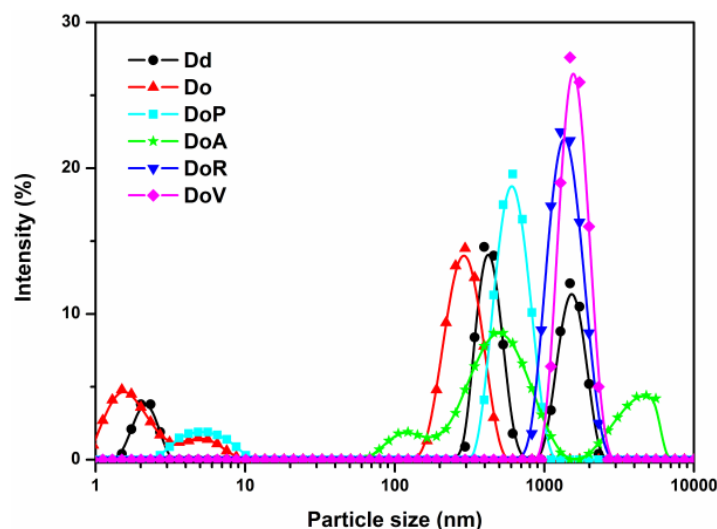
Figure 1. The particle size distribution of the sols.

The TEM image of DoR, Figure 2, containing octylated nanoparticles, clearly shows the presence of these nanoparticles which are less than 10 nm in size and exhibit a higher electron density than the sol-gel material around them, which is in accordance with previous works [16,23]. These small nanoparticles are bound into irregularly shaped agglomerates. Generally, the data obtained by DLS and TEM are difficult to compare as the samples change in time and are exposed to different conditions—in sol for DLS and in solid state after the vaporization of the solvent for TEM.
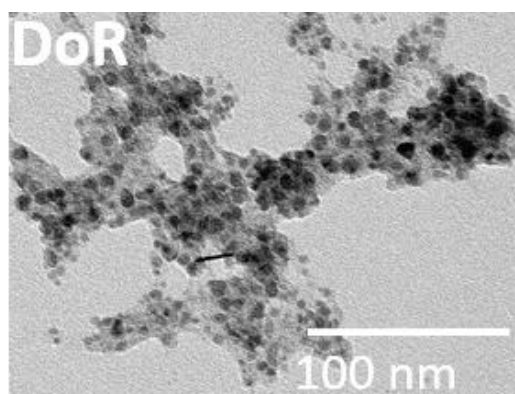
Figure 2. TEM image of the DoR sample.

In order to compare the chemical bonds formed, the sols and powders were analyzed by ATR FTIR spectroscopy [24,25] (Figure 3a,b). As the materials are chemically the same, the sols (Figure 3a) show similar spectra. Owing to the presence of alkyl groups either bonded to the siloxane skeleton or in the solvent, a number of bands were observed (designated as B, C, D, E, H). In the range from 3000 to 2800 cm^{-1}, three bands (B) correspond to the stretching of carbon–hydrogen (C–H) bonds of alkyl chains [26]. The bands in the range from 1480 to 1385 cm^{-1} (C) are due to the stretching of carbon–hydrogen (C–H) bonds of the alkyl chain, i.e., in the $-CH_3$ and $-CH_2-$ groups. Band at 1162 cm^{-1} (E) corresponds to $CH_3-(C)$, those at 1255 and 850 cm^{-1} (D1 and D2) to $-CH_3$ bending and rocking in $-Si(CH_3)_3$, which is the end group of the PDMS chain. The band at 889 cm^{-1} (H) is due to the deformation of CH_3 and CH_2 groups of the isopropanol molecule.
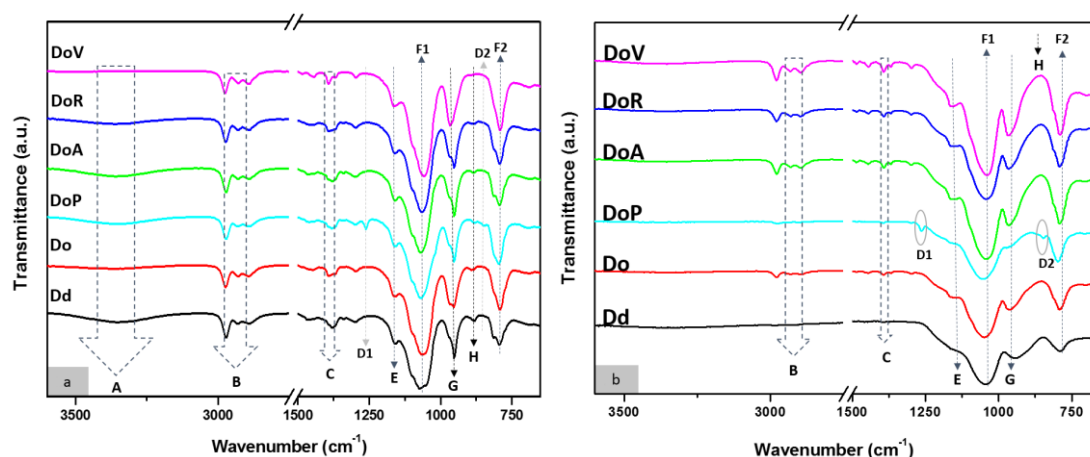
Figure 3. FTIR spectra of sols (**a**) and powders (**b**) of ethylsilicate consolidants with and without particles.

Bands at 1045 and 795 cm^{-1} (F) are associated with the growing siloxane skeleton and the creation of a high molecular weight silica polymer [27]. The band (G) is assigned to the Si–OH stretching vibration in the wet gel. FTIR spectrum also shows a peak with low intensity at around 3000–3700 cm^{-1} (A) attributed to the stretching mode of surface silanols (Si–OH), which can provide hydrophilic capability for water absorption due to the formation of hydrogen bridges.

All the products showed high stability over the period of more than 18 months, with the exception of DoP that gelled in a closed vessel after 12 months. Such storage time is sufficient from the point of view of practical application of these consolidants.

The gel time for the sols casted on a Petri dish and exposed to laboratory conditions are shown in Table 2. Generally, a faster gelation was found if octylamine was used as a catalyst, in comparison with DOTL, which is due to the stronger basicity of the amine. No effect of the addition of nanoparticles or PDMS was observed. The longer gel time is convenient from the application point of view as the consolidant products need to penetrate into the pore structure of the stone. Regarding the appearance of the obtained xerogels, that containing DOTL (Dd) as catalyst was completely cracked, whereas those with *n*-octylamine were monolithic. However, in the case of DoV, a phase separation due to the precipitation of the titania NPs was observed.

The FTIR spectra of xerogels after three months showed some changes in comparison with corresponding sols due to the hydrolysis of ethoxy group and the growth of the siloxane chain (Figure 3). Less significant features were the formation of pores within the gel. The formation of a high molecular weight silica polymer is proved by the intensity of bands at 1045–1162 cm^{-1} (E, F1) and 795 cm^{-1} (F2) [27]. The decrease in the isopropanol concentration due to evaporation is apparent from the gradual disappearance of the band at 889 cm^{-1} (H). Generally, the differences between individual samples are less marked, being connected especially with the different rate of hydrolysis depending on the catalyst used and the presence of particles-bands B because the remaining ethoxy groups are much more pronounced for amine-catalyzed samples and those with embedded particles.

Texture parameters of xerogels were obtained by the analysis of nitrogen sorption isotherms (Figure 4). The isotherm on sample Dd, prepared using DODTL as a catalyst, rises sharply at low relative pressures and reaches a plateau at the relative pressure approaching 1. It belongs to the Type I according to the IUPAC classification [28], which corresponds to microporous materials. All the xerogels prepared with *n*-octylamine exhibit the Type IV isotherms, corresponding to mesoporous materials. For these samples, the hysteresis loops associated with capillary condensation are of the Type H2 common with inorganic oxide gels. The pore structures of these materials are complex made up of interconnected networks of pores of different size and shape [28]. The gel containing titania NPs is also mesoporous, its BET surface area and pore volume being much smaller than those of other materials.
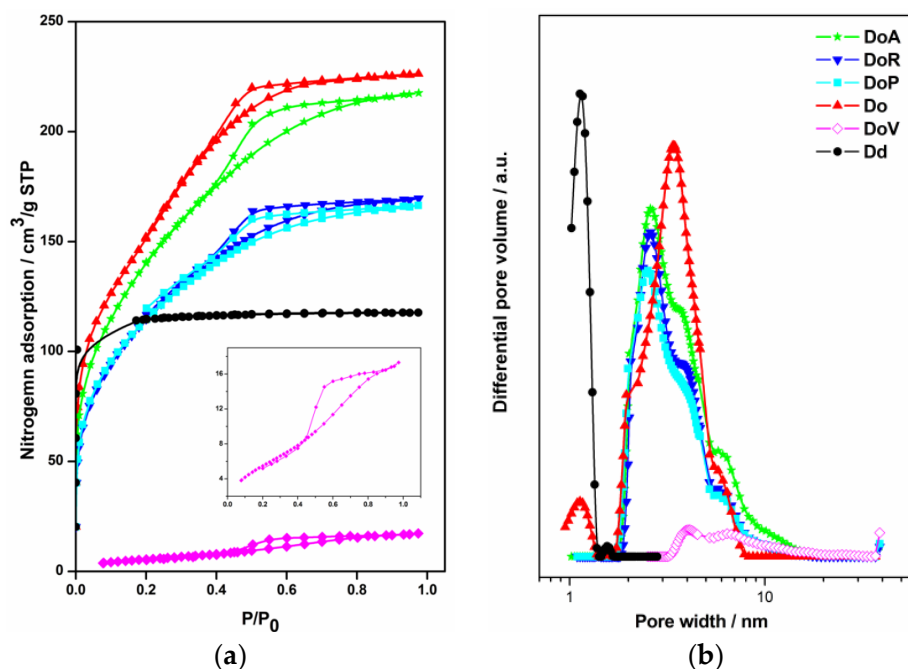
Figure 4. Adsorption-desorption isotherms for xerogels (**a**) and the corresponding pore size distributions (**b**) obtained by the NLDFT method.

The pore size distribution of the xerogels was obtained by the Non-Local Density Functional Theory (NLDFT) method (Figure 4b, Table 3). The pore size distribution for the sample Dd is centered at about 1 nm, which is in agreement with its microporous nature. All xerogels synthesized with *n*-octylamine show pores in the mesoporous range. The samples DoP, DoA, and DoR exhibit similar pore size distributions centered at 2.4 nm with a saddle at 3.2 nm. The sample Do exhibits uniform pore size distribution with a maximum at 3.2 nm. Finally, the pores of the DoV sample with a much smaller surface area and pore volume are larger with maxima at 3.5 and about 7 nm.

Table 3. Texture parameters of xerogels.

Consolidant	Micropore Volume $(cm^3 \cdot g^{-1})$	Mesopore Volume $(cm^3 \cdot g^{-1})$	BET Surface Area $(m^2 \cdot g^{-1})$	Pore Width (nm)	Total Porosity (%) **
Dd	0.15	0.00	1.6 *	0.8	25
Do	0.00	0.35	555.0	3.2	43
DoP	0.00	0.26	414.0	2.4	37
DoA	0.00	0.34	514.0	2.4	45
DoR	0.00	0.26	420.0	2.4	37
DoV	0.00	0.04	32.0	3.5	8

* External surface area; ** calculated from the nitrogen sorption data.

The consistency of the physical properties of xerogels and their structures was tested using correlations developed by Fildalco and Ilharko [29]. Using such a correlation, the percentage of $(SiO)_6$ fold siloxane rings of 10%–12% was assessed for the porosity in the range of 25%–47% (Table 3). From another correlation in [29], it follows that the pore size of xerogels containing 10%–12% of $(SiO)_6$ fold siloxane rings should be in the range of 2.0–2.3 nm, which is in reasonable agreement with the texture data of xerogels given in Table 3. Authors of [29] suggested that hydrophobicity also should depend on the percentages on the siloxane rings. As the percentages of these rings in our samples are similar in a narrow range, a similar range of hydrophobicity should also be expected. The data presented in Table 4 confirm this conclusion as the contact angle for water lies in a narrow range between 120° and 140°.

Table 4. A summary of performance of ethylsilicate consolidants.

Sample	Peeling Test* (mg)	Vickers Hardness Test (kP/mm^2)	ΔE *	Static Angle (°)	Vap. Diffusivity ($\times 10^{-6}$) (m$^2 \cdot$s^{-1})	Porosity (%)	Static Angle after WAC Experiment (°)
Untreated	0.9 ± 0.4	15.41 ± 1.76	–	nd	3.13	37.2	nd
Dd	0	17.5 ± 3.71	3.75 ± 1.05	0	2.71	37.1	nd
Do	0.1 ± 0.1	18.91 ± 1.91	4.68 ± 1.2	140 ± 1	2.78	40.8	nd
DoP	0	19.43 ± 2.53	7.59 ± 0.34	149 ± 6	2.46	42.4	135 ± 5
DoA	0.6 ± 0.1	19.10 ± 2.93	4.74 ± 0.14	144 ± 3	3.05	47.6	125 ± 9
DoR	0.1 ± 0.1	18.44 ± 5.61	5.79 ± 0.42	129 ± 5	3.01	40.5	113 ± 13
DoV	0	17.06 ± 2.74	4.39 ± 0.58	120 ± 5	3.11	43.4	108 ± 8

* Mass of the removed material; nd, the contact angle could not be measured because of a fast soaking of the water drop.

3.2. Application on Stone and Evaluation of the Performance

3.2.1. Stone–Product Interaction

Table 5 shows the uptake, dry-mass, and penetration depth of the products applied on the stone samples. Both uptake and penetration depth depended on the viscosity of the applied sols (Table 2). Do (viscosity 2.99 mPa·s) presented the highest penetration depth (12.5 mm) and uptake (2 wt.%). For the rest of samples, the uptake and penetration are lower because of their higher viscosity. For Dd, the penetration depth could not be measured because of disintegration of the consolidant xerogel in the stone pores (Table 2), which does not allow to identify the two different zones in the cross-section. The evaluation of dry-mass showed values significantly lower than those obtained for uptake due to evaporation of the solvent and hydrolysis of the ethoxy groups. In the case of the samples treated with DoP, this decrease was lower because PDMS does not contain hydrolysable groups.

Table 5. Uptake and depth of penetration of the applied consolidants.

Sample	Uptake (%)	Dry-Matter (%)	Penetration Depth (mm)
Dd	1.0 ± 0.2	0.6 ± 0.1	–
Do	2.2 ± 0.3	1.3 ± 0.2	12.5 ± 1.3
DoP	1.2 ± 0.1	0.8 ± 0.1	9.1 ± 0.9
DoA	1.1 ± 0.1	0.8 ± 0.1	5.4 ± 1.3
DoR	1.2 ± 0.3	0.8 ± 0.2	4.1 ± 0.7
DoV	1.4 ± 0.1	0.9 ± 0.1	8.4 ± 1.5

To investigate the changes in the topography of the stones caused by the consolidation, SEM images were acquired (Figure 5). The untreated sample is mainly composed of grains (Figure 5a). While the surface coated with Dd (Figure 5b) showed cracks, the treatment with Do lead to a crack-free smooth layer covering the surface (Figure 5c). This is due to the formation of a mesoporous material (see the physisorption data, Figure 4 and Table 3), as explained in our previous works [10,19]. Owing to the additives, the roughness of the surface increased. For DoP (Figure 5), this roughness is due to the shrinkage of the xerogel during the drying, because of its high flexibility [24]. For nanoparticle-containing coatings, the roughness is clearly due to the presence of NPs in the composition. The appearances of DoA- and DoR-coated materials (Figure 5e,f, respectively) were similar, since the A200 and R805 nanoparticles had the same size. In the case of DoV, greater aggregates were observed due to the larger VP nanoparticles.

3.2.2. Effectiveness of the Products on Stone

From Figure 6 it is apparent that the untreated sample showed a very low resistance to drilling, which was more or less increased by all the treatments. According to [30], the penetration depth of consolidants should be above 5 mm. In our case, all the products show penetration over 5 mm. For Dd the increase within the first five millimeters was roughly 100%, deeper however practically negligible. This is due to the cracking of the xerogel for sample Dd inside the stone, as seen in the SEM images (Figure 5b).
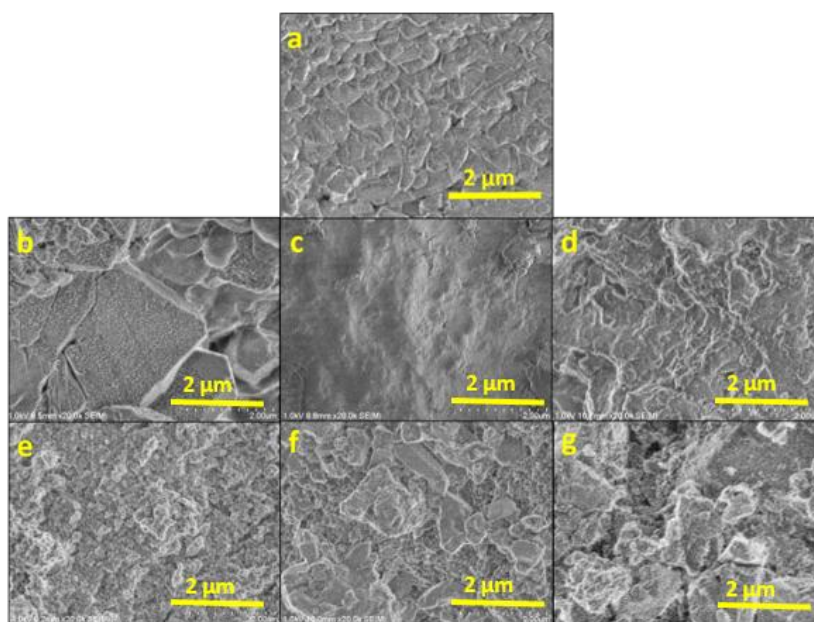
Figure 5. SEM images of the surfaces of the untreated stones and their treated counterparts: (**a**) Untreated, (**b**) Dd, (**c**) Do, (**d**) DoP, (**e**) DoA, (**f**) DoR, (**g**) DoV.
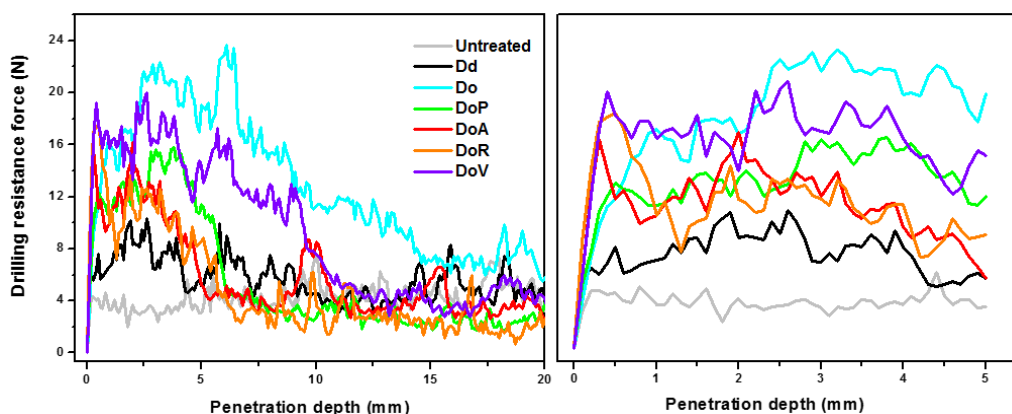

Figure 6. DRMS results for the untreated and treated samples.

On the contrary, all the amine catalyzed consolidant sols lead to a more substantial increase in the resistance force and the results are in good agreement with the observed penetration depth (Table 5) and the uptake of the consolidants. For DoP, there was marked increase (up to 200%) within the first 5 mm, in greater depth practically negligible. This is due to the lower penetration of this consolidant because of its higher viscosity. Moreover, the incorporation of PDMS in the xerogel network promotes the change from quaternary siloxane bonds (from DYN40) to a mixture of quaternary and binary (from PDMS) siloxane bonds [15,30], which provide more flexibility to the silica network, allowing the xerogel to shrink.

The highest degree of consolidation among the samples tested was achieved for Do and the increase in resistance persevered even to the depth of 20 mm. Regarding the particle-modified consolidants, the most promising performance was found for DoV doped with titania particles. For this sample, the range of substantial increase in resistance was wider, up to the depth of 10 mm. This sample was only slightly weaker than the leading Do.

The application of DoA- and DoR-doped consolidants caused the lowest increase in the mechanical properties, among the products catalyzed with *n*-octylamine. This is because of two reasons: the lower penetration depth due to their higher viscosity compared with the rest of products, and the very small

size of both NPs (around 12 nm), which are not able to form big aggregates with DYN40, oppositely to the titania NPs (see SEM, Figure 5).

Alternatively to the DRMS experiments, the determination of the Vickers hardness was performed (Table 4). The obtained data are in a reasonable agreement with the DRMS experiments. While the untreated sample of Lecce stone exhibited a hardness of 15.41 ± 1.76 kP/mm^2, the treatment with octyl amine catalyzed consolidant let to an increase to 18.91 ± 1.91 kP/mm^2. The stones treated with nanoparticle modified consolidants exhibited even higher hardness, such as 19.10 ± 2.93 kP/mm^2 for DoA.

Table 4 shows also the results obtained from the peeling tests. The results demonstrate that all the treatments decrease the amount of material removed by the adhesive tape, confirming the consolidation ability. With the exception of DoA, with all the other consolidants the mass of removed stone fragments was practically negligible. With the sample DoA the cohesion of the surface layers was only slightly better than that of the untreated stone.

Concerning the wettability of the treated samples, Table 4 shows that the contact angle for water substantially increased due to the consolidation, while the untreated stone exhibited a very fast soaking of water.

Actually, such high hydrophobicity was to be expected only for samples containing a hydrophobic component (i.e., DoP and DoR). Clearly, the non-hydrolyzed ethoxy groups from DYN40 fundamentally influenced the wetting properties of the consolidated stones. As these groups decrease the surface energy, they have a hydrophobic effect and function as the hydrophobic components themselves. The hydrophobicity of the Lecce stone is clearly enhanced due to its surface roughness according to the Wenzel model. For DoV, the contact angle is slightly lower than for other particle-modified samples, probably due to the hydrophilic nature of titania particles.

In previous papers from our group [16,17], the addition of the SiO$_2$ nanoparticles to a hydrophobic material increased its hydrophobic performance and promoted water repellence properties due to the creation of a novel roughness on the treated surface. However, in the present study, this effect is negligible as the product is applied to stones with high roughness [25].

The water absorption by capillarity (WAC) is presented in Figure 7. For the untreated stone, the inset shows a very fast increase in the mass of the absorbed water within the first hour, followed by a practically horizontal plateau. For the comparative sample Dd, the mass of absorbed water is only slightly lower because of substantial disintegration of the consolidant xerogels in the stone pores (Figure 5b). However, for consolidants catalyzed by octylamine, the water absorption is drastically reduced, practically by two orders of magnitude. The products with PDMS or R805 (DoP or DoR) are the most effective in decreasing water absorption, confirming their hydrophobic properties. For the stone treated with the consolidant Dd, the decrease in water absorption by capillarity was only about 7%, but for all the samples treated with the novel consolidants it reached 98%–99%.

Finally, the contact angles were measured again after the WAC test, in order to determine the degree of the hydrolysis of surface ethoxy-groups due to a long contact time with water (Table 4). A complete loss of the hydrophobicity was found for both Dd and Do samples, i.e., for those without any dopant. These two samples exhibited a rapid absorption of the water droplets. This is due to the hydrolysis of the ethoxy groups to hydroxyls during the contact with water. DoP and DoR do not show significant variation in contact angles, demonstrating that the hydrophobic behavior of these products is due to the action of PDMS [31,32] or R805 NPs, respectively, reducing the surface energy.

As DoA and DoV do not have any low surface energy component added, their hydrophobic behavior is due to the presence of non-hydrolyzed ethoxy groups. Actually, after long-contact with water, these groups should be hydrolyzed as for Do. This contradictory observation can be explained according to Wang et al. [33]. These authors prepared superhydrophobic coatings on glass controlling the ratio of hydrolysable (ethoxy) and pre-hydrolyzed (hydroxyl) groups. The surfaces were placed under a water rain column for 2 h, and the static contact angle was measured before and after the test. Results showed a lower decrease in the contact angle for the surfaces with higher proportion

of hydroxyl groups. XPS spectra demonstrated that water preferably attacks OH groups (due to its affinity) rather than ethoxy groups. Thus, hydroxyl groups protect ethoxy groups from being hydrolyzed. In our case, both DoA and DoV have hydroxyl groups (from silica or titania NPs, respectively), which interact with water, preventing the hydrolysis of the remaining ethoxy groups from DYN40.

There is some change in color due to the consolidation (Table 4). Depending on the catalysts used, a slightly greater change was observed for octylamine in the comparison with DOTDL, both being within the limits of the generally acceptable color changes. Also, for particle-modified consolidants, the change was within the limits of acceptability. The most significant change was observed for DoP, i.e., for the consolidant with added PDMS. As the change in color was outside the acceptance limits, there is a need for caution when applying this type of consolidant.
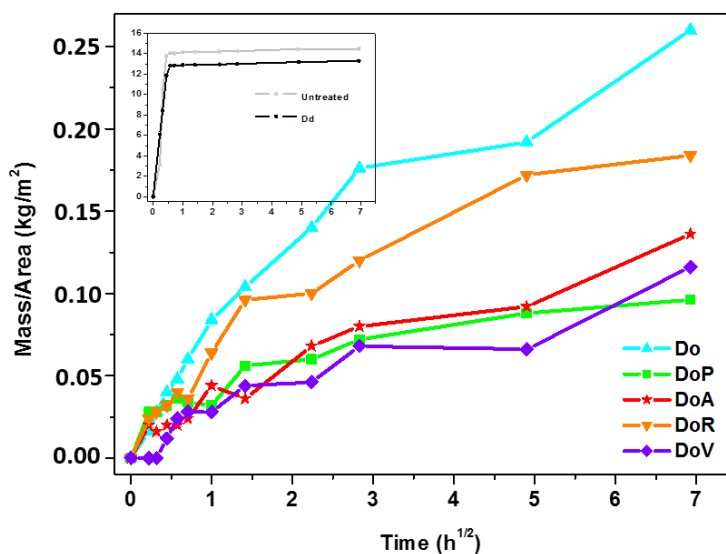
Figure 7. Water absorption by capillarity for stone samples treated with consolidants.

4. Conclusions

To sum up, the systematic study has shown that the effect of the catalyst selected and the nanoparticles or PDMS used as additives on the properties of ethylsilicate consolidants is rather complex, which enables a fine tuning of their performance. Especially the character of the formed porosity with the closely related xerogel cracking depends on the catalyst used and the presence and surface properties of nanoparticles, which also influence the rate of gelation. It is a major advantage of using octylamine as catalysts that the treated stone exhibits a smooth surface without cracks.

Another important functional property, namely the depth of the consolidation, is beneficially influenced by the use of octylamine as a catalyst instead of organometallic compounds, which are most commonly used. Interestingly, the performance concerning the depth of penetration of the consolidant with TiO_2 nanoparticles added is very similar to the undoped one. As these particles additionally suppress the cracking and provide a consolidant with photocatalytic functionality, this type of consolidant is definitely a promising choice for a range of applications.

The wettability and water absorption by capillarity of the treated stones depend on catalysts used as well as on the character of nanoparticles used as a dopant. As this property may be desirable, the method developed in this study provides an efficient way to control it.

Finally, because our modified ethylsilicate consolidants are based on inorganic compounds, they do not significantly alter the natural characteristics of the treated stone, which is very promising for the application in the conservation praxis. To determine the applicability of the developed consolidants, a study into their performance on various types of weathered stones is in progress, including testing the durability of the consolidation treatment by artificial accelerated weathering.

Conflicts of Interest: The authors declare no conflict of interest.

References

1. Wheeler, G.; Goins, E.S. *Alkoxysilanes and the Consolidation of Stone*; The Getty Conservation Institute: Los Angeles, CA, USA, 2005; Volume 46.
2. Xu, F.; Zeng, W.; Li, D. Recent advance in alkoxysilane-based consolidants for stone. *Prog. Org. Coat.* **2019**, *127*, 45–54. [CrossRef]
3. Doehne, E.F.; Price, C.A. *Stone Conservation: An Overview of Current Research*, 2nd ed.; The Getty Conservation institute: Los Angeles, CA, USA, 2010.
4. Scherer, G.W. Effect of drying on properties of silica gel. *J. Non-Cryst. Solids* **1997**, *215*, 155–168. [CrossRef]
5. Scherer, G.W. Influence of viscoelasticity and permeability on the stress response of silica gel. *Langmuir* **1996**, *12*, 1109–1116. [CrossRef]
6. Mosquera, M.J.; De Los Santos, D.M.; Montes, A.; Valdez-Castro, L. New nanomaterials for consolidating stone. *Langmuir* **2008**, *24*, 2772–2778. [CrossRef] [PubMed]
7. Mosquera, M.J.; de los Santos, D.M.; Valdez-Castro, L.; Esquivias, L. New route for producing crack-free xerogels: Obtaining uniform pore size. *J. Non-Cryst. Solids* **2008**, *354*, 645–650. [CrossRef]
8. Miliani, C.; Velo-Simpson, M.L.; Scherer, G.W. Particle-modified consolidants: A study on the effect of particles on sol–gel properties and consolidation effectiveness. *J. Cult. Herit.* **2007**, *8*, 1–6. [CrossRef]
9. Xu, F.; Li, D.; Zhang, Q.; Zhang, H.; Xu, J. Effects of addition of colloidal silica particles on TEOS-based stone protection using *n*-octylamine as a catalyst. *Prog. Org. Coat.* **2012**, *75*, 429–434. [CrossRef]
10. Remzova, M.; Sasek, P.; Frankeova, D.; Slizkova, Z.; Rathousky, J. Effect of modified ethylsilicate consolidants on the mechanical properties of sandstone. *Constr. Build. Mater.* **2016**, *112*, 674–681. [CrossRef]
11. Rodrigues, J.D.; Pinto, A.P.F. Laboratory and onsite study of barium hydroxide as a consolidant for high porosity limestones. *J. Cult. Herit.* **2016**, *19*, 467–476. [CrossRef]
12. Muhyodin, G.; Zhu, X.; Abro, M.; Yasin, G.; Maitlo, I.; Akaram, M.Y.; Nie, J. Preparation and characteristics of self-floating silica. *Prog. Org. Coat.* **2018**, *117*, 1–6. [CrossRef]
13. Pia, G.; Corcione, C.E.; Striani, R.; Casnedi, L.; Sanna, U. Thermal conductivity of porous stones treated with UV light-cured hybrid organic–inorganic methacrylic-based coating. Experimental and fractal modeling procedure. *Prog. Org. Coat.* **2016**, *94*, 105–115. [CrossRef]
14. Elhaddad, F.; Carrascosa, L.A.; Mosquera, M.J. Long-term effectiveness, under a mountain environment, of a novel conservation nanomaterial applied on limestone from a roman archaeological site. *Materials* **2018**, *11*, 694. [CrossRef] [PubMed]
15. Drdácký, M.; Lesák, J.; Niedoba, K.; Valach, J. Peeling tests for assessing the cohesion and consolidation characteristics of mortar and render surfaces. *Mater. Struct.* **2015**, *48*, 1947–1963. [CrossRef]
16. Facio, D.S.; Mosquera, M.J. Simple strategy for producing superhydrophobic nanocomposite coatings in situ on a building substrate. *ACS Appl. Mater. Interfaces* **2013**, *5*, 7517–7526. [CrossRef]
17. Carrascosa, L.A.; Facio, D.S.; Mosquera, M.J. Producing superhydrophobic roof tiles. *Nanotechnology* **2016**, *27*, 095604. [CrossRef] [PubMed]
18. *UNE-EN 1925 Natural Stone Test Methods. Determination of Water Absorption Coefficient by Capillarity*; AENOR: Madrid, Spain, 1999.
19. Mosquera, M.J.; Benítez, D.; Perry, S.H. Pore structure in mortars applied on restoration. *Cem. Concr. Res.* **2002**, *32*, 1883–1888. [CrossRef]

20. *ASTM E96-90 Standard Test Methods for Water Vapor Transmission of Material*; ASTM: West Conshohocken, PA, USA, 1990; pp. 685–695.

21. Berns, R.S. *Billmeyer and Saltzman's Principles of Color Technology*, 3rd ed.; John Wiley & Sons: New York, NY, USA, 2000.

22. Illescas, J.F.; Mosquera, M.J. Producing surfactant-synthesized nanomaterials in situ on a building substrate, without volatile organic compounds. *ACS Appl. Mater. Interfaces* **2012**, *4*, 4259–4269. [CrossRef] [PubMed]

23. Xu, F.; Yu, J.; Li, D.; Xiang, N.; Zhang, Q.; Shao, L. Solvent effects on structural properties of SiO_2 gel using *n*-octylamine as a catalyst. *J. Sol-Gel Sci. Technol.* **2014**, *71*, 204–210. [CrossRef]

24. Illescas, J.F.; Mosquera, M.J. Surfactant-synthesized PDMS/silica nanomaterials improve robustness and stain resistance of carbonate stone. *J. Phys. Chem. C* **2011**, *115*, 14624–14634. [CrossRef]

25. Facio, D.S.; Carrascosa, L.A.; Mosquera, M.J. Producing lasting amphiphobic building surfaces with self-cleaning properties. *Nanotechnology* **2017**, *28*, 265601. [CrossRef]

26. Matos, M.C.; Ilharco, L.M.; Almeida, R.M. The evolution of TEOS to silica gel and glass by vibrational spectroscopy. *J. Non-Cryst. Solids* **1992**, *147–148*, 232–237. [CrossRef]

27. Innocenzi, P. Infrared spectroscopy of sol–gel derived silica-based films: A spectra-microstructure overview. *J. Non-Cryst. Solids* **2003**, *316*, 309–319. [CrossRef]

28. Rouquerol, J.; Rouquerol, F.; Llewellyn, P.; Maurin, G.; Sing, K.S. *Adsorption by Powders and Porous Solids*, 2nd ed.; Academic Press: Oxford, UK, 2014.

29. Fidalgo, A.; Ilharco, L.M. Correlation between physical properties and structure of silica xerogels. *J. Non-Cryst. Solids* **2004**, *347*, 128–137. [CrossRef]

30. Rodrigues, J.D.; Grossi, A. Indicators and ratings for the compatibility assessment of conservation actions. *J. Cult. Herit.* **2007**, *8*, 32–43. [CrossRef]

31. Novotná, P.; Zita, J.; Krýsa, J.; Kalousek, V.; Rathouský, J. Two-component transparent TiO_2/SiO_2 and TiO_2/PDMS films as efficient photocatalysts for environmental cleaning. *Appl. Catal. B* **2008**, *79*, 179–185. [CrossRef]

32. Novotná, P.; Matoušek, J. Preparation and characterization of photocatalytical TiO_2–SiO_2–PDMS layers on glass. *Thin Solid Films* **2006**, *502*, 143–146. [CrossRef]

33. Wang, S.D.; Jiang, Y.S. The durability of superhydrophobic films. *Appl. Surf. Sci.* **2015**, *357*, 1647–1657. [CrossRef]

New Consolidant-Hydrophobic Treatment by Combining SiO₂ Composite and Fluorinated Alkoxysilane: Application on Decayed Biocalcareous Stone from an 18th Century Cathedral

Dario S. Facio, Jose A. Ordoñez, M. L. Almoraima Gil, Luis A. M. Carrascosa and Maria J. Mosquera *

TEP-243 Nanomaterials Group, Department of Physical-Chemistry, Faculty of Sciences, Campus Río San Pedro, University of Cadiz, 11510 Puerto Real, Spain; dario.facio@uca.es (D.S.F.); joseantonio.ordonezperez@alum.uca.es (J.A.O.); almoraima.gil@uca.es (M.L.A.G.); luis.martinez@uca.es (L.A.M.C.)

* Correspondence: mariajesus.mosquera@uca.es; Tel.: +34-956-016331

Abstract: An effective procedure has been developed to consolidate and hydrophobize decayed monumental stones by a simple sol-gel process. The sol contains silica oligomer, silica nanoparticles and a surfactant, preventing gel cracking. The effectiveness of the process on biocalcareous stone samples from an 18th century cathedral has been evaluated, and it was found that the gel creates effective linking bridges between mineral grains of the stone. Silica nanoparticles produced a significant increase in the mechanical resistance and cohesion of the stone. The application of an additional fluorinated oligomer onto the consolidated stone gave rise to a surface with lasting hydrophobicity, preventing water absorption.

1. Introduction

Most stone building materials suffer significant weathering due to different processes such as salt crystallization, biodecay or carbonate cement dissolution, especially when exposed to outdoor conditions. All of these decay processes require water as a weathering agent carrier [1–3]. Susceptibility to deterioration of stone materials is mediated by several factors, including their mineral composition and their structural and textural properties. Stones—characterized by wide and highly accessible pores, such as biocalcareous stones—are especially susceptible to fast and intensive decay when exposed to a potentially aggressive environment [4].

Alkoxysilanes have been used with stone for restoration and conservation worldwide for decades [5]. The advantages of these products are well known: (1) alkoxysilanes penetrate deeply into porous stones, producing their polymerization in situ on the building, by a classic sol–gel process; (2) silica polymers with a silicon–oxygen backbone show good adherence to the stone, high weathering resistance and slight reduction of water vapor permeability. However, the alkoxysilanes have an important drawback associated with their tendency to crack. The presence of cracks obviously reduces their consolidant performance [6].

In the last years, we have prepared crack-free nanomaterials for stone conservation [7–18]. Specifically, the addition of an aqueous solution of *n*-octylamine to an alkoxysilane produces inverse micelles, which act as nanoreactors, generating silica seeds. These seeds grow, promoting a mesoporous

nanostructured xerogel [19]. As previously discussed [20], xerogel cracking is produced due to capillary pressure generated during the drying of the solvent contained in the pores of the gel network. Since this capillary pressure is inversely proportional to the pore radio, the obtained mesoporous xerogels (pore size from 2 to 20 nm) reduce this pressure, preventing cracking. In addition, the surfactant also reduces the capillary pressure by decreasing surface tension. By using this strategy, consolidants [7–12], hydrophobic and superhydrophobic products [10–13], stain-resistant materials [11] and photocatalytic coatings with self-cleaning performance [14–16] have been prepared. The interest in our approach is confirmed by the recent papers from other researchers working in the same field. Other authors [21–24] have employed the same route to produce protective materials for building. In addition, we have even applied our products in an actual cultural heritage building restoration. In recent papers [17,18], we described the restoration of a granitic Romanesque church and a medieval necropolis with a consolidant product synthesized in our laboratory.

In recent years, alkoxysilanes have also been modified in order to increase their mechanical resistance by adding colloidal oxide nanoparticles to the starting sol [6,25–29]. Nanoparticles are dense structures and, thus, they increase the mechanical properties and cohesion of the stone substrate. An increase of salt crystallization resistance of stone substrates treated with these particle-modified composites has been demonstrated [6]. Moreover, the addition of nanoparticles coarsens pore structure of the gel, preventing cracking [6,25].

Since water plays a significant role in building decay, hydrophobic products are commonly employed to prevent or reduce water ingress [11,12]. Specifically, organosilanes and organosiloxanes [11,12,30] and fluorinated compounds [1,31,32] are applied as conservation products on stone buildings because they reduce surface energy and thus produce a hydrophobic coating. Recently, superhydrophobic materials for building were produced [13,33] by adding silica nanoparticles to a low surface energy component. They produce a Cassie–Baxter surface, since air is trapped beneath the water droplets. This minimizes the contact area between droplet and surface, promoting repellence.

The starting point of this work was the restoring intervention on a stone altarpiece affected by efflorescence, superficial detachments and sand disaggregation from the Cathedral of Jerez de la Frontera in the south of Spain. The stone used in this construction easily undergoes weathering, mainly because of its high porosity. In particular, it suffers the weathering induced by salt crystallization, causing a considerable defacement and decohesion of the stone [4]. Thus, a treatment promoting consolidant and hydrophobic performance was applied [34]. A nanocomposite containing silica nanoparticles integrated into a silica matrix was produced. The nanoparticles were added (1) to increase the mechanical resistance of the coating and (2) to increase roughness of the surface in order to produce water repellence. A surfactant, *n*-octylamine, was added to the starting sol to prevent cracking and to act as a catalyst. This product was applied on biocalcareous stones employed in the construction of the Cathedral of Jerez de la Frontera. In addition, a second coating of fluorinated alkoxysilane was applied to produce condensation between labile silanol groups present in the silica nanocomposites and in the fluorinated coating. The objective was to produce a lasting coating, increasing mechanical resistance and giving high hydrophobicity to the stone substrate. The effectiveness for consolidant and hydrophobic purposes was evaluated. For comparison, commercial consolidant and hydrophobic products were also tested.

2. Materials and Methods

2.1. Description of the Monumental Building Stone

The building stone of the Cathedral of Jerez de la Frontera is a biocalcarenite from the San Cristobal quarry located in the southwest of Spain (see map in Figure 1) that has been employed in numerous emblematic monumental buildings in Spain's southwest region, such as the Cathedral of Seville and the Cathedral of Cádiz. It is a yellow-cream stone mainly containing calcite ($\approx$45%) and quartz ($\approx$45%) and a low content in feldspar ($\approx$10%). The mercury accessible porosity value is around 35%.

Figure 1. Geographical location of the San Cristobal Quarry and the Cathedral of Jerez de la Frontera. The biocalcareous stone under study is shown in the inset.

2.2. Consolidant and Hydrophobic Products and Application Procedure

The following treatments were selected for testing.

UCA (from the University of Cádiz) treatments. Starting sols were prepared by mixing a silica oligomer, *n*-octylamine and silica nanoparticles. Wacker TES40 (TES40, Wacker Chemie, Munich, Germany) is a mixture of monomeric and oligomeric ethoxysilanes, with an average chain length of approximately five Si–O units. Aerosil OX50 (OX50, Evonik Industries, Essen, Germany) is hydrophilic fumed silica with an average particle diameter of 40 nm.

The nanomaterial was prepared as follows: (1) an aqueous dispersion of *n*-octylamine, with a significantly higher surfactant concentration than that corresponding to its critical micellar concentration (cmc), was prepared under vigorous stirring. Specifically, a 1.92 M aqueous dispersion of *n*-octylamine was employed; (2) TES40 and OX50 were mixed under ultrasonic stirring (2 W·cm^{-3}) during 1 min; (3) the aqueous dispersion of *n*-octylamine was added dropwise to the TES40/OX50 mixture under ultrasonic stirring (1 W·cm^{-3}). The ultrasonic agitation was maintained for 8 min. The TES40/*n*-octylamine dispersion ratio was 99.5/0.5 *v/v*. The OX50 was added in 2% *w/v* ratio with respect to the total volume of the sol. The nomenclature for this nanomaterial is TS (T for TES40 and S for OX50). For comparison purposes, we also prepared a nanomaterial without the silica colloidal particles by using the same procedure, named T.

These sols were applied by air spraying at 2.0 bar for 5 s on the upper surface of $4 \times 4 \times 4$ cm^3 stone sample cubes, in triplicate. Spraying was chosen as the method of application because it is the preferred procedure employed, in real situations, for large areas, such as buildings or monumental structures. The application was repeated five times with an elapsed time of 1 min to ensure the saturation of all products under study and, thus, the suitable sol penetration into the stone. The products were applied under laboratory conditions (20 °C, 45% RH).

After gel transition took place (2 days after application), a perfluoropolyether silane solution (FS10, Fluorolink S10, Solvay Solexis, West Deptford, NJ, USA) was applied to the stone samples. Prior to its application, it was subjected to acid-catalyzed hydrolysis according to the following procedure: FS10 was mixed with isopropanol, H$_2$O and acetic acid under magnetic stirring. The proportions of the reagents were: 1.0, 94.0, 4.0 and 1.0 wt %, respectively. The fluorinated coating was applied by air spraying at 2.0 bar for 3 s. Finally, the coating was subjected to heating in order to accelerate the polymerization process, at two different temperatures: (1) 100 °C for 15 min and (2) 120 °C for 15 min. According to the technical data sheet, heating is not strictly necessary; room temperature curing is

also possible, but this will lead to a longer time to achieve the final performance. Treatments with the fluorinated layer have the additional keyword "+F" added to their name.

For comparative purposes, a commercial consolidant, Tegovakon V100 (TV100, BASF, Ludwigshafen, Germany), and a hydrophobic product, SILRES BS 290 (BS290, Wacker Chemie, Munich, Germany), were also applied on stone samples. TV100 is a solvent-free one-component consolidant consisting of partially prepolymerized TEOS and dioctyltin dilaurate (DOTL) catalyst. BS290 is a solvent-free silane/siloxane mix with application as a hydrophobic treatment. Following the specifications of the manufacturer, BS290 was diluted in ethanol (12 wt %). The two commercial products were applied by using the same procedure as UCA products.

2.3. Effectiveness Evaluation on Biocalcareous Stone

2.3.1. Effectiveness on Quarry Stone

One month after the application of the products, the evaluation tests described in the following paragraph were carried out. Results are expressed as average values with their standard deviations. In the cases in which the fluorinated coating did not influence the obtained results, these results are not shown in order to prevent duplication of data.

The uptake and dry matter of the products on the stone substrate were evaluated. The uptake of the consolidants was calculated by the difference in weight, expressed in wt %, after and before the treatment. The content of dry matter was determined by difference in weight of the samples left to dry under laboratory conditions until reaching constant weight, expressed in wt %.

Surface fragments of the treated stone specimens and their untreated counterparts were visualized by scanning electron microscopy (SEM) using a JEOL Quanta 200 scanning electron microscope (Tokyo, Japan) in order to observe the distribution and morphology of the coatings on the surface of the biocalcarenite stone.

Mercury accessible porosity and the porosimetric distribution by mercury intrusion porosimetry (MIP) was carried out. The test was carried out on stone specimens from the treated surfaces, each with a surface around 2 cm^2 and a width of around 0.5 cm, in triplicate. In the case of the untreated stone sample, the specimens were collected from any face. A PoreMaster 60 device from Quantachrome Instruments, which generates pressure to 60,000 psia, was used for pore size analysis from 950 to 0.0036 μm pore diameter.

Improvement in mechanical properties of the treated stones was evaluated by using a drilling resistance measurement system (DRMS) [35] by SINT Technology (Calenzano, Italy). Drill bits with 4.8 mm diameter were employed with a rotation speed of 600 rpm and a penetration rate of 10 mm/min. The test was repeated on two samples for each treatment, and five holes were drilled in each specimen. Drilling resistance vs. testing depth profiles were obtained.

The effectiveness of the coating materials in providing hydrophobic protection was characterized by measurement of the contact angles according to the sessile drop method, using a commercial, video-based, software-controlled contact angle analyzer, model OCA 15 plus from Dataphysics Instruments (Filderstadt, Germany). Static contact angle values were determined on the stone surface. For each treatment evaluated, droplets of distilled water (10 μL) were applied by a needle to five different points on two different stone samples. The advancing and receding contact angles were measured using the ARCA (Advancing and Receding Contact Angles) method included in the equipment software (OCA 15 plus), with the volume of the droplet being increased/decreased by 5 μL. Details of this procedure are given in a previous paper [10].

To confirm the hydrophobic behavior of the materials, two stone samples for each treatment were subjected to a test of water absorption by capillarity (WAC), as recommended in UNE-EN 1925 [36].

We also evaluated the possible negative effects, such as color changes and reduction in vapor permeability, induced by the treatments.

Water vapor permeability was determined by means of an automatic setup developed in our laboratory [37], based on the standard cup test [38], on $4 \times 4 \times 1$ cm^3 stone slabs. Two samples were tested for each treatment.

Total color difference (ΔE^*) was determined using a solid reflection spectrophotometer, Colorflex model, from HunterLab (Reston, VA, USA). The conditions used were illuminant C and observer CIE $10°$. CIE $L^*a^*b^*$ scale was used, and variations in color were evaluated [39]. In this case, the color evaluation was carried out after two different elapsed times from the treatment applications: 1 month and 1 year.

2.3.2. Effectiveness on Monumental Stone Extracted from Jerez de la Frontera Cathedral

The most effective treatment, identified in the previous phase, was applied to samples obtained from a restoration intervention on a stone altarpiece of the Cathedral of Jerez de la Frontera in the southwest of Spain (Figure 2a). The building construction began in 1695 and was inaugurated in 1778. The long duration of the construction works of the Cathedral means that three architectural styles can be found in the Cathedral: Neoclassical, Baroque and Gothic [4]. The altarpiece is affected by efflorescence, superficial detachments and sand disaggregation, as can be observed in Figure 2b,c. A stone fragment removed from the altarpiece was cut in a similar way to those collected from San Cristobal quarry ($4 \times 4 \times 4$ cm^3 stone sample cubes, see Figure 1).

Figure 2. (**a**) View of the main facade of the Cathedral of Jerez de la Frontera. (**b**) Stone altarpiece of the Cathedral from which samples were obtained. (**c**) Detail of the stone altarpiece affected by efflorescence, superficial detachments and sand disaggregation.

The treatment was applied by spraying in the same manner as that used for the quarry samples. One month after the treatment, the following experiments were carried out on those samples.

A peeling test was carried out, according to previously reported methods [40,41], using Scotch Magic tape (3M, Maplewood, MN, USA). Three strips of tape were applied and removed consecutively from the stone surface, and the weight of material pulled off in each stripping was recorded.

In addition, the drilling resistance test, water contact angle evaluation, water absorption by capillarity and measurement of color were carried out according the procedures described in the previous section.

3. Results and Discussion

3.1. Evaluation of the Effectiveness on Quarry Stone

Table 1 shows the uptake and dry matter (DM/U) values for the products. Uptake of the products ranged from 3 to 6 wt % in all cases. The dry matter values show a significantly lower value for BS290, its evaporated mass being around 87%. On the other hand, the higher DM/U values observed for the UCA products than those associated with TV100 highlights a slower gel drying.

Table 1. Uptake, dry matter and percentage relationship between dry matter and uptake (DM/U) after the application of the treatments under laboratory conditions.

Treatment	Uptake (%)	Dry Matter (%)	DM/U (%)
TV100	5.70 ± 2.93	3.17 ± 1.43	56
BS290	4.41 ± 2.24	0.58 ± 0.24	13
UCA-T	5.63 ± 1.19	4.11 ± 0.63	73
UCA-TS	5.65 ± 0.72	4.46 ± 0.58	79
UCA-T+F	5.59 ± 0.60	3.97 ± 0.33	71
UCA-TS+F	5.71 ± 0.17	4.10 ± 0.17	72

This finding demonstrates that, in the case of BS290, which was dissolved in ethanol, a thin film is formed on the stone substrate due to the solvent evaporation. It can be observed that the higher DM/U relationship for the UCA treatments is because volatile organic compounds were not added in the synthesis process. In the case of products containing fluorine, no differences from their counterparts without F are observed. This is due to the fluorine being applied in alcoholic solution (90%). We want to highlight that the purpose of this product application is exclusively to functionalize the UCA consolidants previously applied in order to reduce their surface energy and, subsequently, to promote a hydrophobic performance.

Figure 3 shows the SEM micrographs of the stone specimens with the treatments under study and their untreated counterparts. The untreated biocalcarenite reveals the presence of quartz and calcite crystals, typical of this stone (Figure 3a). The stone consolidated with TV100 shows the formation of a dense gel coating severely affected by cracking produced during its drying onto the stone (Figure 3b). Cracking is generated by the high capillary pressures supported by the gel network during drying, which is due to the presence of micropores [7,9], and gel network stiffness promoting cracking. The BS290 coating (Figure 3c) results in a dense and non-particulated polymer matrix due to the gel network compliance, promoting the pores' collapse. The gel compliance is produced by the presence of organic components in the network, as previously described [42]. In contrast, the samples consolidated with UCA-T and UCA-TS present particulated, continuous, homogeneous and crack-free coatings (Figure 3d,e, respectively). We associate particle formation to the role of *n*-octylamine producing inverse micelles that act as nanoreactors, as discussed in the Introduction section [19]. By comparing the two UCA products, the UCA-TS (Figure 3e) coating presents a more particulate texture as a result of the addition of commercial colloidal silica particles into the material. Specifically, the commercial silica particles are aggregated to the silica particles created during sol–gel transition, producing SiO_2 matrix–SiO_2 nanoparticle aggregates of around 240 nm. Thus, larger and more defined particle aggregates are created than those corresponding to the coating without OX50 particles. These micrographs highlight that the novel materials prevent cracking. Figure 4 shows some UCA-TS bridges linking the quartz grains and, consequently, confirming the effective consolidation produced by our products [7,9]. Furthermore, UCA-TS material homogeneously covers the edged surface of the quartz grains.

Figure 5 shows the porosity values and the pore size distributions. After products' application, porosity was reduced in all cases, showing a clear relationship with dry matter values. UCA treatments (T and TS), showing the greatest DM/U proportion values in all cases, produce the greatest reduction in the stone porosity. On the other hand, the commercial treatments are those with the lowest reduction of porosity, with nearly similar values of total porosity (TP), related to their lower DM/U values. The lowest reduction is produced in the samples treated with BS290, because a thin film is produced.
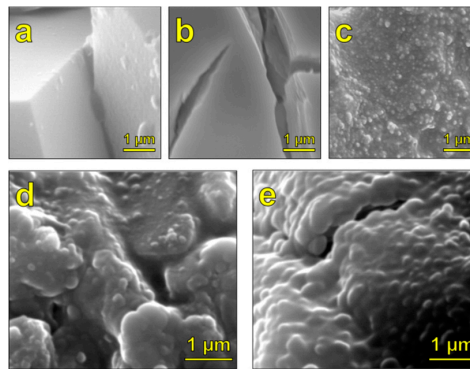
Figure 3. Scanning electron microscopy micrographs of the biocalcareous stone under study: (**a**) untreated; (**b**) treated with TV100; (**c**) treated with BS290; (**d**) treated with UCA-T; and (**e**) treated with UCA-TS.
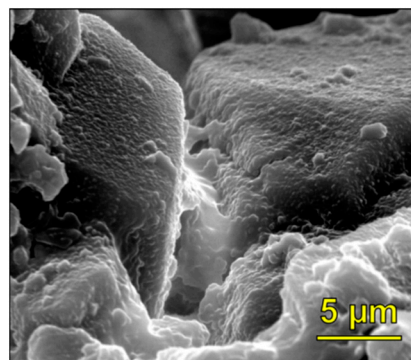

Figure 4. Scanning electron microscopy micrograph of the biocalcareous stone treated with UCA-TS. Nanomaterial bridges linking the quartz grains of the stone together can be clearly observed.
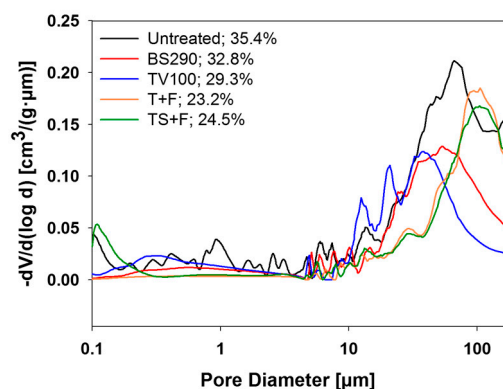

Figure 5. Pore size distribution obtained by mercury intrusion porosimetry (MIP) of the treated biocalcarenite samples and their untreated counterpart. Total porosity values (%) are also included after the corresponding treatment legend.

Comparing the pore size distribution, it is observed that all the treatments reduce the percentage of pores with larger access diameter (>10 μm), whereas the intermediate porosity (1–10 μm) was either increased or maintained in the case of the commercial products, and was reduced after application of UCA products. In the case of the smallest pores, the UCA treatments completely filled the micropores (<1 μm). The disappearance of the smallest pores is an important feature because salt crystallization, which is a damage mechanism in biocalcareous stone, is produced in micropores [17,43].

The consolidant effect of the products on the biocalcareous stone was measured by drilling resistance (see Figure 6). The stones treated with BS290 were not evaluated because it is not a consolidant. The commercial consolidant hardly has consolidant effectiveness on the biocalcareous stone, whereas the stone samples treated with the products synthesized in our laboratory significantly increased the mechanical resistance. This feature occurs because UCA products do not crack inside the porous structure of the stone, and they create effective links between the grains of the stone material, improving its cohesion (Figure 4). The increase in the mechanical resistance of the stone was evident across the full depth of stone tested (40 mm), demonstrating that our products penetrate deeply into the stone structure and they act as effective consolidants. In the case of TV100, its poor effectiveness is associated with the formation of a completely cracking coating (see Figure 3b).

By comparing the two UCA products, it can be observed that the stone treated with the particle-modified product shows a significantly higher mechanical resistance, being improved by a factor of around 1.5, 2 and 5 related to UCAT, TV100 and the untreated sample, respectively. This confirms the role played by the nanoparticles in increasing the consolidant effect of the product, as previously reported by other authors [6,26–29].
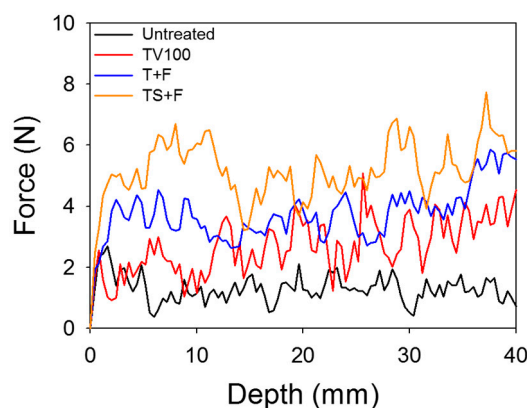

Figure 6. Drilling resistance versus testing depth of treated stone samples and their untreated counterpart.

Figure 7 and Table S1 show water droplet static and dynamic contact angle (CA) values. In the case of the untreated stone, due to its high porosity and hydrophilic nature, it was impossible to measure its CAs because the water was quickly absorbed. Comparing between treatments, the samples of stone treated with the commercial product TV100 present the lowest contact angles, which are below 90°. This is because TV100 is not a hydrophobic product and, subsequently, low surface energy groups are not present on the stone surface. The stones treated with UCA-T and UCA-TS show receding CA values below 90°, but advancing and static CA are above this value, in spite of groups reducing surface energy not being included in these products. We associate these anomalously high CA values with the incomplete hydrolysis of the ethoxy groups from the silica oligomer. This effect is not supposed to persist over time due to the progress of the hydrolysis reaction in both cases. This feature has been confirmed by the ^{29}Si-NMR spectra obtained for gels containing *n*-octylamine in a previous paper [12]. "The products containing *n*-octylamine presented Q1 and Q2 units in conjunction with Q3 and Q4 species six months after the synthesis, which indicated that the silica is not completely condensed and consequently, some ethoxy groups could be present in the material", as previously described [12,44]. However, the TV100 ^{29}Si-NMR spectrum does not show Q1 and Q2 units. The absence of the peaks highlights that ethoxy groups are not present in the TV100 gel and, consequently, the CA values are lower than 90°, as observed in this work (see Figure 7). By comparing CA values obtained in samples treated with UCA-T and UCA-TS, similar values are obtained, showing a slight increase for the gel containing silica nanoparticles. This can be related to the increase in roughness produced by particles in the surface of the stone [13,33].
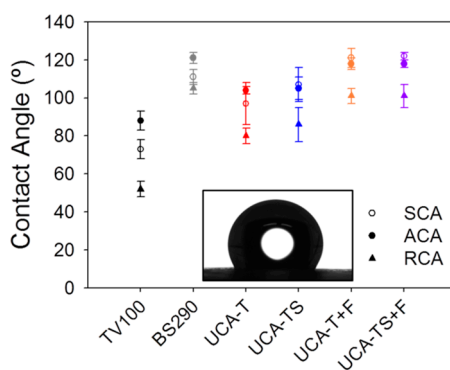
Figure 7. Static contact angle (CA) values and their corresponding advancing and receding CAs for the treated stones. Inset image corresponds to a droplet on stone with TS + F treatment.

Regarding the samples treated with products containing low energy species (BS290, UCA-T + F and UCA-TS + F), significantly higher CA values were obtained, presenting receding CA values higher than 90°. Thus, all treatments can be considered hydrophobic due to the presence of low energy components (fluorinated species) [45]. Comparing the treatments shows that the CA values are similar, with static CA values being slightly higher for UCA products. The silica nanoparticles were added, apart from improving its mechanical properties, to produce a densely packed coating in which the air is trapped. Thus, its addition should promote the movement of water droplets across the surface (repellence), producing a Cassie–Baxter state [46]. This regime is associated with a low CA hysteresis, below 10°. However, the surface treated with the product with nanoparticles (UCA-TS + F) shows the same hysteresis value (17°) as that corresponding to the treatment without particles (UCA-T+F) and, consequently, the repellence effect is not achieved. Since repellence is related to the change produced in the topography of the surfaces, SEM images (see Figure 3) allow this behavior to be explained. When SiO_2 nanoparticles are integrated into the silica gel, they cause clear and visible morphological changes in the coating due to the formation of larger aggregates (see Figures 3 and 4). However, this change does not produce modifications in repellence behavior because the original topography of the stone surface is hardly modified by the coating (see Figure 4). Consequently, as the biocalcareous stone is a high porosity material composed of macropores with distance between roughness peaks in the micrometer range, and a significantly lower distance between roughness peaks in the nanometer range is required to produce a Cassie–Baxter regime [13,33,47]. The coating containing nanoparticles (UCA-TS) cannot produce a repellent surface on which the water droplets do not stick [48]. These high pitch values promote a Wenzel surface [33,48]. In this scenario, water penetrates into the grooves and valleys of roughness, promoting a high adhesion [49].

In order to corroborate the hydrophobicity produced by the materials under study, a water absorption by capillarity (WAC) test was carried out on the stone samples under study. The WAC results are given in Table 2.

Table 2. Vapor diffusivity (*D*), total water uptake by capillarity (TWU) and total color difference (Δ*E**) for each treatment and its untreated counterpart. For each value of *D*, the percentage of reduction (DR) with respect to the untreated stone is also given.

Treatment	$D \cdot 10^{-6}$ $(m^2 \cdot s^{-1})$	DR (%)	TWU (%)	Δ*E** (1 Month)	Δ*E** (1 Year)
Untreated	−10.04 ± 2.12	–	15.31 ± 1.29	–	–
TV100	−7.03 ± 0.22	30	4.02 ± 0.01	2.12 ± 0.69	2.23 ± 1.33
BS290	−8.53 ± 0.36	15	0.48 ± 0.13	10.12 ± 2.11	6.03 ± 0.69
UCA-T	−6.95 ± 0.80	31	0.35 ± 0.10	10.59 ± 1.71	6.12 ± 1.69
UCA-TS	−6.21 ± 0.13	38	0.33 ± 0.00	11.16 ± 3.06	5.97 ± 2.27
UCA-T + F	−6.96 ± 1.12	31	0.22 ± 0.10	8.72 ± 0.81	4.76 ± 0.89
UCA-TS + F	−6.02 ± 0.04	40	0.20 ± 0.04	9.12 ± 0.78	4.91 ± 1.75

As expected, the stone samples treated with TV100 show a significant water uptake. The UCA treatments present the highest reduction in WAC, being significantly higher for those with the fluorine coating. Surprisingly, the commercial hydrophobic product (BS290) produced higher water absorption than that associated with non-hydrophobic UCA products. This could be related to the lower reduction in porosity produced by this coating (see Figure 5). This could favor the existence of pores enabling water absorption. In addition, we think that the existence of chemical bonds between the silica nanocomposite and the fluorine oligomer coating creates a lasting hydrophobic coating preventing water uptake, whereas the commercial hydrophobic product could produce a coating with lower durability for water uptake due to the formation of a discontinuous coating, as described in a previous paper [50].

Regarding the negative effect, we studied changes occurring in the water vapor permeability and in the color of the stone after the treatments. Water vapor diffusivity coefficients are given in Table 2. A treatment is not acceptable for restoration of stone materials if it causes a reduction of water vapor diffusivity coefficient (*D*) by more than 50% [51] because it suppresses the breathability (water vapor transference across the pore structure) of the stone. This critical value was not exceeded by any of the treatments evaluated; the lowest diffusivity reduction (DR) corresponded to the samples treated with BS290. This could be newly associated to the thin film created, producing a low reduction in porosity of the stone (see Figure 5).

To evaluate the color change produced by the treatments, the chromatic variations were quantified by the total color difference values (ΔE^*) (Table 2). All of the treatments, excepting TV100, presented total color difference values higher than the generally accepted threshold value of human eye perception ($\Delta E^* \leq 5$) 1 month after their application [26]. Change in color was evaluated 1 year after application (see Table 2), with all the stones treated showing ΔE^* values around the accepted threshold. Thus, we consider that change in color induced by the UCA products is acceptable for restoration purposes.

3.2. Effectiveness on Monumental Stone Extracted from Jerez de la Frontera Cathedral

Since the stonework of the Cathedral of Jerez de la Frontera is affected by salt decay, with water being the main vehicle for the decay agents, the choice of product with consolidant and hydrophobic performances is highly required. From the results of the tests performed on the biocalcarenite samples extracted from the quarry, we concluded that the UCA-TS + F treatment is the best product to be applied on the Cathedral stonework, as it showed the highest consolidant performance due to the SiO_2 nanoparticles added to the starting sol. Thus, this treatment was applied on stone samples obtained from the altarpiece of the Cathedral. Table 3 shows the values obtained for uptake, dry matter and total color variation. As expected, the results are very close to those obtained for the stone samples from the quarry.

Table 3. Uptake, dry matter and total color difference (ΔE^*) with respect to the untreated stone. Weight of the tape in the adhesion test is also given.

Treatment	Uptake (%)	Dry Matter (%)	ΔE^*	Adhesion Test (mg)
Untreated	–	–	–	9.3 ± 9.4
UCA-TS + F	4.83 ± 0.52	3.64 ± 0.40	10.65 ± 0.99	0.1 ± 0.2

As described in the introduction, stone samples from the altarpiece show evident superficial detachments and sand disaggregation. Therefore, the peeling test was used as a useful tool to confirm the superficial cohesive performance of the UCA-TS + F treatment. The results from the adhesion test (see Figure 8a and Table 3) show a significant amount of material released from the surface of the untreated stone due to significant decohesion. After the application of the UCA treatment, the material removal was negligible (see Figure 8b). These results highlight that this product has a potential use as consolidant of decayed stone with low cohesion, such as the biocalcareous monumental stone under study.
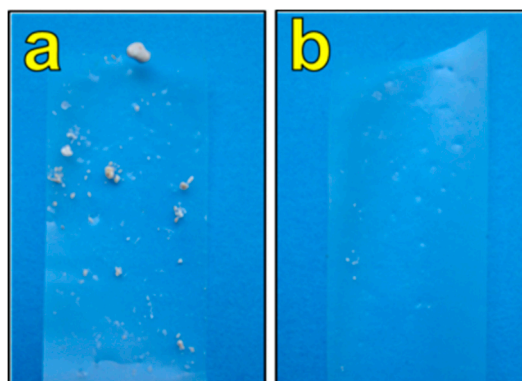
Figure 8. Scotch tape in the adhesion test for (**a**) untreated stone and (**b**) UCA-TS + F treated stone.

In addition to the increase in the cohesion of the external surface produced by the UCA product, a significant increase was observed in drilling resistance (see Figure 9), doubling the value of the untreated stone. Regarding the profile of the untreated stone, we observed a higher mechanical resistance than that obtained from the quarry stone. We associate this with variations in the mineral vein from which they were extracted.
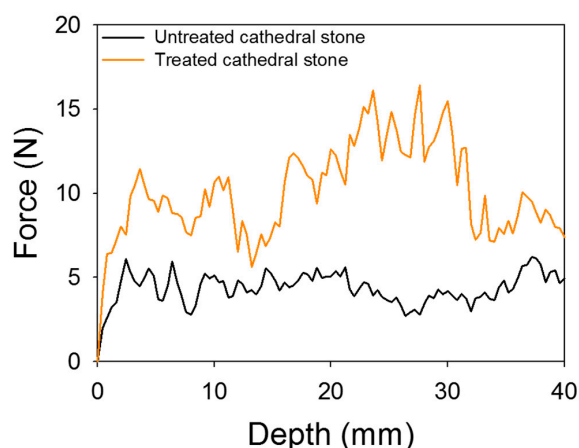
Figure 9. Drilling resistance versus testing depth of UCA-TS + F treated stone and its untreated counterpart.

Regarding the hydrophobic behavior of the treated monumental stone (see Table 4), the results for the effectiveness of the product were close to those obtained from the quarry stones, showing high contact angle values and low water uptake. This confirms the effectiveness of the UCA treatment in conferring hydrophobic properties to the decayed monumental stone.

Table 4. Static CA values and their corresponding advancing and receding CA for the treated stones, and total water uptake by capillarity (TWU).

Treatment	θ_S (°)	θ_A (°)	θ_R (°)	Hysteresis (°)	TWU (%)
Untreated	–	–	–	–	12.50
UCA-TS+F	123 ± 2	118 ± 1.13	101 ± 3	17.91 ± 1.97	0.19

Note: θ_S = Static contact angle; θ_A = advancing angle; θ_R = receding angle; TWU = total water uptake.

Finally, we would like to remark that, in spite of the stones extracted from the altarpiece containing salt efflorescence, the product prepared in our laboratory was effective as a consolidant and hydrophobic agent, showing similar results to those obtained for the quarry stones.

4. Conclusions

A simple procedure has been developed to consolidate decayed stone with low cohesion and evident sand disaggregation, such as the biocalcareous monumental stone under study. Specifically, a sol containing silica oligomer, silica nanoparticles and a surfactant is applied on stone by spraying. The process is so simple that the polymerization is produced in situ, and it can take place on a building in outdoor conditions. We demonstrated that a crack-free coating, filling pores of the decayed stone, was obtained due to the effect of *n*-octylamine. It acts by coarsening the pore structure of the material. The addition of silica nanoparticles to the starting sol produces a significant increase in mechanical resistance and in the cohesion of the stone. We demonstrated that the silica composite creates linking bridges between the mineral grains of the stone. This product shows higher consolidant effectiveness than that obtained from a commercial product tested in this study.

Additionally, the application of a fluorinated alkoxysilane onto the treated stone gives rise to a hydrophobic surface, preventing water absorption. The chemical bonds created between the two applied coatings (silica nanocomposite and fluorinated oligomer) produces a lasting hydrophobic coating, showing a higher reduction in uptake than that obtained by a commercial hydrophobic product tested. The addition of silica nanoparticles does not produce a Cassie–Baxter surface in this specific substrate due to the original topography of the stone surface being hardly modified by the coating. Thus, repellence properties are not achieved.

Finally, we demonstrated that the treatments do not significantly modify the breathability of stone and the color of the stone.

Supplementary Materials: The following are available online at http://www.mdpi.com/2079-6412/8/5/170/s1, Table S1: Static, advancing and receding CA values and their corresponding hysteresis CA for the treated stones.

Author Contributions: D.S.F. and J.A.O. performed the experimental work. M.L.A.G. and L.A.M.C. participated in writing and interpretation of results. M.J.M. planned the experimental work, analyzed the results and wrote the manuscript.

Conflicts of Interest: The authors declare no conflict of interest.

References

1. Poli, T.; Toniolo, L.; Chiantore, O. The protection of different Italian marbles with two partially flourinated acrylic copolymers. *Appl. Phys. A Mater. Sci. Process.* **2004**, *79*, 347–351. [CrossRef]
2. Graedel, T.E.; McGill, R. Degradation of materials in the atmosphere. *Environ. Sci. Technol.* **1986**, *20*, 1093–1100. [CrossRef]
3. Dolske, D.A. Deposition of atmospheric pollutants to monuments, statues, and buildings. *Sci. Total Environ.* **1995**, *167*, 15–31. [CrossRef]
4. Villegas-Sánchez, R.; Arroyo, F. The cathedral of Jerez De La Frontera (Cádiz, Spain): Stone degradation and conservation. *J. Cult. Herit.* **2013**, *14*, e113–e116. [CrossRef]
5. Wheeler, G. *Alkoxysilanes and the Consolidation of Stone*; The Getty Conservation Institute: Los Angeles, CA, USA, 2005.
6. Scherer, G.W.; Wheeler, G.S. Silicate consolidants for stone. *Key Eng. Mater.* **2009**, *391*, 1–25. [CrossRef]
7. Mosquera, M.J.; de los Santos, D.M.; Montes, A.; Valdez-Castro, L. New nanomaterials for consolidating stone. *Langmuir* **2008**, *24*, 2772–2778. [CrossRef] [PubMed]
8. Mosquera, M.J.; Desireé, M.; Valdez-Castro, L.; Esquivias, L. New route for producing crack-free xerogels: Obtaining uniform pore size. *J. Non-Cryst. Solids* **2008**, *354*, 645–650. [CrossRef]

9. Mosquera, M.J.; de los Santos, D.M.; Rivas, T.; Sanmartín, P.; Silva, B. New nanomaterials for protecting and consolidating stone. *J. Nano Res.* **2009**, *8*, 1–12. [CrossRef]

10. Mosquera, M.J.; de los Santos, D.M.; Rivas, T. Surfactant-synthesized ormosils with application to stone restoration. *Langmuir* **2010**, *26*, 6737–6745. [CrossRef] [PubMed]

11. Illescas, J.F.; Mosquera, M.J. Surfactant-synthesized PDMS/silica nanomaterials improve robustness and stain resistance of carbonate stone. *J. Phys. Chem. C* **2011**, *115*, 14624–14634. [CrossRef]

12. Illescas, J.F.; Mosquera, M.J. Producing surfactant synthesized nanomaterials in situ on a building susbstrate, without volatile organic compounds. *ACS Appl. Mater. Interfaces* **2012**, *4*, 4259–4269. [CrossRef] [PubMed]

13. Facio, D.S.; Mosquera, M.J. Simple strategy for producing superhydrophobic nanocomposite coatings in situ on a building substrate. *ACS Appl. Mater. Interfaces* **2013**, *5*, 7517–7526. [CrossRef] [PubMed]

14. Pinho, L.; Mosquera, M.J. Titania-silica nanocomposite photocatalysts with application in stone self-cleaning. *J. Phys. Chem. C* **2011**, *115*, 22851–22862. [CrossRef]

15. Pinho, L.; Mosquera, M.J. Photocatalytic activity of TiO_2-SiO_2 nanocomposites applied to buildings: Influence of particle size and loading. *Appl. Catal. B Environ.* **2013**, *134–135*, 205–221. [CrossRef]

16. Pinho, L.; Rojas, M.; Mosquera, M.J. Ag–SiO_2–TiO_2 nanocomposite coatings with enhanced photoactivity for self-cleaning application on building materials. *Appl. Catal. B Environ.* **2015**, *178*, 144–154. [CrossRef]

17. De Rosario, I.; Elhaddad, F.; Pan, A.; Benavides, R.; Rivas, T.; Mosquera, M.J. Effectiveness of a novel consolidant on granite: Laboratory and in situ results. *Constr. Build. Mater.* **2015**, *76*, 140–149. [CrossRef]

18. De Rosario, I.; Rivas, T.; Buceta, G.; Feijoo, J.; Mosquera, M.J. Surfactant-synthesized consolidants applied to a granitic medieval necropolis in NW Spain. Laboratory and in situ effectiveness evaluation. *Int. J. Archit. Herit.* **2017**, *11*, 1166–1176. [CrossRef]

19. Facio, D.S.; Luna, M.; Mosquera, M.J. Facile preparation of mesoporous silica monoliths by an inverse micelle mechanism. *Microporous Mesoporous Mater.* **2017**, *247*, 166–176. [CrossRef]

20. Scherer, G. Theory of drying. *J. Am. Ceram. Soc.* **1990**, *73*, 3–14. [CrossRef]

21. Xu, F.; Yu, J.; Li, D.; Xiang, N.; Zhang, Q.; Shao, L. Solvent effects on structural properties of SiO_2 gel using *n*-octylamine as a catalyst. *J. Sol-Gel Sci. Technol.* **2014**, *71*, 204–210. [CrossRef]

22. Xu, F.; Li, D.; Zhang, Q.; Zhang, H.; Xu, J. Effects of addition of colloidal silica particles on TEOS-based stone protection using *n*-octylamine as a catalyst. *Prog. Org. Coat.* **2012**, *75*, 429–434. [CrossRef]

23. Simionescu, B.; Olaru, M.; Aflori, M.; Cotofana, C. Silsesquioxane-based hybrid nanocomposite with self-assembling properties for porous limestones conservation. *High Perform. Polym.* **2010**, *22*, 42–55. [CrossRef]

24. Simionescu, B.; Aflori, M.; Olaru, M. Protective coatings based on silsesquioxane nanocomposite films for building limestones. *Constr. Build. Mater.* **2009**, *23*, 3426–3430. [CrossRef]

25. Mosquera, M.J.; Bejarano, M.; de la Rosa-Fox, N.; Esquivias, L. Producing crack-free colloid—Polymer hybrid gels by tailoring porosity. *Langmuir* **2003**, *19*, 951–957. [CrossRef]

26. Miliani, C.; Velo-Simpson, M.L.; Scherer, G.W. Particle-modified consolidants: A study on the effect of particles on sol-gel properties and consolidation effectiveness. *J. Cult. Herit.* **2007**, *8*, 1–6. [CrossRef]

27. Salazar-Hernández, C.; Alquiza, M.J.P.; Salgado, P.; Cervantes, J. TEOS-colloidal silica-PDMS-OH hybrid formulation used for stone consolidation. *Appl. Organomet. Chem.* **2010**, *24*, 481–488. [CrossRef]

28. Liu, R.; Han, X.; Huang, X.; Li, W.; Luo, H. Preparation of three-component TEOS-based composites for stone conservation by sol-gel process. *J. Sol-Gel Sci. Technol.* **2013**, *68*, 19–30. [CrossRef]

29. Pinho, L.; Elhaddad, F.; Facio, D.S.; Mosquera, M.J. A novel TiO_2-SiO_2 nanocomposite converts a very friable stone into a self-cleaning building material. *Appl. Surf. Sci.* **2013**, *275*, 389–396. [CrossRef]

30. Karapanagiotis, I.; Pavlou, A.; Manoudis, P.N.; Aifantis, K.E. Aifantis, Water repellent ORMOSIL films for the protection of stone and other materials. *Mater. Lett.* **2014**, *131*, 276–279. [CrossRef]

31. Kronlund, D.; Bergbreiter, A.; Meierjohann, A.; Kronberg, L.; Lindén, M.; Grosso, D.; Smått, J.H. Hydrophobization of marble pore surfaces using a total immersion treatment method—Product selection and optimization of concentration and treatment time. *Prog. Org. Coat.* **2015**, *85*, 159–167. [CrossRef]

32. Colangiuli, D.; Calia, A.; Bianco, N. Novel multifunctional coatings with photocatalytic and hydrophobic properties for the preservation of the stone building heritage. *Constr. Build. Mater.* **2015**, *93*, 189–196. [CrossRef]

33. Manoudis, P.N.; Karapanagiotis, I.; Tsakalof, A.; Zuburtikudis, I.; Panayiotou, C. Superhydrophobic composite films produced on various substrates. *Langmuir* **2008**, *24*, 11225–11232. [CrossRef] [PubMed]

34. Facio, D.S.; Carrascosa, L.A.; Mosquera, M.J. Producing lasting amphiphobic building surfaces with self-cleaning properties. *Nanotechnology* **2017**, *28*, 265601. [CrossRef] [PubMed]

35. Rescic, S.; Fratini, F.; Tiano, P. On-site evaluation of the "mechanical" properties of Maastricht limestone and their relationship with the physical characteristics. *Geol. Soc. Lond. Spec. Publ.* **2010**, *331*, 203–208. [CrossRef]

36. *UNE-EN 1925:1999 Natural Stone Test Methods. Determination of Water Absorption Coefficient by Capillarity*; AENOR: Madrid, Spain, 1999.

37. Mosquera, M.J.; Beníŧez, D.; Perry, S.H. Pore structure in mortars applied on restoration. *Cem. Concr. Res.* **2002**, *32*, 1883–1888. [CrossRef]

38. *ASTM E 96-90 Standard Test Methods for Water Vapor Transmission of Materials*; ASTM: West Conshohocken, PA, USA, 1990.

39. Berns, R.S. *Billmeyer and Saltzman's Principles of Color Technology*; Wiley-Interscience: New York, NY, USA, 2000.

40. Ling, X.Y.; Phang, I.Y.; Vancso, G.J.; Huskens, J.; Reinhoudt, D.N. Stable and transparent superhydrophobic nanoparticle films. *Langmuir* **2009**, *25*, 3260–3263. [CrossRef] [PubMed]

41. *UNE-EN ISO 2409:2013 Paints and Varnishes. Cross-Cut Test*; AENOR: Madrid, Spain, 2013.

42. Carrascosa, L.A.; Facio, D.S.; Mosquera, M.J. Producing superhydrophobic roof tiles. *Nanotechnology* **2016**, *27*, 095604. [CrossRef] [PubMed]

43. Yu, S.; Oguchi, C.T. Role of pore size distribution in salt uptake, damage, and predicting salt susceptibility of eight types of Japanese building stones. *Eng. Geol.* **2010**, *115*, 226–236. [CrossRef]

44. Noble, K.; Seddon, A.B.; Turner, M.L.; Chevalier, P.; Mackinnon, I.A. Polysiloxane-modified mesoporous materials. *J. Sol-Gel Sci. Technol.* **2000**, *19*, 807–810. [CrossRef]

45. Della Volpe, C.; Penati, A.; Peruzzi, R.; Siboni, S.; Toniolo, L.; Colombo, C. The combined effect of roughness and heterogeneity on contact angles: the case of polymer coating for stone protection. *J. Adhes. Sci. Technol.* **2000**, *14*, 273–299. [CrossRef]

46. Cassie, A.B.D.; Baxter, S. Large contact angles of plants and animal surfaces. *Nature* **1945**, *155*, 21–22. [CrossRef]

47. Manoudis, P.N.; Karapanagiotis, I.; Tsakalof, A.; Zuburtikudis, I.; Kolinkeová, B.; Panayiotou, C. Superhydrophobic films for the protection of outdoor cultural heritage assets. *Appl. Phys. A* **2009**, *97*, 351–360. [CrossRef]

48. Pedna, A.; Pinho, L.; Frediani, P.; Mosquera, M.J. Obtaining SiO_2-fluorinated PLA bionanocomposite with application as reversible and highly-hydrophobic coatings of buildings. *Prog. Org. Coat.* **2015**, *90*, 91–100. [CrossRef]

49. Bhushan, B.; Her, E.K. Fabrication of superhydrophobic surfaces with high and low adhesion inspired from rose petal. *Langmuir* **2010**, *26*, 8207–8217. [CrossRef] [PubMed]

50. Elhaddad, F.; Carrascosa, L.A.M.; Mosquera, M.J. Long-term effectiveness, under coastal environment, of a novel conservation nanomaterial applied on sandstone from Roman archaeological site. *J. Cult. Herit.* **2018**, in press.

51. Rodrigues, J.D.; Grossi, A. Indicators and ratings for the compatibility assessment of conservation actions. *J. Cult. Herit.* **2007**, *8*, 32–43. [CrossRef]
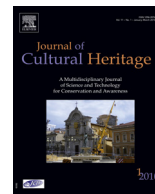
Technoheritage 2017

Long-term effectiveness, under a coastal environment, of a novel conservation nanomaterial applied on sandstone from a Roman archaeological site

Farid Elhaddad , Luis A.M. Carrascosa , Maria J. Mosquera *

TEP-243 Nanomaterials Group, Departamento de Química-Física, Facultad de Ciencias, Campus Universitario Río San Pedro, Universidad de Cádiz, 11510 Puerto Real, Cádiz, Spain

A B S T R A C T

Water is the main factor of degradation in most stone monuments and buildings, and especially in those located next to the sea, since it acts as a vehicle for decay agents. The continuous exposure of the Baelo Claudia Roman archaeological site to marine aerosol has produced severe weathering. The aim of this study was to assess the performance of a novel consolidant/hydrophobic nanomaterial applied on sandstones from this archaeological site. The product durability was evaluated for three years of exposure at the archaeological site. For comparison, two commercial products (a consolidant and a hydrophobic product) were also evaluated. The obtained results showed that the product synthesised in our laboratory maintained the consolidant and hydrophobic properties, after three years of exposure, due to the production of a homogeneous coating with a penetration depth of 20 mm. The commercial consolidant was completely cracked and the hydrophobic product generated a superficial coating without penetration into the pores of the sandstone, which promoted a reduction in durability in both cases.

© 2018 Published by Elsevier Masson SAS.

1. Introduction

Nowadays, most lithotypes employed in archaeological monuments exhibit visible damage, with water being the main vehicle of most decay processes, such as salt crystallisation and freeze-thaw [1–6]. It also contributes to other factors of decay such as microbial contamination [7], which can be favoured by chemical and physical processes and synergy between the two [8]. For these reasons, the most popular conservation treatment is based on the use of two different types of products: (i) consolidants, which promote the cohesion of the decayed stone, and, (ii) hydrophobic products, which prevent water ingress into the stone pore structure. The most popular consolidants on the market are composed of alkosysilanes [9]. Hydrophobic products consist of active components which reduce surface energy, and include fluorinated acrylic polymers and organic siloxanes [10–13]. Our research group has developed an innovative synthesis route for preserving Cultural Heritage stonework [14,15]. Specifically, a surfactant-assisted sol-gel synthesis which produced crack-free nanomaterials *in-situ* to be used as long-term consolidants on the stonework. Recently, an inverse-micelle mechanism has been proposed to explain the formation of crack-free, SiO_2 xerogels produced by this route [16]. Specifically, an aqueous n-octylamine dispersion with a concentration above its critical micelle concentration is mixed with a silica oligomer under ultrasonic agitation. The micelles created by the surfactant act as nanoreactors, producing a structure composed of nearly uniform silica nanoparticles. This mesoporous structure prevents material cracking because it reduces capillary pressure during gel drying. Due to their crack-free structure, these mesoporous materials show an improved consolidant performance and suitable adherence to the stone substrates. Additionally, by simple chemical modifications (addition of polydimethylsiloxane, SiO_2 NPs, fluorinated compounds, TiO_2 NPs, CuONPs, etc.) of the process, it is possible to obtain multifunctional products with a combination of consolidant and hydrophobic/superhydrophobic, oleophobic, photocatalytic and biocidal performance [17].

Most performance studies on innovative conservation products durability have been conducted in laboratories [18–20], with few studies carried out by exposure to real situations [21,22]. Studies about on-site monitoring of the performance of conservation products are even scarcer, and the monitoring period was below one year in all the cited works [23–27].

The aim of this study was to assess the compatibility, *in-situ* performance and durability of a novel consolidant/hydrophobic

* Corresponding author. Tel.: +34 956016331; fax: +34 956016288.
E-mail address: mariajesus.mosquera@uca.es (M.J. Mosquera).

product, developed by our research group, on stones from a significant Roman archaeological site located next to the sea. The study consisted of an initial phase in the laboratory to evaluate the effectiveness of the product. Next, the samples treated with the novel product were maintained at the archaeological site for a period of three years, and properties were evaluated after each year of exposure. For comparison, stone samples treated with a commercially available hydrophobic product and a consolidant were also studied.

2. Materials and methods

2.1. Evaluation of the archaeological site environment and the Baelo Claudia sandstone

The Roman city of Baelo Claudia, located in the province of Cádiz (in the south of Spain), was founded at the end of the second century BC and flourished during the following two centuries (Fig. 1A). The Basilica and the Roman theatre (Fig. 1B and C) are its most representative elements. The site is located in a natural environment, which does not present industrial activity in the proximity. Firstly, an analysis of the environment surrounding the site was carried out. Specifically, meteorological data of temperature, rainfall and wind were collected for 24 months from a National Institute of Meteorology station, situated near to the archaeological site.

In addition, an analysis of sedimentable particles (SP) collected during one month at the archaeological site was carried out. Details about the SP analysis procedure were reported in a previous paper [28]. After collection, SP were rinsed with deionized water and filtered to separate the insoluble fraction. In addition, a JEOL 6460LV Scanning Electron Microscope (SEM) was used to visualise the morphology of the insoluble SP fraction. Energy dispersive X-ray spectroscopy (EDX) spectra were recorded in order to determine their composition.

The stone samples employed in this study were collected from de-contextualised stone located on the site coming from the archaeological site ruins. Biofilms, salt efflorescence or other forms of decay were not visible. Thus, prior to their use, the samples were washed with deionized water in an ultrasonic bath and dried in an oven at 60 °C until constant weight. Petrographic and mineralogical analyses were carried out on thin sections of stone using a Transmitted Light Microscope (Olympus BH-2).

2.2. Nanomaterial synthesis and procedure of application on Baelo Claudia samples

A starting sol containing a commercial silica oligomer (Dynasylan 40 from Evonik), and a hydroxyl-terminated polydimethylsiloxane (PDMS from ABCR) in the presence of a surfactant (n-octylamine, from Aldrich), was synthesised according to a previously described method [15]. The synthesis route was as follows: a 1.57 M aqueous solution of n-octylamine was prepared, and then, PDMS, Dynasylan 40 and the aqueous n-octylamine solution were mixed and homogenised by high-power ultrasonic agitation (60 $W \cdot cm^{-3}$) for 10 minutes. PDMS and aqueous n-octylamine solution proportions were 10 and 0.075%v/v, respectively. The product was named UCA (from University of Cadiz).

The product was sprayed, in the laboratory, onto all the faces of 4 cm-cubed stone samples collected from the Baelo Claudia site, using a pressure of 0.15 MPa for 25 s, promoting the complete saturation of the samples. Spraying was chosen as the method of application because it is the preferred procedure employed, in real situations, for large areas, such as buildings or other monumental structures. Thus, the application was carried out in a similar way to that employed in a real situation. For comparison purposes, two popular commercial products, a consolidant product SILRES

BSOH100 and a hydrophobic product SILRES BS290, manufactured by WACKER, were also applied under the same conditions. According to their corresponding technical data sheets, they should be applied until saturation. BSOH100 is a solvent-free product, consisting of partially pre-polymerised tetraethyl orthosilicate (TEOS) and dibutyltin dilaurate (DBTDL) catalyst. BS290 is a solvent-free silane/siloxane mix. It was diluted in ethanol (12%w/w), following the manufacturer's recommendations.

2.3. Effectiveness and durability evaluation on Baelo Claudia stone

The treated samples were dried under laboratory conditions (20 °C and 60% RH) until constant weight was reached. This occurred one month after application. Effectiveness of the products applied on the Baelo Claudia sandstone was evaluated in the laboratory using three samples for each treatment. In addition, durability of the products was evaluated in samples exposed to the environmental conditions at the Baelo Claudia archaeological site (Fig. 1D). The samples were placed on the roof of the museum building of the archaeological site. They were placed on a grill holder in order that all the faces were exposed to the environmental conditions. The samples were separated from each other by a vertical grill in order to prevent their removal by wind (Fig. 1D). The study was carried out every year, on one sandstone sample for each applied product and their corresponding untreated counterpart, for a total period of three years. The following assessments were carried out on the treated sandstone samples and their untreated counterparts.

2.3.1. Sandstone-product interaction

The samples were weighed before and after application of the products in order to calculate the uptake (U) of the products, and they were re-weighed one month after application to calculate the dry-matter of the products.

Mercury accessible porosity and porosimetric distribution were obtained by Mercury Intrusion Porosimetry (MIP). The measurement was carried out on specimens from the surface stone, each with a surface of around 2 cm² and a width of around 0.5 cm, using a PoreMaster-60 device from Quantachrome Instruments comprising two measurement units: a low pressure unit (Pascal 140), with a pressure range of between 0.69 and 350 kPa, and, a high pressure unit (Pascal 440) with a pressure range of between 0.1 to 420 MPa.

A JEOL Quanta 200 Scanning Electron Microscope (SEM) was used to visualise changes in the topography of the surfaces of the treated sandstone samples and their untreated counterparts. The samples were covered by a 12-nm layer of gold in order to improve their conductivity and prevent charge effects.

2.3.2. Evaluation of the effectiveness of the products

The Vickers hardness test, using a universal durometer (model RB2/200 DA, Centaur), was employed to evaluate the mechanical properties of the surfaces of the stones.

The mechanical properties of treated stone were also evaluated, by using the drilling resistance measuring system (DRMS) by SINT Technology. Drill bits of 4.8 mm diameter were employed with a rotation speed of 900 rpm and a penetration rate of 5 mm/min. A standard supplied by SINT Technology was employed in order to correct for the wear effect of the drills. The study was carried out every year on one sandstone sample for each applied product and their corresponding untreated counterpart. Five perforations per sample were carried out.

The effectiveness of the products in providing hydrophobic protection was characterised by the Static Contact Angle (SCA) test according to the sessile drop method, using a commercial video-based, software-controlled, contact angle analyser, model OCA 15
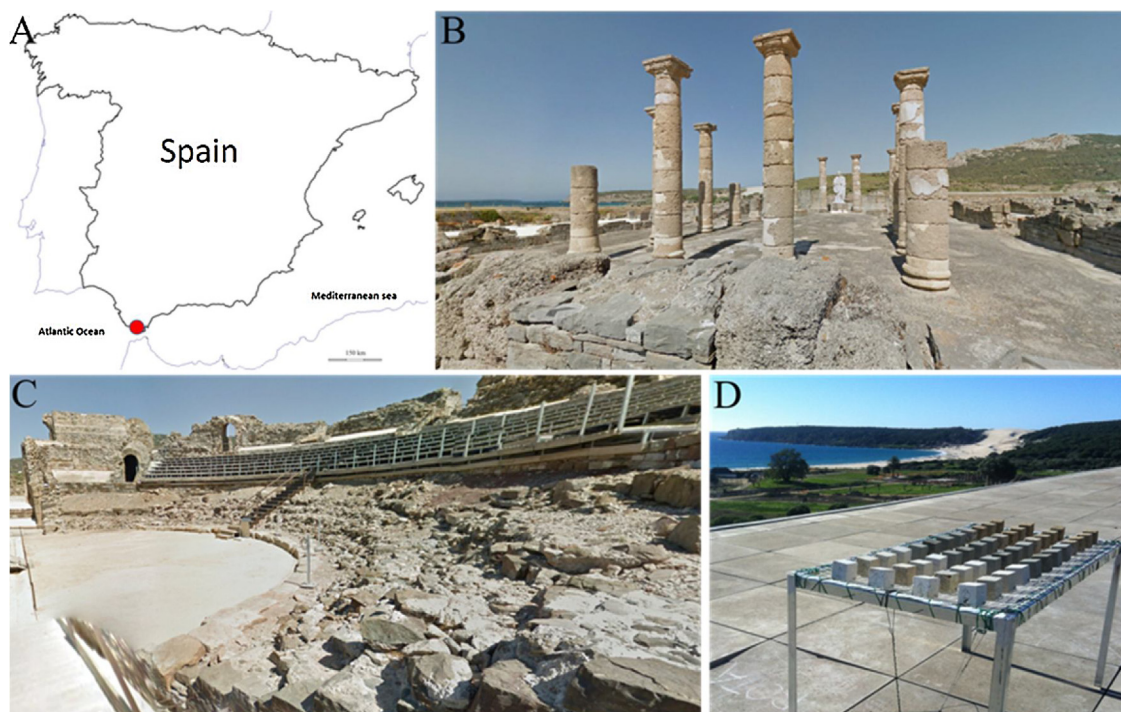
Fig. 1. (A) Location of the archaeological site of Baelo Claudia. (B) The basilica. (C) The theatre. (D) Exposure of the treated and untreated samples at the archaeological site for three years.

plus, from DataPhysics Instruments. The measurement was carried out on five points for each surface (the four corners and the centre).

The reduction in water absorption of the treated samples was confirmed by the evaluation of the Capillary Water Absorption Coefficient (WAC), as recommended in UNE-EN 1925 [29], and the total water uptake was also determined.

2.3.3. Compatibility of the products applied on stone specimens

The chromatic variations, induced by the treatments, were determined by the total colour difference ΔE^*. The conditions were illuminant C and observer $10°$ by using a solid reflection spectrophotometer (ColorFlex model, from HunterLab) [30]. The measurement was carried out on five different points for each surface sample (the four corners and the centre).

The changes in water vapour diffusivity induced by the treatments were evaluated by an automatic setup, developed in our laboratory [31]. Specifically, a slab of $4 \times 4 \times 1$ cm was obtained from each stone sample under study. The sample was placed as a cover over a cup consisting of a methacrylate cube, maintaining an interior moisture saturated ambient (RH 98%). The cup with the sample was placed into a methacrylate climatic chamber. Specifically, the sample inside the chamber was hung from a modified balance connected to weight recording software. The laboratory temperature was maintained at $17\,°C$ during the experiment. A RH of 3% was achieved in the chamber by means of a desiccating agent. The moisture gradient between the cup and the chamber promoted a water vapour flux. The monitoring of the cup weight allowed the determination of the vapour transport.

2.3.4. Behavior of products within the stone pore structure

The change in the morphology of the treated samples was evaluated on the cross-sectional surfaces of the sandstones by the SCA test carried out at different depths. In addition, to confirm the penetration depth of the products under study: (1) Water droplets with methylene blue were deposited on cross-sectional surfaces of treated and untreated samples. (2) The changes in the topography

of the treated and untreated samples were visualised at a depth of 5 mm by a JEOL Quanta 200 Scanning Electron Microscope (SEM) under laboratory conditions, prior to exposure to archaeological site conditions.

3. Results and discussion

3.1. Evaluation of the archaeological site environment and the Baelo Claudia sandstone

The meteorological data obtained during the sampling period show monthly maximum average temperatures ranging from $30.8\,°C$ in August to $11.5\,°C$ in December. The monthly minimum temperatures, ranged from $24.6\,°C$ in August to $2.5\,°C$ in February. The distribution of the rainfall values during the period of study was completely heterogeneous. The period from June to August exhibited values near to 0 mm, whereas the highest rainfall was recorded in the month of November, with a value of 55.6 mm. Regarding the Relative Humidity (RH), the average value was around 72% during the whole period because of the proximity to the sea. Concerning wind, it had a heterogeneous speed distribution (with an annual average value around 10 km/h) with prevailing Easterly components, which reached monthly maximum average values around 77 km/h in November.

The chemical analysis of the soluble fraction of SP revealed high concentrations of Cl^- and Na^+. It can be related to the deposition of marine aerosol (NaCl) transported by wind. The values obtained for the metals analysis show a low concentration of metals (Ba, Fe and Zn) associated to anthropogenic activities. [32]. The EDX analyses of the insoluble SP fraction showed typical elements of natural environments (Si, Al, Ca, Mg and Fe) [33]. In addition, some particles of biological origin, which are composed of insect remains, diatomite and plant debris, are also observed in the SP.

The sandstone from Baelo Claudia shows a yellowish-beige colour and pores which are visible to the naked eye (Fig. 2A), where different bioclasts can be recognised, mainly fragments of shells, as
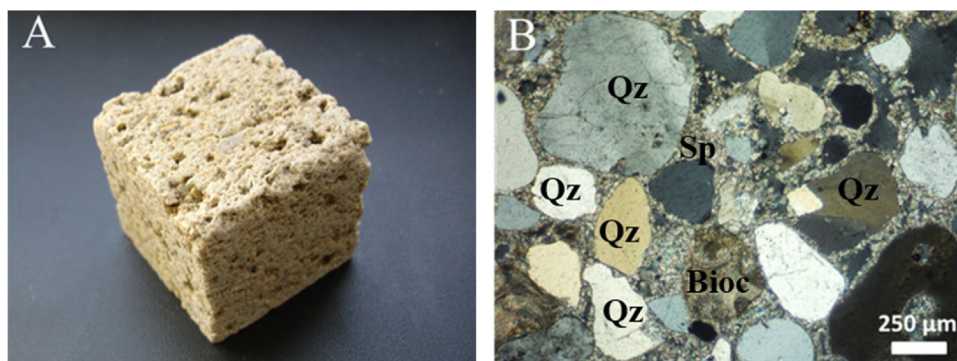
Fig. 2. (A) Photograph of sandstone sample extracted from Baelo Claudia quarry; (B) Optical photomicrograph of Baelo Claudia sandstone.

Table 1
Uptake and dry-matter values of the products applied on the stone samples.

Sample	Uptake, U (%w/w)	Dry-matter, D (%w/w)	D/U (% w/w)
BSOH100	6.98 ± 0.37	2.82 ± 0.49	40.40
BS290	5.93 ± 0.25	0.78 ± 0.17	13.15
UCA	6.40 ± 0.22	4.39 ± 0.96	68.59

well as small clasts of quartz (Qz). A large number of quartz clasts with sizes ranging from 50 μm to 500 μm, and a low proportion of bioclasts (Bioc) can be observed in the optical micrograph Fig. 2B. Regarding the matrix, re-crystallisation of sparite or microsparite (Sp) is clearly observed.

3.2. Evaluation of effectiveness and durability on sandstone

3.2.1. Sandstone-product interaction

Table 1 shows the uptake (U) and dry-matter (D) values for the products under study. The uptake values were similar for the three applied products. This can be related to the close viscosity values of the products (2.49, 3.13 and 5.35 mPa·s for BSOH100, BS290 and UCA, respectively). However, significant differences were observed for the dry-matter values. Specifically, BS290 showed the lowest dry-matter value as a consequence of its dilution in ethanol, as reported in a previous paper [34]. Its D/U ratio (13%) demonstrated that practically all the solvent was evaporated. In the case of the solvent-free products (BSOH100 and UCA), they showed higher D/U values (40 and 68%, respectively). In this case, the mass reduction is due to the removal of water and ethanol, produced during hydrolysis and condensation reactions, during the drying process.

Fig. 3 shows the percentage weight variation with respect to the dry-matter value (which is taken as zero at 0 years) of the treated and untreated samples placed at the archaeological site. The untreated samples showed gradual loss of weight over a three-year exposure period, this loss being higher during the third year. These stone material losses, during the exposure time, can be related to the dissolution of carbonate cement as a consequence of NaCl crystallisation processes [35], due to marine aerosols, which are very abundant in this area [2]. In addition, the material loss can also be related to the effect of the strong winds in this area, which exert an abrasive effect on the stone surface [5].

Similar behaviour was observed in the stones treated with the three products after exposure to outdoor conditions, which resulted in a reduction of dry matter during the first year. This can be associated with condensation/drying processes of the products being completed during the first year. In a previous paper [14], the presence of ethoxy groups from non-hydrolysed oligomers was observed in the UCA product after 6 months of the synthesis, confirming the incomplete condensation of the product. This decrease was more significant in the case of samples treated with BSOH100

and UCA. Regarding the second and third years of exposure, the weight was maintained as stable, with a slight increase shown for BSOH100 during the third year, which can be attributed to experimental fluctuations in the weight of the samples.

Changes in the porosity after exposure to the environmental conditions were evaluated by MIP. The average values of total porosity are presented in Fig. 3C. In addition, these values are also presented as numbers in Table S1, in Supplementary Material. The untreated samples presented a total porosity of around 20. All the products promoted a reduction in total porosity, due to their presence in the pores of the sandstone [36,37]. BSOH100 and BS290 showed a porosity of around 15%, whereas UCA caused a higher decrease (porosity of 12%). Regarding the porosity evolution during the archaeological site exposure, the values were maintained practically constant with the following exceptions: (i) the porosity of BS290-treated samples increased in the years 2–3 as a consequence of the material decay, as discussed later in the SEM results; (ii) the UCA treated samples increased their porosity during the first year due to the product condensation/drying processes.

Fig. 4 shows the distribution of the pore diameter obtained by MIP. The untreated sample presents a pore distribution, mainly located in two intervals: 5–30 and 30–200 μm, corresponding to 20% and 76% of the porous volume, respectively. In addition, 2% of the porosity is located in the microporous region ($<0.1\ \mu$m). In the case of the treated samples, a significant reduction in the macropores (30–200 μm) is observed for the products BSOH100 and UCA (34%), while the samples treated with the product BS290, presented a significantly lower reduction (4%), due to the presence of less dry-matter, as previously discussed.

After the exposure to outdoor conditions, a significant increase in the 30–200 μm pore range was observed for the untreated and BS290 treated samples, due to the material loss in the superficial area, as a consequence of the cracking of the product on the surface, as discussed later in the SEM results. In the other pore ranges, the changes were negligible. As previously reported [38,39], salt deposition mainly occurs in the larger pores of the stone, near to the surface.

The morphology of the sandstone surfaces was investigated by SEM. The images obtained are shown in Fig. 5. Before *in-situ* exposure, the untreated sample (Fig. 5A) shows heterogeneous surfaces, due to the fragments of quartz crystals and calcite, which form the stone. The samples treated with the three products under study significantly modified their morphology. The BSOH100 product (Fig. 5B) shows a dense silica gel coating, where typical cracks of a microporous gel are observed, which are generated by the high capillary pressure supported by this gel during its drying into the stone [40]. The samples treated with the BS290 product show a continuous crack-free coating on the stone surface (Fig. 5C), due to the effect of the organosiloxane reducing the surface tension and subsequently the capillary pressure [41]. In the case of the
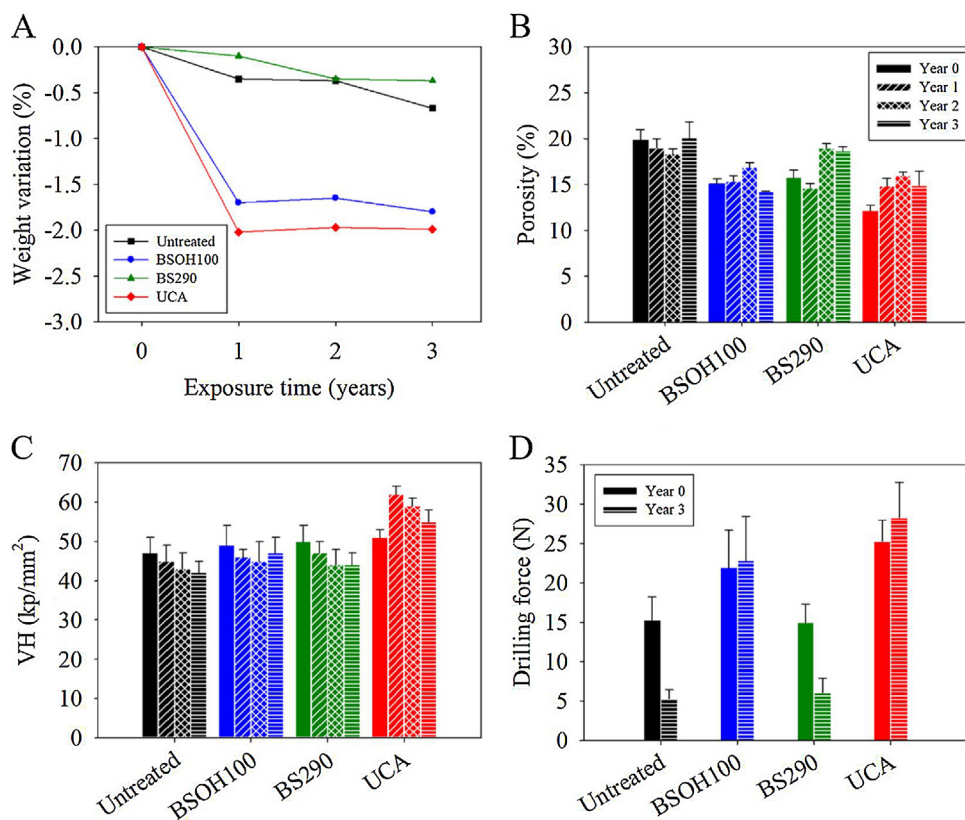
Fig. 3. (A) Weight variation, (B) Porosity, (C) Vickers hardness (VH) and (D) Drilling force values of the treated sandstone samples and their untreated counterpart under laboratory conditions (0 years) and after each year of exposure.
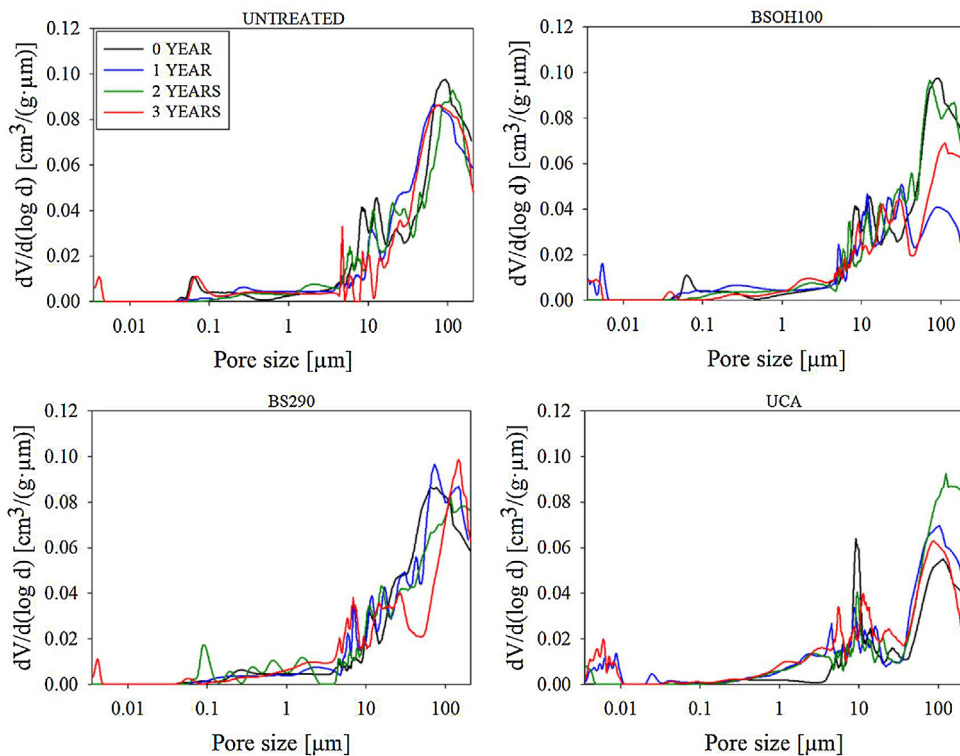

Fig. 4. Pore size distributions of the treated and untreated stones, before (0 years) and after each year of exposure.

UCA product (Fig. 5D), a continuous crack-free coating was produced as a consequence of the role played by n-octylamine. This promotes the formation of a mesoporous gel by an inverse micelle mechanism, reducing capillary pressure during drying [15]. In addition, the presence of PDMS also contributes to reducing capillary pressure [37,41].
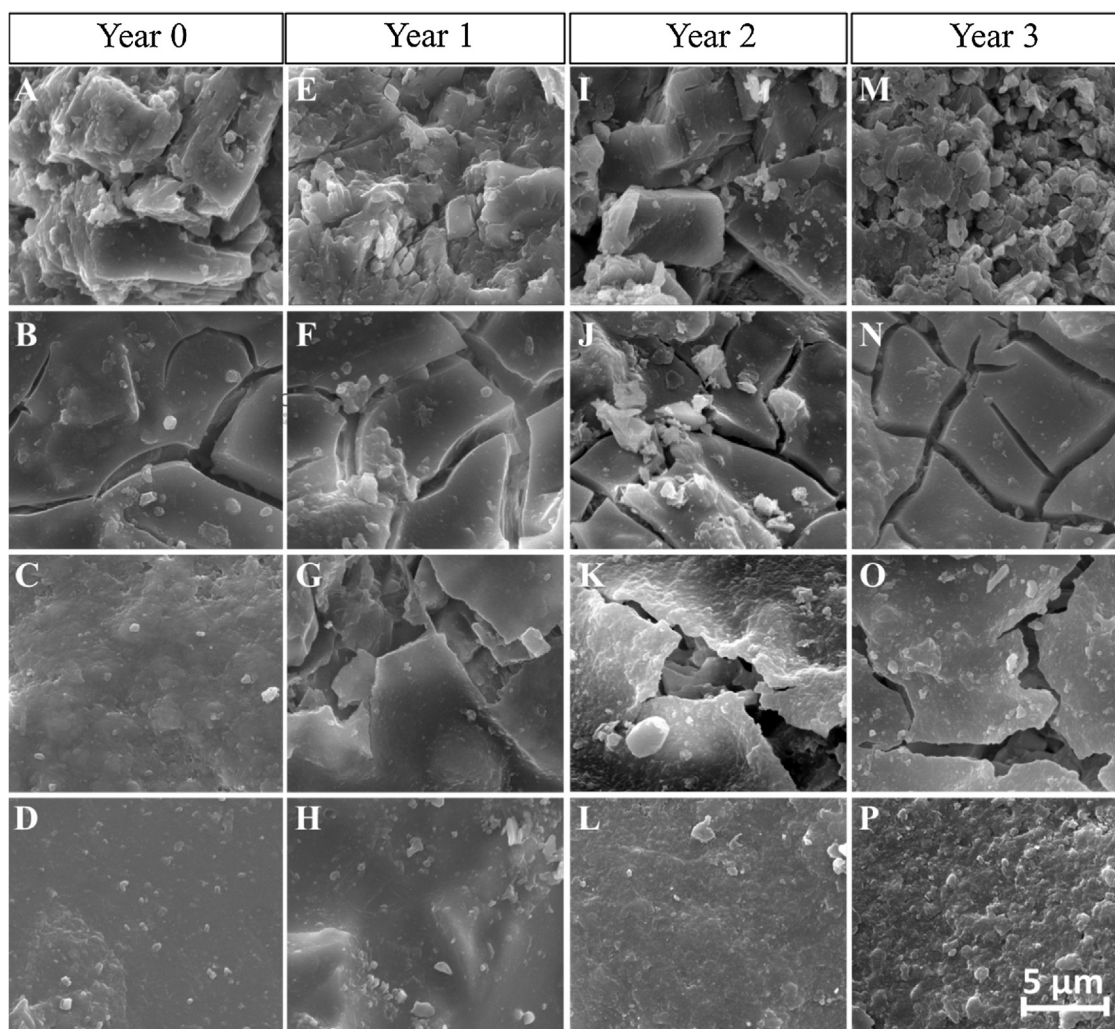
Fig. 5. SEM images of the stone surface, before, during and after, three years of exposure: (A, E, I, M) untreated, (B, F, J, N) BSOH100, (C, G, K, O) BS290, (D, H, L, P) UCA.

After each year of exposure to environmental conditions, cracking gradually increased in the BSOH100 coating (Fig. 5F–N), as a consequence of the weathering effects, reducing its mechanical properties. The BS290 product suffered gradual cracking in its coating, due to its low penetration into the pore structure of the stone promoting a low durability, as discussed later. After the three years of evaluation the UCA product showed a slight increase in stone surface roughness due to decay agents. However, a continuous crack-free coating was observed even after three years of exposure. It highlights that the UCA product was able to adhere firmly to the surface, providing high stability and resistance over a long period [42].

3.2.2. Evaluation of the effectiveness of the products

The consolidant effectiveness of the products on the sandstone surface was calculated by the Vickers hardness test. The obtained results are presented in Fig. 3C. In addition, these values are also presented as numbers in Table S2, in Supplementary Material. All the treatments increased the resistance of the sandstone surfaces compared to the untreated samples, the highest increase corresponding to the UCA product. After the exposure to outdoor conditions, the untreated samples showed a gradual reduction in Vickers hardness values with the time of exposure. In the case of the two commercial products, the Vickers hardness values were similar to those obtained for the untreated samples after the first year of exposure. This reduction in hardness can be related to the presence

of cracks in the coatings, as observed in SEM images (Fig. 5). The samples treated with the UCA product showed an increase in Vickers hardness at the end of the first year, which could be associated with the condensation/drying processes. The weight loss and the increase in porosity observed for UCA treated samples after the first year support this hypothesis. It is also supported by the changes in colour and vapour diffusivity observed, as discussed later. These processes also took place for BSOH100. However, the cracking of this product during drying promoted the observed reduction in hardness.

The consolidant effectiveness of the different treatments was also evaluated by a DRMS test. The obtained results are presented in Fig. 3D. In addition, these values are also presented as numbers in Table S3, in Supplementary Material. The untreated samples showed a significant decrease in their resistance in line with the exposure time. After the application of the treatments, BSOH100 and UCA products improved the mechanical resistance of the stones. In the case of BS290, the increase in mechanical resistance was not significant. The UCA product showed the best performance compared to the two commercial products, due to the formation of an homogeneous coating that was maintained during the three years of exposure to the archaeological site conditions.

The effectiveness of the coatings in providing hydrophobic properties was characterised by measuring the SCA of water droplets deposited on the surfaces of the treated and the untreated samples (Fig. 6A). In addition, these values are also presented as numbers in
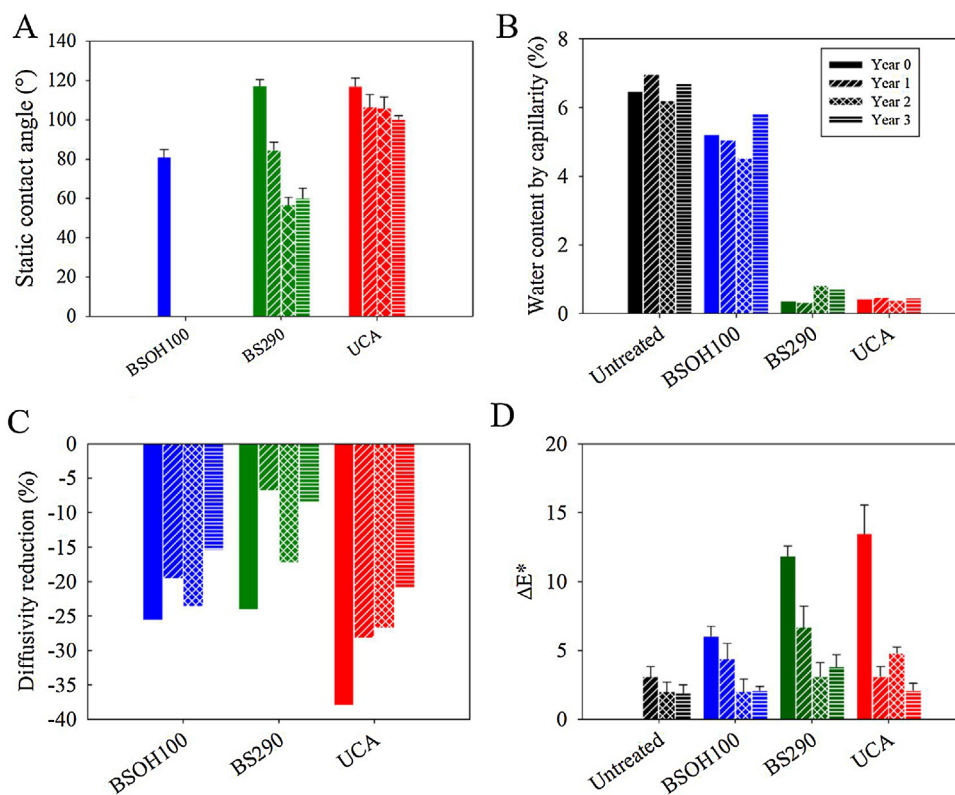
Fig. 6. (A) Static Contact Angle, (B) Water content by capillarity, (C) Vapour diffusivity reduction and (D) Total colour difference (ΔE^*) of the treated and untreated stones, before and after three years of exposure.

Table S4, in Supplementary Material. In the case of the untreated samples, the SCA value was zero, indicating the totally hydrophilic character of this stone. In spite of BSOH100 not being a hydrophobic product, the surfaces treated with it showed an SCA of 80° due to the presence of ethoxy groups [15]. The BS290 and UCA products created hydrophobic coatings on the surfaces of the stones, presenting SCA values greater than 90°. The hydrophobic properties of the UCA product were obtained by the effect of the organic component (PDMS), reducing the surface energy of the stone. The hydrophobic properties of BS290 were attributed to the alkyl groups directly attached to silicon [42].

The durability of the hydrophobic properties was assessed by determining the SCA on the surfaces after each year of exposure to the outdoor conditions (Fig. 6A). As expected, BSOH100 showed a total loss of SCA, during the first year of exposure, due to the hydrolysis of ethoxy groups. BS290 showed a gradual reduction in SCA during the three years of exposure, reaching values of 60° after the third year of exposure. This reduction can be related to the formation of cracks on the surface of the coating. The UCA product presented a gradual reduction of SCA during the three years of exposure, however, hydrophobic properties were maintained (SCA > 100°).

To confirm the hydrophobic behaviour of the materials under study, a water absorption test by capillarity was carried out (Fig. 6B and Table S5 in Supplementary Material). The untreated sample showed the higher water uptake, being practically unmodified during the three years of exposure. In the case of samples treated with the BSOH100 product, a decrease in water uptake with respect to the untreated samples was observed due to two reasons: (i) reduction of porosity because the product fills the stone pores; (ii) incomplete condensation of BSOH100 during the first year, involving the presence of ethoxy groups in the product which is responsible for the water absorption reduction during this period, as discussed in previous papers [43]. The reduction in weight of

Table 2
Static CA values on the cross-sections of the untreated and the treated sandstone, before, during and after three years of exposure.

Sample	Interval (mm)	Static contact angle (°)			
		0 year	1 year	2 years	3 years
BSOH100	0	81 ± 4	–	–	–
	0–5	–	–	–	–
	5–10	–	–	–	–
	10–15	–	–	–	–
	15–20	–	–	–	–
BS290	0	117 ± 3	85 ± 4	57 ± 4	60 ± 5
	0–5	53 ± 3	61 ± 2	60 ± 2	74 ± 8
	5–10	57 ± 4	76 ± 5	52 ± 2	74 ± 8
	10–15	47 ± 3	73 ± 6	69 ± 6	65 ± 9
	15–20	70 ± 2	69 ± 2	57 ± 4	64 ± 3
UCA	0	117 ± 4	106 ± 6	106 ± 5	100 ± 2
	0–5	128 ± 1	109 ± 1	111 ± 1	95 ± 9
	5–10	118 ± 1	110 ± 1	110 ± 1	96 ± 6
	10–15	108 ± 7	100 ± 1	93 ± 7	95 ± 4
	15–20	100 ± 4	102 ± 1	100 ± 3	87 ± 6

samples treated with BSOH100 during the first year, as previously discussed (Fig. 3A), also confirm this hypothesis. The samples treated with the BS290 and UCA products presented water uptakes close to zero, before their exposure to the archaeological site conditions, due to their hydrophobic properties. In the case of BS290, a slight increase in the water absorption values was observed, due to the loss of hydrophobic properties, whereas the UCA product remained unaltered after three years of exposure.

3.2.3. Compatibility of the products applied on stone specimens

Fig. 6C shows the percentage reduction in vapour diffusivity for the treated samples with respect to the untreated samples (numeric values are included in Table S6 in Supplementary Material). All the products promoted a reduction in the coefficient of
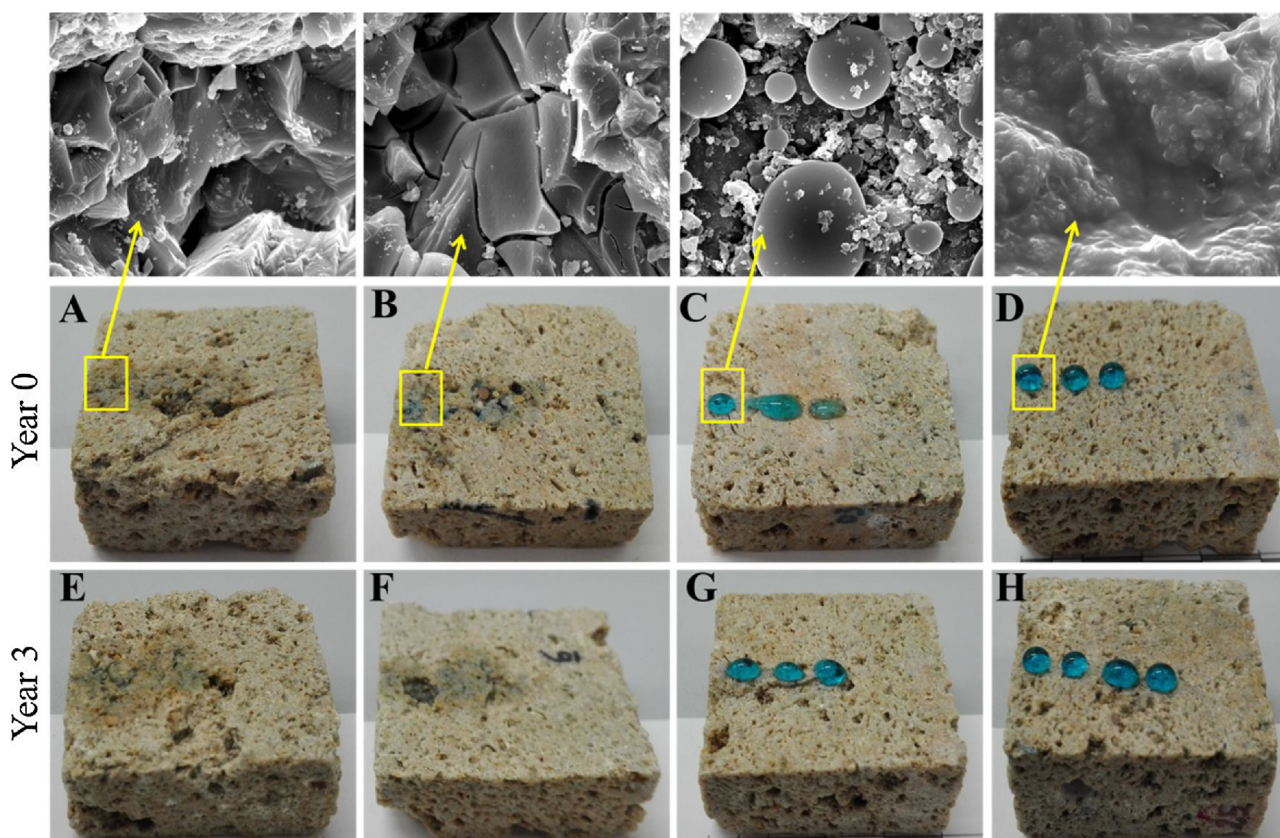
Fig. 7. Photographs of cross-sections and SEM images of the sandstone samples, before and after exposure: (A, E) untreated, (B, F) BSOH100, (C, G) BS290, (D, H) UCA.

vapour diffusivity of below 25%, except for the UCA product (38%), prior to archaeological site exposure. Reduction values between 10–50% show an acceptable compatibility with the substrate [44] (medium risk incompatibility). As a general trend, all the treated stones showed a lower reduction in vapour diffusivity values as the exposure time is increased. From these results, a clear relationship between permeability and porosity, and even dry matter values is observed.

The colour variations induced by the different products were evaluated by the ΔE^* (total colour difference). The values obtained are shown in Fig. 6D. In addition, Tables S7 and S8, in Supplementary Material, show numeric values for ΔE^* and Δb^*, respectively. According to Delgado-Rodrigues and Grossi [44], values between 3 and 5 imply a medium risk of incompatibility. In addition, Berns [30] indicate that 3 is the limit for human eye perception. After application on stones, all treatments presented values of ΔE^* greater than 5. The samples treated with the UCA product showed the highest value, which is mainly caused by a significant reduction in the luminosity parameter ($\Delta L^* = -12.6$). Moreover, Δb^* showed an increase in value (5.20), which matches a yellowing of the treated surface. After exposure to the environmental conditions, a significant reduction in the ΔE^* values were observed for all the treatments under study, after the first year of exposure. This can be related to the condensation and drying of the products during this first year, as previously discussed. In all the cases, the ΔE^* values were below the threshold of compatibility ($\Delta E^* < 3$) [33,44]. After the first year of exposure, the ΔE^* values were not significantly modified for the three products under study.

3.2.4. Behaviour of products within the stone pore structure

The behaviour of the products within the pore structure was evaluated based on the hydrophobic performance of the products under study. Specifically, SCAs were obtained for cross-sections of the specimens at different depths, ranging from the surface (0 mm) to 20 mm. The obtained results are shown in Table 2. In the case of the untreated samples, the SCA value was zero at all intervals evaluated, indicating the totally hydrophilic character of this stone. The commercial consolidant BSOH100 showed an SCA of around 80° under laboratory conditions, becoming completely hydrophilic at the different evaluated depths and after archaeological site exposure. The commercial product BS290 showed a high SCA at the surface, while hydrophobicity was lost at all depths evaluated. The same trend was observed after exposure to outdoor conditions. SCA values below 90° were obtained after the first year of exposure. In the case of the UCA product, the SCA values were maintained above 90° at all the evaluated depths. These values were maintained after exposure to the environmental conditions. To illustrate the behaviour of the products within the pore structure, Fig. 7 shows photographs of water droplets stained with methylene blue, deposited on cross-sectional surfaces of treated, and untreated samples, prior to exposure to archaeological site conditions (0 years). In the case of the untreated samples and samples treated with the BSOH100 product, all the drops deposited were completely absorbed, whereas the CAs of the UCA-treated sample were significantly higher than those observed in BS290-treated sample at all depths evaluated. The cross-sections of the samples under study corresponding to the 5 mm depth were visualised by SEM. The images obtained are shown in Fig. 7. In the case of the samples treated with BSOH100, a cracking coating is observed in the porous structure of the stone, with a similar appearance to that observed on the surface (Fig. 5B). The sample treated with BS290 showed a different appearance to that obtained in the surface (Fig. 5C). In the stone surface, a homogeneous coating of product is observed, whereas isolated siloxane aggregates are clearly

observed in the porous structure at the 5 mm depth (Fig. 7). This result shows that the BS290 product only created a thin coating layer on the surface, as expected in a hydrophobic coating. Finally, the UCA product produced a homogeneous coating in the pores of the stone. The SEM image showed quartz grains covered by the mesostructured coating. From these results, it can be concluded that BSOH100 and UCA products were able to penetrate into the porous structure of the stone. However, BSOH100 cracked, with the consequent loss of effectiveness. Thus, UCA was the only one, which presented suitable performance and durability during the three years of exposure to the archaeological site conditions.

4. Conclusions

The present study represents a preliminary investigation about long-term effectiveness of a novel stone conservation nanomaterial by exposure, during 3 years, to real conditions, at an archaeological site. The obtained results allow it to be concluded that the hydrophobic/consolidant nanomaterial under study produced a crack-free coating, with homogeneous penetration into the pore structure of the stone, maintaining its properties after 3 years of exposure to the Baelo Claudia conditions. In the case of the commercial products evaluated, they produced crack-free coatings with poor penetration, promoting a significant loss of their properties after in-situ exposure for three years. Regarding the negative effects caused by the treatments, the UCA product gave rise to a reduction of permeability and a significant colour change. However, both negative effects were reduced after one year of exposure due to the drying of the product. Finally, in order to corroborate the conclusions obtained from this preliminary study, a more complete investigation will be carried out in the future by increasing the number of tested samples.

Appendix A. Supplementary data

Supplementary data associated with this article can be found, in the online version, at https://doi.org/10.1016/j.culher.2018.04.013.

References

[1] F. Zezza, F. Macrì, Marine aerosol and stone decay, Sci. Total Environ. 167 (1) (1995) 123–143, http://dx.doi.org/10.1016/0048-9697(95)04575-L.
[2] K. Torfs, R. Van Grieken, Chemical relations between atmospheric aerosols, deposition and stone decay layers on historic buildings at the Mediterranean coast, Atmos. Environ. 31 (15) (1997) 2179–2192, http://dx.doi.org/10.1016/S1352-2310(97)00038-1.
[3] D. Benavente, S. Sanchez-Moral, A. Fernandez-Cortes, J.C. Cañaveras, J. Elez, C. Saiz-Jimenez, Salt damage and microclimate in the Postumius Tomb, Roman Necropolis of Carmona, Spain, Environ. Earth Sci. 63 (7) (2011) 1529–1543, http://dx.doi.org/10.1007/s12665-010-0815-9.
[4] N.A. Stefanis, P. Theoulakis, C. Pilinis, Dry deposition effect of marine aerosol to the building stone of the medieval city of Rhodes, Greece, Build. Environ. 44 (2) (2009) 260–270, http://dx.doi.org/10.1016/j.buildenv.2008.03.001.
[5] A. Erkal, D. D'Ayala, L. Sequeira, Assessment of wind-driven rain impact, related surface erosion and surface strength reduction of historic building materials, Constr. Build. 57 (2012) 336–348, http://dx.doi.org/10.1016/j.buildenv.2012.05.004.
[6] P.K. Sharma, M. Khandelwal, T.N. Singh, Variation on physico-mechanical properties of Kota stone under different watery environments, Build. Environ. 42 (12) (2007) 4117–4123, http://dx.doi.org/10.1016/j.buildenv.2006.11.032.
[7] Th. Warscheida, J. Braams, Biodeterioration of stone: a review, Int. Biodeterior. Biodegrad. 46 (4) (2000) 343–368, http://dx.doi.org/10.1016/S0964-8305(00)00109-8.
[8] S. Siegesmund, R. Snethlage (Eds.), Stone in architecture: properties, durability, Springer, London, 2014.
[9] G. Wheeler, Alkoxysilanes and the consolidation of stone, The Getty conservation institute, Los Angeles, 2005.
[10] T. Poli, L. Toniolo, O. Chiantore, The protection of different Italian marbles with two partially fluorinated acrylic copolymers, Appl. Phys. A 79 (2) (2004) 347–351, http://dx.doi.org/10.1007/s00339-004-2530-4.
[11] S.R. Coulson, I. Woodward, J.P.S. Badyal, S.A. Brewer, C. Willis, Super-repellent composite fluoropolymer surfaces, J. Phys. Chem. B 104 (37) (2000) 8836–8840, http://dx.doi.org/10.1021/jp0000174.
[12] I. Karapanagiotis, A. Pavlou, P.N. Manoudis, K.E. Aifantis, Water repellent ORMOSIL films for the protection of stone and other materials, Mater. Lett. 131 (15) (2014) 276–279, http://dx.doi.org/10.1016/j.matlet.2014.05.163.
[13] H. Zhanga, Q. Liub, T. Liub, B. Zhanga, The preservation damage of hydrophobic polymer coating materials in conservation of stone relics, Prog. Org. Coat. 76 (7) (2013) 1127–1134, http://dx.doi.org/10.1016/j.porgcoat.2013.03.018.
[14] M.J. Mosquera, D.M. de los Santos, T. Rivas, P. Sanmartín, B. Silva, New nanomaterials for protecting and consolidating stone, J. Nano Res. 8 (2009) 1–12, http://dx.doi.org/10.4028/www.scientific.net/JNanoR.8.1.
[15] J.F. Illescas, M.J. Mosquera, Producing surfactant-synthesized nanomaterials in situ on a Building Substrate, without Volatile Organic Compounds, A.C.S, Appl. Mater. Interfaces 4 (8) (2012) 4259–4269, http://dx.doi.org/10.1021/am300964q.
[16] D.S. Facio, M. Luna, M.J. Mosquera, Facile preparation of mesoporous silica monoliths by an inverse micelle mechanism, Microporous Mesoporous Mater. 247 (2017) 166–176, http://dx.doi.org/10.1016/j.micromeso.2017.03.041.
[17] R. Zarzuela, M. Luna, L.A.M. Carrascosa, M.J. Mosquera, Preserving cultural heritage stone: innovative consolidant, superhydrophobic, self-cleaning and biocidal products In: M. Hosseini, I. Karapanagiotis (Eds.), Advanced materials for the conservation of stone, vol. 1, Springer International Publishing.
[18] M. Favaro, R. Mendichi, F. Ossola, S. Simon, P. Tomasin, P.A. Vigato, Evaluation of polymers for conservation treatments of outdoor exposed stone monuments. Part I: Photo-oxidative weathering, Polym. Degrad. Stabil. 91 (12) (2006) 3083–3096, http://dx.doi.org/10.1016/j.polymdegradstab.2006.08.012.
[19] M. Favaro, R. Mendichi, F. Ossola, S. Simon, P. Tomasin, P.A. Vigato, Evaluation of polymers for conservation treatments of outdoor exposed stone monuments. Part II: Photo-oxidative and salt-induced weathering of acrylic-silicone 92 (3) (2007) 335–351, http://dx.doi.org/10.1016/j.polymdegradstab.2006.12.008.
[20] M.J. Mosquera, L.A.M. Carrascosa, N. Badreldin, Producing superhydrophobic/oleophobic coatings on Cultural Heritage building materials, Pure Appl. Chem. 90 (3) (2017) 1–12, http://dx.doi.org/10.1515/pac-2017-0404.
[21] I. De Rosario, F. Elhaddad, A. Pan, R. Benavides, T. Rivas, M.J. Mosquera, Effectiveness of a novel consolidant on granite: laboratory and in situ results, Constr. Build. Mater. 76 (2015) 140–149, http://dx.doi.org/10.1016/j.conbuildmat.2014.11.055.
[22] I. De Rosario, T. Rivas, G. Buceta, J. Feijoo, M.J. Mosquera, Surfactant-Synthesized consolidants applied to a granitic medieval Necropolis in NW Spain. Laboratory and In situ effectiveness evaluation, Int. J. Archit. Herit. 11 (8) (2017) 1166–1176, http://dx.doi.org/10.1080/15583058.2017.1354097.
[23] L. de Ferri, P.P. Lottici, A. Lorenzi, A. Montenero, E. Salvioli-Mariani, Study of silica nanoparticles–polysiloxane hydrophobic treatments for stone-based monument protection, J. Cult. Herit. 12 (4) (2011) 356–363, http://dx.doi.org/10.1016/j.culher.2011.02.006.
[24] G. Cappelletti, P. Fermo, M. Camiloni, Smart hybrid coatings for natural stones conservation, Prog. Org. Coat. 78 (2015) 511–516, http://dx.doi.org/10.1016/j.porgcoat.2014.05.029.
[25] C.E. Corcione, N. De Simone, M.L. Santarelli, M. Frigione, Protective properties and durability characteristics of experimental and commercial organic coatings for the preservation of porous stone, Prog. Org. Coat. 103 (2017) 193–203, http://dx.doi.org/10.1016/j.porgcoat.2016.10.037.
[26] A. Bonazza, G. Vidorni, I. Natali, C. Ciantelli, C. Giosuè, F. Tittarelli, Durability assessment to environmental impact of nano-structured consolidants on Carrara marble by field exposure tests, Sci. Total Environ. 575 (2017) 23–32, http://dx.doi.org/10.1016/j.scitotenv.2016.10.004.
[27] F. Gherardi, D. Gulotta, S. Goidanich, A. Colombo, L. Toniolo, On-site monitoring of the performance of innovative treatments for marble conservation in architectural heritage, Herit. Sci. 5 (2017) 1–15, http://dx.doi.org/10.1186/s40494-017-0118-5.
[28] J.M. Bernabe, M.I. Carretero, E. Galan, Mineralogy and origin of atmospheric particles in the industrial area of Huelva (SW Spain), Atmos. Environ. 39 (36) (2005) 6777–6789, http://dx.doi.org/10.1016/j.atmosenv.2005.07.073.
[29] UNE-EN 1925, Natural stone test methods, Determination of water absorption coefficient by capillarity, AENOR, 199.
[30] R.S. Berns, Billmeyer and Saltzman's principles of color technology, Wiley-Interscience, New York, 2000.
[31] M.J. Mosquera, D. Benitez, S.H. Perry, Pore structure in mortars applied on restoration: effect on properties relevant to decay of granite buildings, Cem. Concr. Res. 32 (12) (2002) 1883–1888, http://dx.doi.org/10.1016/S0008-8846(02)00887-6.

[32] N. Prieto-Taboada, I. Ibarrondo, O. Gómez-Laserna, I. Martinez-Arkarazo, M.A. Olazabal, J.M. Madariaga, Buildings as repositories of hazardous pollutants of anthropogenic origin, J. Hazard. Mater. 248–249 (2013) 451–460, http://dx.doi.org/10.1016/j.jhazmat.2013.01.008.

[33] Z. Cong, S. Kang, X. Liu, G. Wang, Elemental composition of aerosol in the Nam Co region, Tibetan Plateau, during summer monsoon season, Atmos. Environ. 41 (6) (2007) 1180–1187, http://dx.doi.org/10.1016/j.atmosenv.2006.09.046.

[34] D.S. Facio, M.J. Mosquera, Simple strategy for producing superhydrophobic nanocomposite coatings in situ on a building substrate, ACS Appl. Mater. Interfaces 5 (15) (2013) 7517–7526, http://dx.doi.org/10.1021/am401826.

[35] C. Cardell, F. Delalieux, K. Roumpopoulos, A. Moropoulou, A. Auger, R. Van Grieken, Salt-induced decay in calcareous stone monuments and buildings in a marine environment in SW France, Constr. Build. Mater. 17 (3) (2003) 165–179, http://dx.doi.org/10.1016/S0950-0618(02)00104-6.

[36] P. Maravelaki-Kalaitzaki, N. Kallithrakas-Kontos, D. Korakaki, Z. Agioutantis, S. Maurigiannakis, Evaluation of silicon-based strengthening agents on porous limestones, Prog. Org. Coat. 57 (2006) 140–148, http://dx.doi.org/10.1016/j.porgcoat.2006.08.007.

[37] J.F. Illescas, M.J. Mosquera, Surfactant-Synthesized PDMS/Silica Nanomaterials improve robustness and stain resistance of carbonate stone, J. Phys. Chem. C 115 (2011) 14624–14634, http://dx.doi.org/10.1021/am300964q.

[38] E. Ruiz-Agudo, F. Mees, P. Jacobs, C. Rodriguez-Navarro, The role of saline solution properties on porous limestone salt weathering by magnesium and sodium sulfates, Environ. Geol. 52 (2) (2007) 269–281, http://dx.doi.org/10.1007/s00254-006-0476-x.

[39] C. Rodriguez-Navarro, E. Doehne, Salt weathering: influence of evaporation rate, supersaturation and crystallization pattern, Earth Surf. Process. Landforms 24 (3) (1999) 191–209, http://dx.doi.org/10.1002/(SICI)1096-9837.

[40] M.J. Mosquera, J. Pozo, L. Esquivias, Stress during drying of two stone consolidants applied in monumental conservation, J. Sol-Gel Sci. Technol. 26 (2003) 1227–1231, http://dx.doi.org/10.1023/A:1020776622689.

[41] M.J. Mosquera, D.M. de los Santos, T. Rivas, Surfactant-synthesized ormosils with application to stone restoration, Langmuir 26 (2010) 6737–6745, http://dx.doi.org/10.1021/la9040979.

[42] L.A.M. Carrascosa, D.S. Facio, M.J. Mosquera, Producing superhydrophobic roof tiles, Nanotechnology 27 (9) (2016) 095604–095616, http://dx.doi.org/10.1088/0957-4484/27/9/095604.

[43] L. Pinho, M.J. Mosquera, Titania-silica nanocomposite photocatalysts with application in stone self-cleaning, J. Phys. Chem. C. 115 (46) (2011) 22851–22862, http://dx.doi.org/10.1021/jp2074623.

[44] J. Delgado-Rodrigues, A. Grossi, Indicators and ratings for the compatibility assessment of conservation actions, J Cult Herit. 8 (1) (2007) 32–43, http://dx.doi.org/10.1016/j.culher.2006.04.007.

MDPI

Article

Long-Term Effectiveness, under a Mountain Environment, of a Novel Conservation Nanomaterial Applied on Limestone from a Roman Archaeological Site

Farid Elhaddad, Luis A. M. Carrascosa [ID] **and Maria J. Mosquera** * [ID]

TEP-243 Nanomaterials Group, Departamento de Química-Física, Facultad de Ciencias, Campus Universitario Río San Pedro, Universidad de Cádiz, Puerto Real, 11510 Cádiz, Spain; farid.elhaddad@uca.es (F.E.); luis.martinez@uca.es (L.A.M.C.)

* Correspondence: mariajesus.mosquera@uca.es; Tel.: +34-956-016-331

check for updates

Abstract: A novel alkoxysilane-based product was applied on limestone samples from a Roman archaeological site. The study consisted of an initial phase to evaluate site environmental conditions in order to choose the most suitable product type to be applied. The decay that was produced in the site is mainly caused by natural action, with water being the main vehicle for the decay agents. Thus, the effectiveness of an innovative product with hydrophobic/consolidant properties and two commercial products (consolidant and hydrophobic agent) were evaluated on limestone from Acinipo site, under laboratory conditions. Next, the long-term effectiveness of the three products under study was evaluated by the exposure of limestone samples in the archaeological site for a period of three years. Since the recognized incompatibility between alkoxysilanes and pure carbonate stones, the interaction between the products and the limestones was widely investigated. The results that were obtained allow for it to be concluded that the innovative product presents adequate compatibility and adherence to the limestone under study, producing a long-term effective, homogeneous, and continuous coating with a depth of penetration of up to 10 mm. However, the commercial products produced discontinuous aggregates on the limestone surface, did not penetrate into its porous structure and it did not produce long-lasting effects.

Keywords: archaeological site; hydrophobic/consolidant product; effectiveness; durability; in situ exposure

1. Introduction

Alkoxysilanes are commonly applied in the conservation of stone-based monuments. These products polymerize in situ within the pore structure of the disintegrating stone, and significantly increase the cohesion of the material [1]. Since water is the main vehicle of stone building decay agents, such as salts, microorganism, and other pollutants, organic components can be added to alkoxysilanes to produce hydrophobic products [2]. However, these products present two significant drawbacks: (1) their tendency to form brittle gels that are susceptible to cracking [3,4], and (2) their poor compatibility with carbonate stones [1,5].

Our research group has previously developed crack-free consolidants and hydrophobic products by mixing an aqueous surfactant solution and an alkoxysilane [6–8]. The surfactant, n-octylamine, prevents cracking of the gel because: (1) it increases the pore size of the gel network; and, (2) it decreases surface tension, both of which reduce capillary pressure, which is responsible for the cracking. Additionally, we

observe a suitable effectiveness of these products in limestones [9]. Recently, other studies have used our strategy in order to obtain effective consolidant and hydrophobic products [10,11].

The effectiveness and the durability of novel conservation products are commonly evaluated under standard laboratory conditions [12–17]. However, their performance and durability are rarely tested in situ, under outdoor conditions [18–25]. Specifically, our research group has evaluated the performance of the novel consolidant consisting of a silica oligomer and a surfactant (n-octylamine). It was applied on two granitic monuments in Spain: a Romanesque church [18] and a medieval necropolis [19]. In the two cases, the novel product showed a better performance than that associated to the commercial products (an acrylic resin and an ethoxysilane) tested in the study.

Nwaubani et Dumbelton [20] evaluated the effectiveness of different commercial hydrophobic and consolidating treatments that were applied to the surfaces of three historic buildings and monuments in the UK. The surface treatments were applied in the range of 7–18 years at the time of testing. The results that were obtained highlighted that some treatments were deteriorated and a re-treatment should be applied.

Bonazza et al. [21] evaluated the efficiency and durability of two calcium-based consolidant on Carrara marble samples after outdoor exposure in four different European cities for 11 months. Both of the conservative products were found to remain mainly on surface and did not penetrate deeply in the substrate. It promoted a significant loss of the consolidating layers for the samples that were exposed in the sites characterized by heavy rain events.

De Ferri et al. [22] prepared two hydrophobic products by mixing hydrophobic silica nanoparticles with oligomeric ethoxysilanes, or alternatively, with epoxy resins. The obtained products were applied on three different building stones (marbles and sandstone). The treated samples were placed outdoors for 4 months, significantly reducing their hydrophobic performance.

Cappelletti et al. [23] also produced hydrophobic coatings by mixing an oligomeric polysiloxane and TiO_2NPs. The obtained products were applied onto marble dolostone. The samples were placed at outdoor conditions for 7 months. The treatment clearly prevented the growing of salts.

Corcione et al. [24] prepared UV-cured nano-filled products by mixing trimethylolpropane trimethacrylate with a vinyl-terminated polydimethylsiloxane and an organically modified boehmite. The products were applied on two different calcarenite stones with high porosity. For comparison, two commercial products (alkylsilane-based product and acrylic resins) were also applied. The treated stones were placed outdoors at the region of Lecce (Italy) for 10 months. All of the treated stones maintained their hydrophobic properties, whereas they were significantly reduced in the case of the commercial products.

Finally, Gherardi et al. [25] dispersed TiO_2NPs in different siloxanes and organosiloxanes. The obtained products were applied on the façade of the Cathedral of Monza (Italy), which is composed of two kinds of marbles. The treated façade was evaluated for 12 months showing good effectiveness and durability for most of the evaluated products. Nevertheless, the authors highlighted that 12 months is not enough for performing a real durability test, being necessary to carry out the evaluation for three or five years. These studies about on site monitoring of the performance of conservation products were, in all the cases, below 1 year. Moreover, most of them evaluated performance evolution with a single property.

Recently, our research group carried out an ambitious project to evaluate the durability of an innovative alkoxysilane-based product that was prepared in our laboratory [8] with hydrophobic and consolidant performance under real conditions, in two different Archaeological sites. The first study was carried out on the Baelo Claudia site built of sandstone and was subjected to a coastal environment [26]. In the present work, we evaluate the effectiveness and durability of the product previously described [8], on a limestone from Acinipo archaeological site, subjected to a mountain environment. As a prior phase to this study, we evaluated the environmental conditions and discussed the possible decay mechanism of the limestone from the archaeological site under study in order to select a suitable product for its correct preservation. For comparison, two commercial products

were also evaluated. The effectiveness of these products was tested on limestone samples that were kept in situ, under the archaeological site conditions for a three-year period. Evaluation was carried out after each year of exposure. Since the recognized incompatibility between alkoxysilanes and carbonate stones [9,27], the interaction between the products under study and the limestones was widely investigated.

2. Materials and Methods

2.1. Evaluation of the Archaeological Site Environment and the Acinipo Limestone

The city of Acinipo was founded by the Romans in the first century BC. Nowadays, the Roman Theatre (Figure 1B) is the best-preserved building. In addition, ruins of the pre-Roman occupations, such as Neolithic Tartessian and Iberian villages (VIII-II centuries BC), are also preserved in this archaeological site. Acinipo is located in the south of Spain, specifically (Figure 1A) in the northeast of Ronda Mountains (Malaga) at 1000 m above sea level, and in an area of low pollution. Firstly, an analysis of the environment surrounding the site was carried out. Specifically, meteorological data of temperature, rainfall, and wind were collected for 24 months (corresponding to 2011 and 2012) from a National Institute of Meteorology station, which was situated near to the archaeological site (Figure 1A).
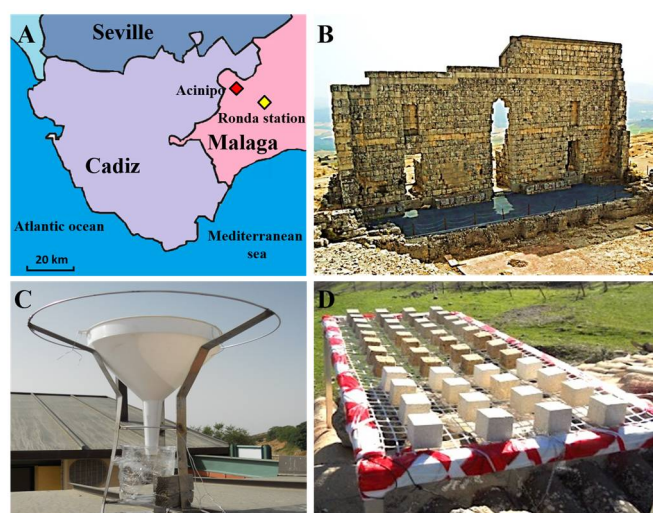

Figure 1. (**A**) Location of the archaeological site of Acinipo; (**B**) Roman theatre in the Acinipo site; (**C**) Particle collector; and, (**D**) The treated and untreated samples located at the archaeological site for three years.

In addition, an analysis of sedimentable particles (SP) that were collected during one month (August, 2012) at the archaeological site was carried out (see the SP collector in Figure 1C). Details about the SP analysis procedure are reported in a previous paper [28]. After collection, SP were rinsed with de-ionized water and filtered to separate the insoluble fraction. The chemical composition of the soluble SP fraction was determined, as follows: (1) Cl^- by titrimetry with silver nitrate; (2) $CO_3^=$ and HCO_3^- by titrimetry with HCl; (3) $SO_4^=$ and $NO_3^=$ were quantified with a UV-Vis Spectrophotometer ZUZI 4210/50 (I.C.T, S.L., La Rioja, Spain); (4) cations (Ca^{2+}, Mg^{2+}, Na^+, and K^+) by Atomic Absorption Spectroscopy (AAS) using a Perkin Elmer spectrophotometer (Perkin Elmer, Waltham, MA, USA); and, (5) identification of trace metals (see analysed metals in Figure 2) by Inductively Coupled Plasma-Mass Spectrometry (ICP-MS) with a Horiba Jobin Yvon Ultima 2 ICP (Horiba Scientific, Kyoto, Japan).
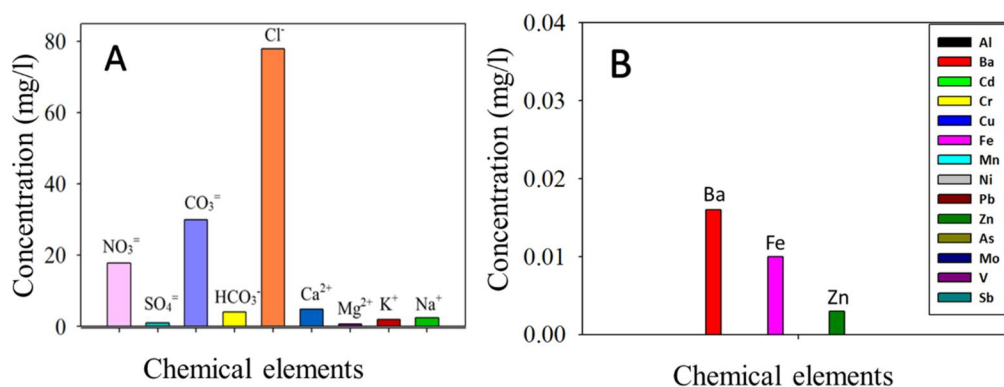
Figure 2. Chemical analysis of the soluble sedimentable particles (SP) fraction. (**A**) Ion concentrations; (**B**) Metal concentrations (The analysed metals are included in the inset).

A JEOL 6460LV Scanning Electron Microscope (SEM, JEOL, Tokyo, Japan) was used to visualize the morphology of the insoluble SP fraction. Energy dispersive X-ray spectroscopy (EDX) spectra were recorded in order to determine their elemental composition.

2.2. Product Synthesis and Application on Acinipo Limestone Samples

A starting sol containing a commercial silica oligomer (Dynasylan 40, Evonik Industries, Essen, Germany) and a hydroxyl-terminated polydimethylsiloxane (PDMS from ABCR) in the presence of a surfactant (n-octylamine, from Aldrich) was synthesized, according to a previously described method [8]. According to their respective technical data sheets, Dynasylan 40 is a mixture of monomeric and oligomeric ethoxysilanes with a SiO_2 content of 40%, and PDMS is an oligomer with a polymerization degree of 12 and an OH percentage ranging from 4 to 6% *w/w*. The synthesis route was as follows: A 1.57 M aqueous solution of n-octylamine was prepared. Next, PDMS, Dynasylan 40, and the aqueous n-octylamine solution were mixed and homogenized by high-power ultrasonic agitation (60 W·cm^{-3}) for 10 min. PDMS and aqueous n-octylamine solution proportions were 10 and 0.075% *v/v*, respectively. The product was named UCA (after University of Cadiz).

The limestone was extracted from Acinipo theatre area and it was cut as 4 cm-cubed samples. Petrographic and mineralogical analyses were previously carried out on thin sections of stone using a Transmitted Light Microscope (Olympus BH-2). The UCA product was sprayed on the 4 cm-cubes using a pressure of 1.5×10^5 Pa for 25 s. For comparison purposes, two popular commercial products, which were manufactured by Wacker (Munich, Germany) were also applied under the same conditions. Specifically, a consolidant product BSOH100 and a hydrophobic product BS290 were selected. BSOH100 is a solvent-free product, consisting of partially pre-polymerized tetraethylorthosilicate (TEOS) and dibutyltin dilaurate (DBTL) catalyst. BS290 is a solvent-free silane/siloxane mix. It was diluted in ethanol (12% *w/w*), following the recommendations of the manufacturer.

2.3. Assessment of Effectiveness and Durability

The treated samples were dried under laboratory conditions (20 °C, 60% RH) until constant weight was reached. This occurred one month after application. Effectiveness of the products applied on the Acinipo limestone was evaluated in the laboratory using three samples for each treatment. In addition, the durability of the products was evaluated in samples exposed to the environmental conditions of Acinipo archaeologic site. The study was carried out every year on a limestone sample, for a total period of three years. The following assessments were carried out on the treated limestone samples and their untreated counterparts. In the case of the samples that were exposed to archaeological site conditions, in the tests requiring the whole sample: evolution of mass, water absorption by capillarity, and water vapor diffusivity studies, one specimen per year was tested. In the other cases, the number of the replicates is described for each specific test.

2.3.1. Limestone-Product Interaction

Uptake of products and their corresponding dry matter were determined. Both parameters were measured by the change in the mass of the specimens.

Mercury accessible porosity and porosimetric distribution were obtained by Mercury Intrusion Porosimetry (MIP). The test was carried out on three specimens per stone sample under study, each with a volume of around 1 cm^3, using a PoreMaster-60 device from Quantachrome Instruments (Boynton Beach, FL, USA) comprising two measurement units: a low-pressure unit (Pascal 140), whose pressure range is between 0.69 and 350 kPa, and a high- pressure unit (Pascal 440), whose pressure range is between 0.1 to 420 MPa.

A JEOL Quanta 200 Scanning Electron Microscope (SEM, JEOL, Tokyo, Japan) was used to visualize changes in the morphology of the limestone samples. The samples were covered by a 12-nm layer of gold in order to improve their conductivity and prevent charge effects. Energy Dispersive X-ray Spectroscopy (EDX) spectra were recorded, on the whole SEM area under study, in order to elucidate the variations in surface elemental composition after the application of the products.

The topography of the stone surfaces was observed using Atomic Force Microscopy (AFM, Nanotec Electrónica S.L, Madrid, Spain) operated in tapping mode. The root-mean-square (RMS) roughness values were calculated from 2.5 μm × 2.5 μm images. Five scans were obtained for surface sample under study.

Fourier Transformer Infrared Spectra (FTIR) was employed to study the interaction between Acinipo limestone and the products under study using a FTIR-8400S (Shimadzu, Kyoto, Japan), 4 cm^{-1} in resolution, in the region from 4000 to 650 cm^{-1}. 20 scans were performed per sample. The experiments were carried out in Attenuated Total Reflection mode (ATR). In order to enhance the intensity of the signals, the samples for FTIR were prepared. Specifically, the untreated stone sample powder was mixed with the products under study (as sols) at 50% *w/w* powder/product. In the case of BS290, it was mixed without previous dilution in ethanol. Next, they were left to gel and dry under laboratory conditions. Then, the obtained composites stone-product were powdered and analyzed by FTIR. In the case of durability studies, powder that was obtained from the surface of the samples at laboratory conditions and subjected to weathering at the archaeological site was employed. The powder was obtained by scratching the treated surface of the samples under study.

2.3.2. Effectiveness of the Products on the Limestone

Improvement in mechanical properties of the treated stones and their untreated counterparts were evaluated by using the Vickers Hardness Test (Centaur RB2/200 DA, Metrol Centaur S.L., Vizcaya, Spain). Five indentations per each sample surface sample under study were carried out.

The adherence of the coatings to the stone surface was evaluated by performing a Peeling Test using Scotch Magic tape (3M). The test was carried out according to a previously reported method [29,30]. The attach/detach cycles were carried out on five different areas for each sample under study.

The effectiveness of the products in providing hydrophobic protection was characterized by the contact angle test, according to the sessile drop method, using a commercial video-based, software-controlled contact angle analyser, model OCA 15 plus, from DataPhysics Instruments (Filderstadt, Germany). The static contact angle values were determined on the stone surface. The advancing and receding contact angles were measured using the ARCA method included in the equipment software (OCA15 plus, DataPhysics Instruments, Filderstadt, Germany). The measurement was carried out on five points for each surface (the four corners and the centre).

To confirm the hydrophobic behaviour of the materials, stone samples were subjected to a test to determine the Capillary Water Absorption Coefficient (WAC), as recommended in UNE-EN [31] and the total water uptake was determined.

2.3.3. Negative Effects Induced by the Products on the Limestone

The changes in color were evaluated by using a solid reflection spectrophotometer (HunterLab, Reston, VA, USA), ColorFlex model. The conditions used were as follows: illuminant C and observer 10°. CIE L*a*b* color space was used and colour variations were evaluated using the total color difference parameter (ΔE*) [32]. The measurement was carried out on five different points for each surface sample (the four corners and the center).

Water vapor diffusivity was determined using an automatic setup developed in our laboratory [33], based on the standard cup test, in $4 \times 4 \times 1$ cm stone slabs.

2.3.4. Evaluation of the Depth of Product Penetration

The penetration depth of the products was evaluated on the cross-sectional surfaces of the limestones by the static contact angle test carried out at different depths.

In addition, to confirm the penetration depth of the products under study, images of the cross-sections of the treated limestone samples and their untreated counterparts were obtained using a Nikon model SMZ800 stereoscopic microscope (Nikon, Tokyo, Japan), according to the following procedure: the samples were immersed in water. Then, they were cut and visualized by microscopy. The non-wetted area can be associated with the penetration depth of the products across the pore structure of the limestone.

3. Results and Discussion

3.1. Evaluation of the Archaeological Site Environment and the Acinipo Limestone

The meteorological data obtained during the sampling period (Figure S1 in supplementary materials) show the monthly maximum average temperatures ranging from 33 °C in August to 11 °C in February. The monthly minimum temperatures ranged from 17 °C in August to 0.5 °C in February. The distribution of the rainfall values during the period of study was completely heterogeneous. The period from June to August exhibited values near to 0 mm, whereas the highest rainfall was recorded in the months of April and October, with values of 90 and 80 mm, respectively. Concerning wind, it had a moderate speed (around 20 km/h) with North prevailing components.

The chemical analysis of the soluble fraction of SP (Figure 2A) revealed high concentrations of Cl^- (78 mg/L), $CO_3^=$ (30 mg/L), and $NO_3^=$ (18 mg/L), and concentrations of <5 mg/L of HCO_3^-, Mg^{2+}, K^+, Ca^{2+}, Na^+, and $SO_4^=$. The highest concentration of Cl^- can be related to the deposition of marine aerosol (NaCl) transported by wind (the distance to the sea is 40 km). The values that were obtained for the metals analysis (Figure 2B) show a low concentration of Ba, Fe, and Zn. According to Prieto-Taboada et al. [34], the absence of the following metal elements: Pb, As, Cu, Cr, Ni, Cd, Mn, and Sr, and the presence of a low concentration of Ba and Zn, all of them related to traffic pollution and nearby industrial activity, clearly highlights the absence of anthropogenic activities in the Acinipo site surroundings. In the case of the Fe, this is an abundant element on Earth, being part of many minerals. Thus, its presence cannot also be associated to anthropogenic activity.

The insoluble SP fraction images that were obtained by SEM are shown in Figure 3. Most particles observed are irregular with sizes below 50 μm and some larger particles with 200 μm in size (Figure 3A). The EDX analyses of this area show typical elements of natural environments (O, C, Si, Al, Ca, Mg, and Fe) [35]. Particles of biological origin, which are composed of insect remains, diatomite and plant debris, are also observed in the SP fraction (see Figure 3B,C).
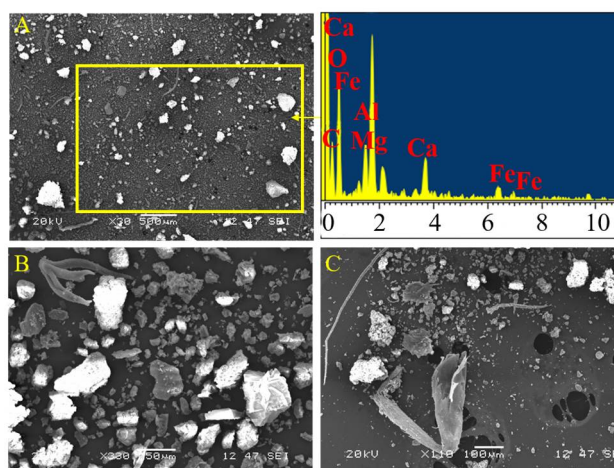
Figure 3. (**A**) Scanning electron microscope (SEM) images of particles obtained from the insoluble SP fraction and their corresponding energy dispersive X-ray spectroscopy (EDX) spectrum; SEM images of biological remains that were obtained from their insoluble SP fraction: (**B**) plant debris; and (**C**) insect remains.

The results previously described highlight that the Acinipo environment, in terms of climatic features, does not present extreme temperatures, and the rainfall and wind phenomena are moderate. In addition, the SP fraction analysis allows the conclusion that the Acinipo archaeological site is a natural environment without anthropogenic activity. Therefore, the main mechanisms of the Acinipo limestone decay could be associated with the crystallization of salts (mainly NaCl from marine aerosol) and the growth of microorganisms that are favored by the absence of extreme temperatures [36]. Following these conclusions, consolidant products with hydrophobic properties preventing water ingress into the stone pores, which is the vehicle of salts and microorganisms, were considered for Acinipo limestone conservation.

Regarding the Acinipo limestone evaluation, the optical micrograph (Figure S2A) presents a bioclastic packstone that is characterized by an abundance of fragments of bryozoan-coralline algae up to 1 mm in length. In addition, echinoderms, foraminifers, and shell fragments are observed. The matrix of this stone is micrite, with part of this micrite being recrystallized to sparite or microsparite. The EDX spectra (Figure S2B) show that Acinipo Limestone is composed of calcite ($CaCO_3$) and a very low proportion of quartz (SiO_2). Finally, the limestone shows a medium porosity (11%, see Figure 4).
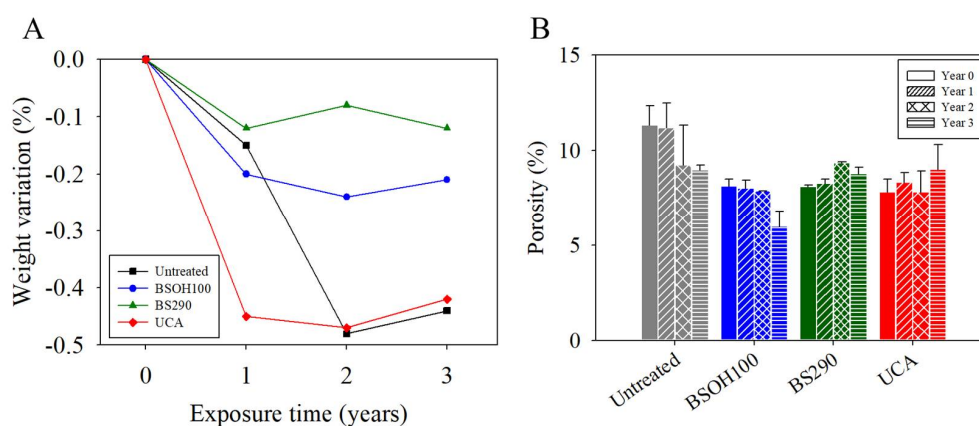

Figure 4. (**A**) Weight variation and (**B**) Porosity of the treated limestone samples and their untreated counterpart under laboratory conditions (0 year) and after each year of exposure to the environmental conditions of the Acinipo archaeological site.

3.2. Assessment of Effectiveness and Durability

3.2.1. Limestone-Product Interaction

The Table S1, which is included in supplementary information, shows the uptake (U) and dry-matter (D) values for the products under study. The uptake values of UCA and BSOH100 were similar due to their close viscosity values [26], whereas BS290 was slightly lower due to the quick evaporation of the ethanol solvent. However, significant differences were observed for the dry-matter values. Specifically, BS290 showed the lowest dry-matter value as a consequence of its dilution in ethanol [37]. Its D/U ratio (16%) demonstrated that practically all of the solvent was evaporated. In the case of the two solvent-free products (BSOH100 and UCA), they showed higher D/U ratios (45 and 69%, respectively). In this case, the mass reduction is due to the removal of water and ethanol, which is produced during hydrolysis and condensation reactions.

Figure 4A shows the evolution of weight for the samples under study with respect to their corresponding weight at year 0. A scarce weight loss (<0.5% w/w) was observed for all of the samples under study. By comparing between samples, the highest reduction corresponded to the untreated sample and its UCA treated counterpart. In the case of the UCA product, this reduction took place in the first year of exposure to the archaeological site. This behavior can be associated with the condensation/drying processes of the products being complete during the first year. In a previous paper [8], the presence of ethoxy groups from non-hydrolyzed oligomers was observed in the UCA product after six months of the synthesis, confirming the incomplete condensation of the product. In addition, a significant reduction in weight of the sample treated with the UCA product was observed after the first year of exposure at Baelo Claudia archaeological site due to the condensation/drying process [26].

Finally, the samples that were treated with BS290 showed a similar trend to their untreated counterparts, which can be related to the formation of a thin and discontinuous coating of the product being removed during the in situ exposure. During the third year, an increase in weight was observed as a consequence of the deposition of atmospheric particles and biological materials [34]. This result confirms that BS290 does not produce an effective and long-lasting treatment for the limestone under study.

In order to confirm the deposition of particles, after three years exposure in situ, the surfaces of the untreated samples were visualized by SEM. Figure 5 shows the obtained micrographs and their corresponding EDX analysis. These images (Figure 5A,B) clearly show the presence of particles with a diameter of around 10–20 μm, deposited on the limestone surface. The analysis of these particles by EDX shows the presence of Si, Al, Ca, Mg, and Fe, elements typical of natural environments without contamination [35].

In addition, the presence of NaCl (halite) (Figure 5C) was observed on the limestone surface. EDX analysis confirms its presence at low concentration. Na^+ and Cl^- were also observed in the environmental study of Acinipo. The low NaCl concentration in the limestone can be related to its high solubility, which favors its dissolution and elimination by rain [38]. The presence of biological particles (Figure 5D) was also observed by SEM. Similarly, atmospheric particles, halite, and biological material were observed in the surface of the limestones treated with BS290 after three years exposure.

Micrographs of untreated limestone surface and its treated counterparts, after three years exposure, are shown in the Figure S3. The growth of microorganisms is clearly observed in the untreated and the commercial products treated samples, whereas it is not observed in the sample that was treated with UCA product. These results confirm that UCA produces an effective coating on the surface, which prevents water presence and the subsequent growth of microorganism for at least 3 years. To confirm the presence of these microorganisms, the colonized surface of the untreated limestone was put in contact with a favorable culture medium (potato dextrose agar, PDA) for one week. A significant fungal hyphal growth can be observed in the culture medium, confirming that live microorganisms are present in the limestone (Figure S4 in supplementary information).
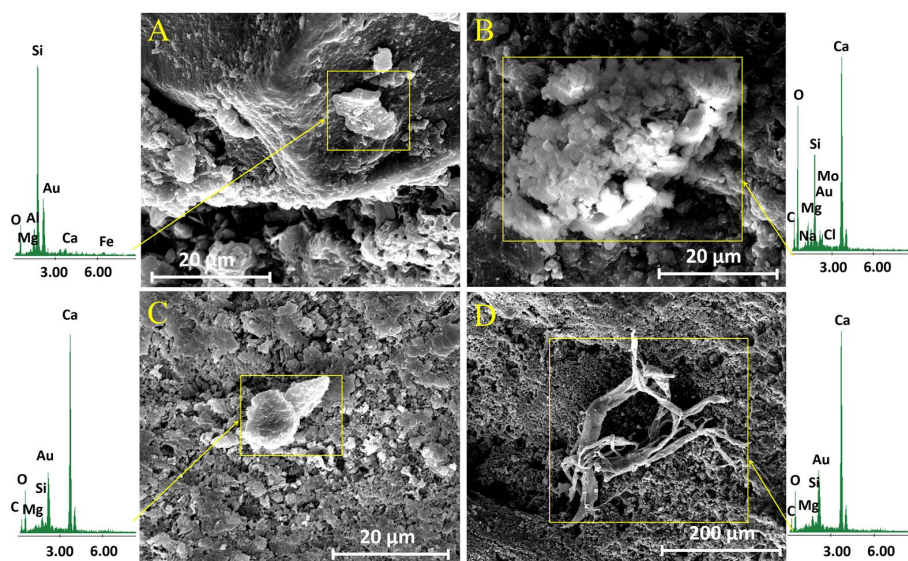
Figure 5. SEM images of the mineral particles (**A**–**C**) and (**D**) particle of biological remains on the surface of the untreated limestone, and their corresponding EDX spectra, after three years of exposure to the environmental conditions of the Acinipo archaeological site.

To evaluate the changes in the limestone porous structure during exposure to the environmental conditions, a Mercury Intrusion Porosimetry (MIP) test was carried out on samples that were extracted from the limestone surface. The changes generated in the MIP porosity can be explained by the presence of the product in the pores on the surface region of the limestone [39], which modifies its total porosity and pore diameter [40]. The average porosity values are presented in Figure 4B. After the treatments, all of the products reduced the total porosity by approximately 30%, with no significant differences between the products.

During three years of exposure to environmental conditions, the untreated samples and those that were treated with BSOH100 showed a gradual decrease in their total porosity values (Figure 4B), with slight fluctuations, as a consequence of deposition of salts and atmospheric particles in the pores of the stone [41], and as previously observed by SEM (Figure 5). In addition, the presence of biological material can also reduce the porosity and the pore size distribution of the stone [42].

Finally, the stone that was treated with the hydrophobic products BS290 and UCA do not present a reduction of porosity with exposure time, and their value remains practically unchanged, due to the hydrophobic effect of these coatings preventing the penetration of aqueous solutions containing salts or other contaminants into the stone. Striegela et al. [43] highlights that the ingress rate of pollutants into the pore structure is significantly lower in the case of the stones treated with hydrophobic products.

Figure S5 in Supplementary Materials shows the distribution of the pore diameter obtained by MIP. The untreated sample, before in situ exposure, presented pores that were mainly located in two ranges: 0.03–0.5 and 0.9–5 µm, corresponding to 40% and 36% of the porous volume, respectively. In addition, 4% of the porosity is located in the microporous region (<0.01 µm) and 11% in the macroporous region (5–200 µm). In the case of the treated samples, in all cases, a significant reduction in the pores that were located between 0.9–5 µm is promoted, while an increase of porosity in the range 0.03–0.5 µm is observed, as a consequence of the partial pore block by the applied products [39]. The reduction is higher for the samples treated with the UCA product, and lower in the case of BS290. Regarding the reduction of porosity caused by the three products in the micropore fraction, significant differences were not observed. Finally, it must be mentioned that the macropore fraction was not modified by any of the applied products.

After archaeological site exposure, in all the cases, and especially in the untreated limestone and its counterpart that was treated with BSOH100, a significant decrease in the 0.9–5 µm pore size

range to values in the 0.03–0.5 µm range was observed as a consequence of the deposition of salts and other previously discussed contaminants. For BS290 and UCA products, the changes that were observed were significantly lower. This confirms that material ingress into the pore structure is lower in limestone treated with these products.

The morphology and structure of the surfaces of the treated and untreated limestone samples were visualized by SEM, and their corresponding EDX spectra were obtained. The presence of the alkoxysilane-based products was evaluated from the Ca/Si ratio. The images obtained, and their spectra, are shown in Figures 6 and 7. Under laboratory conditions, the limestone minerals are clearly observed in the untreated sample (Figure 6A). The three studied products significantly modify the surface morphologies of the treated samples. Specifically, the surface that was treated with BSOH100 (Figure 6E) shows a discontinuous coating, which is formed by isolated aggregates of the gel, with large areas of uncoated surface. The EDX spectrum (Figure 7E) presents a similar spectrum to that corresponding to the untreated sample, with a slight increase in Si peak intensity. It confirms the presence of an uncoated part in the analyzed sample. The surface treated with BS290 produced a coating of siloxane aggregates but it was not homogenous and continuous (Figure 6I). The EDX spectrum shows a clear Si peak associated with the siloxane aggregates (Figure 7I). The presence of Ca in the analyzed surface corroborates the existence of some discontinuity in the coating. The formation of discontinuous coatings from the two commercial products is due to their poor interaction with the limestone under study. The UCA product creates a continuous, dense, and homogeneous coating on the limestone sample (Figure 6M). The significant reduction in the Ca peak (Figure 7M) corroborates the presence of a homogeneous coating. The formation of a discontinuous coating in BS290 has been observed in a previous work [14] and is associated with the high dilution of the product in ethanol. The low dry matter of the coating confirms this trend.

In the case of the two commercial products, the formation of aggregates of isolated gel could also be related to the low compatibility between limestone and alkoxysilanes [1,5], which could prevent the formation of a continuous and well-adhered coating on the limestone. In a previous study, Zendri et al. [44] evaluated the reactivity between alkoxysilanes and calcium carbonate by using NMR techniques. The results showed that the presence of $CO_3^=$ modifies the reactivity of the silica precursor, promoting the reaction of short chains of the gel in order to generate isolated aggregates of product with low adherence to the substrate, as observed by SEM in this study (Figure 6).

After in situ exposure of the samples, the surfaces that were treated with BSOH100 and BS290 products clearly show a significant loss of the coating over exposure time, especially in the second and third years, where the presence of the mineral grains of the stone can be clearly appreciated. The loss of the coating is confirmed by the EDX spectra, where the Si peak was significantly reduced and the Ca peak was increased from one year of exposure. The surfaces treated with the UCA product do not show significant changes after three years of exposure, maintaining the intensity of the Si and Ca peaks without modification. It confirms that the UCA product is able to adhere firmly to the stone surface, providing resistance to alteration for a period over three years.

In addition, the analysis of SEM images reveals a significant change in limestone roughness after exposure to the archaeological site conditions. For this reason, the surface roughness of the samples before and after their exposure for three years was studied. Figure 8 shows the three-dimensional (3D) images of the limestone surfaces obtained by AFM (Atomic Force Microscopy). The untreated stone surface presents a random roughness associated with the heterogeneity of the stone. The morphology of the limestone is slightly modified after the treatment with the commercial product. Figure 8 gives the size distribution for the roughness of the limestone surfaces under study, and the RMS roughness that was obtained. All of the applied products reduce the surface roughness of the limestone, creating coatings that tend to fill the existing holes in the untreated stone. The higher reduction in the roughness of the untreated stone was observed in the case of the samples that were treated with the UCA product (55% reduction). This reduction confirms the formation of a continuous and homogeneous coating, as observed by SEM (see Figure 6).
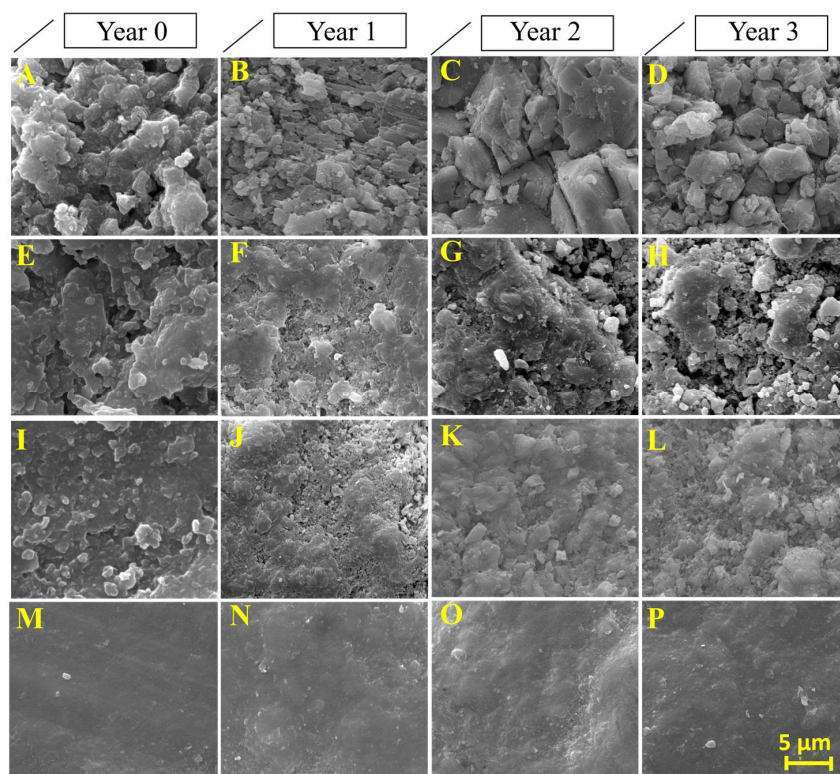
Figure 6. SEM images of the stone surface, before and after three years of exposure to the environmental conditions of the Acinipo archaeological site: (**A–D**) untreated; (**E–H**) BSOH100; (**I–L**) BS290; and, (**M–P**) University of Cadiz (UCA).
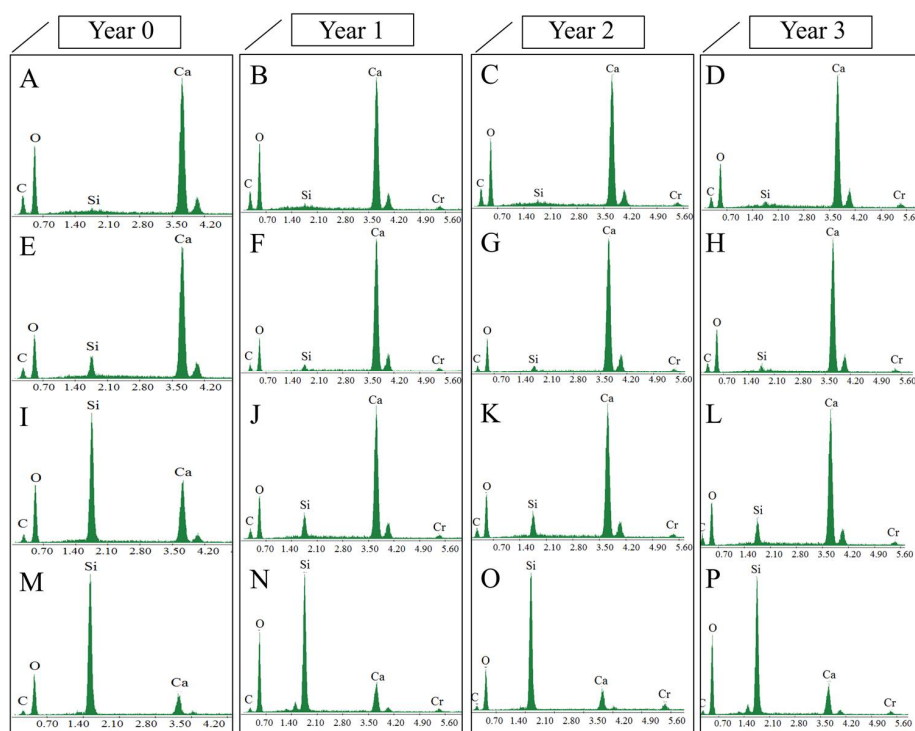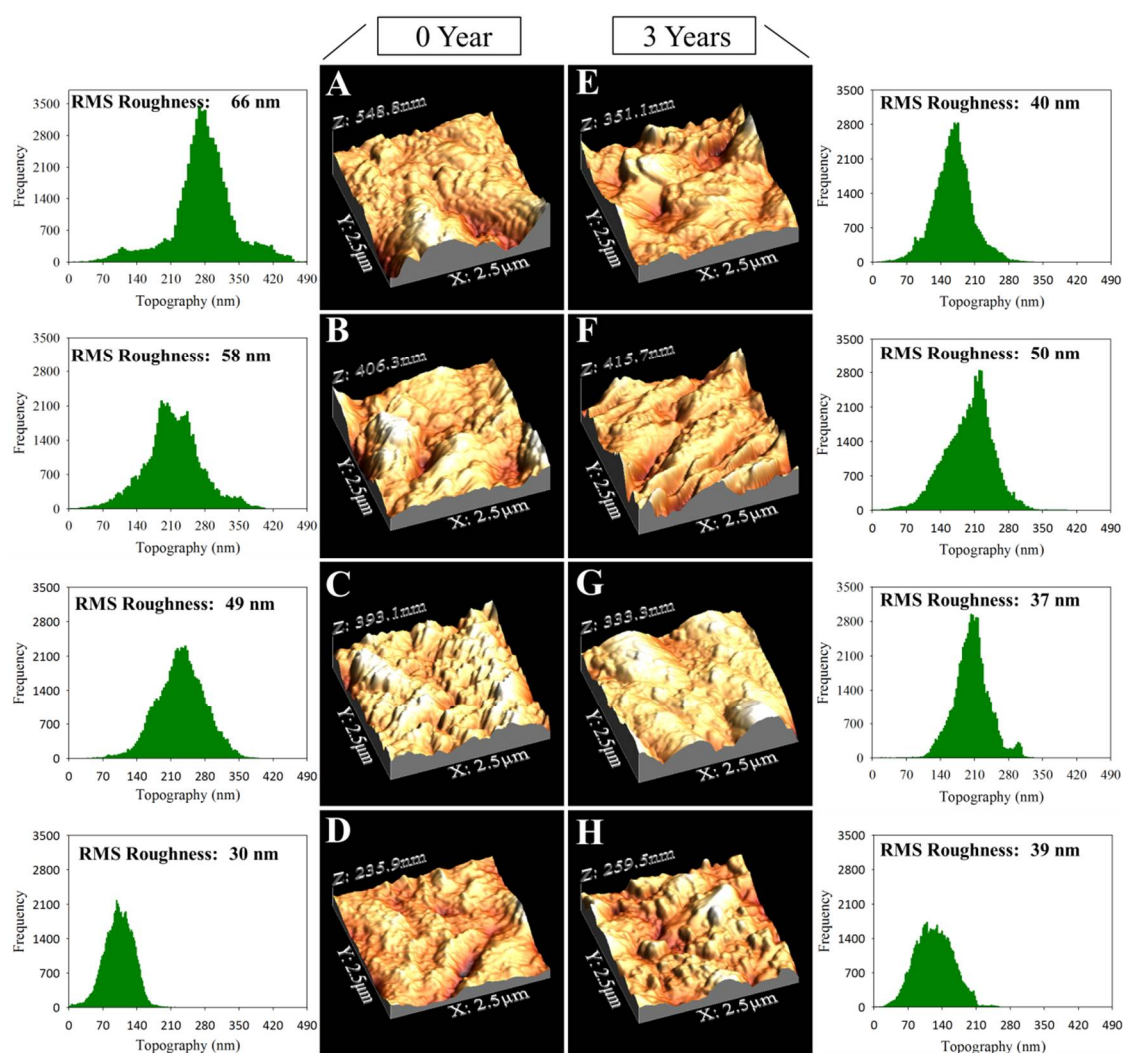

Figure 7. EDX spectrum of the stone surface, before and after three years of exposure to the environmental conditions of the Acinipo archaeological site: (**A–D**) untreated; (**E–H**) BSOH100; (**I–L**) BS290; and, (**M–P**) UCA.

Figure 8. AFM (Atomic Force Microscopy) three-dimensional (3D) topographic images and their corresponding size distribution of the roughness on the limestone surfaces under study, before and after three years of exposure to archaeological site conditions: (**A**,**E**) untreated; (**B**,**F**) BSOH100; (**C**,**G**) BS290; (**D**,**H**); and, UCA.

After three years of exposure to environmental conditions, the untreated samples showed a clear reduction in surface roughness. This can be associated with stone erosion, by the action of rain and wind, causing the loss of grains that were less attached to the surface or by mineral dissolution. In addition, this reduction of roughness could be associated with the deposition of particles and salts filling the spaces of the stone surface. The treated samples do not show a significant change in the roughness after three exposure years.

To confirm the compatibility between the carbonated substrate and the applied products, FTIR spectra were obtained (see Figure 9). In addition, Table S2 in supplementary information shows the relative intensity of the main siloxane band with respect to the main carbonate band for each spectrum. They confirm the composition of Acinipo limestone that was previously obtained by petrography (Figure S2). Specifically, the spectra of the untreated samples show bands at 712, 870, and 1400 cm^{-1}, assigned to $CO_3^=$ [45–47]. It confirms that calcite ($CaCO_3$) is the main component in the Acinipo limestone. In addition, a weak band was observed at 1080 cm^{-1}, which is assigned to a Si–O–Si bond [7], and confirms the presence of a small proportion of quartz (SiO_2) in the limestone.
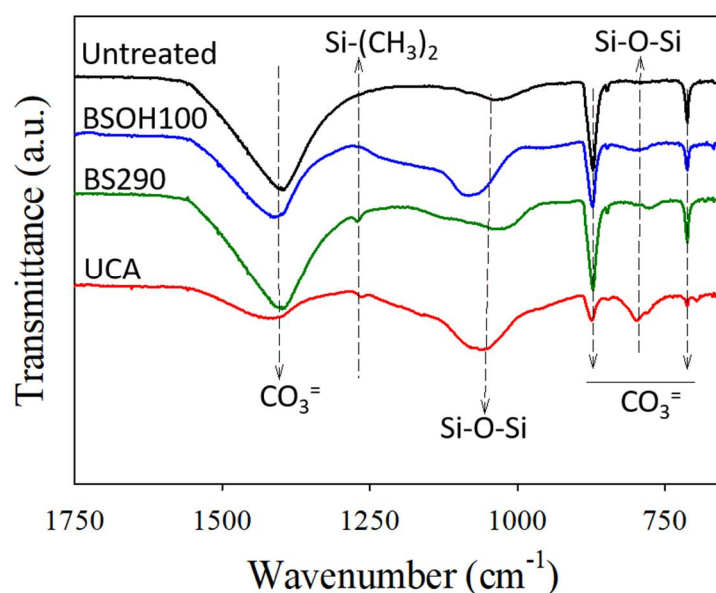
Figure 9. Fourier Transformer Infrared Spectra (FTIR) spectra of the treated and untreated limestones.

In the spectra corresponding to samples of limestone mixed with the products, new bands were observed: a typical silica band, absent in the untreated sample, located at 800 cm^{-1}, assigned to the bonding vibration of Si–O–Si [6,48]. This band confirms the presence of siloxane bonds from the products that are in the limestone. In a comparison between products, the intensity of this band was significantly higher in the spectrum of the sample containing the UCA product than those corresponding to the commercial products. In the case of the spectra corresponding to samples treated with the products BS290 and UCA, an additional band, which is located at 1265 cm^{-1}, is attributed to Si–(CH$_3$)$_2$ bonds of the organic component that is present in both products and responsible for its hydrophobic properties [48,49]. In the UCA product, the presence of this bond confirms the integration of the PDMS into the silica gel, due to the existence of a co-polymerization process between the PDMS and the silicon oligomer [14,37].

On the other hand, a significant change in the intensity and position of the bands of CO$_3^=$ (located at 712, 870, and 1400 cm^{-1}) with respect to those that were observed in the untreated and commercial products spectra is observed in the UCA spectrum. According to Wheeler et al. [50], the intensity of the bands of CO$_3^=$ that is present in calcite can be modified as a consequence of their interaction with another chemical species that produces a change in the counter ion bound to CO$_3^=$. In this previous work, the –NH$_2^+$ group of the aminopropyltriethoxysilane, used as the coupling agent, interacts with the CO$_3^=$ producing this effect. In the present study, the amino group of n-octylamine, which is present in the UCA product, could interact with the ion CO$_3^=$ and be responsible for the modification of the intensity of its peaks. Similar results were also observed by Xu et al. [51], as calcite interacts with an aminosiloxane.

In order to demonstrate the possible interaction between n-octylamine and Acinipo limestone, the stone powder was mixed with this catalyst in a limestone:n-octylamine ratio, 1:0.5. The Figure S6 in supplementary information shows the spectrum that was obtained after 24 h of interaction between the two species. For comparative purposes, the spectrum corresponding to the untreated limestone is also included.

The two spectra show the peaks corresponding to the limestone. In particular, the three bands characteristic of CO$_3^=$ and a weak band associated with Si–O–Si bonds [45–47], which are associated with the small proportion of quartz present in the stone [7]. In addition, the limestone-n-octylamine spectrum shows new bands that may be associated with the existence of interactions between these two species [52]. Specifically, the peaks that were observed at 2922 and 2852 cm^{-1} correspond to the

asymmetric vibration of the CH_2 and symmetric vibration of CH_3 and CH_2. These bands may be associated with the alkyl chain of the n-octylamine. On the other hand, the band observed at 3322 cm^{-1} can be associated with the N–H bond present in amides, and the bands at 1640 and 1563 cm^{-1} correspond to the vibrations of C=O and N–H, respectively, of secondary amides [53]. According to Demjén et al. [52], the formation of amides could be the result of the reaction of the $CO_3^=$ of the limestone with the amino group of n-octylamine. In addition, another band is observed at 1790 cm^{-1}, which is associated with the symmetric vibration of imides, this band may be related to the possible interaction of the previously formed secondary amide with another carbonyl group.

On the other hand, as we previously reported [8], n-octylamine can also produce a silica nitridation [54,55]. In a previous paper, Han et al. [55] investigated interactions between methylamine and zeolites. They concluded that the strong hydrogen bonding interaction results in the H atom of the amine group attacking the Si–O framework to form a Si–O...H...N bond, which leads to the formation of Si–N bonds in the zeolites. We think that a similar silica nitridation process could occur in the UCA products. Finally, the band at 1342 cm^{-1} could be assigned to the C–N vibration of n-octylamine [8,56]. It confirms the presence of residual n-octylamine in the mix.

All the previously described findings allow it to be concluded that the presence of n-octylamine in the UCA product can promote its suitable adhesion to the Acinipo limestone.

In order to confirm the long-term effectiveness of the products after three years exposure to archaeological site conditions, the spectra before and after exposure of the limestone samples were obtained (Supplementary Information, Figure S7). As a relevant feature, the silica bands, which are located at 1080 and 800 cm^{-1} [7,48], are more intense in the stone treated with the UCA product, and they remained after three years of exposure. It confirms the long-term effectiveness of the UCA product.

3.2.2. Effectiveness of the Products on the Limestone

The consolidant effectiveness of the products on the stone surface was evaluated by the Vickers hardness test. The hardness values (VH) are shown in Figure 10. The results indicate that all products increase the resistance of the limestone surface when compared to the untreated samples. In particular, the surface that was treated with the UCA product shows the highest increase in hardness (36%), whereas BSOH100 and BS290 produce increases of 23% and 17%, respectively. This highest increase for UCA can be associated with the formation of a continuous and homogeneous coating [6,7], while the commercial products produced discontinuous coatings, as observed by SEM (Figure 6). All of the treatments present a gradual reduction in the Vickers hardness with time of exposure. The commercial products BSOH100 and BS290 show the higher reduction, with values that were approaching the values of the untreated stone after three years of exposure, whereas the UCA product maintains the highest values of hardness. These results newly highlight the low durability of the commercial products.

The material cohesion and adhesion of the coatings were evaluated by a peeling test. Figure S8 shows photographs of the adhesive tapes after being applied to the surface of the limestone samples, before and after three years of exposure to archaeological site conditions. Before archaeological site exposure, the untreated limestone and the samples that were treated with BSOH100 present a material loss, whereas after three years of exposure, all the surfaces, excepting that treated with UCA, show material loss due to the alteration of the surface during exposure to environmental conditions. The Figure 10 presents the corresponding weight removed from the limestone surfaces. All the treated stones show higher resistance than their untreated counterpart. The untreated sample, and the samples that were treated with the BSOH100 and BS290 products, present an increase in the weight of the material removed with increasing time of exposure, whereas the material removed from the surface treated with the UCA product was practically negligible after three years of exposure to archaeological site conditions. These results newly confirm the long-term effectiveness of UCA products under Acinipo archaeological site conditions.
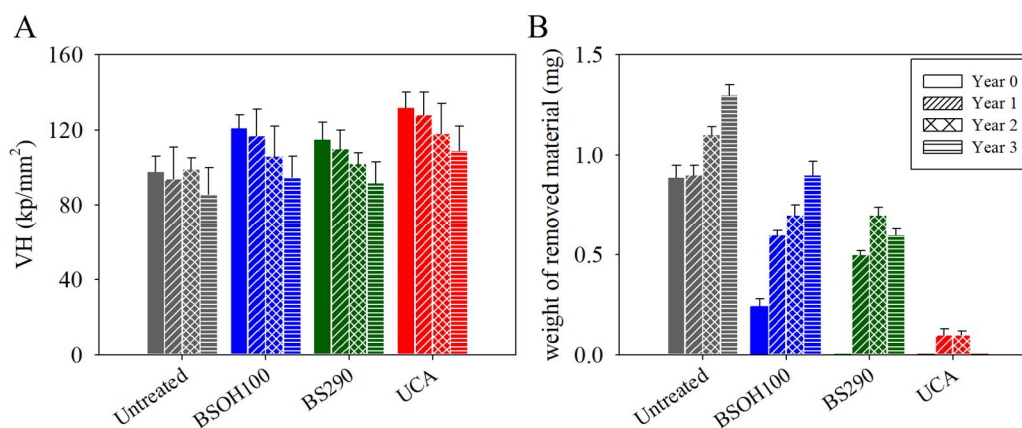
Figure 10. (**A**) Vickers hardness (VH) values and (**B**) weight of removed material of the treated and untreated stones, before and after three years of exposure to the environmental conditions of the Acinipo archaeological site.

The durability of the hydrophobic properties of all the investigated products was evaluated by a study of the static and dynamic contact angles. The contact angle (CA) values obtained on the treated and untreated limestone surfaces are shown in Figure 11. Figure S9 in supplementary information shows images of water droplets deposited on Acinipo limestone samples, before and after three years of exposure to Acinipo conditions. The untreated limestone presents a static CA of around 50°. The dynamic CA could not be evaluated due to the hydrophilic nature of the stone. Before exposure, all of the treated limestones show receding angles higher than 90° (106, 132, and 131° for BSOH100, BS290 and UCA, respectively), essential requirements for a product to be able to prevent the penetration of water into the stone [57]. The BSOH100 product, without stable organic groups in its composition, confers hydrophobic properties to the stone due to the slow hydrolysis process of ethoxy groups, as discussed in a previous paper [9]. The hysteresis values, the difference between advancing and receding CA, which characterize repellence [37], were significantly lower for the limestones that were treated with the two hydrophobic products evaluated.

After the limestone exposure to the archaeological site conditions, a progressive reduction in static CA over time was observed. After three years of exposure, the static CA for the limestones that were treated with the two commercial products practically presented the same value as that corresponding to the untreated stone. The dynamic CA could not be evaluated in any case, confirming the loss of repellence properties. The surface that was treated with the UCA product maintained the value of the static and dynamic CA after one year of exposure (Figure 11). A progressive reduction in CA is observed for the following years, showing a static CA of around 110° and a hysteresis of 15° after three years. These results allow it to be concluded that UCA was the only product maintaining hydrophobic properties after three years of exposure. The reduction in CA can be related to the coatings removal and the change in surface roughness, observed after limestone exposure under site conditions [14].

In order to confirm the results that were obtained by the CA evaluation, a water absorption test by capillarity was carried out (see Figure 12). Before the archaeological site exposure, the untreated samples showed the highest total water uptake (TWU) values, followed by the limestone samples treated with the BSOH100 product. These results confirm that the commercial BSOH100 had lost its hydrophobic capacity in contact with water during the capillary absorption test due to the complete hydrolysis of the ethoxy groups [14]. In the case of the samples that were treated with the UCA and BS290 products, with hydrophobic properties, low water absorption, close to zero, was observed.
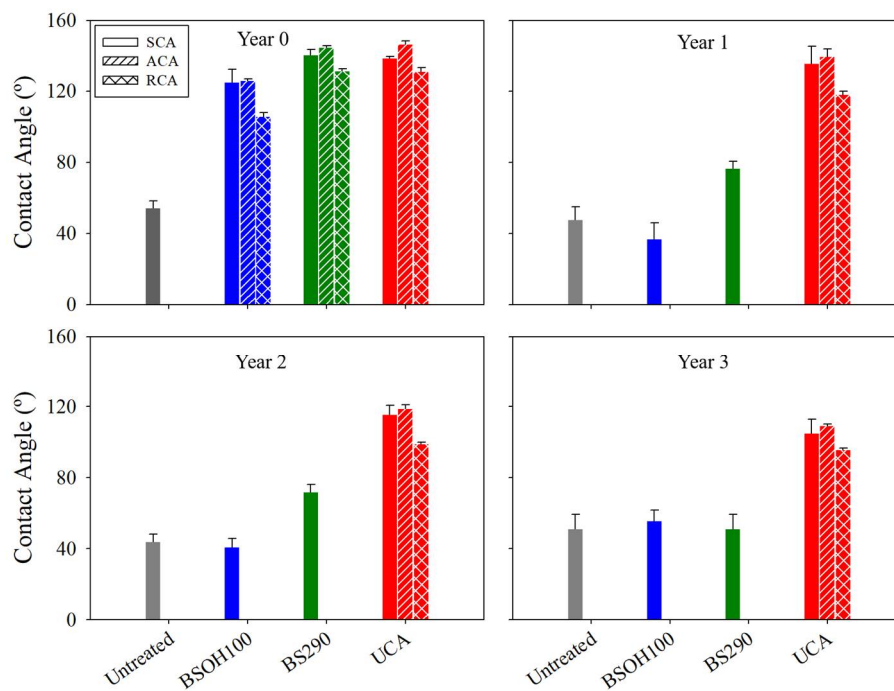
Figure 11. Static contact angle (CA) (SCA) values and their corresponding advancing (ACA) and receding CA (RCA) values, for the treated and untreated stones, before and after three years of exposure to the environmental conditions of the Acinipo archaeological site.
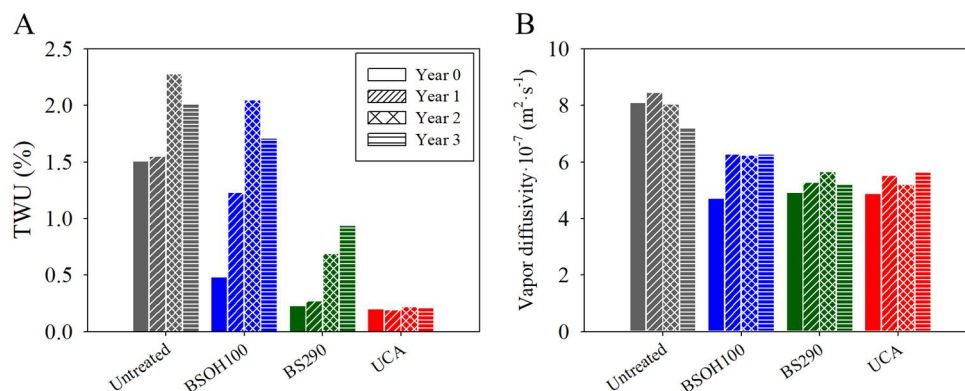

Figure 12. (**A**) Total water uptake (TWU) and (**B**) water vapour permeability values of treated stone and their untreated counterpart, before and after three years of exposure to the environmental conditions of the Acinipo archaeological site.

After three years of exposure to Acinipo conditions, the untreated samples and their counterpart treated with BSOH100 showed the same trend: a gradual increase, with slight fluctuations, in the water absorption. It could be associated to a significant loss of the coatings over the exposure time (see Figure 6). In the case of the samples that were treated with the UCA product, the water absorption values were maintained at around 0.2%, without visible changes during the three years of exposure. Moreover, a direct relationship between the CA and TWU values was observed. The surfaces with receding CA values lower than 90°, observed for all of the samples except for those that were treated with UCA, showed significant water absorption by capillarity.

3.2.3. Negative Effects Induced by the Products on the Limestone

The changes in the water vapor permeability and in the color of the Acinipo Limestone induced by the products were evaluated. The values of water vapor diffusivity are given in Figure 12. All of the products promoted a reduction of the vapor diffusivity coefficient of below 50%. It highlights that breathability of the stone was only slightly reduced, these results being acceptable for use in cultural heritage preservation [27,58]. After three years of exposure to Acinipo conditions, all of the products maintained the reduction in diffusivity below the threshold of 50%.

In addition, the color variations produced by the different products were evaluated, by using the color differences that were obtained in coordinates (ΔL *, Δa *, Δb *) and the ΔE* (total colour difference). The values that were obtained are shown in Figure 13. Before exposure to the archaeological site conditions, the samples treated with the product BSOH100 showed total colour difference values of around 5, and the products BS290 and UCA values were below 5, which is the maximum color change acceptable for cultural heritage materials [59]. The color variations are due to darkening (negative values of ΔL*) and yellowing (positive values of Δb *) of the samples after being treated.
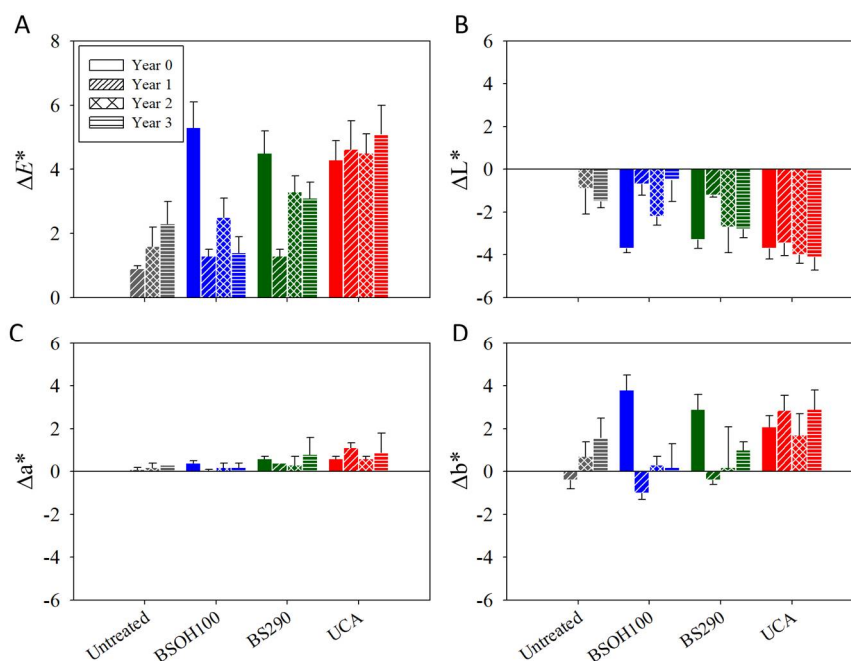

Figure 13. Colour data for the treated limestone and their untreated counterpart, before and after three years of exposure to the environmental conditions of the Acinipo archaeological site. (**A**) Total colour difference (ΔE*); (**B**) Black-white (ΔL*); (**C**) Green-red (Δa*); (**D**) Yellow-blue (Δb*).

After the exposure of samples to Acinipo conditions, the samples that were treated with the commercial products BSOH100 and BS290 presented a progressive reduction in the values of ΔE*. This change is probably due to the partial or total loss of the coating in the samples treated with the commercial products, after exposure to the outdoor conditions, as previously described. Therefore, these samples tend to recover their initial color. In the case of the samples that were treated with the UCA product, the total color difference value recorded before Acinipo exposure remained practically unaltered, confirming the durability of this product after exposure to the outdoor conditions for three years.

3.2.4. Evaluation of the Depth of the Products Penetration

The depth of penetration was determined based on the hydrophobic effect of the products. The penetration of conservation products is important to achieve a durable treatment against the

atmospheric agents [60]. In this regard, the static CA values of water droplets deposited at different depths on the cross-section of the samples were determined. The results that were obtained are shown in Figure 14. Before the archaeological site exposure, the samples that were treated with the products under study show CA values in the surface ranging from 125 to 140°, whereas the untreated surface shows CA values of around 50°. However, for all of the depths evaluated, the samples treated with the two commercial products exhibit CA values of around 50°. In the case of the limestone that was treated with UCA, the static CA is maintained above 90° up to 10 mm of depth. These results show that the UCA product is able to adhere to and penetrate into the porous structure of the stone, whereas the other products form a surface coating. After the Acinipo exposure, the same trend is observed with slight reductions in the CA values.
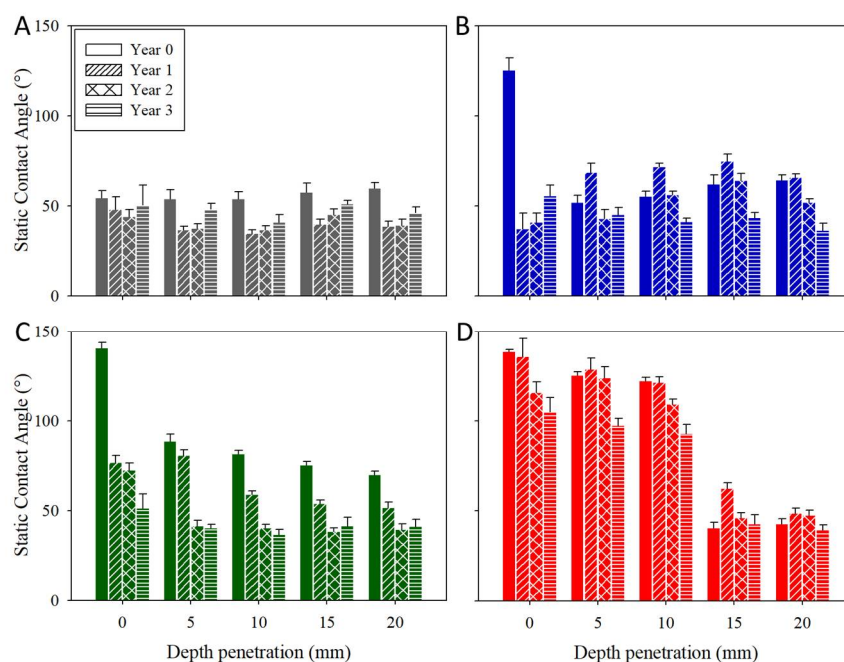

Figure 14. Static CA values on the cross-sections of the untreated and the treated limestone, before and after three years of exposure to the environmental conditions of the Acinipo archaeological site. (**A**) Untreated; (**B**) BSOH100; (**C**) BS290; (**D**) UCA.

In order to confirm the results that were obtained by CA measurement, Figure 15 shows photographs of the cross-sections of treated and untreated samples after immersion in water. In the case of the untreated samples and their counterparts treated with the commercial products, all of the surfaces are completely wet, confirming the low penetration of the products, as previously observed for BS290 applied by spraying on roof tiles [14]. The samples treated with the UCA product, show a dry zone of up to 15 mm of depth, before exposure to outdoor conditions, which confirms the existence of product up to that depth. After three years of exposure, the penetration depth of UCA remains unchanged. These results confirm that the BSOH100 and BS290 products do not penetrate into the pore structure of the stone, whereas the UCA product is able to penetrate into the pore structure of the stone, increasing the durability of the treatment against the influence of outdoor conditions.
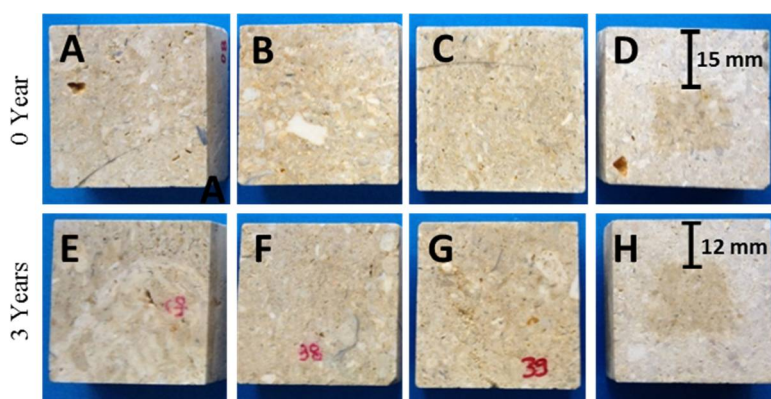
Figure 15. Photographs of cross-sections of the limestone samples, before and after exposure to the environmental conditions of the Acinipo archaeological site: (**A,E**) untreated; (**B,F**) BSOH100; (**C,G**) BS290; and (**D,H**) UCA.

4. Conclusions

This study represents an investigation about the long-term effectiveness of a novel stone conservation nanomaterial by exposure to real conditions. The following conclusions has been obtained:

- The environmental study carried out in the Acinipo Archaeological site highlights that the limestone decay was caused by salts, deposition of other pollutants, and the growth of microorganisms, with water being the main vehicle for the decay agents. Thus, effectiveness of an innovative alkoxysilane-based product with hydrophobic and consolidant properties, preventing water ingress, was tested on limestone samples that were extracted from the Acinipo Roman Theatre.
- The evaluated commercial products showed a poor compatibility with the carbonate stone under study, producing discontinuous aggregates on its surface. In addition, a low penetration and an absence of long-lasting performance were observed for these commercial products.
- In the case of the innovative nanomaterial under study, an adequate compatibility and adherence to the limestone, producing a long-term effective, homogeneous, and continuous coating with a depth of penetration of up to 10 mm, were observed. This compatibility was explained in terms of the presence of effective interactions between the n-octylamine integrated in the product and the carbonate substrate.

Negative effects, including significant changes in color and reduction in water vapor diffusivity, were not induced by the products under study.

5. Patents

The product under study was previously patented (Spanish Patent N° ES2423356. Priority Date: 16 February 2012).

References

1.　Wheeler, G. *Alkoxysilanes and the Consolidation of Stone*, 1st ed.; The Getty Conservation Institute: Los Angeles, CA, USA, 2005; ISBN 13 978-0-89236-815-0.

2.　Kapridaki, C.; Maravelaki-Kalaitzaki, P. TiO$_2$–SiO$_2$–PDMS nano-composite hydrophobic coating with self-cleaning properties for marble protection. *Prog. Org. Coat.* **2013**, *76*, 400–410. [CrossRef]

3.　Scherer, G.W.; Wheeler, G.E. *Proceedings of the 4th International Symposium on the Conservation of Monuments*; Zezza, M., Papachristodoulou, K., Eds.; Technical Chamber of Greece: Rhodes, Greece, 1997; Volume 3, p. 355.

4.　Mosquera, M.J.; Pozo, J.; Esquivias, L.; Rivas, T.; Silva, B. Application of mercury porosimetry to the study of xerogels used as stone consolidants. *J. Non-Cryst. Solids* **2002**, *311*, 185–194. [CrossRef]

5.　Doehne, E.; Price, C.A. *Stone Conservation*, 2nd ed.; The Getty conservation institute: Los Angeles, CA, USA, 2010; ISBN 978-1-60606-046-9.

6.　Mosquera, M.J.; de los Santos, D.M.; Montes, A.; Valdez-Castro, L. New nanomaterials for consolidating Stone. *Langmuir* **2008**, *24*, 2772–2778. [CrossRef] [PubMed]

7.　Mosquera, M.J.; de los Santos, D.M.; Rivas, T. Surfactant-synthesized ormosils with application to stone restoration. *Langmuir* **2010**, *26*, 6737–6745. [CrossRef] [PubMed]

8.　Illescas, J.F.; Mosquera, M.J. Producing surfactant-synthesized nanomaterials in situ on a Building Substrate, without Volatile Organic Compounds. *ACS Appl. Mater. Interfaces* **2012**, *4*, 4259–4269. [CrossRef] [PubMed]

9.　Illescas, J.F.; Mosquera, M.J. Surfactant-synthesized PDMS/silica sanomaterials improve robustness and stain resistance of carbonate stone. *J. Phys. Chem. C* **2011**, *115*, 14624–14634. [CrossRef]

10.　Remzova, M.; Sasek, P.; Frankeova, D.; Slizkova, Z.; Rathousky, J. Effect of modified ethylsilicate consolidants on the mechanical properties of sandstone. *Constr. Build. Mater.* **2016**, *112*, 674–681. [CrossRef]

11.　Xu, F.; Li, D.; Zhang, Q.; Zhang, H.; Xu, J. Effects of addition of colloidal silica particles on TEOS-based stone protection using n-octylamine as a catalyst. *Prog. Org. Coat.* **2012**, *75*, 429–434. [CrossRef]

12.　Salazar-Hernandez, C.; Alquiza, M.J.P.; Salgado, P.; Cervantes, J. TEOS-colloidal silica-PDMS-OH hybrid formulation used for stone consolidation. *Appl. Organomet. Chem.* **2010**, *24*, 481–488. [CrossRef]

13.　Luo, Y.; Xiao, L.; Zhang, X. Characterization of TEOS/PDMS/HA nanocomposites for appliation as consolidant/hydrophobic products on sandstones. *J. Cult. Herit.* **2015**, *16*, 470–478. [CrossRef]

14.　Carrascosa, L.A.M.; Facio, D.S.; Mosquera, M.J. Producing superhydrophobic roof tiles. *Nanotechnology* **2016**, *27*, 095604. [CrossRef] [PubMed]

15.　Favaro, M.; Mendichi, R.; Ossola, F.; Simon, S.; Tomasin, P.; Vigato, P.A. Evaluation of polymers for conservation treatments of outdoor exposed stone monuments. Part I: Photo-oxidative weathering. *Polym. Degrad. Stab.* **2006**, *91*, 3083–3096. [CrossRef]

16.　Favaro, M.; Mendichi, R.; Ossola, F.; Simon, S.; Tomasin, P.; Vigato, P.A. Evaluation of polymers for conservation treatments of outdoor exposed stone monuments. Part II: Photo-oxidative and salt-induced weathering of acrylic-silicone. *Polym. Degrad. Stab.* **2007**, *92*, 335–351. [CrossRef]

17.　Mosquera, M.J.; Carrascosa, L.A.M.; Badreldin, N. Producing superhydrophobic/oleophobic coatings on Cultural Heritage building materials. *Pure Appl. Chem.* **2017**, *90*. [CrossRef]

18.　De Rosario, I.; Elhaddad, F.; Pan, A.; Benavides, R.; Rivas, T.; Mosquera, M.J. Effectiveness of a novel consolidant on granite: Laboratory and in situ results. *Constr. Build. Mater.* **2015**, *76*, 140–149. [CrossRef]

19.　De Rosario, I.; Rivas, T.; Buceta, G.; Feijoo, J.; Mosquera, M.J. Surfactant-Synthesized consolidants applied to a granitic medieval Necropolis in NW Spain. Laboratory and in situ effectiveness evaluation. *Int. J. Archit. Herit.* **2017**, *11*, 1166–1176. [CrossRef]

20. Nwaubani, S.O.; Dumbelton, J. A practical approach to in-situ evaluation of surface-treated structures. *Constr. Build. Mater.* **2001**, *15*, 199–212. [CrossRef]

21. Bonazza, A.; Vidorni, G.; Natali, I.; Ciantelli, C.; Giosuè, C.; Tittarelli, F. Durability assessment to environmental impact of nano-structured consolidants on Carrara marble by field exposure tests. *Sci. Total Environ.* **2017**, *575*, 23–32. [CrossRef] [PubMed]

22. De Ferri, L.; Lottici, P.P.; Lorenzi, A.; Montenero, A.; Salvioli-Mariani, E. Study of silica nanoparticles—Polysiloxane hydrophobic treatments for stone-based monument protection. *J. Cult. Herit.* **2011**, *12*, 356–363. [CrossRef]

23. Cappelletti, G.; Fermo, P.; Camiloni, M. Smart hybrid coatings for natural stones conservation. *Prog. Org. Coat.* **2015**, *78*, 511–516. [CrossRef]

24. Corcione, C.E.; De Simone, N.; Santarelli, M.L.; Frigione, M. Protective properties and durability characteristics of experimental and commercial organic coatings for the preservation of porous stone. *Prog. Org. Coat.* **2017**, *103*, 193–203. [CrossRef]

25. Gherardi, F.; Gulotta, D.; Goidanich, S.; Colombo, A.; Toniolo, L. On-site monitoring of the performance of innovative treatments for marble conservation in architectural heritage. *Herit. Sci.* **2017**, *5*. [CrossRef]

26. Lhaddad, F.; Carrascosa, L.A.M.; Mosquera, M.J. Long-term effectiveness, under a coastal environment, of a novel conservation nanomaterial applied on sandstone from a Roman archaeological site. *J. Cult. Herit.* **2018**, in press.

27. Mosquera, M.J.; Santos, D.; Rivas, T.; Sanmartín, P.; Silva, B. New nanomaterials for protecting and consolidating stone. *J. Nano Res.* **2009**, *8*. [CrossRef]

28. Bernabe, J.M.; Carretero, M.I.; Galan, E. Mineralogy and origin of atmospheric particles in the industrial area of Huelva. *Atmos. Environ.* **2005**, *39*, 6777–6789. [CrossRef]

29. Drdàcký, M.; Lesàk, J.; Rescic, S.; Slìžkovà, Z.; Tiano, P.; Valach, J. Standardization of peeling tests for assessing the cohesion and consolidation characteristics of historic stone surfaces. *Mater. Struct.* **2012**, *45*, 505–552. [CrossRef] [PubMed]

30. Drdàcký, M.; Lesàk, J.; Niedoba, K.; Valach, J. Peeling tests for assessing the cohesion and consolidation characteristics of mortar and render surfaces. *Mater. Struct.* **2015**, *48*, 1947–1963. [CrossRef]

31. *UNE-EN 1925, Natural Stone Test Methods, Determination of Water Absorption Coefficient by Capillarity*; AENOR: Madrid, Spain, 1999.

32. Berns, R.S. *Billmeyer and Saltzman's Principles of Color Technology*, 3rd ed.; Wiley-Interscience: New York, NY, USA, 2000; ISBN 978-0-471-19459-0.

33. Mosquera, M.J.; Benitez, D.; Perry, S.H. Pore structure in mortars applied on restoration: Effect on properties relevant to decay of granite buildings. *Cem. Concr. Res.* **2002**, *32*, 1883–1888. [CrossRef]

34. Prieto-Taboada, N.; Ibarrondo, I.; Gomez-Laserna, O.; Martinez-Arkarazo, I.; Olazabal, M.A.; Madariaga, J.M. Buildings as repositories of hazardous pollutants of anthropogenic origin. *J. Hazard. Mater.* **2013**, *248–249*, 451–460. [CrossRef] [PubMed]

35. Cong, Z.; Kang, S.; Liu, X.; Wang, G. Elemental composition of aerosol in the Nam Co region, Tibetan Plateau, during summer monsoon season. *Atmos. Environ.* **2007**, *41*, 1180–1187. [CrossRef]

36. Turkington, A.V.; Martin, E.; Viles, H.A.; Smith, B.J. Surface change of sandstone samples exposed to a polluted urban atmosphere over a six-year period: Belfast, Northern Ireland. *Build. Environ.* **2003**, *38*, 1205–1216. [CrossRef]

37. Facio, D.S.; Mosquera, M.J. Simple Strategy for Producing Superhydrophobic Nanocomposite Coatings in Situ on a Building Substrate. *ACS Appl. Mater. Interfaces* **2013**, *5*, 7517–7526. [CrossRef] [PubMed]

38. Maravelaki-kalaitzaki, P.; Bertoncello, R.; Biscontin, G. Evaluation of the initial weathering rate of Istria stone exposed to rain action, in Venice, with X-ray photoelectron spectroscopy. *J. Cult. Herit.* **2002**, *3*, 273–282. [CrossRef]

39. Maravelaki-kalaitzaki, P.; kallithrakas-kontos, N.; Korakaki, D.; Agioutantis, Z.; Maurigiannakis, S. Evaluation of silicon-based strengthening agents on porous limestones. *Prog. Org. Coat.* **2006**, *57*, 140–148. [CrossRef]

40. Moropoulou, A.; Kouloumbi, N.; Haralampopoulos, G.; Konstanti, A.; Michailidis, P. Criteria and methodology for the evaluation of conservation interventions on treated porous stone susceptible to salt decay. *Prog. Org. Coat.* **2003**, *48*, 259–270. [CrossRef]

41. Cardell, C.; Delalieux, F.; Roumpopoulos, K.; Moropoulou, A.; Auger, A.; Van Grieken, R. Salt-induced decay in calcareous stone monuments and buildings in a marine environment in SW France. *Constr. Build. Mater.* **2003**, *17*, 165–179. [CrossRef]

42. Papida, S.; Murphy, W.; May, E. Enhancement of physical weathering of building stones by microbial populations. *Int. Biodeterior. Biodegrad.* **2000**, *46*, 305–317. [CrossRef]

43. Striegela, M.F.; Guin, E.B.; Hallett, K.H.; Sandoval, D.; Swingle, R.; Knox, K.; Best, F.; Fornea, S. Air pollution, coatings, and cultural resources. *Prog. Org. Coat.* **2003**, *48*, 281–288. [CrossRef]

44. Zendri, E.; Biscontin, G.; Nardini, I.; Riato, S. Characterization and reactivity of silicatic consolidants. *Constr. Build. Mater.* **2007**, *21*, 1098–1106. [CrossRef]

45. Sdiri, A.; Higashi, T.; Hatta, T.; Jamoussi, F.; Tase, N. Mineralogical and spectroscopic characterization, and potential environmental use of limestone from the Abiod formation, Tunisia. *Environ. Earth Sci.* **2010**, *61*, 1275–1287. [CrossRef]

46. Gunasekaran, S.; Anbalagan, G. Spectroscopic study of phase transitions in natural calcite mineral. *Spectrochim. Acta Mol. Biomol. Spectrosc.* **2008**, *69*, 1246–1251. [CrossRef] [PubMed]

47. Cardell, C.; Guerra, I.; Romero-Pastor, J.; Cultrone, G.; Rodriguez-Navarro, A. Innovative Analytical Methodology Combining Micro-X-ray Diffraction, Scanning Electron Microscopy-Based Mineral Maps, and Diffuse Reflectance Infrared Fourier Transform Spectroscopy to Characterize Archeological Artifacts. *Anal. Chem.* **2009**, *81*, 604–611. [CrossRef] [PubMed]

48. Tellez, L.; Rubio, J.; Rubio, F.; Morales, E.; Oteo, J.L. Synthesis of inorganic-organic hybrid materials from TEOS, TBT and PDMS. *J. Mater. Sci.* **2003**, *38*, 1773–1780. [CrossRef]

49. Zhang, X.; Ye, H.; Xiao, B.; Yan, L.; Lv, H.B. Jiang. Sol−Gel Preparation of PDMS/Silica Hybrid Antireflective Coatings with Controlled Thickness and Durable Antireflective Performance. *J. Phys. Chem. C* **2010**, *114*, 19979–19983. [CrossRef]

50. Wheeler, G.; Méndez-Vivar, J.; Fleming, S. The Use of Modified Zr-nPropoxide in the Consolidation of Calcite: A Preliminary Study Focused into the Conservation of Cultural Heritage. *J. Sol-Gel Sci. Technol.* **2003**, *26*, 1233–1237. [CrossRef]

51. Xu, F.; Xiang, N.; Li, D.; Yu, J.; Wu, D.; Zhang, Q. Use of coupling agents for increasing passivants and cohesion ability of consolidant on limestone. *Prog. Org. Coat.* **2004**, *77*, 1613–1618. [CrossRef]

52. Demjén, Z.; Pukánszky, B.; Nagy, J. Possible coupling reactions of functional silanes and polypropylene. *Polymer* **1999**, *40*, 1763–1773. [CrossRef]

53. Demjén, Z.; Pukánszky, B.; Földes, E.; Nagy, J. Interaction of Silane Coupling Agents with CaCO$_3$. *J. Colloid Interface Sci.* **1997**, *190*, 427–436. [CrossRef]

54. Mrowetz, M.; Balcerski, W.; Colussi, A.J.; Hoffmann, M.R. Oxidative power of nitrogen-doped TiO$_2$ photocatalysts under visible illumination. *J. Phys. Chem. B* **2004**, *108*, 17269–17272. [CrossRef]

55. Han, A.J.; Guo, J.; Yu, H.; Zeng, Y.; Huang, Y.F.; He, H.Y.; Long, Y.C. The Leading Role of Association in Framework Modification of Highly Siliceous Zeolites with Adsorbed Methylamine. *ChemPhysChem* **2006**, *7*, 607–613. [CrossRef] [PubMed]

56. Prado, A.G.S.; Airoldi, C.J. Different neutral surfactant template extraction routes for synthetic hexagonal mesoporous silicas. *J. Mater. Chem.* **2002**, *12*, 3823–3826. [CrossRef]

57. Della Volpe, C.; Penati, A.; Peruzzzi, R.; Siboni, S.; Toniolo, L.; Colombo, C. The combined effect of roughness and heterogeneity on contact angles: The case of polymer coating for stone protection. *J. Adhes. Sci. Technol.* **2000**, *14*, 273–299. [CrossRef]

58. Delgado-Rodrigues, J.; Grossi, A. Indicators and ratings for the compatibility assessment of conservation actions. *J. Cult. Herit.* **2007**, *8*, 32–43. [CrossRef]

59. Miliani, C.; Velo Simpson, M.L.; Scherer, G.W. Particle-modified consolidants: A study on the effect of particles on sol–gel properties and consolidation effectiveness. *J. Cult. Herit.* **2007**, *8*, 1–6. [CrossRef]

60. Camaiti, M.; Bugani, S.; Bernard, E.; Morselli, L.; Matteini, M. Effects of atmospheric NOx on biocalcarenite coated with different conservation products. *Appl. Geochem.* **2007**, *22*, 1248–1254. [CrossRef]

Producing lasting amphiphobic building surfaces with self-cleaning properties

Dario S Facio, Luis A M Carrascosa and María J Mosquera

TEP-243 Nanomaterials Group. Departamento de Quimica-Fisica, Facultad de Ciencias, Campus Rio San Pedro, Universidad de Cadiz, E-11510 Puerto Real (Cadiz), Spain

E-mail: mariajesus.mosquera@uca.es

CrossMark

Abstract

Nowadays, producing building surfaces that prevent water and oil uptake and which present self-cleaning activity is still a challenge. In this study, amphiphobic (superhydrophobic and oleophobic) building surfaces were successfully produced. A simple and low-cost process was developed, which is applicable to large-scale building surfaces, according the following procedure: (1) by spraying a SiO_2 nanocomposite which produces a closely-packed nanoparticle uniform topography; (2) by functionalizing the previous coating with a fluorinated alkoxysilane, producing high hydrophobicity and oleophobicity. The formation of a Cassie–Baxter regime, in which air pockets could be trapped between the aggregates of particles, was confirmed by topographic study. The building surface demonstrated an excellent self-cleaning performance. Finally, the surface presented lasting superhydrophobicity with high stability against successive attachment/detachment force cycles. This high durability can be explained by the effective grafting of the silica nanocomposite coating skeleton with the substrate, and with the additional fluorinated coating produced by condensation reactions.

Supplementary material for this article is available online

Keywords: building materials, lasting effectiveness, superhydrophobicity, oleophobicity, Cassie–Baxter regime, self-cleaning

(Some figures may appear in colour only in the online journal)

1. Introduction

Building materials exposed to weathering conditions, such as roof tiles, facade claddings or floorings, are subjected to different decay processes related to water, including freezing, thawing, salt crystallization and biodecay [1]. Thus, a crucial strategy to protect these materials and, consequently, to increase their service life, is to prevent water uptake. In the building field, obtaining superhydrophobic surfaces has also attracted great interest because of their properties of self-cleaning, contamination prevention and repellence [2]. Superhydrophobic surfaces are obtained by the combination of: (1) surface chemical modification, reducing surface energy and (2) surface topography modification, giving rise to a Cassie–Baxter state [3, 4]. Some superhydrophobic building surfaces were recently produced by spraying nanoparticles (NPs), modifying roughness, dispersed in low surface energy media, such as polymers or oligomeric solutions, on different building substrates [5–9]. However, some of these products [5, 6] present some significant drawbacks, such as film cracking and especially low durability. We have also produced superhydrophobic building surfaces by integrating silica NPs in a low-energy surface silica matrix in the presence of a surfactant [10]. We [11] also demonstrated the durability of these products by an ageing test. The surfactant plays a valuable role, acting as a sol-gel transition catalyst and by reducing gel capillary pressure during drying, by an inverse micelles formation mechanism, preventing cracking [12]. This strategy has been also effective to obtain hydrophobic coatings [13, 14], photoactive products with self-cleaning properties [15–18] and biocides [19].

A number of building materials, such as kitchen and bathroom worktops and flooring, are susceptible to suffering oil- and water-based staining in their daily use. Thus, it is a

additional challenge to obtain surfaces that prevent water and oil uptake, offering highly effective protection against stains. As reduction in surface energy produced by organic species is not enough to avoid oil absorption, fluorinated organic coatings are broadly applicable as protective coatings on different substrates such as glass [20], silicon wafers [21], paper [22] or cotton [23]. In order to give additional repellence properties to the substrate, the application of a fluorinated ethoxysilane (producing oleophobicity and hydrophobicity) has been combined with different strategies promoting the Cassie–Baxter state, such as: (1) decorating the surface with silica NPs [22, 24] or carbon nanotubes [25]; (2) by using a colloidal monolayer as a template [26, 27]; and even (3) by irradiating an electron beam onto silicone grease films [28]. In the specific case of building surfaces, different fluorinated coatings have also been applied on marble and other building stones [29–32] in order to give rise to hydrophobic/oleophobic performances. However, to our knowledge, synthesis route to produce building materials with oleo- and super-hydrophobic properties are not found in the literature. The methodology previously described is too complicated and expensive for large scale applications, as required for these kinds of substrates. Thus, the objective of the present study is to produce building materials with lasting amphiphobicity (oleo- and superhydrophobic properties) and consequent self-cleaning activity by using a simple procedure for applying on bulding substrates. Specifically, our strategy consists of producing: (1) a silica nanocomposite coating, inducing roughness and (2) a fluorinated film, reducing surface energy. The presence of labile silanol and ethoxy groups in the coatings and the substrate, gives rise to effective condensation reactions between them, conferring long-service life to the material.

The paper is organized as follow: firstly, the synthesis processes developed in our laboratory are described, together with a complete characterization of the materials synthesized. For comparison, an alternative synthesis without particles was also evaluated. Secondly, an evaluation is given of the effectiveness as a superhydrophobic, oleophobic and self-cleaning surface of a common building stone treated with the developed products. In addition, the durability of the building surfaces was evaluated. Finally, the results of an in-depth study of the topography of the modified surfaces are presented in order to establish a relationship with its superhydrophobic-oleophobic properties.

2. Materials and methods

2.1. Synthesis

A starting sol was prepared by mixing, under ultrasonic agitation, silica oligomers, colloidal silica particles (hereafter CSP), and a surfactant (n-octylamine from Aldrich, hereafter n-8). The silica oligomer, TES 40 WN from Wacker, is a mixture of monomeric and oligomeric ethoxysilanes, with an average chain length of approximately 5 Si–O units. The CSP, AEROSIL OX50 from Evonik, are hydrophilic fumed

silica particles with a diameter of 40 nm. The nanomaterial was synthesized as follows: (1) a 1.92 M aqueous dispersion of n-octylamine, with a concentration above its critical micellar concentration [13], was prepared under vigorous stirring. (2) Silica oligomer and CSP were mixed under ultrasonic stirring ($2\,W\,cm^{-3}$) for 1 min. (3) The aqueous dispersion of n-8 was added, dropwise, to the silica oligomer/CSP mixture under ultrasonic stirring ($1\,W\,cm^{-3}$). The ultrasonic agitation was maintained for 8 min. The TES40/n-8 dispersion ratio was 99.5/0.5%v/v. The CSP was added in a 2%w/v ratio with respect to the total volume of the sol. The nomenclature for this nanomaterial is TS (T for TES40 and S for CSP). For comparison purposes, we also prepared a nanomaterial, named T, without the silica colloidal particles, by using the same procedure.

2.2. Characterization of nanomaterials

Immediately after synthesis, the viscosities of the sols were studied using a concentric cylinder viscometer (model DV-II + with a UL/Y adapter) from Brookfield. Experiments were performed at 25 °C maintained by re-circulated water from a thermostatic bath. A shear stress versus shear rate flow curve was generated.

Next, the sols were cast in glass Petri dishes of 3.0 cm diameter, adding 3 ml per cast. The cast sols were kept under laboratory conditions (60% RH and 20 °C). Gel transition took place spontaneously and the gel time was recorded. The stability of the sols was also evaluated by measuring the gel time in the enclosed condition. Gels were left to dry until a constant weight was reached. The presence of cracks in the xerogels obtained was checked by visual inspection. Finally, all the experiments described below were carried out one month after the synthesis.

The pore volume, pore size distribution and Brunauer, Emmett and Teller surface area of the materials under study were characterized by nitrogen physisorption (Autosorb IQ, from Quantachrome).

Transmission electron microscopy (TEM) studies were performed using a JEOL 2010F TEM/STEM microscope, operating at 200 kV with 0.19 nm spatial resolution. The samples were prepared by depositing a small amount of the powders directly onto Lacey-Carbon coated Cu grids.

Single-pulse MAS-NMR experiments were carried out on a Bruker ADVANCE WB400 spectrometer equipped with a multinuclear probe. Samples of powdered materials were packed in 4 mm zirconia rotors and spun at 8 kHz. ^{29}Si MAS NMR spectra were acquired at a frequency of 79.49 MHz, a delay time of 60 s and scan number of 2000. ^{1}H MAS NMR spectra were acquired at a frequency of 400.1 MHz, a delay time of 3 s and scan number of 32. ^{13}C CPMAS NMR spectra were acquired at a frequency of 100.6 MHz, a delay time of 4 s and scan number of 1000. The chemical shift values were reported in ppm using tetramethylsilane as reference.

The chemical bonds in the coatings under study were analyzed by Fourier Transformer Infrared Spectrophotometry (FTIR). The spectra were recorded for powders using a FTIR-8400S from Shimadzu ($4\,cm^{-1}$ resolution) in the region from
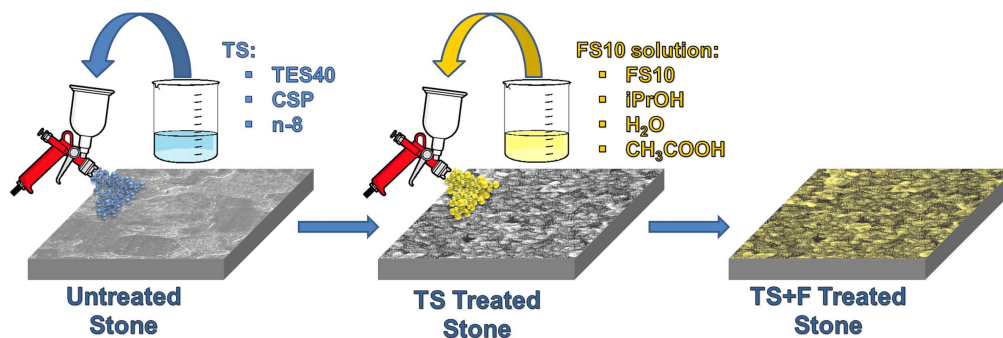
Figure 1. Synthesis route and application on building substrate developed in this study.

4000 to 600 cm^{-1}. The experiments were carried out in attenuated total reflection mode.

2.3. Application of nanomaterials on building substrate

The starting sols were applied on a building stone, which is commonly employed to manufacture floors and worktops. The stone selected was a sandstone with a porosity of around 4.5%. It is composed of quartz (60%), feldspar (25%) and phyllosilicates (10%) and a low content of calcite.

The sols under study were applied by air spraying at 2.0 bar for 5 s on the upper surface of $5 \times 5 \times 2$ cm samples of the selected sandstone, as shown in figure 1.

2.4. Functionalization of treated building surfaces by fluorinated-coating

In order to give hydro- and oleophobicity to the surface, an additional low surface energy coating was applied to the previously treated stone samples. For comparison, the fluorinated coating was also applied on untreated stone samples. A perfluoropolyether silane solution (FS10, Fluorolink S10, Solvay Solexis) was used for surface functionalization. As a previous phase of the application, in order to promote hydrolysis of the fluorinated alkoxysilane, FS10 was dissolved in isopropyl alcohol (94.0%w/w), then water was added (4.0%w/w), and acetic acid (1.0%w/w) as catalyst under magnetic stirring for 30 min.

In the case of the stone samples previously treated with T and TS, the fluorinated coating was applied, after gel transition took place (2 days after the nanomaterial application), by air spraying at 2.0 bar for 3 s (see figure 1). In order to accelerate the condensation process of the fluorinated coating, it was cured in two steps: (1) heating at 100 °C for 15 min and (2) heating at 120 °C for 15 min. This heating process is not strictly necessary because curing can take place at room temperature, but a longer time is required to get the final performance. The samples treated with this additional fluorinated coating were named with '+F' added to their name.

2.5. Effectiveness of the treatments on the building substrates

Untreated stone samples, and their treated counterparts, were characterized one month after the application of the products by the procedures described below. Effectiveness was evaluated on stones with the fluorinated coating (T + F, TS + F, F) and those samples without F (T, TS). All the results reported correspond to average values obtained from three stone samples.

The effectiveness of the coating materials for providing hydrophobic protection was characterized by a water contact angle test (sessile drop method), using a commercial video-based, software-controlled contact angle analyzer, model OCA 15plus, from Dataphysics Instruments. Static contact angle (SCA) values were determined on the stone surface according the following procedure: droplets of distilled water (10 μl) were applied with a syringe at five different points on each sample under study. In addition, repellence behavior was evaluated by measuring advancing (ACA) and receding contact angles (RCA). The ARCA method, with the volume of the droplet being increased/decreased by 5 μl was employed. Details of this procedure are given in a previous paper [13]. SCA values were also determined for commercial olive oil in order to test the effectiveness of the coatings for providing oleophobicity.

As an additional experimental test of the water-repellent behavior, several water droplets (40 μl) were dropped on each surface under study from a height of 3 cm. The surfaces were oriented in two different positions (horizontal and tilted 10°). The experiment was recorded with a high-speed camera (Basler scA1000-32gc GigE) at 70 frames s^{-1}.

Self-cleaning properties of the surface presenting the best hydrophobic performance were also tested according to a previously described procedure [4]. For comparison, untreated samples were also evaluated. Specifically, the surfaces of the selected samples were made dirty with two different staining agents (red brick and methylene blue powders). Next, water droplets were poured onto the surfaces. The samples were tilted at 10°. These experiments were recorded by a digital compact camera (Sony Cyber-Shot model DSCP200) at 30 frames s^{-1}.

The mechanical stability of the surface presenting the best hydrophobic performance was assessed 10 months after the synthesis by pressing adhesive tape onto the surface and subsequent removal [4, 33, 34]. In order to test the duration of the hydrophobic behavior, static and dynamic contact angles were measured again after 1 and 20 attachment/detachment processes.

Scanning Electron Microscopy (SEM) was used to visualize changes in the morphology of the stone after the treatments. The microscope employed was a model Sirion FEGSEM from the FEI Company, with a structural resolution of 1.5 nm. Images were captured using a secondary electron detector at a voltage of 10 kV. Fragments of the samples were coated with a thin conducting layer of gold as a prior phase to the visualization. In addition, an elemental analysis of the surfaces under study was carried out by x-ray energy dispersive spectroscopy (EDS) by using an EDS detector from EDAX.

The topography of the surfaces under study was observed by using Atomic Force Microscopy (AM-AFM, Nanotec Electrónica S.L.), operating in tapping mode. The root mean square (RMS) roughness values were calculated from 2.5 μm $\times$ 2.5 μm and 0.5 μm $\times$ 0.5 μm images.

The possible negative effect of color changes induced by the treatments was also evaluated. Total color difference (ΔE^*) was determined using a solid reflection spectrophotometer, a Colorflex model, from HunterLab. The conditions used were: illuminant C and observer CIE 10°. The CIE L*a*b* scale was used, and variations in color were evaluated [35].

3. Results and discussion

3.1. Sol-gel characterization

The starting sols presented a Newtonian behavior with viscosity values of 4.28 and 4.70 mPa s for T and TS, respectively. As expected, the value was slightly higher for the sol containing CSP. Viscosity is a key parameter to be evaluated for sols being applied on porous substrates, such as the building material under study, because the sols should be able to penetrate into the pore structure of the substrate, which is desirable to achieve an effective adhesion between coating and substrate. The viscosity values obtained in this study presented values in the same range as those from common commercial ethoxysilanes sols employed as protective agents for buildings, which are in the range 3–5 mPa s [14, 36].

Both sols spontaneously gelled in Petri dishes in the first 24 h after synthesis, but it was not instantaneous. This lack of instantaneous gelling is required to promote the sol penetration into the pore structure of the substrate. The initial objective to reduce gel time according to industrial application requirements was achieved. Previously, n-8/TES40 sols were prepared with a longer gel transition time (5 days) [27] due to the significantly lower n-8 content (n-8/sol ratio of 0.04 instead of 0.16%v/v used in the present study). In addition, the sols showed a long period of stability in closed containers (>6 months). This feature is an important advantage for their practical application because the sols can be stored for a long period of time.

Figure S1 is available online at stacks.iop.org/NANO/28/265601/mmedia presents the homogeneous crack-free and transparent monoliths obtained after sol-gel transition. The absence of cracking demonstrates the role played by n-8,
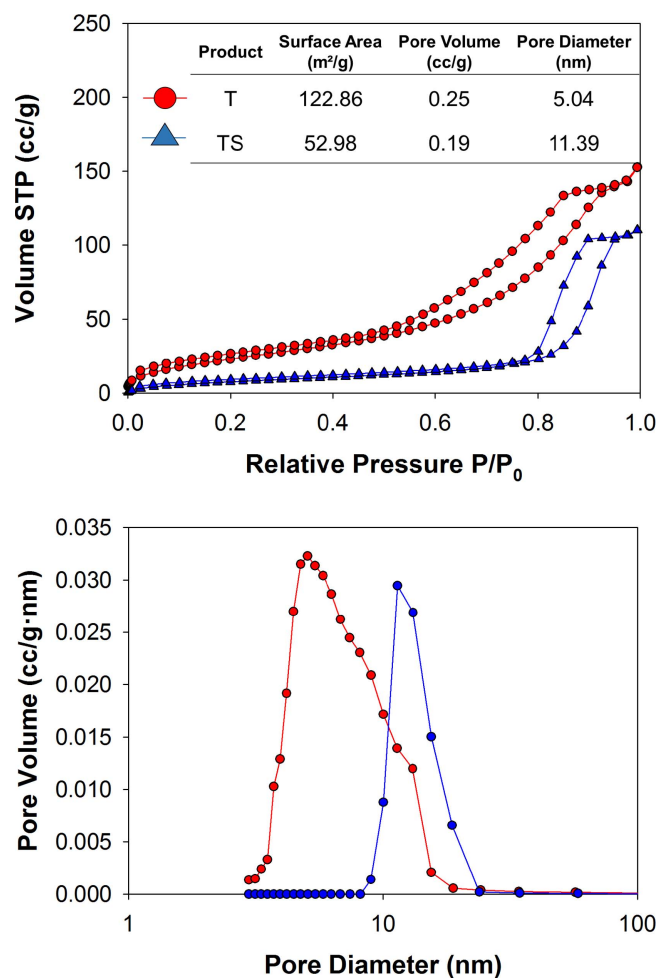

Figure 2. Nitrogen isotherms (top) and BJH pore size distribution (bottom) for the nanomaterials under study. Textural parameters are also shown in the inset.

reducing capillary pressure during gel drying, as described in previous papers [36, 37]. In spite of the considerable increase in n-8 content, a monolithic gel was obtained because the water/silica oligomer ratio in the sol was increased, favoring hydrolysis of the alkoxysilosane species. This feature prevents phase separation between n-8 and the silica precursor, observed for higher n-8 content in a previous paper [36]. Phase separation can also be prevented by using a lower ultrasound power. The xerogel containing CSP (TS formulation) showed a typical slight whiteness due to the presence of 40 nm particles. The suitable integration of these CSP into the gel matrix was confirmed by the homogeneous appearance of the material [10].

Figure 2 (top) presents the N$_2$ adsorption/desorption isotherms and the textural parameters obtained for the studied xerogels. Both xerogels presented typical isotherms of mesoporous materials (type IV). Regarding the hysteresis loop, the two xerogels showed parallel, and nearly vertical, branches, being classified as H1 type. This kind of hysteresis is attributed to materials consisting of agglomerated particles or compacted clusters of spherical particles [36, 38, 39]. This loop is more clearly observed for the xerogel containing commercial nanoparticles (TS). In a previous paper [10], CSP

were also integrated into a hybrid organic-inorganic matrix. In this case, the hysteresis loop obtained was the H2 type, characterized by a triangular shape. It can be associated with a particulate material with lower pore connectivity than that obtained for H1 type materials. Regarding the pore volume (see figure 2), the values obtained were significantly higher than those corresponding to the previously prepared ormosil [10]. These two features (reduction in pore connectivity and pore volume) are a consequence of the high shrinkage of the organic component during gel drying, as discussed in a previous paper [36]. By comparing the texture of the two xerogels studied in this work, it was observed that the addition of non-porous CSP, significantly decreased the pore volume and, consequently, the surface area (see figure 2).

Figure 2 (bottom) shows the pore size distribution according to the Barret–Joyner–Halenda (BJH) model [40]. The distributions of pore size obtained are centered on 5 nm and 11 nm for T and TS, respectively. These results highlight that the presence of CSP doubles the pore size. In the case of the materials of the ormosils, the presence of CSP hardly modifies the pore size. This can be explained as a consequence of the shrinkage of the organic chains during gel drying.

Figure 3 shows representative images of T and TS xerogels acquired by TEM at two different magnifications. In order to establish the effect produced by the surfactant in the gel structure, a xerogel obtained from TES40 sol by using HCl as catalyst was additionally synthesized and visualized (see figures 3(a) and (b)). As shown in figure 3(a), the xerogel prepared without n-8 presents a dense structure, which is typical of gels obtained by acid catalyst. By contrast, the xerogels containing n-8 show a particulate texture clearly observed in the images (see figures 3(c)–(f)), due to the effect of the surfactant [10, 36].

Comparison of the two xerogels under study, the image of T product (without CSP) clearly shows a silica matrix composed of particles of nearly homogeneous size of about 11 nm (see figures 3(c), (d)). Similar structures were obtained by using n-octylamine [10, 36, 41] or other basic catalyst [42, 43]. The xerogel containing CSP (TS) shows a particulate network with particle sizes around 100 nm integrated into a silica network, which is similar to that corresponding to the T structure. These larger particle sizes correspond to the aggregation of the CSP (with sizes around 40 nm) with the particles produced during the sol-gel process (see figures 3(e), (f)). This confirms the integration of the commercial NPs into the material during the sol-gel process.

The TEM results also allow the textural data obtained by physisorption to be explained. It is assumed that the pores detected correspond to the voids between the silica particles, and that the significant increase in the pore size is due to the CSP integration (with larger pore size) into the silica network.

The ^{29}Si NMR spectra for both xerogels are shown in figure 4. Both xerogels present Q1–Q4 peaks corresponding to single, bi- tri- and tetra-functional SiO$_2$ structural units. This high reticulation pattern is associated with particulate

silica gels [36, 44, 45], which is confirmed by images obtained by TEM (see figure 3). Regarding the differences between the materials, the TS spectra (with CSP) present more intense Q1 and Q2 signals and a higher Q3/Q4 ratio than that associated with T (without CSP), showing that a lower degree of condensation is obtained for the material containing CSP. This can be explained as a consequence of possible interactions produced between CSP and n-octylamine. As previously reported [46–48], amine compounds may be adsorbed onto silica surfaces via electrostatic interactions. Thus, less n-octylamine is available to catalyze the sol-gel transition as CSP are present in the starting sol, promoting a suppressive effect of the silica condensation [17].

The previous hypothesis is confirmed by solid-state ^{1}H MAS NMR spectra (see figure 4(b)). The signals observed at +1.2 and +3.8 ppm can be associated with oxomethylene and methyl group protons from ethoxy species, respectively [49]. In addition, the solid-state ^{13}C MAS NMR spectra of the xerogels (figure 4(c)), show the signals at +59.7 and +18.0 ppm corresponding to oxomethylene and methyl group carbons from ethoxy species, respectively [50, 51]. These peaks confirm the presence of residual ethoxy groups, which were maintained in the xerogel even after hydrolysis and condensation processes, confirming the existence of non-completed condensed species (Q1–Q3), as observed in the ^{29}Si NMR spectra. In the case of the ^{1}H spectra, a higher intensity of the peaks corresponding to ethoxy groups is clearly observed for TS. This confirms the suppressive effect played by CSP during the condensation process.

FTIR spectra of T and TS, obtained as sols and gels, are presented in figure S2. The two sols do not present differences in their spectra, showing typical peaks of siloxanes (792 and 1043 cm^{-1}) [13, 52]. The peak at 970 cm^{-1} is attributed to Si–OH stretching vibration [13] and the broad band at 3750–3250 cm^{-1} is associated with hydrogen-bonded silanol groups with absorbed molecular water. The peaks related to C-H vibrations are observed at 3000–2800 cm^{-1}, 1440–1020 cm^{-1} and 1163 cm^{-1} [53]. The presence of CH signals confirms the presence of ethoxy groups and the subsequent incomplete condensation of the xerogels, as discussed from NMR experiments.

3.2. Effectiveness on the building subtrate

The sols were applied by spraying onto stone samples commonly employed as building materials. The uptake was 0.20%w/w for both products. Dry matter values were also similar (0.10%w/w). The functionalization of the treated building surfaces by the fluorinated coating did not modify the previous dry matter values, due to its high solvent content and consequent evaporation during drying. This result suggests that the fluorinated alkoxysilane creates a film on the silica coating, or on the stone (in the case of the untreated sample), but does not penetrate into the pore structure of the stone.

Tables S1 and S2 show water droplet SCA values and their corresponding advancing and receding CA values for the
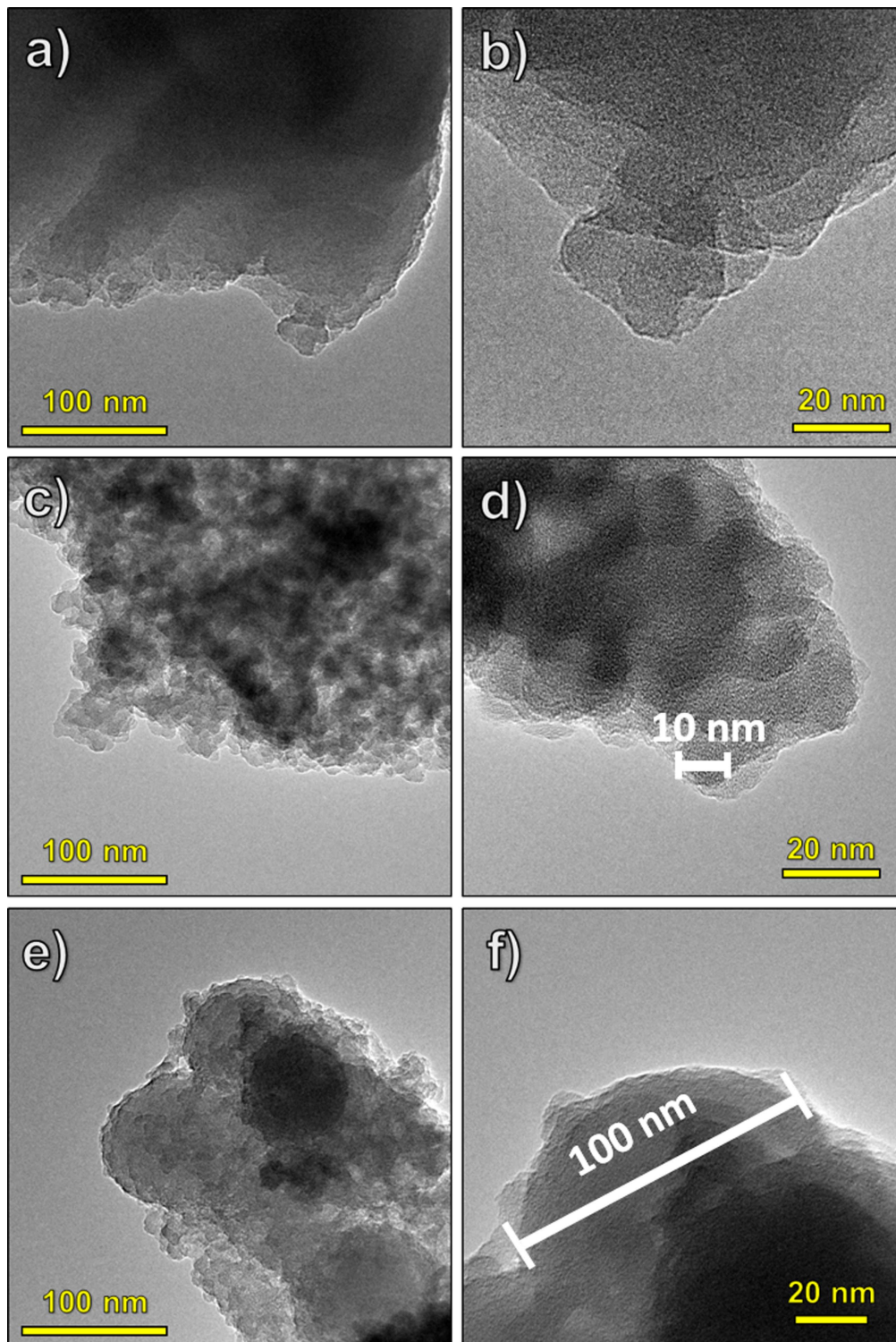
Figure 3. Images obtained in TEM with different magnifications for acid-catalysed TES40 xerogel (a), (b), T (c), (d) and TS (e), (f).

surfaces of treated stone samples and their untreated counterparts, 1 and 4 months after the application of the products, respectively. Figure S3 presents the RCA values of the treated samples, 1 and 4 months after the application of the products, with the RCA values characterizing the hydrophobic behavior of the surface [54]. The low static CA value ($<30°$) for the untreated surface evidenced the hydrophilic nature of the substrate. In this sample, the dynamic CA could not be measured because the water droplets were absorbed during the measurement.

In the case of the treated samples, RCA values higher than $90°$ were obtained for all the products 1 month after the application. This highlights the hydrophobic behavior of all the surfaces. This behavior is expected for the samples presenting the additional fluorinated coating due to the reduction of surface energy produced by the halogenated component. In
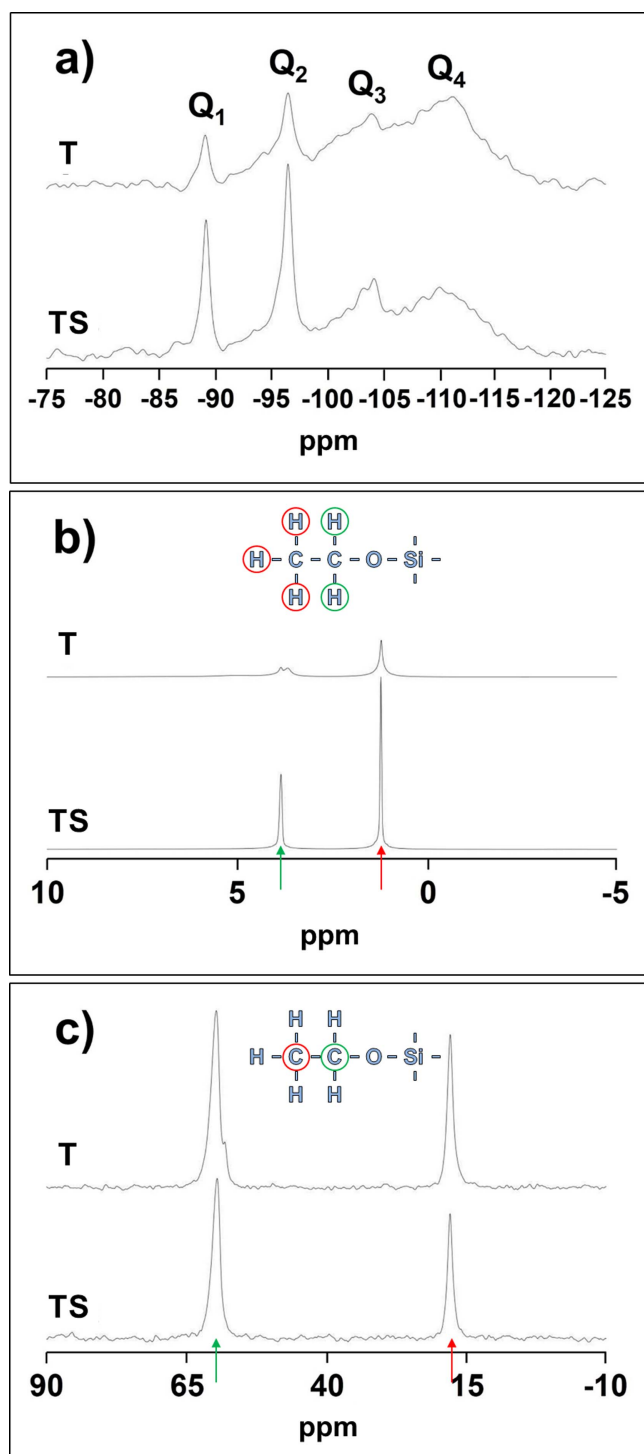
Figure a), b), c) NMR spectra.

Figure 5. Static CA values and their corresponding advancing and receding CA for the treated surfaces and their untreated counterpart. The hysteresis value for each treatment is represented in the line and scatter plot.

Figure 4. ^{29}Si (a), ^{1}H (b) and ^{13}C (c) MAS NMR spectra of the xerogels under study. The peaks marked as green correspond to ^{13}C and ^{1}H from oxomethylene groups from ethoxy species. The peaks marked as red correspond to ^{13}C and ^{1}H from methyl groups from ethoxy species.

hydrophobic behavior after several months of the synthesis, was previously reported [55, 56]. This effect is not supposed to be maintained in time due to the progress of the condensation. After 4 months, T gave rise to a hydrophilic surface, but TS still maintained its hydrophobic behavior, with high CA values, of around 130°. This can be related to the formation of a nanostructure induced by the CSP added to the sol. As previously discussed [57–59], this nanoroughness can produce air pockets in the surface where the water cannot totally penetrate, promoting a significant increase in the CA values, even for surfaces of a hydrophilic nature. The hydrophobic behavior is discussed in depth from AFM results in a next paragraph. In addition, the presence of CSP slows down the hydrolysis and condensation of silica oligomer species, as previously discussed according to the NMR spectra (see figure 4). Thus, ethoxy groups, producing a reduction in surface energy, could still be maintained in the xerogel after 4 months. It is obvious the surfaces will become hydrophilic (with RCA values below 90°) as ethoxy groups are hydrolyzed.

Regarding the surfaces with an additional fluorinated coating, all of them presented RCA values above 130° after 1 month, these values being practically maintained 4 months after application, confirm the duration of these treatments over time. The highest RCA values (>150°) were obtained for surfaces treated with TS + F. This is explained as a consequence of the combination of nanoroughness induced by the CSP and the low surface energy achieved by the presence of the fluorine atoms in the coating.

Figure 5 shows static CA and dynamic CA and their corresponding hysteresis between advancing and receding 1 month after application. The values obtained after 4 months are shown in table S2. Regarding the water repellence, which is characterized by a hysteresis below 10°, this property was only achieved by the surface treated with TS + F (Hysteresis value of 6°). This feature is newly produced by the combined effect of the nanoroughness induced by the CSP and the low surface energy produced by the fluorinated coating. However, T + F and F surfaces (without CSP) showed higher hysteresis

the case of the surfaces without fluorinated coating (T and TS), the hydrophobic behavior can be explained as a consequence of the incomplete condensation of ethoxy groups as previously discussed according the results obtained by NMR and FTIR experiments. The presence of residual ethoxy groups in silica gels applied on stones, maintaining
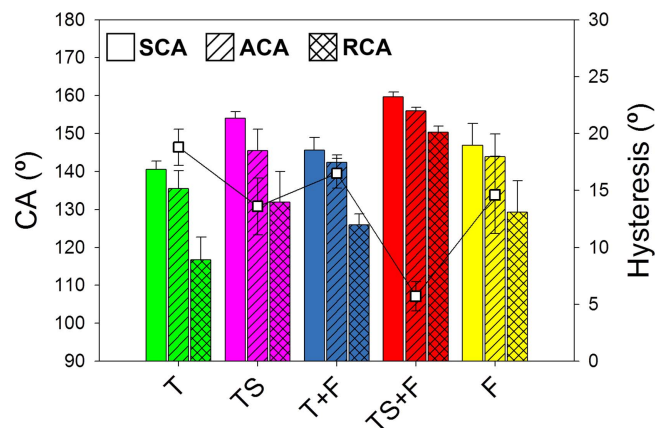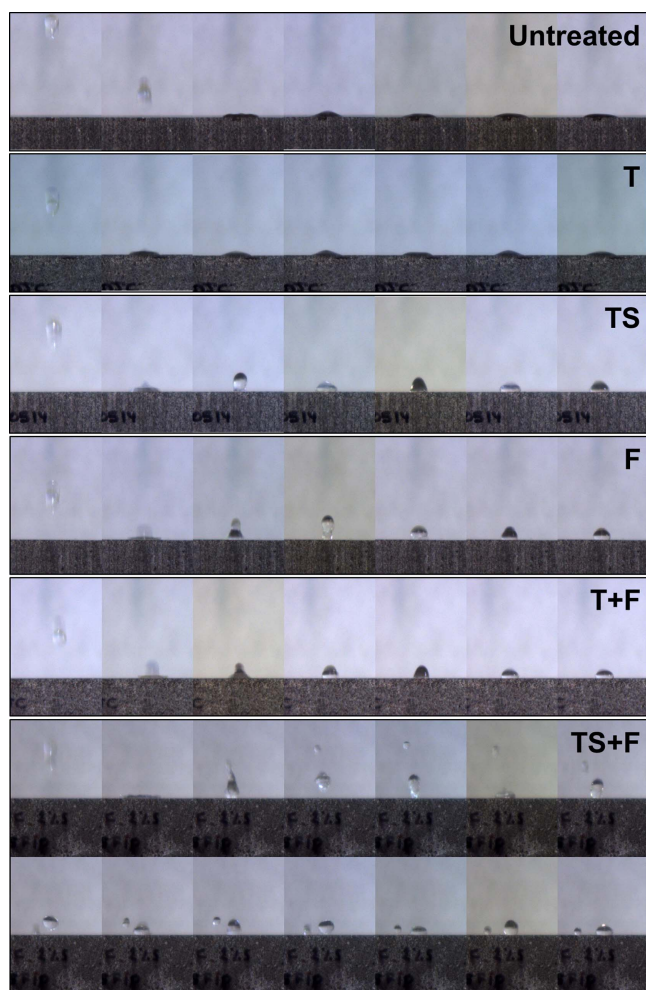
Figure 6. Time-lapse sequence of water droplets hitting on the surface of the untreated substrate and its treated counterparts.

values. A clear influence of the CSP was also observed in the hysteresis values, with the CSP (TS and TS + F) treatments showing lower values than those obtained for materials without particles (T and T + F). The hysteresis values were practically maintained 4 months after application, as shown in the table S2. Finally, we wish to remark that the TS + F coating converts the stone building material into a super-hydrophobic surface (CA values >150° and a hysteresis of 6°). This surface can be considered to be a Cassie–Baxter wetting state [60], as discussed later.

In order to confirm the water-repellent behavior of the studied surfaces, a simple experiment was carried out, which involved hitting the surfaces with water droplets falling from a height of 3 cm, as carried out in previous papers [61]. The figure 6 shows the snapshots of the test for each surface under study. In the case of the untreated surface, and that treated with T, the drop clearly spreads onto the surface due to its hydrophilic nature and high hysteresis as observed in figure 5, respectively. In the case of the surfaces with the TS, F and T + F coatings, it was observed that the droplet began to bounce but it remained pinned to the surface. For the surface treated with the superhydrophobic TS + F coating, the

droplet bounced off the surface, as clearly shown in frames 4 and 8 corresponding to the aforementioned treatment. In addition, a video of the water droplets being poured over the surfaces under study with a tilting of 10° is available in the supporting information (video S1). Again, the surface treated with TS + F presented water repellence behavior, shown by the droplets quickly bouncing and rolling off the surface. The other surfaces did not show a repellence effect, the water droplets staying pinned on the substrate.

The superhydrophobic behavior demonstrated by the TS + F coatings suggests that a self-cleaning effect could also be observed in this surface. Thus, a test was carried out consisting of pouring water droplets onto a TS + F surface previously made dirty with two different staining agents (red brick powder and methylene blue). A snapshot sequence of the cleaning process of the red brick powder is shown in figure 7. The powders were completely removed from the surface by the droplets rolling off. A video of a similar cleaning process of the methylene blue is available in the supporting information (video S2). In this case, it can be observed that the methylene blue is dissolved in water droplets during sliding, leaving a clean surface. For comparison, an untreated surface was also subjected to the methylene blue self-cleaning test. In this case, the water droplets dissolved the staining agent and the hydrophilic nature of the surface promoted the solution absorption by the pores of the substrate. A blue stain was permanently maintained on the untreated surface.

The oleophobicity of the surfaces was also studied by measuring the static CA of olive oil droplets deposited on coated substrates and their uncoated counterpart (see figure 8 and table S1). As expected, oleophobicity (CA > 90°) was only achieved in the samples treated with the fluorinated coatings. The CA values obtained from oil droplets were significantly lower than those observed for water droplets, because oil surface energy is considerably lower than that of water [62].

The figure S4 shows images of the surface of the stone substrate treated with TS + F and untreated. To compare the organic-inorganic hybrid coating with the superhydrophobic behavior developed previously by our group [10], the image of a surface treated with this product is also included in the figure. As shown in the images, the ormosil superhydrophobic coating does not produce any oleophobic effect, while the fluorinated coating creates an effective oleophobic surface. This is a consequence of the greater reduction in surface energy produced by the oleophobic treatment with regard to that produced by the coating containing an organic comp-onent (polydimethylsiloxane).

The presence of Fluor in TS + F coating was demon-strated by means of x-ray EDS. The figure S5 shows the spectra of TS and TS + F coatings. Both spectra were acquired at low voltages (0.2–1.0 eV) in order to be able to see the Fluor signal (around 0.70 eV). Thus, the signal corresponding to silicon (around 1.90 eV) was not observed for the tested samples. Both spectra showed peaks at 0.30 eV
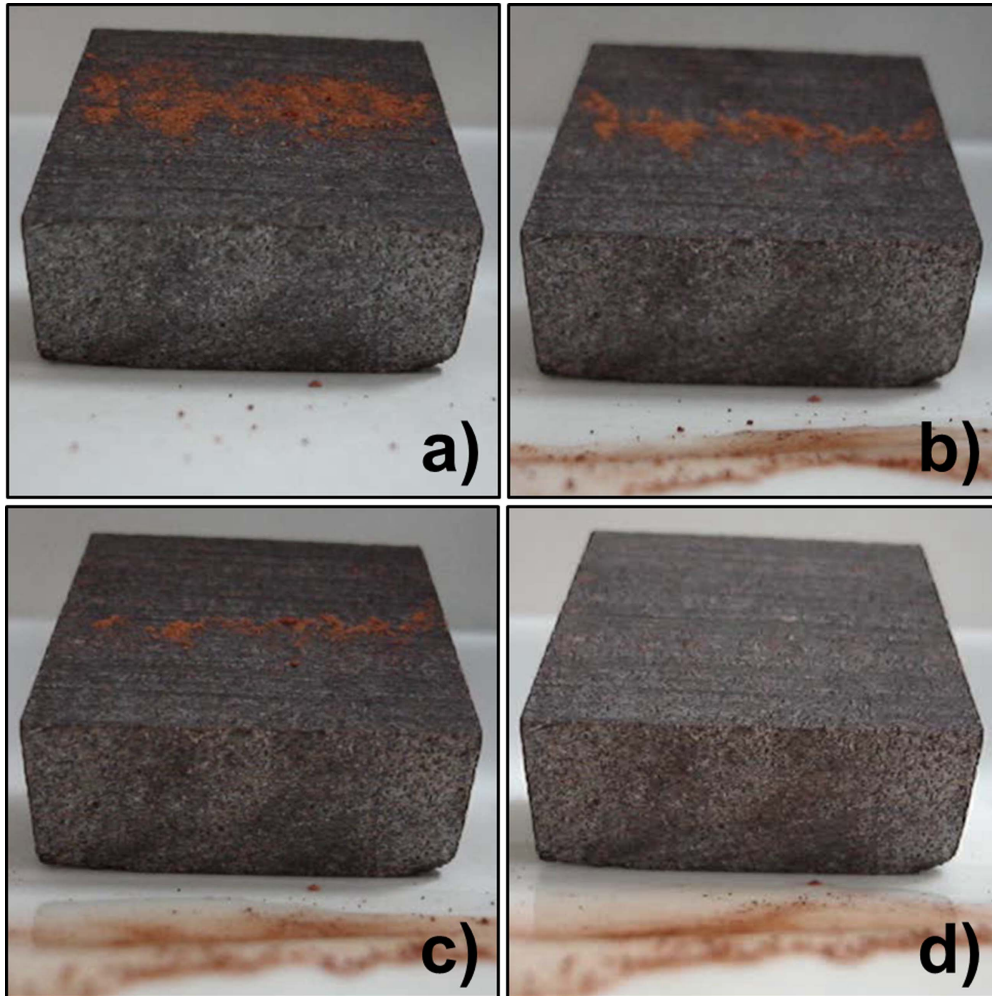
Figure 7. Time sequence (a)–(d) of the self-cleaning process on the superhydrophobic surface.
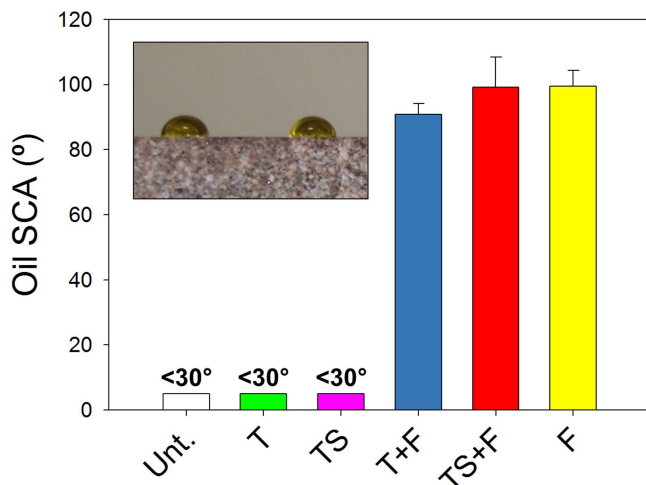

Figure 8. Oil static contact angle values for the treated surfaces and their untreated counterpart. An image of the oleophobic effect in the TS + F treated stone sample is also shown in the inset.

and 0.55 eV corresponding to Carbon and Oxygen, respectively. In the specific case of the fluorinated surface (TS + F), a signal at 0.72 eV was clearly observed, confirming the presence of Fluor.

As the TS + F coated surface presents a super-hydrophobic behavior, which should be a consequence of the combination of roughness and the reduction of the surface energy, the morphology of the surfaces under study was examined to investigate the contribution of their nanostructure to the production of the superhydrophobic effect. The figure 9 shows AFM and SEM images obtained for the surfaces under study. As the addition of the fluorinated coating does not introduce any topographical change, only images of the untreated surface and those treated with T + F and TS + F are shown. The surface topographies obtained by the AFM technique perfectly match those from SEM. The untreated surface shows a random roughness associated with the stone heterogeneity. The surface morphology is hardly modified as the T + F coating is applied, while the coating including CSP (TS + F), substantially changes the morphology of the surface, showing a closely-packed rough coating. As discussed for TEM in a previous paragraph (see figure 3), the CSP are aggregated to the silica particles created during sol-gel transition, inducing this roughness. This is explained by the closely-packed topography producing a non-wettable surface with a Cassie–Baxter regime, in which air pockets
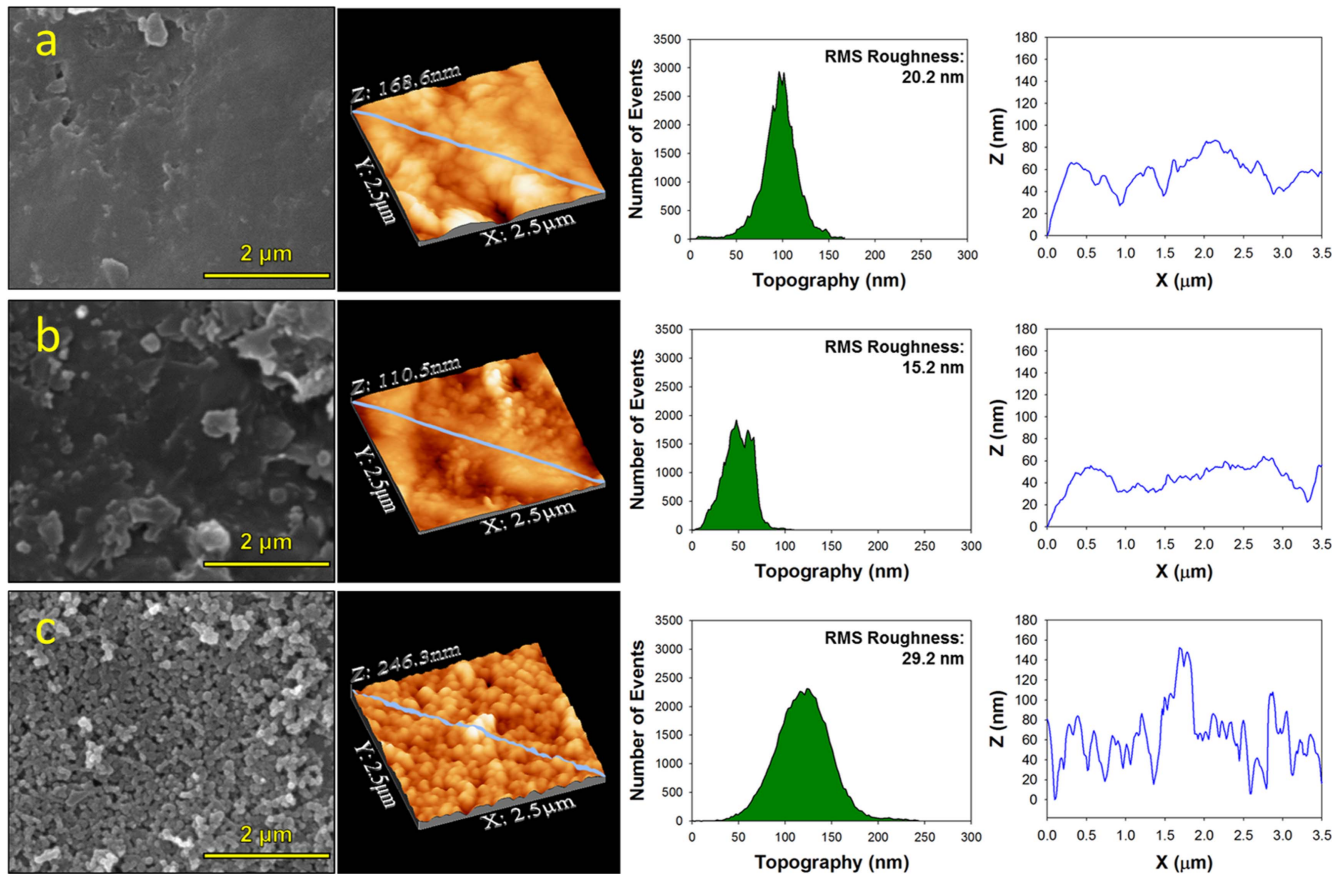
Figure 9. AFM 3D topographic images, size distribution of the roughness and 2D profiles of the roughness of the surface under study: (a) untreated. (b) T + F. (c) TS + F. The blue lines in the AFM 3D topographic images show the path followed to obtain the profile.

could be trapped between the aggregates of particles [5, 10, 63, 64].

The 3D topography and the roughness size distribution with RMS values are shown in figure 9. The untreated surface shows a higher RMS roughness value than that from the surface with the T + F coating. It highlights that this coating fills the grooves present in the stone substrate. In the case of the TS + F coating, the nanoroughness induced by CSP increased the RMS value and, importantly, it also increased the coating uniformity.

In order to avoid the influence of the microroughness of the stone substrate, the scan area for the RMS roughness analysis was reduced to 500 nm per 500 nm square, consequently taking into account only the nanometic roughness produced by the coatings [64]. At this scale, the roughness value of the untreated surface (5.7 nm) was increased as the T coating was applied (6.8 nm). It demonstrated that the T + F coating presents a roughness produced by NPs created during sol-gel transition. In the case of the TS + F coating, the roughness induced by CSP was significantly higher (17.4 nm).

From the roughness profiles obtained (see figure 9), it can be observed that the superhydrophobic TS + F surface presented completely different roughness peaks to those obtained from the other studied surfaces. Specifically, the TS + F surface showed fairly uniform distance values between pitches, of around 140 nm, which can be related to the particle

size measured by TEM (see figures 3(e), (f)). In the case of the other coatings (without CSP) and the untreated surfaces, they showed distances between pitches ranging from 500 to 1000 nm, associated to the substrate roughness. This greater distance between pitches is responsible for the water penetration, whereas the TS + F produced a reduction of droplet-surface contact area, resulting in the Cassie–Baxter state [10, 65].

To corroborate the existence of a Cassie–Baxter state, an analysis of the portion of the surface exposed to water contact can be carried out from the 2D AFM images by using WSxM NANOTEC Software. The images of roughness height gradient were employed to obtain images contrasting portions of surface area corresponding to peaks and troughs (see figure 10). The surface ratio values were given by dividing the surface area portion corresponding to peaks by the total surface area. As Di Fonzo *et al* previously explained [64], lower surface ratios (<0.8) are associated with surface area profiles with islands of peaks, with the consequent appearance of air pockets inducing a Cassie–Baxter wetting regime. This hypothesis perfectly matches the results obtained in the current study, because a surface ratio below 0.80 was only obtained for the surface presenting superhydrophobic behavior (TS + F, see figure 5). Moreover, the presence of islands of peaks is clearly observed in its contrasting image (see figure 10).
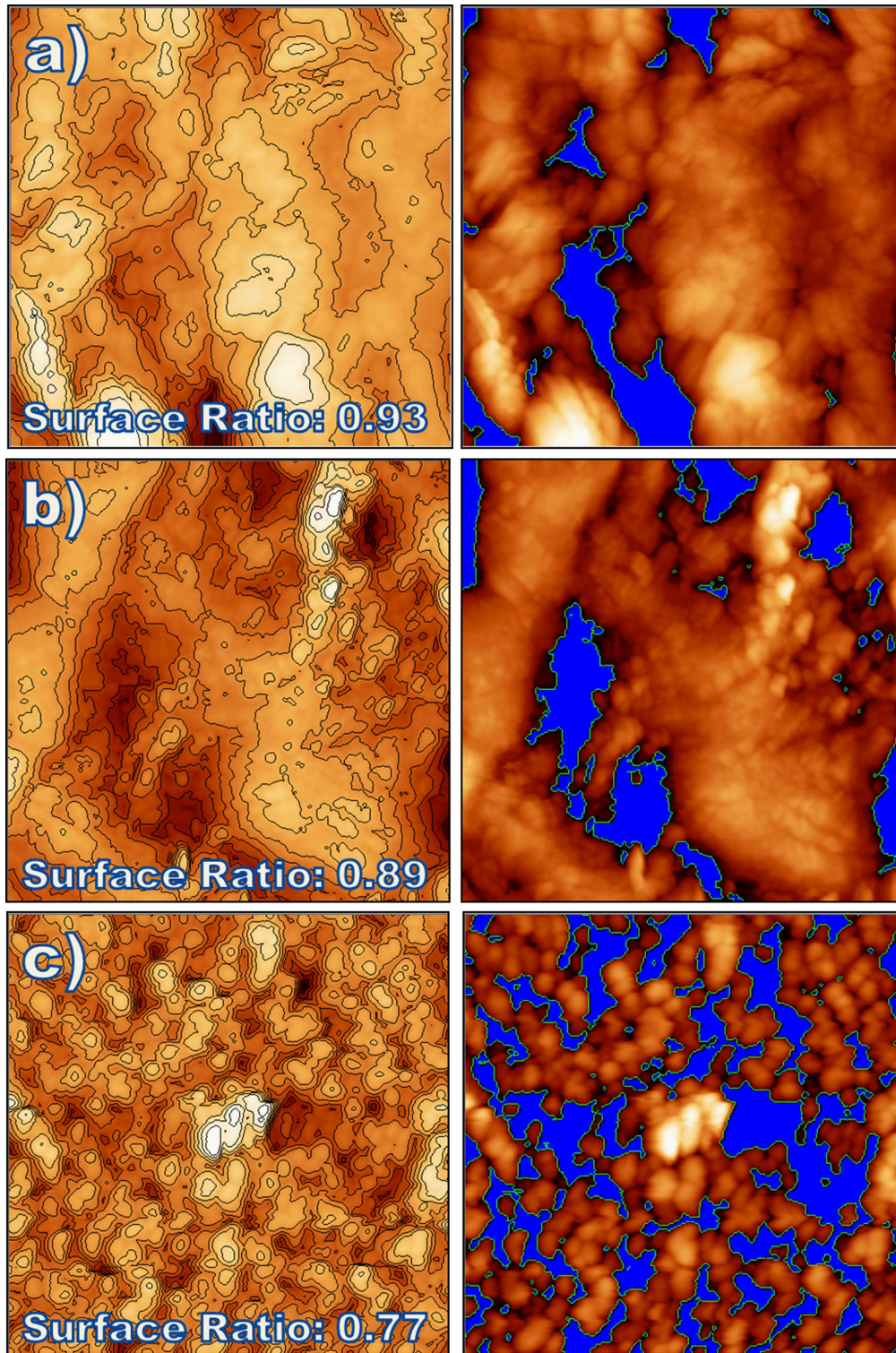
Figure 10. Column 1: roughness height gradient obtained from 2D AFM images and Column 2: peaks and troughs contrasting images for (a) untreated, (b) T + F and (c) TS + F surfaces.

Finally, we want to indicate that the TS surface with the same surface ratio as that from TS + F could promote the formation of air pockets in the nanostructure into which liquid only partially penetrates, even if the surface chemistry is hydrophilic due to the absence of the fluorinated coating. Consequently, a Cassie-impregnating state [57, 66] could be produced, which is an intermediate state between the Wenzel and Cassie–Baxter

models, with high CA values (130°) but a high water droplet adhesion due to its high CA hysteresis (see figure 5).

For potential application of the self-cleaning super-hydrophobic surface developed in this study, a long-term life of its effectiveness is required. Thus, two different studies were carried out: (1) evolution of static and dynamic CA over time under indoor conditions (they were measured at 1, 4 and
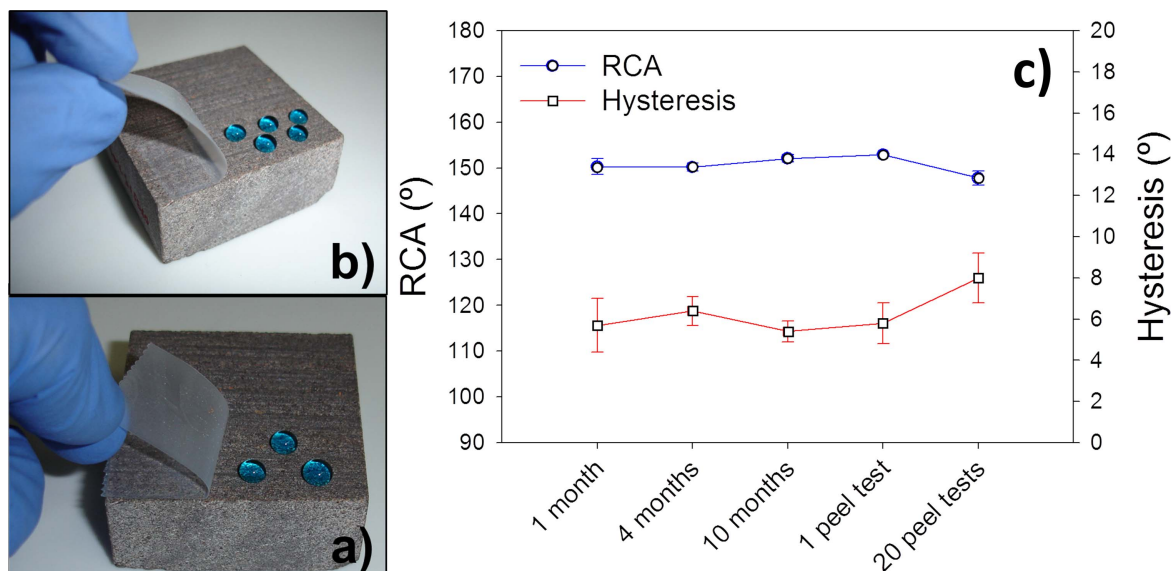
Figure 11. Receding CA and hysteresis values for the TS + F coated surface for the different elapsed times tested and after 1 and 20 peeling cycles.

10 months elapsed time from the application) and (2) the mechanical stability of the TS + F treatment was studied by a peeling test, which consisted of attachment/detachment cycles by using an adhesive tape applied by pressure. In this case, changes in static and dynamic CA were evaluated after 1 and 20 attachment/detachment cycles. The figure 11 presents the evolution of the RCA and hysteresis values for the different elapsed times tested. The changes of these parameters after attachment/detachment cycles are also presented. The CA values obtained are presented in table S3.

Receding CA was practically constant after 10 months, whereas hysteresis values, characterising repellence behaviour, were even slightly reduced. In the case of the attachment/detachment cycles, the hydrophobicity and water repellence behaviour was still maintained, showing a very slight variation for the receding CA (from 152° to 148°) and for the hysteresis contact angle (from 5° to 8°) after 20 attachment/detachment cycles. These results highlight that a lasting superhydrophobic behaviour is clearly achieved. Figure 11 also shows images of water droplets coloured with methylene blue, deposited on the surfaces tested after 1 and 20 cycles. As observed, the appearance of the droplets was not modified.

The long-time wear resistance presented by the TS + F coating under study can be explained as a consequence of the lasting grafting reactions that occurred between the substrate and the two consecutive coatings applied. Firstly, successive condensation reactions were produced between Si–OH, or even Si–OEt, from the silica oligomer and labile Si–OH species from the building substrate, which is a sandstone with 60% quartz. Thus, after 24 h, a lasting SiO_2 nanocomposite coating, in which CSP are integrated, as previously reported, is produced. As the additional hydrolyzed fluorinated alkoxysilane is applied, effective functionalization of the SiO_2 nanocomposite is achieved. The grafting reactions that possibly occurred are shown in figure 12. In this case, labile Si–OH groups from the hydrolyzed fluorinated alkoxysilane
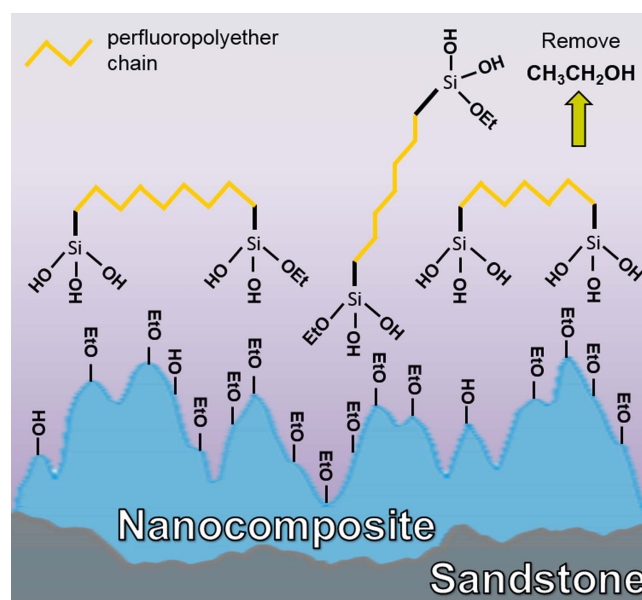
Figure 12. Schematic illustration of the possible functionalization process between the fluorinated alkoxysilane and the SiO_2 nanocomposite coating.

condensed with Si–OEt and Si–OH groups present in the nanocomposite surface. This functionalization process was previously recognized to produce a lasting hydrophobic/oleophobic coating with significant mechanical resistance [23, 67, 68]. The presence of two ethoxysilanes grafting end groups for each fluorinated oligomer assures an effective functionalization process.

4. Conclusions

Amphiphobic (superhydrophobic and oleophobic) surfaces with practical application as self-cleaning building materials

were successfully produced by the application of two successive coatings: (1) a SiO_2 nanocomposite producing a closely-packed uniform topography. This promotes a non-wettable surface with a Cassie–Baxter regime, in which air pockets could be trapped between the aggregates of particles. (2) Hydrolyzed fluorinated alkoxysilane giving rise to hydrophobic and oleophobic properties. The surfaces demonstrated lasting performance due to the effective grafting by condensation reactions between the coatings and the substrate. Additionally, mechanical durability is demonstrated by superficial attachment/detachment cycles. Finally, we wish to note that the simple and low-cost synthesis route developed meets the requirements for practical application in building materials, including application to large areas and even the possibility of being applied on floors, buildings and other construction elements under outdoor conditions.

Acknowledgments

References

[1] Siegesmund S and Snethlage R 2014 *Stone in Architecture: Properties, Durability* 4th edn (London: Springer)

[2] Gao L and McCarthy T J 2009 Wetting 101° *Langmuir* **25** 14105–15

[3] Öner D and McCarthy T J 2000 Ultrahydrophobic surfaces. Effects of topography length scales on wettability *Langmuir* **16** 7777–82

[4] Huang J Y *et al* 2015 Robust superhydrophobic TiO_2@fabrics for UV shielding, self-cleaning and oil-water separation *J. Mater. Chem.* A **3** 2825–32

[5] Manoudis P N, Karapanagiotis I, Tsakalof A, Zuburtikudis I and Panayiotou C 2008 Superhydrophobic composite films produced on various substrates *Langmuir* **24** 11225–32

[6] De Ferri L, Lottici P P, Lorenzi A, Montenero A and Salvioli-Mariani E 2011 Study of silica nanoparticles–polysiloxane hydrophobic treatments for stone-based monument protection *J. Cult. Herit.* **12** 356–63

[7] Matziaris K, Stefanidou M and Karagiannis G 2011 Impregnation and superhydrophobicity of coated porous low-fired clay building materials *Prog. Org. Coat.* **72** 181–92

[8] Karapanagiotis I, Manoudis P N, Savva A and Panayiotou C 2012 Superhydrophobic polymer-particle composite films produced using various particle sizes *Surf. Interface Anal.* **44** 870–5

[9] Pedna A, Pinho L, Frediani P and Mosquera M J 2015 Obtaining SiO_2-fluorinated PLA bionanocomposites with

[10] Facio D S and Mosquera M J 2013 Simple strategy for producing superhydrophobic nanocomposite coatings *in situ* on a building substrate *ACS Appl. Mater. Interfaces* **5** 7517–26

[11] Carrascosa L A M, Facio D S and Mosquera M J 2016 Producing superhydrophobic roof tiles *Nanotechnology* **27** 095604

[12] Facio D S, Luna M and Mosquera M J 2017 Facile preparation of mesoporous silica monoliths by an inverse micelle mechanism *Micropor. Mesopor. Mat.* **247** 166–76

[13] Mosquera M J, De Los Santos D M and Rivas T 2010 Surfactant-synthesized ormosils with application to stone restoration *Langmuir* **26** 6737–45

[14] Illescas J F and Mosquera M J 2011 Surfactant-synthesized PDMS/Silica nanomaterials improve robustness and stain resistance of carbonate stone *J. Phys. Chem.* C **115** 14624–34

[15] Pinho L and Mosquera M J 2011 Titania-silica nanocomposite photocatalysts with application in stone self-cleaning *J. Phys. Chem.* C **115** 22851–62

[16] Pinho L, Elhaddad F, Facio D S and Mosquera M J 2013 A novel TiO_2-SiO_2 nanocomposite converts a very friable stone into a self-cleaning building material *Appl. Surf. Sci.* **275** 389–96

[17] Pinho L and Mosquera M J 2013 Photocatalytic activity of TiO_2-SiO_2 nanocomposites applied to buildings: influence of particle size and loading *Appl. Catal.* B Environ. **134-135** 205–21

[18] Pinho L, Rojas M and Mosquera M J 2015 Ag-SiO_2-TiO_2 nanocomposite coatings with enhanced photoactivity for self-cleaning application on building materials *Appl. Catal.* B Environ. **178** 144–54

[19] Zarzuela R, Carbu M, Gil M L A, Cantoral J M and Mosquera M J 2017 CuO/SiO_2 nanocomposites: a multifunctional coating for application on building stone *Mater. Des.* **114** 364–72

[20] Park J, Urata C, Masheder B, Cheng D F and Hozumi A 2013 Long perfluoroalkyl chains are not required for dynamically oleophobic surfaces *Green Chem.* **15** 100–4

[21] Kim E K, Kim J Y and Kim S S 2013 Synthesis of superhydrophobic SiO_2 layers via combination of surface roughness and fluorination *J. Solid State Chem.* **197** 23–8

[22] Yang H and Deng Y 2008 Preparation and physical properties of superhydrophobic papers *J. Colloid Interface Sci.* **325** 588–93

[23] Ferrero F and Periolatto M 2013 Application of fluorinated compounds to cotton fabrics via sol-gel *Appl. Surf. Sci.* **275** 201–7

[24] Raza M A, Kooij E S, van Silfhout A, Zandvliet H J W and Poelsema B 2012 A colloidal route to fabricate hierarchical sticky and non-sticky substrates *J. Colloid Interface Sci.* **385** 73–80

[25] Li Y, Huang X J, Heo S H, Li C C, Choi Y K, Cai W and Cho S O 2007 Superhydrophobic bionic surfaces with hierarchical microsphere/SWCNT composite arrays *Langmuir* **23** 2169–74

[26] Li Y, Cai W, Cao B, Duan G, Sun F, Li C and Jia L 2006 Two-dimensional hierarchical porous silica film and its tunable superhydrophobicity *Nanotechnology* **17** 238–43

[27] Li Y, Duan G and Cai W 2007 Controllable superhydrophobic and lipophobic properties of ordered pore indium oxide array films *J. Colloid Interface Sci.* **314** 615–20

[28] Lee E J, Lee H M, Li Y, Hong L Y, Kim D P and Cho S O 2007 Hierarchical pore structures fabricated by electron irradiation of silicone grease and their applications to superhydrophobic and superhydrophilic films *Macromol. Rapid Commun.* **28** 246–51

[29] Poli T, Toniolo L and Chiantore O 2004 The protection of different Italian marbles with two partially fluorinated acrylic copolymers *Appl. Phys. A Mater. Sci. Process* **79** 347–51

[30] Kronlund D, Bergbreiter A, Meierjohann A, Kronberg L, Lindén M, Grosso D and Smått J H 2015 Hydrophobization of marble pore surfaces using a total immersion treatment method-product selection and optimization of concentration and treatment time *Prog. Org. Coat.* **85** 159–67

[31] Colangiuli D, Calia A and Bianco N 2015 Novel multifunctional coatings with photocatalytic and hydrophobic properties for the preservation of the stone building heritage *Constr. Build. Mater.* **93** 189–96

[32] Aslanidou D, Karapanagiotis I and Panayiotou C 2016 Tuning the wetting properties of siloxane-nanoparticle coatings to induce superhydrophobicity and superoleophobicity for stone protection *Mater. Des.* **108** 736–44

[33] Ling X Y, Phang I Y, Vancso G J, Huskens J and Reinhoudt D N 2009 Stable and transparent superhydrophobic nanoparticle films *Langmuir* **25** 3260–3

[34] Drdácký M, Lesák J, Rescic S, Slížková Z, Tiano P and Valach J 2012 Standardization of peeling tests for assessing the cohesion and consolidation characteristics of historic stone surfaces *Mater. Struct.* **45** 505–20

[35] Berns R S 2000 *Billmeyer and Saltzman's Principles of Color Technology* 3rd edn (New York: Wiley-Interscience)

[36] Illescas J F and Mosquera M J 2012 Producing surfactant-synthesized nanomaterials *in situ* on a building substrate, without volatile organic compounds *ACS Appl. Mater. Interfaces* **4** 4259–69

[37] Mosquera M J, De Los Santos D M, Montes A and Valdez-Castro L 2008 New nanomaterials for consolidating stone *Langmuir* **24** 2772–8

[38] Kruk M and Jaroniec M 2001 Gas adsorption characterization of ordered organic-inorganic nanocomposite materials *Chem. Mater.* **13** 3169–83

[39] Thommes M, Kaneko K, Neimark A V, Olivier J P, Rodriguez-Reinoso F, Rouquerol J and Sing K S W 2015 Physisorption of gases, with special reference to the evaluation of surface area and pore size distribution (IUPAC technical report) *Pure Appl. Chem.* **87** 1051–69

[40] Barret E P, Joyner L G and Halenda P P 1951 The determination of pore volume and area distributions in porous substances: I. Computations from nitrogen isotherms *J. Am. Chem. Soc.* **73** 373–80

[41] Kosuge K and Singh P S 2001 Mesoporous silica spheres via 1-alkylamine templating route *Micropor. Mesopor. Mater.* **44** 139–45

[42] Orcel G and Hench L L 1988 Effect of formamide additive on the chemistry of silica sol-gels: II. Gel structure *J. Non. Cryst. Solids* **105** 223–31

[43] Bogush G and Zukoski C 1991 Studies of the kinetics of the precipitation of uniform silica particles through the hydrolysis and condensation of silicon alkoxides *J. Colloid Interface Sci.* **142** 1–18

[44] Babonneau F 1994 Hybrid siloxane-oxide materials via sol-gel processing: structural characterization *Polyhedron* **13** 1123–30

[45] Tanev P T and Pinnavaia T J 1996 Mesoporous silica molecular sieves prepared by ionic and neutral surfactant templating: a comparison of physical properties *Chem. Mater.* **8** 2068–79

[46] Wang X, Liu J, Du H and Miller J D 2010 States of adsorbed dodecyl amine and water at a silica surface as revealed by vibrational spectroscopy *Langmuir* **26** 3407–14

[47] Guo C and Holland G P 2014 Investigating lysine adsorption on fumed silica nanoparticles *J. Phys. Chem. C* **118** 25792–801

[48] Bharti B, Meissner J, Gasser U and Findenegg G H 2012 Surfactant adsorption and aggregate structure at silica nanoparticles: effects of particle size and surface modification *Soft Matter* **8** 6573

[49] Alam T M and Fan H 2003 Investigation of templated mesoporous silicate thin films using high speed, solid-state 1H MAS and double quantum NMR spectroscopy *Macromol. Chem. Phys.* **204** 2023–30

[50] Yokogawa H and Yokoyama M 1995 Hydrophobic silica aerogels *J. Non. Cryst. Solids* **186** 23–9

[51] Choi J Y, Kim C H and Kim D K 1998 Formation and characterization of monodisperse, spherical organo-silica powders from organo-alkoxysilane-water system *J. Am. Ceram. Soc.* **81** 1184–8

[52] Tellez L, Rubio J, Rubio F, Morales E and Oteo J L 2003 Synthesis of inorganic-organic hybrid materials from TEOS, TBT and PDMS *J. Mater. Sci.* **38** 1773–80

[53] Koganti V R, Das S and Rankin S E 2014 *In situ* FTIR Investigation of the kinetics of silica polycondensation in surfactant templated, mesostructured thin films *J. Phys. Chem. C* **118** 19450–61

[54] Della Volpe C, Penati A, Peruzzi R, Siboni S, Toniolo L and Colombo C 2000 The combined effect of roughness and heterogeneity on contact angles: the case of polymer coating for stone protection *J. Adhes. Sci. Technol.* **14** 273–99

[55] Scherer G W and Wheeler G S 2009 Silicate consolidants for stone *Key Eng. Mater.* **391** 1–25

[56] Franzoni E, Graziani G and Sassoni E 2015 TEOS-based treatments for stone consolidation: acceleration of hydrolysis-condensation reactions by poulticing *J. Sol-Gel Sci. Technol.* **74** 398–405

[57] Ebert D and Bhushan B 2012 Wear-resistant rose petal-effect surfaces with superhydrophobicity and high droplet adhesion using hydrophobic and hydrophilic nanoparticles *J. Colloid Interface Sci.* **384** 182–8

[58] Cao L, Hu H A and Gao D 2007 Design and fabrication of micro-textures for inducing a superhydrophobic behavior on hydrophilic materials *Langmuir* **23** 4310–4

[59] Liu J L, Feng X Q, Wang G and Yu S W 2007 Mechanisms of superhydrophobicity on hydrophilic substrates *J. Phys. Condens. Matter* **19** 356002

[60] Cassie A B D and Baxter S 1944 Wettability of porous surfaces *Trans. Faraday Soc.* **40** 546–551e

[61] Bird J C, Dhiman R, Kwon H M and Varanasi K K 2013 Reducing the contact time of a bouncing drop *Nature* **503** 385–8

[62] Xiong D, Liu G and Scott Duncan E J 2013 Robust amphiphobic coatings from bi-functional silica particles on flat substrates *Polymer* **54** 3008–16

[63] Xu L, Karunakaran R G, Guo J and Yang S 2012 Transparent, superhydrophobic surfaces from one-step spin coating of hydrophobic nanoparticles *ACS Appl. Mater. Interfaces* **4** 1118–25

[64] Passoni L, Bonvini G, Luzio A, Facibeni A, Bottani C E and Di Fonzo F 2014 Multiscale effect of hierarchical self-assembled nanostructures on superhydrophobic surface *Langmuir* **30** 13581–7

[65] Bhushan B and Her E K 2010 Fabrication of superhydrophobic surfaces with high and low adhesion inspired from rose petal *Langmuir* **26** 8207–17

[66] Webb H K, Crawford R J and Ivanova E P 2014 Wettability of natural superhydrophobic surfaces *Adv. Colloid Interface Sci.* **210** 58–64

[67] Kessman A J and Cairns D R 2011 Template-assisted encapsulation of fluorinated silanes in silica films for sustained hydrophobic-oleophobic functionality *J. Colloid Interface Sci.* **360** 785–92

[68] Wongchitphimon S, Wang R and Jiraratananon R 2011 Surface modification of polyvinylidene fluoride-co-hexafluoropropylene (PVDF-HFP) hollow fiber membrane for membrane gas absorption *J. Memb. Sci.* **381** 183–91

Producing superhydrophobic roof tiles

Luis A M Carrascosa, Dario S Facio and Maria J Mosquera

TEP-243 Nanomaterials Group. Physical-Chemistry Department, Faculty of Sciences, University of Cadiz, E-11510 Puerto Real, Cádiz, Spain

E-mail: mariajesus.mosquera@uca.es

CrossMark

Abstract

Superhydrophobic materials can find promising applications in the field of building. However, their application has been very limited because the synthesis routes involve tedious processes, preventing large-scale application. A second drawback is related to their short-term life under outdoor conditions. A simple and low-cost synthesis route for producing superhydrophobic surfaces on building materials is developed and their effectiveness and their durability on clay roof tiles are evaluated. Specifically, an organic–inorganic hybrid gel containing silica nanoparticles is produced. The nanoparticles create a densely packed coating on the roof tile surface in which air is trapped. This roughness produces a Cassie–Baxter regime, promoting superhydrophobicity. A surfactant, n-octylamine, was also added to the starting sol to catalyze the sol–gel process and to coarsen the pore structure of the gel network, preventing cracking. The application of ultrasound obviates the need to use volatile organic compounds in the synthesis, thereby making a 'green' product. It was also demonstrated that a co-condensation process effective between the organic and inorganic species is crucial to obtain durable and effective coatings. After an aging test, high hydrophobicity was maintained and water absorption was completely prevented for the roof tile samples under study. However, a transition from a Cassie–Baxter to a Wenzel state regime was observed as a consequence of the increase in the distance between the roughness pitches produced by the aging of the coating.

S Online supplementary data available from stacks.iop.org/NANO/27/095604/mmedia

(Some figures may appear in colour only in the online journal)

1. Introduction

In recent years, numerous superhydrophobic materials have been developed by using a combination of two strategies: reducing the surface free energy and roughening the surface [1]. The effect of the roughness is that a layer of air is trapped beneath the water droplet, thus assisting the water droplets to roll off the surface, producing repellence in a similar way to various natural plant leaves, such as those of the lotus [2]. Superhydrophobic materials find applications in the field of building due to their interesting properties, such as self-cleaning, anti-fouling, stain-resistance and ice-repellence [3]. However, most of the synthesis routes developed involve tedious multi-stage processes, which prevent their large-scale application, such as on building materials and facades exposed to the weather [4]. A second and important drawback

for superhydrophobic materials application on buildings is related to the short-term life of the effectiveness of these materials under outdoor conditions [5]. Roughness in the surface is induced by top down (removing material from a bulk matrix) or bottom up procedures (coating constructed from the substrate upward). This surface architecture of roughness in the coating contributes significantly to poor mechanical properties and, subsequently, to low durability [6]. Thus, fabrication of durable superhydrophobic surfaces exposed to the weather under outdoor conditions still remains a challenge.

Most of the trials to produce superhydrophobic products with applications in the building field are based on simple processes consisting of spraying nanoparticles dispersed in different media, such as polymers or oligomeric solutions on different building materials, such as stone [7–9], wood [8],

concretes [10] or clay roof tiles [11]. Some drawbacks associated with the developed products are the requirement to use volatile organic compounds (VOCs) [7, 9], cracking of the films and reduced durability [9].

Our research group has recently developed an ultrasound-assisted, sol–gel route to produce cracking-free nanomaterials, *in situ*, on a substrate. These products have been specifically designed for restoring and protecting building materials. Specifically, we have prepared consolidant products [12, 13] hydrophobic and superhydrophobic materials [4, 13–15] and photoactive products with self-cleaning properties [16–20]. A surfactant added to the starting sol provides an efficient means of preventing cracking of the gel, as the result of two factors: (1) coarsening of the gel network, and (2) decreasing surface tension. These two factors reduce capillary pressure during gel drying, which is responsible for cracking [12]. In order to prevent the use of a co-solvent such as ethanol or other VOCs, and thereby make 'green' products, the starting sol is mixed under high-ultrasonic agitation [13]. As is well-documented in the literature [21], sonication does not require the use of alcoholic solvents. Another reason to use an ultrasound-assisted preparation is to promote the homogeneous mixing of the reagents employed in the synthesis and rapid and easy preparation of the sols under study [22].

It should be noted that our products are produced by a low cost process; and, of particular relevance, they meet the operational and commercial requirements for application to exterior surfaces of large buildings and structures [23]. The interest in our approach is confirmed by the recent papers from other researchers working in the same field. These authors [24–27] employed the strategy of n-octylamine addition to obtain crack-free products for building protection.

The objective of the present paper is to produce a coating for clay roof tiles in order to convert them into a superhydrophobic building material. Clay has been employed to make roof tiles for more than 3000 years and it still remains the most popular material [28]. Water is the most important decay factor in clay-based building materials due to significant hydric expansion of clay minerals [29]. The absorption of water causes the swelling of clay and its evaporation gives rise to shrinking and cracking [29, 30]. Superhydrophobic behavior could prevent the clay decay by water and ice accumulation in roofs, a common process in real-life. A simple and low-cost synthesis to produce superhydrophobic surfaces was developed by using a bottom-up strategy in which roughness is constructed by silica nanoparticles. This route, produced at ambient temperature, can be applied on roof tiles and other building elements, or even on other kinds of substrates requiring low-temperature and simple synthesis procedures. Specifically, silica nanoparticles were added to a mixture of organic and inorganic silica oligomers in the presence of n-octylamine. The nanoparticles were added to produce a coating of closely packed particles able to repel water. The organic component reduces the surface free energy of the material, resulting in a high hydrophobicity. Finally, the surfactant plays a valuable role, acting as a sol–gel transition catalyst and, by coarsening the pore

structure of the gel network, prevents the coating material from cracking. The synthesis process is assisted by ultrasound in order to produce a material free of VOCs.

An important practical and commercial requirement of the synthesized sol is to be able to store it for considerable lengths of time prior to its application onto substrates. In order to meet this requirement, water was not added to the sol, as was commonly added in previous syntheses by our group [4], to prevent its spontaneous hydrolysis and, consequent, condensation. In addition, the power and time of ultrasound were limited to prevent spontaneous hydrolysis [31]. In order to investigate the formation of an organic–inorganic hybrid gel and its subsequent effect on material durability, two alkylsiloxanes with different reactivity were employed as the organic components in the starting sol. Specifically, the presence of co-condensation between inorganic and organic species was investigated. The two synthesized sols were applied on clay roof tile samples, and its effectiveness, in terms of producing a superhydrophobic surface, was evaluated by dynamic and static contact angle (SCA) values. To make a comparison, a commercial hydrophobic product, commonly employed as a water repellent on building substrates, was also applied on tile samples. In order to evaluate the coating potential for long-term applications, one of the most important properties in the building field, contact angles were also determined on the samples under study after different lapsed times intervals. In addition, an artificial weathering test in a climatic chamber was carried out. Finally, and importantly, an in-depth investigation of the nanostructure surfaces was made, before and after the weathering test, to establish the relationship between the superhydrophobic property and the nanostructure.

2. Material and methods

2.1. Synthesis

A starting sol was obtained by mixing, under high-power ultrasonic agitation, TES40 WN (hereafter TES40) from Wacker Chemie AG, a hydroxyl-terminated poly-dimethylsiloxane (hereafter PDMS) from ABCR and AEROSIL OX50 (hereafter OX50) colloidal silica particles, obtained from Evonik in the presence of the surfactant n-octylamine, obtained from Sigma-Aldrich. For comparative purposes, a sol was prepared by the same route, but replacing the organic component PDMS by an organic-substituted siloxane, SILRES BS 290 (hereafter BS290) from Wacker. According to the technical data sheet, TES40 is an ethoxysilane (average degree of polymerization of 5) providing approximately 41% of silica upon complete hydrolysis. PDMS is a hydroxyl-terminated polydimethylsiloxane with a degree of polymerization of 12 and a molecular mass of between 400 and 700. Its OH percentage ranges from 4 to 6% w/w. OX50 consists of hydrophilic fumed silica nanoparticles with an average diameter of 40 nm and a surface area of $50 \, m^2 \, g^{-1}$. BS290, according to its technical sheet, is a
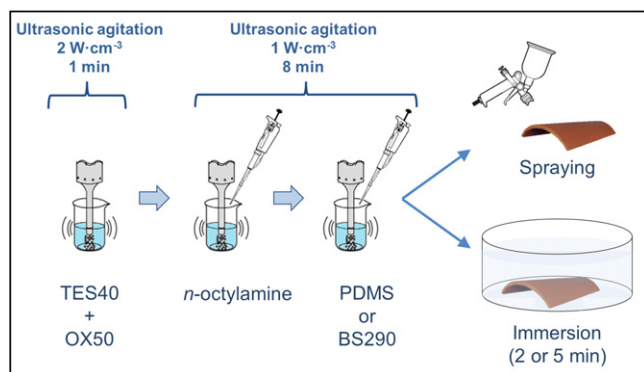
Figure 1. Synthesis route and application on roof tile samples.

solventless silicone concentrate that is based on a mixture of silane and siloxane.

This synthesis route was carried out on a BANDELIN ultrasonic HD 3200 (maximum 150 W at 20 kHz). The titanium probe, model TT25 (25 mm diameter), was used to produce ultrasonic irradiation and homogenize the reaction mixture. Syntheses were carried out as follows, an illustration of the route being presented in figure 1: (1) TES40 was mixed with OX50 under ultrasonic agitation for 1 min in order to avoid the precipitation of the silica particles. The ultrasonic power was 2 W cm^{-3}; (2) PDMS, or alternatively BS290, and pure n-octylamine were added under ultrasonic agitation (1 W cm^{-3}), and ultrasonic irradiation was maintained for 8 min. The proportion of n-octylamine and the organic component (PDMS or BS290) were 0.039 and 10%v/v, respectively. OX50 nanoparticles were in a 5% w/v concentration with respect to the total volume of the sol. For comparative purposes, BS290, which is commonly employed as a water-repellent product, was also investigated. Due to its high viscosity (15 mPa s), and according to the manufacturer's specifications, BS290 was dissolved in isopropyl alcohol (7% w/w). The products synthesized in our laboratory were named UCA (after the University of Cadiz) followed by P (initial letter of PDMS) or B (initial letter of BS290). The commercial product was denoted as BS290.

2.2. Sol–Gel characterization

Immediately after the synthesis of the sols, their rheological properties were studied using a concentric cylinder viscometer (model DV-II+ with UL/Y adapter) from Brookfield Engineering Laboratories Inc. Experiments were performed at a constant temperature of 25 °C maintained by recirculated water from a thermostatic bath. A shear stress versus shear rate flow curve was generated.

Next, xerogels of the materials under study were obtained by the casting of 3 ml of sol in open polypropylene vials. In order to study the stability of the sols for commercial storage, these were also maintained in closed vials. Gelation and drying took place by simple exposure of the open vials to laboratory conditions (at a relative humidity of 60% and a temperature of 20 °C). The xerogels obtained were

characterized according the techniques described below, one month after the synthesis.

Visual inspection was used to check for the presence of cracks in the xerogels. The contraction in volume of the materials during drying was calculated from the volume change undergone by the xerogel monoliths, using a digital caliper from Comecta.

Fourier transform infrared spectra (FTIR) were recorded in the surface of the xerogels using a FTIR-8400S from Shimadzu (4 cm^{-1} in resolution) in the region from 4000 to 650 cm^{-1}. Experiments were carried out in attenuated total reflection mode. Spectra were registered at two different elapsed times after synthesis (1 month and 1 year) in order to check the evolution of the xerogels. In addition, the effectiveness of copolymerization between inorganic (TES40) and organic (PDMS or BS290) oligomers, and subsequent organic–inorganic hybrid gel formation was tested by carrying out spectra of the xerogels after solid–liquid extraction in a Soxhlet apparatus. Absolute ethanol was chosen as the solvent, and the extraction was performed during 4 days.

In order to determine differences in reactivity between PDMS and BS290 products, their corresponding FTIR spectra were obtained. In addition, their gHSQCAD nuclear magnetic resonance spectra (NMR) were recorded on a Agilent 400 MHz MR spectrometer equipped with a 5 mm One NMR probe, at 100.484 MHz for ^{13}C and 399.582 MHz for ^{1}H, using deuterated methanol (CD$_3$OD) as the solvent and internal standard.

2.3. Application on roof tiles and characterization

Commercial clay roof tiles were chosen as substrates. The tiles were cut as $3 \times 3 \times 2$ cm samples. Three different application methods were employed: spraying of starting sols on the tile surfaces (S); immersion of tile samples in the sols for 2 min (2′ I) and immersion for 5 min (5′ I). The tiles were weighed before and after the application of sols in order to calculate the uptake, and they were re-weighed one month after application (when they reached constant weight) to calculate dry matter. All of the evaluation assays described below were carried out one month after the application of the products. The depth of penetration of the products under study was measured. Images of the cross-sections of the treated tile samples and their untreated counterparts were obtained using a Nikon model SMZ800 stereoscopic microscope, according to the following procedure: first the samples were immersed in water, then, they were cut and visualized by microscopy. The non-wetted area can be associated with the penetration depth of the products across the pore structure of the tile.

The wetting behavior of the tile samples was determined by measuring static and dynamic contact angles of droplets on the tile surfaces. A commercial video-based software-controlled contact angle analyzer, model OCA 15plus, from DataPhysics Instruments was used. The procedure was the same as that reported previously [14]. This test was carried out at two different time intervals (15 and 30 days) in order to check the life of the applied coatings. SCA values were

determined on the roof tile surfaces according the following procedure: droplets of distilled water (10 μl) were applied with a syringe at 5 different points on each surface under study. The advancing (ACAs) and receding contact angles (RCAs) were measured using the ARCA method, with the volume of the droplet being increased/decreased by 5 μl.

To test the repellence properties of the superhydrophobic roof tile surface, two different dynamic tests were carried out: (1) several water droplets (around 40 μl) were deposited on the UCATP roof tile surface and its untreated counterpart. Next, the samples were tilted. This experiment was additionally carried out on a typical wavy roof tile treated with the UCATP product. (2) The treated roof tile surface and their untreated counterpart were subjected to the following dynamic tests: firstly, several water droplets (around 40 μl) were dropped on each surface under study from a height of 1.5 cm. The surfaces were tilted around 25°. Secondly, the surfaces under study were hit by a water stream. These experiments were recorded by a digital compact camera (Sony Cyber-Shot model DSCP200) at 30 frames s^{-1}.

To confirm the hydrophobic properties of the tile samples under study, they were subjected to a test of water absorption by capillarity as recommended in UNE-EN 1925 [32].

The topographies of the surfaces of the treated tiles and their untreated counterparts were observed using atomic force microscopy (AFM), from NanotecElectrónica S.L., operating in tapping mode. The root mean square (rms) roughness values were evaluated from 2.5 μm × 2.5 μm images.

The possible disadvantages of these products, associated with changes in the color of the tiles, were also evaluated. Total color difference (ΔE^*) was determined using a solid reflection spectrophotometer, Colorflex model, from Hunterlab. The conditions used were: illuminant C and observer CIE 10°. CIE $L^* a^* b^*$ scale was used [33].

Finally, in order to check the durability of the applied coatings, the treated tiles and their untreated counterparts were submitted to artificial aging which was carried out in a Solarbox 3000e RH solar degradation chamber from Cofomegra, according to UNE-EN 16474-2 standards [34]. The chamber is equipped with a xenon lamp (300–800 nm) to simulate the solar spectrum. The experiment was carried out for 1000 h under the following conditions: temperature of 50 °C, relative humidity of 80%, and a xenon lamp power of 550 W m^{-2}. After aging, changes in hydrophobic behavior of the tile samples were evaluated by contact angles and capillarity tests. In addition, changes in the roughness of the surfaces were evaluated by AFM. Finally, changes in the color of tiles were also evaluated after aging.

3. Results and discussion

3.1. Sol–gel characterization

The sols were prepared in a one-step synthesis and applied at ambient temperature on the clay roof tile samples. Sols with lower viscosity should be able to penetrate deeper into the tiles, which, *a priori*, could be desirable. Further, a low

Table 1. Sol–gel properties.

Product	Viscosity (mPa s)	Gel time (hours)	Stability (months)	Vol. reduction (%)
BS290	2.59	168 ± 24	>12[a]	—
UCATB	7.15	72 ± 12	>20	50.29
UCATP	8.02	72 ± 12	>20	48.82

[a] According to the manufacturer's specifications.

viscosity makes the use of an aerosol generator easier for applying the product *in situ*. Thus, the evaluation of rheological properties is a key factor in this study. The viscosity data were obtained immediately after ultrasonic stirring of the starting sols. For comparison purposes, the viscosity of the commercial product (BS290) was also evaluated. All the sols exhibited a Newtonian behavior over the evaluated shear range. Therefore, the viscosity was calculated as the slope of the shear rate versus shear stress curve. In all the cases, the linear regression coefficients were above 0.99. The viscosity values for all the sols under study are shown in table 1. The products prepared in our laboratory showed higher viscosity values than that corresponding to the commercial products because BS290 was diluted in isopropanol, according to the manufacturer's suggestion. Moreover, the addition of SiO$_2$ nanoparticles to the UCA sols also contributed to increasing their viscosity. On comparing the two products prepared in our laboratory, the viscosity values were similar to each other. In addition, the values obtained were close to those corresponding to typical commercial products employed as coatings of building materials, such as the popular consolidant Tegovakon V100 from Evonik [19]. Thus, it was concluded that the sols prepared in our laboratory must penetrate into substrates in a way similar to that of the commercial sols, assuring adequate penetration into the pore structure. This is confirmed by the results obtained in the penetration evaluation test carried out as described in a later paragraph of this discussion.

Sol–gel transition of the UCA sols deposited on open polypropylene vials took place spontaneously under laboratory conditions, as required. This confirms the action of n-octylamine as a catalyst of the sol–gel transition [4, 13]. Moreover, the gel times obtained (see table 1) highlight that sol–gel transition did not take place instantaneously, which must be avoided to ease the sol penetration into the pore structure of the roof tiles or other porous substrates. On the other hand, all the products stored in closed vials presented stability times of over one year, which is desirable for commercial purposes (see table 1).

Figure 2 shows photographs of the two UCA xerogels obtained under laboratory conditions. After drying under laboratory conditions, the two sols synthesized in our laboratory produced homogeneous, crack-free, and transparent monoliths. The BS290 alcoholic solution produced a thin film after the solvent was completely evaporated. The homogeneity of the two xerogels prepared in our laboratory demonstrates that the silica particles were uniformly distributed throughout the silica network. The slight whiteness
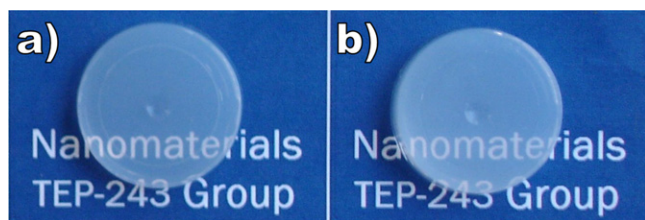
Figure 2. Photographs of the two xerogels obtained under laboratory conditions: (a) UCATB, (b) UCATP.
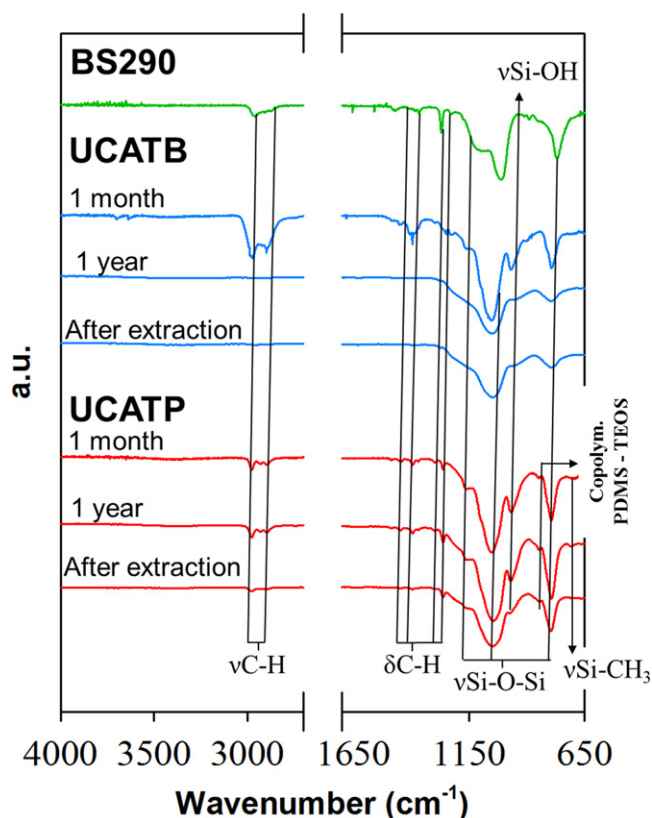

Figure 3. FTIR spectra of the xerogels under study.

observed in the two composites is associated with the added nanoparticles [4].

The volume reduction values are shown in table 1. Both UCA products showed a volume reduction of around 50%, due to the presence of organic compounds (PDMS or BS290) with high compliance. As previously reported [35], the organic chains shrank significantly during the drying phase, producing a high volume reduction in the xerogels.

The chemical bonds in the surface of the xerogels under study were analyzed by FTIR, and the corresponding spectra are shown in figure 3. In addition, the spectra of the UCA products obtained after 1 year, and after their exhaustive extraction with ethanol to remove the organic component not bonded to the silica, as suggested by Zhang *et al* [36], are shown in figure 3.

According to the results obtained, it was hypothesized that the polymerization process between TES40 and the organic siloxanes was completely different using PDMS or BS290. Specifically, the results obtained highlight that

copolymerization between TES40 and PDMS took place, producing an organic–inorganic hybrid gel. In the case of the product containing BS290, the organic component was integrated into the structure, but covalent bonds were not created between TES40 and BS290. It is considered that auto-condensation of the two chains is produced separately.

In order to delve into the differences between PDMS and BS290 polymerization mechanisms, the FTIR spectra of the two raw products is included in figure 4. The two commercial products showed the typical peaks corresponding to silica oligomers, such as siloxanes and alkyl groups [13, 37, 38]. Comparing the two spectra, some differences are clearly observed. Specifically, the typical broad band shown for silica gels at $3750 - 3250 \, \mathrm{cm}^{-1}$ associated with hydrogen-bonded silanol groups with absorbed molecular water is exclusively shown in the PDMS spectrum [12]. It suggests that OH terminal species are exclusively presented in PDMS. This is confirmed by the absence of the peak at $970 \, \mathrm{cm}^{-1}$ in the BS290 spectrum, which is attributed to the Si–OH stretching vibration. It is hypothesized that the presence of reactive OH groups in PDMS, which are available for condensation with TES40, can promote the copolymerization process.

Regarding the –CH_3 groups, a double band peak at 1379 and $1361 \, \mathrm{cm}^{-1}$, which is exclusively observed in the BS290 spectrum, deserves particular attention. It could be attributed to geminal CH_3 groups from isoalkyl chains [39]. It suggests the presence of isoalkyl substituents in the BS290 product.

In order to determine the structure of the organic groups of BS290, a two-dimensional heterogeneous (^{1}H, ^{13}C–HSQC) NMR spectrum was acquired. This spectrum can be seen in figure 4. Both ^{1}H and ^{13}C-NMR spectra presented high multiplicity in all their peaks because of the presence of different sized oligomers. Specifically, ^{1}H-NMR presented three close signals at 0.11, 0.16 and 0.22 ppm which showed correlations with ^{13}C signals at -8.10, -6.20 and -3.80 ppm, respectively. These signals correspond to methyl groups (CH_3), which usually appear at around 0.90 and 15.00 ppm in ^{1}H and ^{13}C-NMR, respectively. This large upfield shift of all signals with respect to their usual position is due to the presence of an electropositive atom (Si) attached to the methyl group [40, 41]. This feature highlights that the methyl group is directly joined to silicon, conferring hydrophobic properties to the product.

On the other hand, two ^{1}H signals can be seen at 0.57 and 0.75 ppm, which match with the same ^{13}C signal at 21.60 ppm. This correlation indicates the presence of a methylene group (CH_2). The upfield shift with respect to the typical position (approximately 0.80 and 15.90 ppm in proton and carbon, respectively) again highlights the presence of a silicon atom attached to a methylene group. Another ^{1}H signal at 1.85 ppm can also be seen, which shows correlation with a ^{13}C peak at 24.70 ppm, which can be attributed to a methine group (CH). Finally, ^{1}H-NMR shows a signal at 0.91 ppm which matches with a ^{13}C signal at 29.20 ppm. The high intensity of the proton signal (at least double the value of the first methyl groups) indicates the presence of two equivalent methyl groups. Therefore, the presence of an isobutyl group attached to a silicon atom [40, 41] can be
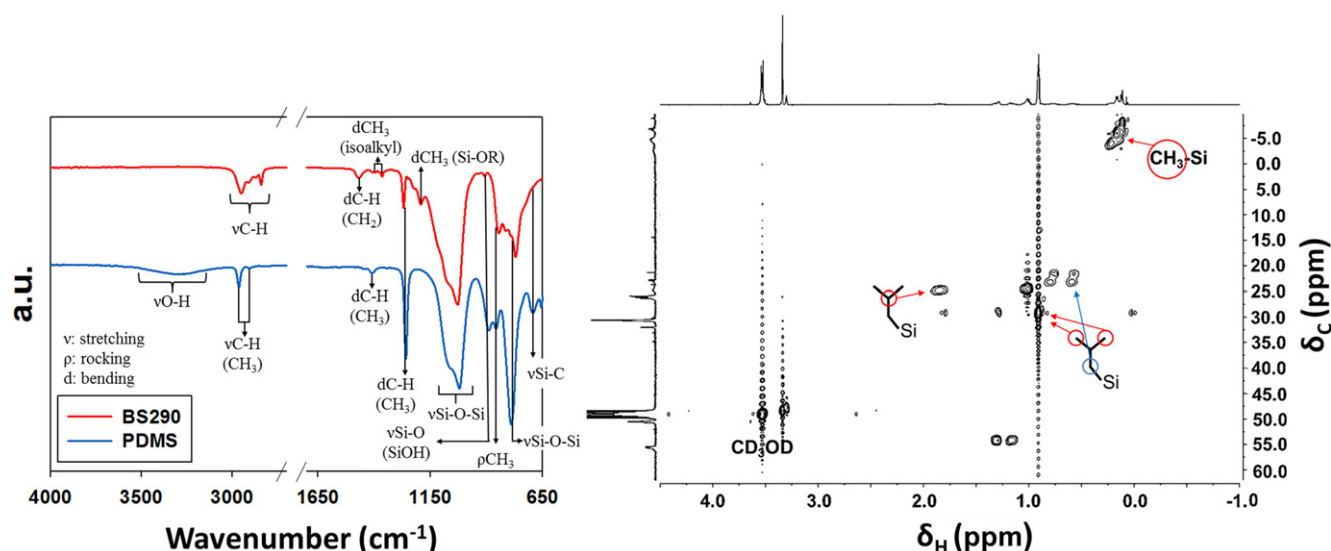
Figure 4. FTIR spectra of PDMS and BS290 (left) and 2D ^{1}H, ^{13}C HSQC spectrum of BS290 (right).

Table 2. Parameters obtained on the roof tile samples.

Product	Appl.	Uptake (%)	Dry matter (%)	Penetration depth (mm)	TWU before[a] (%)	TWU after[a] (%)
BS290	S	0.97 ± 0.02	0.20 ± 0.03	—	0.14 ± 0.02	10.78 ± 0.01
	2′ I	2.56 ± 0.08	0.20 ± 0.00	2.4 ± 0.01	0.11 ± 0.01	0.14 ± 0.01
	5′ I	6.18 ± 0.11	0.30 ± 0.05	3.9 ± 0.01	0.12 ± 0.01	0.12 ± 0.02
UCATB	S	1.56 ± 0.15	1.04 ± 0.08	1.2 ± 0.01	0.47 ± 0.03	2.62 ± 0.02
	2′ I	3.94 ± 0.30	2.63 ± 0.02	3.2 ± 0.02	0.35 ± 0.05	1.24 ± 0.04
	5′ I	4.29 ± 0.18	3.12 ± 0.11	4.5 ± 0.02	0.29 ± 0.01	0.80 ± 0.03
UCATP	S	1.56 ± 0.15	1.04 ± 0.10	1.3 ± 0.01	0.18 ± 0.01	0.18 ± 0.01
	2′ I	3.91 ± 0.26	2.66 ± 0.18	4.3 ± 0.01	0.24 ± 0.03	0.12 ± 0.03
	5′ I	4.56 ± 0.38	2.84 ± 0.13	5.4 ± 0.02	0.24 ± 0.05	0.28 ± 0.05

[a] Total water uptake (TWU) percentage values for the capillarity absorption water test.

deduced, confirming the FTIR results. According to the data described, it can be concluded that the BS290 product contains both methyl and isobutyl groups, which are responsible of its hydrophobic behavior. These isobutyl groups could also be responsible for the lack of copolymerization between BS290 and TES40, due to the steric effect of this group.

In addition, two signals can be observed at 3.29 and 3.53 ppm in ^{1}H-NMR which show correlation with signals at 47.90 and 49.00 ppm in ^{13}C. These signals are generated by the solvent used for the measurement (deuterated methanol, CD$_3$OD). However, the FTIR spectrum of BS290 showed a band at 1184 cm^{-1} which matches with in-plane (CH$_3$) bending in Si–O–R [42]. According to these data, BS290 contains methoxy groups (CH$_3$O) instead of the ethoxy groups (CH$_3$CH$_2$O), which are present in TES40. As found by Peeters *et al* [43], methoxy groups in the presence of ethanol presents higher reactivity than that corresponding to ethoxy groups. Since the UCATP product exclusively contains ethoxy groups (from TES40) which produce ethanol, whereas UCATB contains ethoxy groups (from TES40) and methoxy groups (from BS290), BS290 in the presence of the ethanol, generated by TES40, self-condensation should condensate faster than TES40 oligomers. Thus, this could be

another reason preventing the copolymerization between TES40 and BS290.

3.2. Application on roof tiles and characterization

The uptake and dry matter values obtained for the roof tile samples under study are shown in table 2. In all the cases, both the uptake and dry matter values varied according the chosen method of application, the highest values being for 5 min immersion, and the lowest for spraying. For comparison between products, the uptake values were close for the three products evaluated. In the case of the dry matter, the BS290 value was significantly lower than those corresponding to UCA products, due to their high VOC content.

The durability of the products is highly dependent on the penetration of the product into the building material, thus achieving a good adherence to the substrate. Therefore, the depth of penetration of the products in cross-sections of specimens after immersion in water was investigated. The photographs obtained are shown in figure 5, and the penetration depth values are included in table 2. The values obtained perfectly match those associated with the uptake and dry matter values. On comparing application methods, the highest penetration depth reached corresponds to 5 min
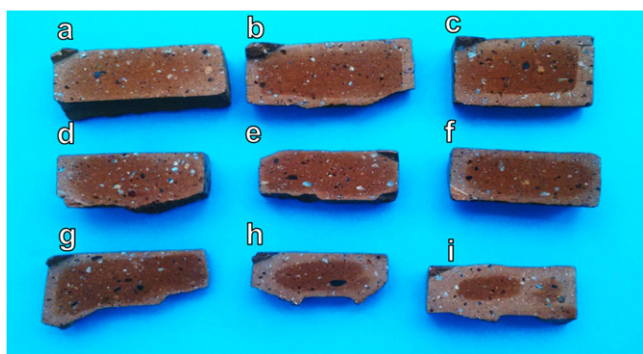
Figure 5. Wet cross-sections of the treated roof tiles. BS290: spraying (a), 2 min immersion (b), 5 min immersion (c); UCATB: spraying (d), 2 min immersion (e), 5 min immersion (f); UCATP: spraying (g), 2 min immersion (h), 5 min immersion (i).

immersion and the lowest to spraying. Regarding the differences between products, the highest values were obtained for the UCA products, being slightly higher for UCATP.

On the other hand, it is important to note that, according to the results obtained, penetration depth is not influenced by viscosity values. Specifically, the BS290 sol with the lowest viscosity induced the lowest penetration depth. This fact suggests that: (1) the viscosity of all the sols under study is within a suitable range to penetrate into the evaluated building material, and (2) the evaporation of isopropanol from the BS290 sol induces a lower product penetration. In the case of BS290 application by spraying, a thin film is produced on the surface of the roof tiles, but it does not penetrate into their porous structure. These results perfectly matched the low dry matter values obtained for the BS290 product applied by spraying.

We chose SCA and hysteresis (HCA, difference between ACA and RCA) measurements as indicators of the coating quality in terms of hydrophobicity. These two parameters were monitored at different times in order to investigate the evolution of the behavior of coatings during their drying phase. For comparative purposes, the SCA of the untreated samples was also tested. Specifically, SCA and HCA were measured for 15 and 30 days after application on the roof tile samples. Also, the durability of the coatings was assessed by carrying out an accelerated aging test in a climatic chamber. The evolution of SCA and HCA values after these experiments is given in figures 6 and 7, respectively. The values obtained for SCA and HCA can be found in the supporting information (see table S1).

Figure 8 shows pictures of water droplets on the surfaces under study 30 days after application, and after the aging study in the climatic chamber. The pictures shown correspond to application by 5 min immersion. As expected, the SCA of the untreated tiles corresponded to a hydrophilic material ($57 \pm 1°$), the SCA remaining unaltered with time and after aging. In the case of the treated samples, the SCA and HCA values showed a significantly different evolution for the tiles treated with both UCA products and those treated with the commercial product. For short times (15 days), all the

surfaces showed high SCA, around $150°$, and low HCA (ranging from $10°$ to $12°$).

In the case of the UCA products, these values remained unaltered 30 days after application. Nevertheless, the surfaces treated with the BS290 product showed a significant decrease of the contact angle values at 30 days after application. Specifically, the SCA values of the BS290 surfaces treated by spraying and 2 min immersion were significantly reduced, becoming hydrophilic materials. In the case of the BS290 samples applied by 5 min immersion, the SCA values were still hydrophobic but the values were significantly reduced, being near to $90°$. In all cases, dynamic contact angles could not be measured since the droplets were rapidly absorbed by the surfaces (see figure 7). These results clearly highlight that the BS290 coating was not retained on the surface of the clay roof tiles under study after 30 days. It is considered that the solution of BS290 in isopropanol did not firmly adhere to the substrate because it is partially evaporated during the drying phase and thus, the BS290 product hardly remained in the surface, creating a non-uniform coating. However, as discussed later, the BS290 was retained in the porous structure of the treated roof tiles.

On the other hand, the presence of isobutyl groups in BS290, as previously demonstrated by FTIR and NMR (see figure 4), could be responsible for the coating degradation. As previously discussed, the stability of organopolysiloxanes against UV degradation decreased with the length of the alkyl group [44]. Thus, BS290 could be more easily degradable than UCATP containing PDMS (with methyl groups).

Comparing the two UCA products, both of them showed close SCA values after 30 days, being slightly higher for UCATP. As previously reported [4, 13, 45], the organic component (PDMS or BS290), which promotes the reduction of surface energy, increases CA values. The presence of organic components (PDMS or BS290) at 30 days after product application has been clearly confirmed by FTIR for the two UCA products under study (see figure 3).

It is important to note that since the water contact angle cannot be increased beyond $120°$ by a purely chemical process on a smooth surface [45, 46], the higher SCA for the two UCA products evaluated are obviously due to the combined effect of the organic component and surface roughness, induced by the coating and/or the substrate [1, 4].

Regarding the hysteresis between ACA and RCA obtained after 30 days, this parameter is greatly different for the two UCA products, being slightly increased for UCATB ($14°$) and significantly reduced for UCATP ($7°$) with respect to the values obtained at 15 days. This demonstrates that only the surface treated with UCATP achieves water repellence (HCA $< 10°$) [4]. In order to confirm the repellence properties of the tile surfaces treated with UCATP, two different dynamic tests were carried out. Firstly, a simple repellence test was carried out by observing the movement of water droplets deposited on the roof tile surfaces under study. The video of this experiment can be found in the supporting information (video S1). A rapid rolling motion of droplets was observed on the tile surface treated with UCATP as the surface was slightly tilted: they did not stick on the surface.
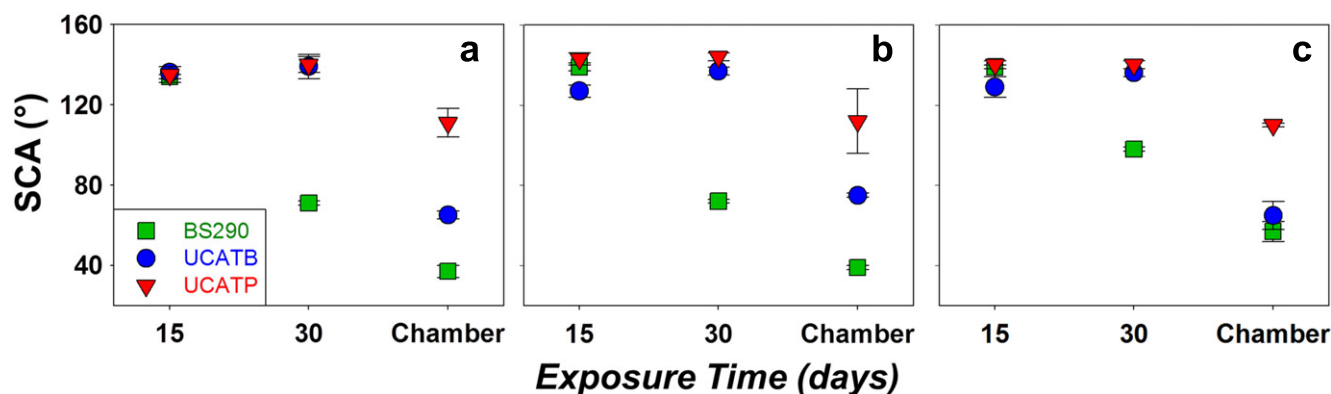
Figure 6. Evolution of SCA in function of time for the roof tile samples treated by: spraying (a), 2 min immersion (b) and 5 min immersion (c). SCA values after accelerated aging are also included.

Figure 7. Evolution of hysteresis between advancing and receding contact angles (HCA) in function of time for the roof tile samples treated by: spraying (a), 2 min immersion (b) and 5 min immersion (c). HCA values after accelerated aging are also included.
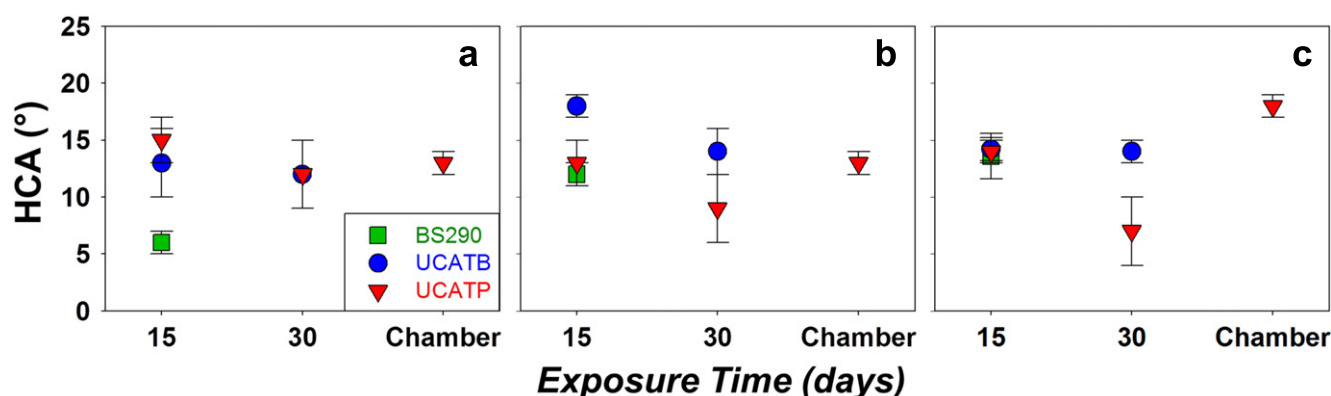
This confirms that the product synthesized in our laboratory confers water repellent properties to the clay roof tiles under study. In the case of the untreated tile surface, water droplets completely adhered to the surface. A similar behavior was observed for the wavy roof tiles treated with UCATP (see video S2 in supplementary information).

Secondly, a dynamic test carried on the tilted surfaces can be found in the supporting information (video S3). As shown, droplets hitting the tilted surface treated with UCATP were quickly rolling off it. In the case of the untreated surface, droplets adhered to the roof tile. A water stream experiment was also registered. In this case, the untreated roof tile was evidently wet whereas the UCATP surface remained completely dry, demonstrating that water does not penetrate in the sample.

After the accelerated aging test (see figures 6, 7 and 8), a completely different behavior was observed between the surfaces treated with BS290 and UCATB, and those corresponding to the surface with the UCATP product. Specifically, BS290 and UCATB totally lost their hydrophobic behavior, showing SCA values below 90°. Regarding HCA values, the dynamic contact angles could not be measured because water droplets were absorbed by the surfaces under study. In the case of the UCATP surfaces, the SCA was reduced but it was maintained above 90°, ranging from 120° to 105°, and the HCA value was only slightly reduced,

ranging from 13° to 15°. The differences observed for these two parameters are due to the method of application employed.

The different behavior observed for the two UCA products is easily explained according to the FTIR results (see figure 3). The organic component was completely removed from the UCATB formulation after aging (1 year or ethanol extraction) because copolymerization between BS290 and TES40 had not taken place, as previously discussed. Thus, it was concluded that the organic component was removed from the surface of the materials treated with UCATB during the aging test in the climatic chamber, with subsequent loss of the hydrophobic properties. In the case of the surfaces treated with BS290, as previously discussed, it evaporated during drying. For the surfaces treated with the UCATP formulation, a copolymerization between the organic and inorganic component was produced, as demonstrated by FTIR, and subsequently hydrophobic properties remained after the aging test.

Since superhydrophobicity is a combination of reducing surface energy and roughness, images of the tile surfaces were obtained by AFM in order to delve into the effect of roughness on the hydrophobic behavior of the surfaces under study. 3D images of the surfaces obtained by AFM are represented in figure 9. The images were obtained 30 days after the application of products (left column) and after the aging test
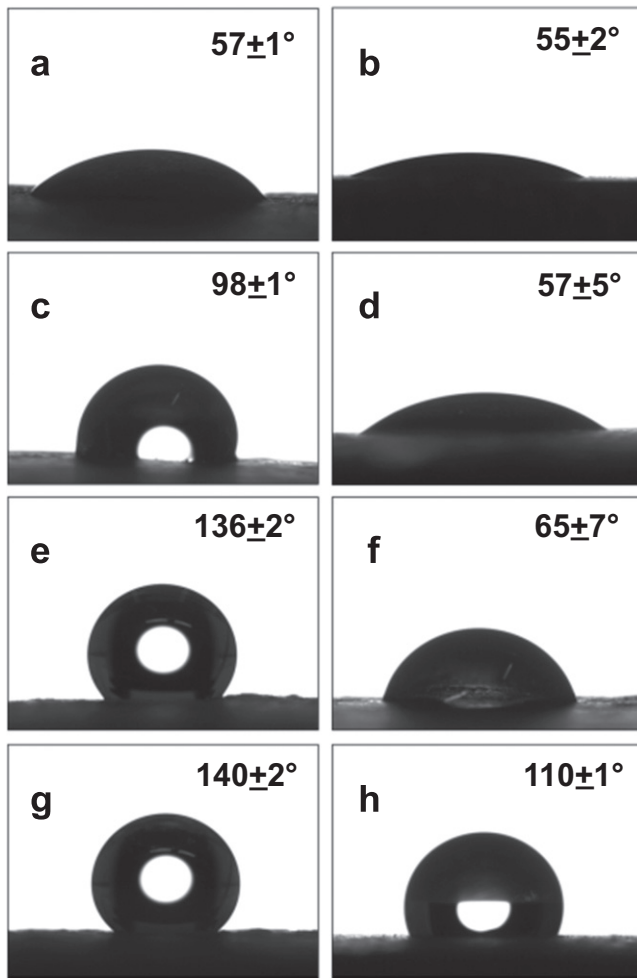
Figure 8. Images of a sessile water droplet on the surfaces of roof tiles treated with the different products under study: before (left column) and after (right column) accelerated aging. (a), (b) untreated; BS290 (c), (d); UCATB (e), (f); UCATP (g), (h).

(right column). The rms roughness values obtained for each surface evaluated are also shown in figure 9. In order to reduce the number of data, the images presented in figure 9 correspond to application of products by 5 min immersion. The application of the products by the other two methods under study did not produce significant changes in the images.

The untreated surface presented a random roughness associated with the heterogeneity of the roof tile. As expected, the morphology of the untreated surface is practically unmodified after the aging test. The surface treated with BS290 does not show significant changes in the surface. It suggests that BS290 is not capable of totally covering the underlying substrate. In the case of the UCA products, a completely different behavior was observed. UCATB produces a smoother coating with random roughness on the tile surface, in which silica particles are not clearly observed. The morphology of the UCATP treated surface is substantially different. A coating is clearly observed on the tile surface, composed of densely packed uniform particles of around 100–120 nm. Specifically, OX50 silica particles have been
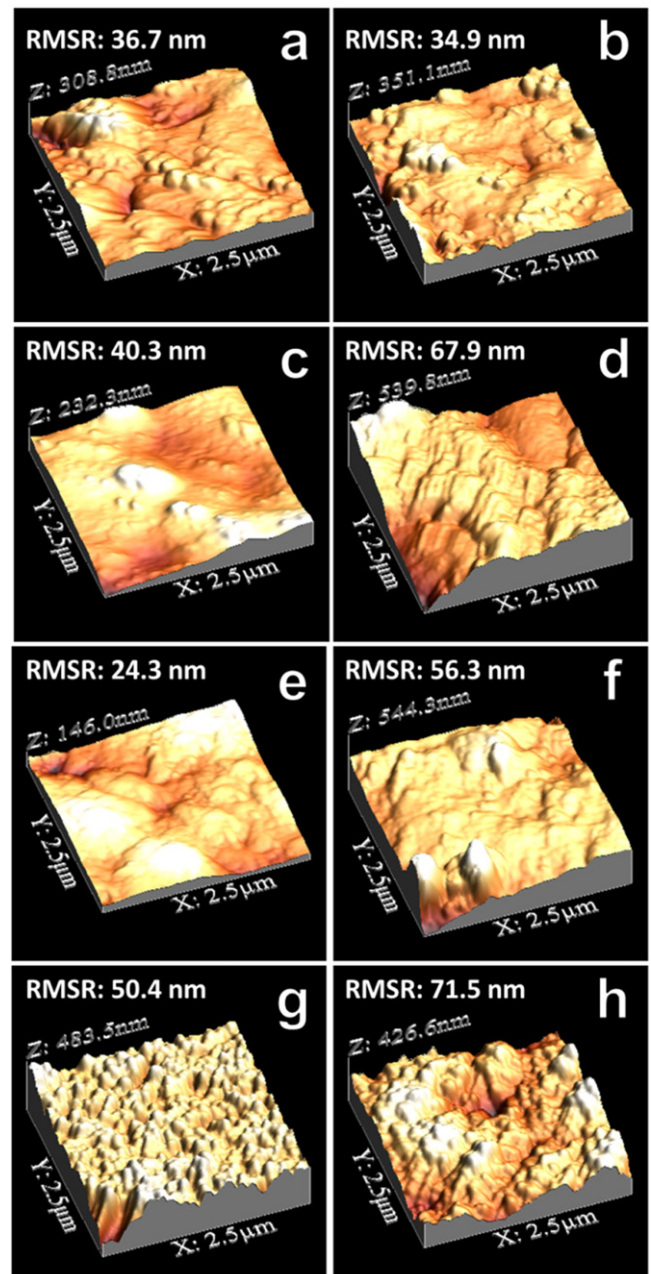

Figure 9. 3D images of the topography of the untreated tile and their treated counterparts before (left column) and after (right column) accelerated aging. (a), (b) untreated; (c), (d) BS290; (e), (f) UCATB; (g), (h) UCATP.

integrated in the organic–inorganic hybrid gel created, producing the uniform packing observed by AFM. As previously discussed [4], the formation of this close-packed coating on the roof tile surface is the key factor that induces the property of superhydrophobicity. This surface could be considered a Cassie–Baxter non-wettable surface with air pockets trapped between the aggregates of particles [46, 47].

Figure 10 presents the 2D AFM profiles for the tile surfaces before (left column) and after (right column) accelerated aging. It should be noted that the spacing between the textural peaks is important in order to trap air pockets [48]. From the images obtained, it can be seen that the
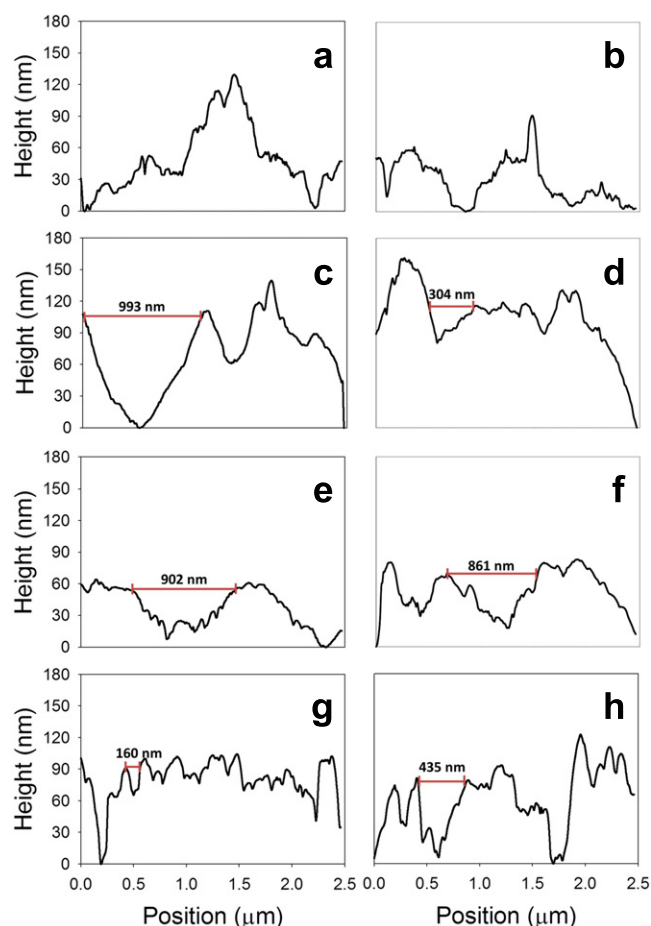
Figure 10. Profile roughness of the untreated roof tile surfaces and their treated counterparts before (left column) and after (right column) accelerated aging. (a), (b) untreated; (c), (d) BS290; (e), (f) UCATB; (g), (h) UCATP.

superhydrophobic UCATP surface presents a significantly different profile to those corresponding to the other surfaces under study. Less distance between roughness peaks (i.e., the pitch) is clearly shown for the UCATP surface, with fairly uniform values of around 100 nm. The other coatings and the untreated surfaces show heterogeneous pitch values ranging from 1000 to 500 nm. These results suggest that the water droplet will be less able to penetrate the pitch profile created by the UCATP coating on the roof tile, hence the contact area between droplet and surface will be minimized, resulting in a high SCA and low adhesion [4, 48]. In the other surfaces evaluated, their larger pitch values indicates a lower contact area between surface and coating, so water can more easily penetrate the grooves and valleys. This produces a decrease in the contact angle values and an increase in contact angle hysteresis and in adhesion.

After accelerated aging in the climatic chamber, all the treated surfaces were modified. All of them presented an increase of roughness (see figures 9 and 10), as a consequence of partial removal of the coatings during the aging test. In the case of the UCATP surface, the close-packed coating morphology can still be clearly appreciated in the surface. This result suggests that this coating presented a higher

resistance compared with the other two products evaluated. However, some changes in roughness induced by the aging test explain the reduction produced in SCA and HCA (see figures 7 and 8). Specifically, the distance between pitches was increased after the aging test, promoting transition from a Cassie–Baxter to a Wenzel state and, inducing loss of superhydrophobic behavior. The differences observed in roughness profiles obtained suggest that this roughness modification is responsible for the reduction in hydrophobic properties. It matches with previous results showing that PDMS presents a high resistance to photo-oxidation [49].

In order to confirm the hydrophobic properties of the roof tile samples under study, a capillary water absorption test was carried out. Total water uptake (TWU) percentage values of the treated samples obtained before and after accelerated aging are included in table 2. In the case of the untreated roof tile samples, the TWU percentage values, before and after the aging test, were 11.77 ± 0.01 and 11.80 ± 0.01, respectively. As expected, the untreated samples absorbed water due to their hydrophilic behavior, with the TWU value remaining almost the same after the aging test. As shown in the table, none of the treatments permitted water absorption before the aging test. Specifically, the three products under study reduced the water uptake values to almost zero (below 1%), confirming that water does not penetrate into the treated clay roof tile specimens after immersion for 48 h. After aging, these values were only maintained for the surfaces treated with UCATP. These results confirm the preservation of hydrophobic properties for UCATP surfaces after the aging test, as previously suggested, according to the contact angles evaluation. In the case of the commercial product, BS290, two completely different behaviors were observed according the method of product application. Specifically, BS290 application by spraying induced loss of hydrophobicity after the aging test because the product does not penetrate into the porous structure of the tile samples (see penetration depth in figure 5), and the coating is completely removed after the aging test, as confirmed by AFM (see figure 9). However, BS290 applied by immersion penetrated into the pore structure of the tile samples, preventing water absorption into the porous structure, although the surface coating was removed. In the case of the UCATB surfaces, slight water absorption is observed ranging from 2% to 0.8% according to the method of product application and the consequent penetration depth of the product. The highest penetration produces the highest reduction in the TWU value. It is considered that this water absorption is produced because the BS290 did not integrate into the silica network. Thus, after the aging test, the organic component could be partially removed from the surface and from the porous structure, promoting water absorption.

Finally, changes in color induced by the products under study were evaluated, because this could be an important limitation for their application on building materials. The values obtained for chromatic coordinates (ΔL^*, Δa^* and Δb^*) can be found in the supporting information (see table S2), and figure 11 shows the total color values (ΔE^*) of the treated roof tile samples, before and after the aging test. All the products induced some change in color above the
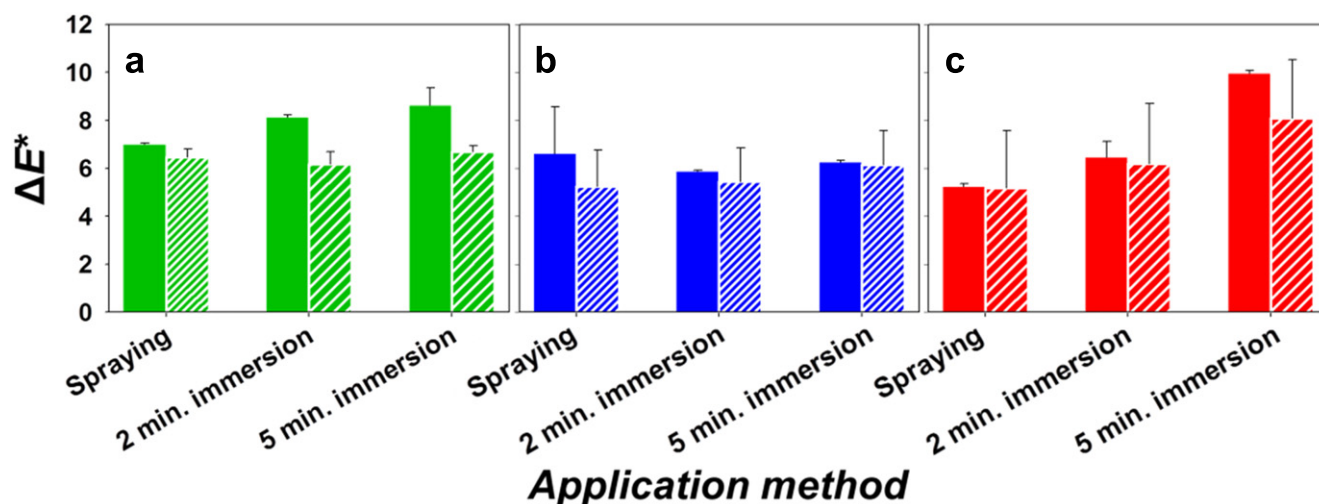
Figure 11. Total color difference of the treated tiles before (solid bars) and after aging (streaked bars) induced by the products: (a) BS290; (b) UCATB; (c) UCATP.

accepted threshold value given for restrictive standards of cultural heritage elements ($\Delta E^* = 5$) [50], as a consequence of the slight darkening (negative values for ΔL^*) induced by the products. However, these changes could be acceptable for other kinds of building materials, especially in the case of roof tiles. After the aging test, all the surfaces reduced their color change due to the partial removal of the coatings, as previously discussed.

4. Conclusions

A simple and low-cost synthesis route for producing super-hydrophobic surfaces on clay roof tiles was developed. This synthesis can be applied to other building materials, and it meets the requirements for application to buildings under outdoors conditions. Specifically, silica nanoparticles were added to a mixture of organic and inorganic silica oligomers in the presence of n-octylamine. The copolymerization between the organic and the inorganic components produced a hybrid gel with hydrophobic properties which firmly adhered to the substrate. The nanoparticles induced a new roughness on the surface by creating a densely packed coating in which air is trapped. This roughness produced a Cassie–Baxter regime, promoting superhydrophobicity. Finally, the surfactant acted as a sol–gel transition catalyst and also coarsened the pore structure of the gel network, preventing cracking. The use of ultrasound was required to avoid the use of VOCs and to obtain a homogeneous sol.

Two alkylsiloxanes, with different reactivity, were employed in the synthesis to delve into the mechanism of organic–inorganic hybrid gel formation. The results obtained lead to the conclusion that co-condensation between organic and inorganic species is crucial to obtain durable and effective coatings. The co-condensation is prevented for two reasons: (1) the existence of different condensation rates for the organic and inorganic species, promoting the self-condensation of the two chains, and (2) the presence of voluminous alkyl groups avoiding copolymerization by a steric effect.

In the case of the coating in which organic and inorganic species are covalently bonded, hydrophobicity is maintained and water absorption is completely prevented after the aging test for the roof tiles samples under study. However, a transition from a Cassie–Baxter to a Wenzel state regime is observed as a consequence of the increase in the distance between roughness pitches, produced by the aging of the coating.

References

[1] Gao L and McCarthy T J 2006 'Artificial lotus leaf' prepared using a 1945 patent and a commercial textile *Langmuir* **22** 5998–6000
[2] Barthlott W and Neinhuis C 1997 Purity of the sacred lotus, or escape from contamination in biological surfaces *Planta* **202** 1–8
[3] Söz C K, Yilgör E and Yilgör I 2015 Influence of the average surface roughness on the formation of superhydrophobic polymer surfaces through spin-coating with hydrophobic fumed silica *Polymer* **62** 118–28

[4] Facio D S and Mosquera M J 2013 Simple strategy for producing superhydrophobic nanocomposite coatings in situ on a building substrate *ACS Appl. Mater. Interfaces* **5** 7517–26

[5] Callies M and Quéré D 2005 On water repellency *Soft Matter* **1** 55–61

[6] Dyett B P, Wu A H and Lamb R N 2014 Mechanical stability of surface architecture consequences for superhydrophobicity *ACS Appl. Mater. Interfaces* **6** 18380–94

[7] Manoudis P N, Karapanagiotis I, Zuburtikudisd I and Panayiotoua C 2009 Fabrication of super-hydrophobic surfaces for enhanced stone protection *Surf. Coat. Technol.* **203** 1322–8

[8] Manoudis P N, Karapanagiotis I, Tsakalof A, Zuburtikudis I and Panayiotou C 2008 Superhydrophobic composite films produced on various substrates *Langmuir* **24** 11225–32

[9] de Ferri L, Lottici P P, Lorenzi A, Montenero A and Salvioli-Mariani E 2011 Study of silica nanoparticles-polysiloxane hydrophobic treatments for stone-based monument protection *J. Cult. Herit.* **12** 356–63

[10] Flores-Vivian I, Hejazi V, Kozhukhova M I and Nosonovsky M 2013 Self-assembling particle-siloxane coatings for superhydrophobic concrete *ACS Appl. Mater. Interfaces* **5** 13284–94

[11] Matziaris K, Stefanidou M and Karagiannis G 2011 Impregnation and superhydrophobicity of coated porous low-fired clay building materials *Prog. Org. Coat.* **72** 181–92

[12] Mosquera M J, de los Santos D M, Montes A and Valdez-Castro L 2008 , New nanomaterials for consolidating stone *Langmuir* **24** 2772–8

[13] Illescas J F and Mosquera M J 2012 Producing surfactant-synthesized nanomaterials in situ on a building substrate, without volatile organic compounds *ACS Appl. Mater. Interfaces* **4** 4259–69

[14] Mosquera M J, de los Santos D M and Rivas T 2010 Surfactant-synthesized ormosils with application to stone restoration *Langmuir* **26** 6737–45

[15] Illescas J F and Mosquera M J 2011 Surfactant-synthesized PDMS/silica nanomaterials improve robustness and stain resistance of carbonate stone *J. Phys. Chem.* C **115** 14624–34

[16] Pinho L and Mosquera M J 2011 Titania-silica nanocomposite photocatalysts with application in stone self-cleaning *J. Phys. Chem.* C **115** 22851–62

[17] Pinho L, Hernandez-Garrido J C, Calvino J J and Mosquera M J 2013 2D and 3D characterization of a surfactant-synthesized TiO_2–SiO_2 mesoporous photocatalyst obtained at ambient temperature *Phys. Chem. Chem. Phys.* **15** 2800–8

[18] Pinho L and Mosquera M J 2013 Photocatalytic activity of TiO_2–SiO_2 nanocomposites applied to buildings: influence of particle size and loading *Appl. Catal.* B **134–135** 205–21

[19] Pinho L, Elhaddad F, Facio D S and Mosquera M J 2013 A novel TiO_2–SiO_2 nanocomposite converts a very friable stone into a self-cleaning building material *Appl. Surf. Sci.* **275** 389–96

[20] Pinho L, Rojas M and Mosquera M J 2015 Ag–SiO_2–TiO_2 nanocomposite coatings with enhanced photoactivity for self-cleaning application on building materials *Appl. Catal.* B **178** 144–54

[21] Ramirez-Del-Solar M, de La Rosa-Fox N, Esquivias L and Zarzycki J 1990 Kinetic study of gelation of solventless alkoxide–water mixtures *J. Non-Cryst. Solids* **121** 40–4

[22] Xue B, Sun T, Wu J-K, Mao F and Yang W 2015 AgI/TiO_2 nanocomposites: ultrasound-assisted preparation, visible-light induced photocatalytic degradation of methyl orange and antibacterial activity *Ultrason. Sonochem.* **22** 1–6

[23] de Rosario I, Elhaddad F, Pan A, Benavides R, Rivas T and Mosquera M J 2015 Effectiveness of a novel consolidant on granite: laboratory and in situ results *Constr. Build. Mater.* **76** 140–9

[24] Simionescu B, Aflori M and Olaru M 2009 Protective coatings based on silsesquioxane nanocomposite films for building limestones *Constr. Build. Mat.* **23** 3426–30

[25] Simionescu B, Olaru M, Aflori M and Cotofana C 2010 Silsesquioxane-based hybrid nanocomposite with self-assembling properties for porous limestones conservation *High Perform. Polym.* **22** 42–55

[26] Xu F, Li D, Zhang Q, Zhang H and Xu J 2012 Effects of addition of colloidal silica particles on TEOS-based stone protection using n-octylamine as a catalyst *Prog. Org. Coat.* **75** 429–34

[27] Xu F, Yu J, Li D, Xiang N, Zhang Q and Shao L 2014 Solvent effects on structural properties of SiO_2 gel using n-octylamine as a catalyst *J. Sol–Gel Sci. Technol.* **71** 204–10

[28] Sebastián E, Cultrone G, Benavente D, Linares-Fernández L, Elert K and Rodriguez-Navarro C 2008 Swelling damage in clay-rich sandstones used in the church of San Mateo in Tarifa (Spain) *J. Cult. Herit.* **9** 66–76

[29] Delgado-Rodrigues J 2001 Swelling behavior of stones and its interest in conservation. An appraisal *Mater. Constr.* **51** 183–95

[30] Calabria J A, Vasconcelos W L and Boccaccini A R 2009 Microstructure and chemical degradation of adobe and clay bricks *Ceram. Int.* **35** 665–71

[31] Donatti D A and Vollet D R 2000 Effects of the water quantity on the solventless TEOS hydrolysis under ultrasound stimulation *J. Sol–Gel Sci. Technol.* **17** 19–24

[32] AENOR 1999 Natural stone test methods determination of water absorption coefficient by capillarity *Report No*: UNE-EN 1925 (Madrid: AENOR)

[33] Berns R S 2000 *Billmeyer and Saltzman's Principles of Color Technology* 3rd edn (New York: Wiley-Interscience)

[34] AENOR 2014 Paint and varnishes methods of exposure to laboratory light sources part II: xenon arc lamps *Report No* UNE-EN ISO 16474-2 (Madrid: AENOR)

[35] Mackenzie J D, Chung Y J and Hu Y 1992 Rubbery ormosils and their applications *J. Non-Cryst. Solids* **147–148** 271–9

[36] Zhang X, Ye H, Xiao B, Yan L, Lv H and Jiang B 2010 Sol–gel preparation of PDMS/silica hybrid antireflective coatings with controlled thickness and durable antireflective performance *J. Phys. Chem.* C **114** 19979–83

[37] Kapridaki C and Maravelaki-Kalaitzaki P 2013 TiO_2–SiO_2–PDMS nano-composite hydrophobic coating with self-cleaning properties for marble protection *Prog. Org. Coat.* **76** 400–10

[38] Téllez L, Rubio J, Rubio F, Morales E and Oteo J L 2003 Synthesis of inorganic–organic hybrid materials from TEOS, TBT and PDMS *J. Mat. Sci.* **38** 1773–80

[39] Pretsch E, Bühlmann P and Baderschen M 2009 *Structure Determination of Organic Compounds* 4th edn (Berlin: Springer)

[40] Tsai M F, Lee Y D and Chen K N 2002 NMR spectroscopic studies of dimethyldiethoxysilane hydrolysis and polysiloxane conversion *J. Appl. Polym. Sci.* **86** 468–77

[41] Kim B G, Moon J K, Sohn E H and Lee J C 2008 Polysiloxanes containing alkyl side groups: synthesis and mesomorphic behavior *Macromol. Res.* **16** 36–44

[42] Cuzman O A, Camait M, Sacchi B and Tiano P 2011 Natural antibiofouling agents as new control method for

phototrophic biofilms dwelling on monumental stone surfaces *Int. J. Conserv. Sci.* **2** 3–16

[43] Peeters M P J, Bernards T N M and Van Bommel M J 1998 17O-NMR of sol–gel processes of TEOS and TMOS *J. Sol–Gel Sci. Technol.* **13** 71–4

[44] Israeli Y, Philippart J L, Cavezzan J, Lacoste J and Lemaire J 1992 Photo-oxidation of polydimethylsiloxane oils: I. Effect of silicon hydride groups *Polym. Degrad. Stab.* **36** 179–85

[45] Wu Y L, Chen Z and Zeng X T 2008 Nanoscale morphology for high hydrophobicity of a hard sol–gel thin film *Appl. Surf. Sci.* **254** 6952–8

[46] Bhagat S D, Kim Y H and Anh Y S 2006 Room temperature synthesis of water repellent silica coatings by the dip coat technique *Appl. Surf. Sci.* **253** 2217–21

[47] Xu L, Karunakaran R G, Guo J and Yang S 2012 Transparent, superhydrophobic surfaces from one-step spin coating of hydrophobic nanoparticle *ACS Appl. Mater. Interfaces* **4** 1118–25

[48] Bhushan B and Her E K 2010 Fabrication of superhydrophobic surfaces with high and low adhesion inspired from rose petal *Langmuir* **26** 8207–17

[49] Virlogeux F, Bianchini D, Delor-Jestin F, Baba M and Lacoste J 2004 Evaluation of cross-linking after accelerated photo-ageing of silicone rubber *Polym. Int.* **53** 163–8

[50] Miliani C, Velo-Simpson M L and Scherer G W 2007 Particle-modified consolidants: a study on the effect of particles on sol–gel properties and consolidation effectiveness *J. Cult. Herit.* **8** 1–6

Anexo III-Capítulos de libro

- Rain simulation device to test durability on building materials. Libro: 4th International Congress Science and Technology for the Conservation of Cultural Herigate. *Editorial: Balkema*. (Pendiente de publicación)..

- Preserving cultural heritage stone: innovative consolidant, superhydrophobic, self-cleaning, and biocidal products. Libro: Advanced materials for the conservation of the stone. *Editorial: Springer*. Pág. 259. 2018.

Rain Simulation Device to Test Durability of Building Materials.

M.L.A. Gil[1], L.A.M. Carrascosa[1], A. Gonzalez[1], M.J. Mosquera[1], M. Galán[1]
TEP-243 Nanomaterial Group. Departamento de Química Física. Universidad de Cádiz. Campus de Puerto Real, Puerto Real, Cádiz. almoraima.gil@uca.es

A. Morgado-Estevez[3], J. Vilaverde-Ramallo[3]
[3]Departamento Ingeniería en Automática, Electrónica, Arquitectura y Redes de Computadores. Universidad de Cádiz. Campus de Puerto Real, Puerto Real, Cádiz.

M. Palomo-Duarte [4]
[4]Departamento de Ingeniería Informática. Universidad de Cádiz. Campus de Puerto Real, Puerto Real, Cádiz.

ABSTRACT: Water is the agent of decay which more aggressively attacks building materials. For this reason, the research on hydrophobic and superhydrophobic materials has experimented an increment in the last years. These treatments present a series of drawbacks, such as low-adhesion to the substrates and subsequently, low durability. In the present work we develop an automatic rain test simulation, based in an Arduino microcontroller to automatize the process. The simulator includes temperature, flow, and pH, sensors. The combination of these variables allow tprograming different cycles of assays. This portable device permits to evaluate the durability of the materials testing the chemical stability of the coatings against contact with a continuous water dropping.
In order to test the new device, different building materials were treated with two superhydrophobic products a commercial product and one developed in our research group. After each essay, the dynamic and static contact angle were evaluated.

1 INTRODUCTION

Water is the most aggressive agent of decay which continuously attacks building materials through different mechanisms, such as salt crystallization, acid rain or ice swelling (Allen 2000). For this reason, the research on hydrophobic and superhydrophobic materials (with hydrophobic and repellent properties), has experimented an increment in the last years (Liu 2013). Most of the currently available treatment are coatings that produce functionalized surfaces, therefore the persistence of these properties for a long time in particular environmental conditions, is a critical factor. These treatments present a series of drawbacks, mainly low-adhesion to the substrates and subsequently, low durability. Among others, a critical issue is the loss of the chemical functionalities of the surface under the rainwater and acid rainwater attack. This irreversible loss reduces the materials lifetime and increases the costs involved in its maintenance and repair. In spite of this fact, the number of works published studying the durability of hydrophobic and superhydrophobic treatments on building materials is significantly scarce. In this work, we have developed a simple, portable and automatic device to simulate in the laboratory the effects of rainwater and acid rainwater in order to evaluate the durability of the coatings.

2 METHODOLOGY

The rain simulation is a portable device that was thought to be used in any place with little requirements, just requiring power supply and a water drain. It can be hanged on the door of a laboratory cabinet above the sink, using the tap as a water supplier for the test. The device allows to program cycles combining three variables the water flow, pH and temperature in real time. The operation of the device is controlled via an Arduino microcontroller that runs a specifically developed software program.

2.1 Components of the rain simulation device

As can be seen in Figure 1, the rain simulation device has seven components: (1) two electro valves that open and closes the circuit, regulating the flow of water from the tap (6), which provides water pressure and/or acid solution. The acid solution is stored in a tank (7) and allows to adjust the pH of the rain. There are three devices to make the measures: a flowmeter (3) that measures the volume of water per unit of time. A pH sensor, (4) to measure the acidity of the solutions used for the test. A temperature sensor, (5) to measure the water outlet temperature. Finally, a shower head allows the distribution of the water over the sample.
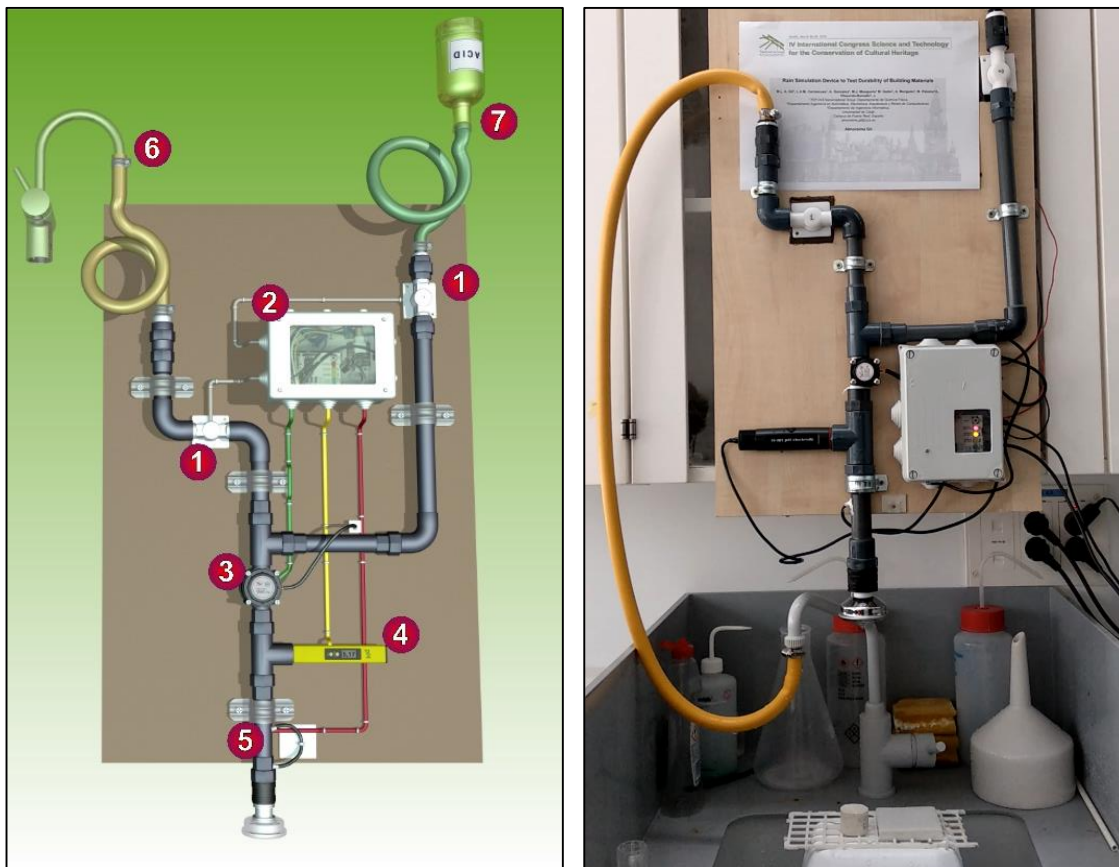

Figure 1. Left: Rain simulator scheme (1) Electro valves, (2) Microcontroller, (3) Flowmeter, (4) pHmeter, (5) Thermometer, (6) Water inlet, (7) Acid inlet. Right: Photograph of the rain simulator device.

All these sensors are controlled from the Arduino module microcontroller (2), protected in a waterproof box. The Arduino module includes a USB port to connect with a computer, a real-time clock, a micro SD card reader to save the data a reset button that reset the system and a set of LEDs to shows in real time the state of the device according to the following code: a red LED indicates that the power input is open. A yellow1 LED that open the electro-valve 1 and allow the water input. A yellow2 LED that open the electro-valve 2 for the acid solution input. A green LED that informs that the process is being executed and finally a blue LED that open the sensors of flow, temperature or pH.

2.2 Durability evaluation

To carry out a durability test we applied by brush, two superhydrophobic products: a commercial product and a product (UCA), synthesized by our research group (Facio 2013, Carrascosa 2016) on four different materials: Concrete, granite, wood, and sandstone. For the test, four cycles of 300, 900, 1800 and 2000L/m^2 with a flow of 45mL/s were performed at pH 7, after every test samples were dried for 24 h in an oven at 100 °C and was carried out a study of the dynamic and

static contact angles values with a commercial video-based, software-controlled contact angle analyzer, model OCA 15plus, from Dataphysics Instruments.

3 RESULTS

3.1 *Data obtained from the rain simulator*

The data obtained from the rain simulator is saved in real time on a micro SD card, in a CSV text file that can be easily processed by spreadsheet software. As an example, Figure 2 shows the results obtained in an experiment that takes 7,5 min, saving data every 2 s. In the experiment, the flow took three different values: 55mL/min during the first 6 minutes, 133mL/ min during the next 48 seconds and finally 200mL/min during the last 34 seconds. The total accumulated flow during the experiment was 15 L, the pH was varied from 8.00 to 7.60 and the temperature from 22ºC to 20ºC.
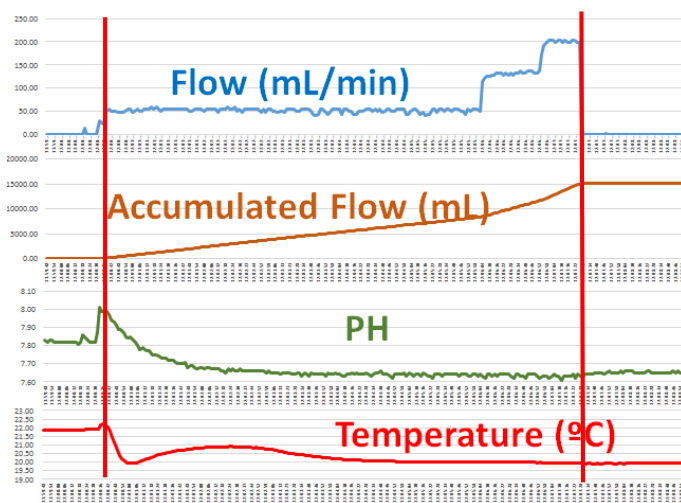

Figure 2. Output data, the red lines point out the start and finish of the test

3.2 *Roughness performed after the treatments*

In order to verify that the surfaces have developed roughness with the treatment, Atomic Force Microscopy (AFM) images have been taken. Results (Figure 3) show that in general all of the coatings produced roughness on all the surfaces.
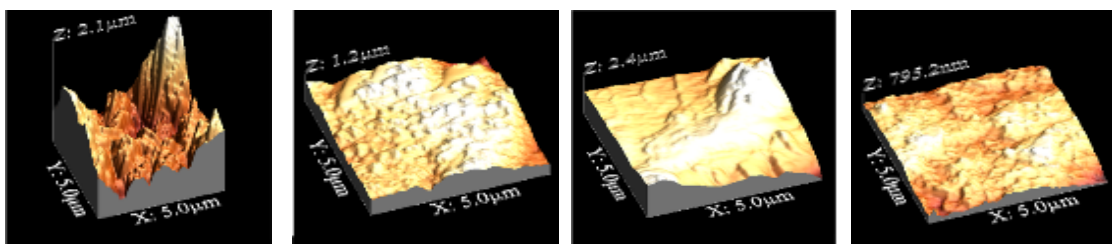

Figure 3. AFM images from left to right concrete, wood, granite, and sandstone

3.3 *Contact angle and hysteresis*

After the rainwater simulator test, the durability was evaluated measuring the static and dynamic contact angles and the hysteresis. As we can see in Figure 4 a decrease of the static contact angle has been obtained for all the materials tested.
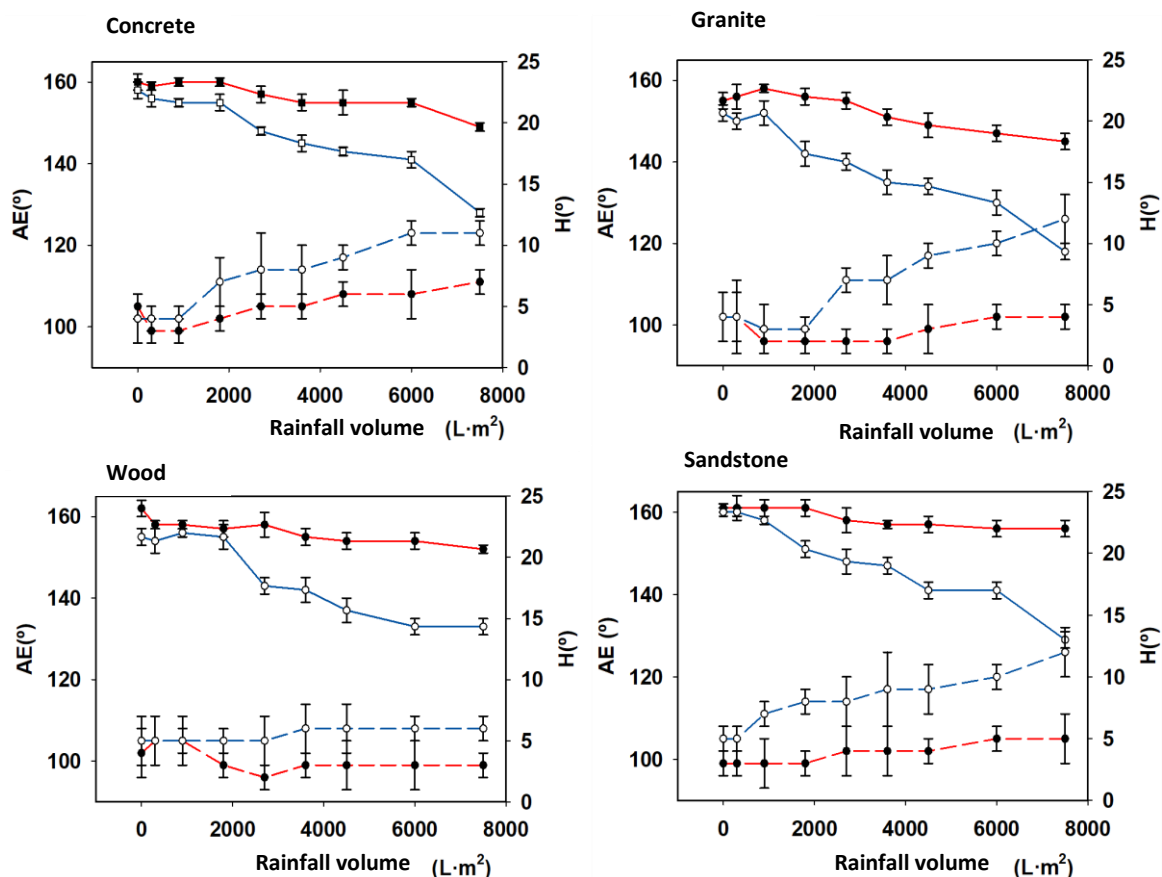
Figure 4. Contact angle and hysteresis obtained after the rainwater simulator test. The blue line and dotted blue line indicate static angle and hysteresis of a commercial product. Redline and dotted red line indicate static angle and hysteresis of UCA product.

4 CONCLUSIONS

A simulator rain device to perform durability measures in different materials has been designed to be portable. It combining three experimental variables and allows to store the data in a micro SD card using a CSV text file that can be easily processed by spreadsheet software.

To test the results of the device, we evaluated the durability of two products in four different materials. The UCA product obtains, for all the materials, a higher resistance of the coating under conditions of continued rain, maintaining static angles of 150° (condition of superhydrophobicity). Additionally, hysteresis decreases as the receding angle decreased. These results confirm the utility of the simulator.

5 REFERENCES

Allen, G. C. El-Turki. A.; Hallam. K. R.; McLaughlin, D.; Stacey, M. 2000. Role of NO_2 and SO_2 in degradation of limestone *Br. Corros. J.*, (35): 35-38.

Liu, Y. Liu, J. Li S. Liu, J. Han, Z. Ren, L. 2013. Biomimetic superhydrophobic surface of high adhesion fabricated with micronano binary structure on aluminum alloy. *ACS Appl. Mater. Interfaces* (5): 8907.

Facio, D. S. Mosquera, M. J. 2013. Simple Strategy for Producing Superhydrophobic Nanocomposite Coatings in Situ on a Building Substrate. *ACS Appl. Mater. Interfaces* 5(15) 7517–7526.

Carrascosa, L. A. M. Facio, D. S. Mosquera, M. J. 2016. Producing Superhydrophobic Roof Tiles. *Nanotechnology* 27(9): 095604

Chapter 12

Preserving Cultural Heritage Stone: Innovative Consolidant, Superhydrophobic, Self-Cleaning, and Biocidal Products

Rafael Zarzuela, Manuel Luna, Luis A.M. Carrascosa, and Maria J. Mosquera

12.1 Introduction

Stone structures, such as buildings, monuments, sculptures, and archeological remains, are vulnerable to deterioration as they are constantly exposed to outdoor environments. Stone decay is caused by the combined, and often synergistic, action of biological, physical, and chemical agents. The promoted structural damage entails high maintenance and restoration costs. Most popular decay mechanisms are associated with thermal and freeze/thaw cycles [1, 2], abrasion by sand [3], acid rain [4], salt crystallization [5], and microbial colonization (by both chemical [6, 7] and physical [8] mechanisms). Apart from structural damage, the decay agents can lead to evident aesthetical alterations, specifically, the deposition of atmospheric contaminants (soot, dirt particles, etc.) and staining from pigment-rich organisms [8, 9], and even acts of vandalism (graffiti) are a major concerns in cultural heritage preservation.

Moreover, a synergistic effect exists between the different decay mechanisms. For example, damage caused by physical–chemical agents accentuates biological decay and vice versa [10–12]. Therefore, the development of multifunctional conservation treatments that combine either consolidant, hydrophobic, self-cleaning, or antifouling effects has become promising alternatives to the application of consecutive treatments.

R. Zarzuela • M. Luna • L.A.M. Carrascosa • M.J. Mosquera (✉)

TEP-243 Nanomaterials Group, Dto. Química-Física, Facultad de Ciencias, Campus Universitario Río San Pedro, Universidad de Cádiz, Puerto Real, Cádiz, Spain

e-mail: mariajesus.mosquera@uca.es

Nowadays, there is a variety of consolidant, hydrophobic, and biocide products, all of which are commercially available and reported in scientific literature [13]. However, most of these products have not been specifically developed for preserving such elements of cultural heritage. Consequently, they are plagued by limited performance and structural drawbacks, specifically resin-based coating products (e.g., urethanes, acrylic resins) which have been widely used as consolidant and hydrophobic treatments on various substrates [14]. However, they present some disadvantages when applied on stone, namely, poor penetration, weak interaction with the substrate, and a sharp decrease in water vapor permeability. Another popular strategy is the use of products based on nanoparticles (NPs) dispersed in a solvent [15]. Some examples include $Ca(OH)_2$ [16] and SiO_2 NPs for consolidation, hydrophobic SiO_2 NPs, TiO_2 NPs for self-cleaning and biocidal effect [17], as well as biocide metallic NPs [18]. The main disadvantage of these treatments lies in their low durability compared with other products due to poor penetration and interaction with the stone. A different strategy consists of the application of products obtained by a sol–gel route [19]. Commonly, SiO_2 oligomer/monomer-based products (e.g., tetraethoxysilane (TEOS)) are widely used for the consolidation of stone materials. Their advantages are well-known. Their low viscosity allows them to penetrate deeply into porous stone, and, after polymerization which occurs upon contact with environmental moisture, a stable gel with a silicon–oxygen backbone (with a similar composition to most stone materials) is formed. However, they suffer from disadvantages such as their poor interaction with carbonate minerals [20] and form cracks caused by the action of the high capillary pressure supported during their drying process [21]. Finally, another disadvantage is the requirement for most of the available products to be dissolved in volatile organic compounds (VOCs), which pose an environmental and human health risk.

Herein, the development of an innovative sol–gel route for preserving cultural heritage stonework is discussed. This is a surfactant-assisted sol–gel synthesis to produce, in situ, mesoporous nanomaterials on stone substrates, with long-term consolidant performance [22–24]. The drawbacks associated with the commercial products such as cracking, short-lasting effectiveness, poor penetration depth, low adherence, low chemical affinity to the stones, and high content in VOCs have been eliminated or minimized in the synthesis routes developed. Moreover, by simple chemical modifications of this synthesis route, hydrophobic, water-repellent [25, 26], self-cleaning [27, 28], and biocidal [29] properties can be incorporated into the product.

This chapter reviews the research carried out in the laboratory with the objective of obtaining innovative nanomaterials with applications in stone conservation. First, the mechanism by which the proposed strategy prevents cracking is described, and then the effectiveness of these materials as stone consolidants is examined. Finally, the different chemical modifications adopted in order to achieve multifunctional treatments and the effectiveness of these new materials are discussed.

Fig. 12.1 (**a**) Photograph of the commercial consolidant Tegovakon and (**b**) photograph of a xerogel prepared by the developed route

12.2 Inverse Micelle Mechanism Producing Crack-Free Xerogels

The starting point of this research was focused on the drying process of two popular commercial consolidant products, Wacker OH100 and Tegovakon, produced by Wacker Chemie and Evonik, respectively [21]. These products consist of a silica monomer/oligomer and a neutral catalyst. The results showed that both consolidants generate compact microporous xerogels with pores less than 1 nm, which are prone to cracking (Fig. 12.1a). The gel cracking is a consequence of the capillary pressure produced by the solvent evaporation in the pores of the material [21]. The capillary pressure is described by the Young–Laplace equation (Eq. (12.1)) which establishes that the capillary pressure increases as the pore size is reduced. Therefore, the microporosity of these commercial products promotes a capillary pressure higher than the xerogel structural resistance.

$$p_c = \frac{2\gamma \cos\theta}{r_p} \tag{12.1}$$

where p_c is capillary pressure, γ is surface tension, θ is meniscus curvature angle, and r_p is pore radius.

The synthesis strategy for preventing xerogel cracking is based on the use of *n*-octylamine [30], which plays two important roles: (1) it reduces the surface tension, and (2) it promotes the formation of a particulated xerogel with a mesoporous structure. This combination of surface tension reduction and increasing of pore size results in a lowering of capillary pressure that allows monolithic xerogels to be obtained (Fig. 12.1b). Additionally, *n*-octylamine also acts as the basic catalyst for the sol–gel reaction.

Recently, the authors have proposed an inverse micelle mechanism to explain the formation of crack-free, SiO$_2$ xerogels produced by this route [31]. More specifically, an aqueous *n*-octylamine dispersion with a concentration above its critical
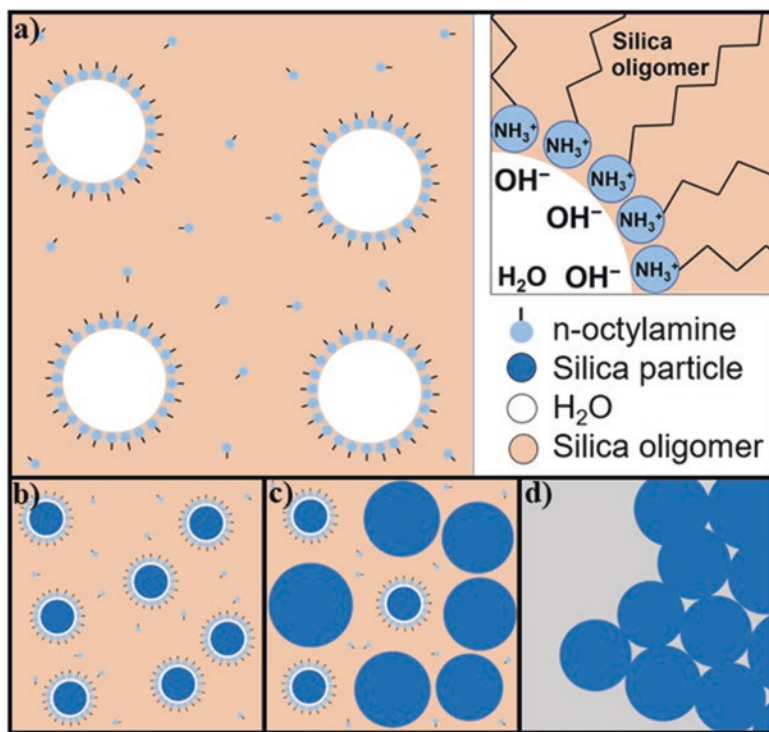
Fig. 12.2 Schematic representation of the sequences involved in the inverse micelle mechanism (**a**) formation of the inverse micelles, (**b**) SiO$_2$ seeds formation, (**c**) growth of the SiO$_2$ seeds, (**d**) packing of the SiO$_2$ particles

micelle concentration is mixed with a silica oligomer under ultrasonic agitation. The proposed mechanism takes place according to the following sequences detailed below.

12.2.1 Formation of a Microemulsion Containing n-*Octylamine Inverse Micelles*

Water is immiscible with the SiO$_2$ oligomer, due to the nonpolar nature of the latter, but the SiO$_2$ oligomer and the *n*-octylamine aqueous dispersions produce stable microemulsions under ultrasound homogenization. This homogeneous system is constituted by *n*-octylamine inverse micelles containing encapsulated water which are dispersed in the SiO$_2$ oligomer (Fig. 12.2a). The interaction between the water and the SiO$_2$ oligomer in the micelle interphase produces the hydrolysis of ethoxy groups from the SiO$_2$ oligomer. Next, the hydroxyl groups increase the polarity of the oligomer molecules, facilitating their diffusion within the inverse micelles. In addition, *n*-octylamine produces a basic pH within the micelles promoting the

condensation of the hydrolyzed oligomer. Thus, the inverse micelles act as nanoreactors for the SiO_2 formation.

12.2.2 Formation of SiO_2 Seeds Within the Inverse Micelles

The reactions of hydrolysis and condensation continue in the micelles until stable SiO_2 seeds are formed (Fig. 12.2b). This step takes place until the initial water included in the system is totally consumed or is insufficient to maintain the micelles. Therefore, the number of seeds formed is determined by the original number of micelles in the system.

12.2.3 Growth of SiO_2 Seeds in the SiO_2 Oligomer Media

The SiO_2 seed growth continues due to the condensation of additional SiO_2 oligomers around them (Fig. 12.2c). During this stage, the formation of new SiO_2 seeds is prevented because this process is thermodynamically disfavored. The seeds have a high surface/bulk ratio, and their formation increases the system energy, whereas the growth of existing particles reduces their surface/bulk ratio. The absence of new seed means that the growth and, thereby, the size of the particles depend on the number of SiO_2 seeds formed in the previous stage.

12.2.4 Packing of the SiO_2 Nanoparticles and Formation of the Mesoporous Xerogel

The aggregation of SiO_2 particles gives rise to a xerogel composed of close-packed amorphous SiO_2 particles (Fig. 12.2d). The xerogel pore structure is due to the interstitial holes produced by the packing of the SiO_2 particles. Thus, the pore size distribution and the textural properties of the xerogel are directly related to the size of the SiO_2 NPs. Therefore, it can be concluded that the xerogel nanostructure, responsible for crack prevention, is directly related to the amount of water and n-octylamine employed in the sol–gel synthesis.

12.3 Consolidant Products

A consolidant product must fulfill a series of criteria in order to be considered acceptable in the context of cultural heritage preservation [32]. The treatment should (1) increase the cohesion of mineral grains and the mechanical properties of stone, (2) penetrate deep into the structure, (3) have a good adhesion to the stone substrate

(chemical compatibility), and (4) avoid significant alterations of color and water vapor permeability of the stone.

In a preliminary study carried out by the authors, the consolidant performance of the products, prepared according to the previously described synthesis route, was evaluated [30], on a biocalcareous stone, commonly used in monumental buildings in southern Spain, and was employed in the construction of the Seville Cathedral. For comparison, the commercial consolidant Tegovakon V100 from Evonik was also evaluated. The compressive strength measurements revealed a 20–45% increase in the strength of the stones treated with the product prepared in the laboratory, whereas the commercial product had no discernible effect. Additionally, the decrease in water vapor diffusivity after the treatment was lower than 25%, and the color change was not significant (<3).

In order to accelerate the sol–gel transition, the synthesis was modified by increasing the amount of *n*-octylamine in the starting sol [24]. The consolidant effectiveness was evaluated on the same biocalcarenite and compared with a commercial consolidant (TV 100, Evonik) by a drilling resistance test. The commercial product had almost no consolidant effect on the stone, whereas the stone samples treated with the product prepared in the laboratory significantly increased the drilling resistance of the stone (up to 500%). Moreover, this increase was evident across the full depth of tested stone (30 mm), demonstrating that the University of Cadiz (UCA) product efficiently penetrated into the pore structure of the stone.

In a recent work, the consolidant product was applied during the restoration of a granitic Romanesque church in Galicia, Spain (Church of Santa María del Campo) [33] (Fig. 12.3). The performance and possible negative effects of the experimental product were compared with two commercial products, Paraloid B-82 (acrylic-based) and Estel 1000 (TEOS-based product). In a previous laboratory validation, the UCA product promoted a significantly higher resistance against salt crystallization than the commercial products. The UCA product was applied on different areas of the monument by brush. The consolidant effectiveness was evaluated, in situ, by a peeling test, showing an average 83% decrease of weight loss compared to the

Fig. 12.3 Application and in situ evaluation of the UCA consolidants in the Church of Santa María del Campo (Galicia, Spain)

untreated stone. The color variation was 3 (being below 5, the human perception threshold limit), and the decrease in water permeability was 31% (50% being the maximum value allowed), thus proving the suitability of the products for the conservation of the monumental building.

12.4   Consolidant/Hydrophobic and Superhydrophobic Products

Water is the main vehicle for degradation agents in both cultural heritage and modern building materials [34–36]. Thus, the development of products which prevent water penetration inside the porous structure of stones is an important issue. A hydrophobic surface should have a static water contact angle (CA) value higher than 90°. According to Young's equation, it is necessary to decrease surface energy to achieve this hydrophobic behavior [37]. In the case of a superhydrophobic surface, a static water CA above 150° and a high repellence characterized by a CA hysteresis (difference between advancing and receding CA values) lower than 10° [38, 39] should be achieved. Considering that reducing surface energy does not generate CA values higher than 130° [40], it is necessary to create a roughness which is capable of trapping air beneath water droplets (Cassie–Baxter state), increasing the CA and repellence [41, 42].

In order to protect stone building materials against water damage, several routes for synthesizing hydrophobic and superhydrophobic products have been developed by the authors. In a first approach [22], a hydrophobic/consolidant product was prepared by adding hydroxyl-terminated polydimethylsiloxane (PDMS) to the previously described synthesis route. The sol–gel reaction was catalyzed by the nonionic surfactant *n*-octylamine, which also plays a valuable role preventing cracking. Another role played by *n*-octylamine is the promotion of co-condensation between the SiO_2 oligomer and PDMS, which permits a homogeneous ORMOSIL (organically modified SiO_2) to be obtained. Regarding the effectiveness on stone, the synthesized sol was applied onto the previously described biocalcareous stone, giving rise to a CA value of around 130° due to the role played by PDMS in reducing surface energy. Regarding the evaluation of negative effects, the reduction of water vapor permeability was around 35%, whereas a color change of around 2 was measured.

The previous synthesis was modified by adding a higher quantity of PDMS in order to increase stain resistance [23]. The obtained sol was applied onto a pure limestone from the Estepa quarry. An increase of between 100 and 300% in drilling resistance was achieved for the experimental product compared with the untreated stone, whereas the commercial product (Silres BS OH100, Wacker Chemie) barely showed any consolidant effect. Moreover, PDMS played a valuable role in reducing surface energy and, therefore, gave rise to hydrophobic properties. Again, an improvement of hydrophobicity was observed when PDMS concentration was

increased, with static CA values of around 140° for the highest proportion (56%). This effect is due to the combination of (1) PDMS reducing surface energy and (2) an increase in the stone roughness enhancing hydrophobicity, with a low water repellence (demonstrating a Wenzel state creation) [43]. These results were compared with a hydrophobic commercial product (Silres BS290, Wacker Chemie), which produced CA values of around 90°, again demonstrating the greater effectiveness of the new products. In addition, a suitable stain resistance was achieved, no negative effect was observed, and the reduction of vapor permeability was lower than 50%. Regarding color change, the treatment gave values lower than 5.

In addition, the consolidant product previously described in the consolidant products section [24] was also modified by adding PMDS (from 2 to 10% v/v) in the sol. The obtained sols were applied onto the biocalcareous stone previously described. In this case, the drilling resistance test showed that the addition of PDMS reduced the consolidant ability of these products. Nevertheless, they still demonstrated an increase in drilling resistance of around 100%, being higher than the commercial product (TV 100, Evonik) which practically did not produce consolidation, as previously explained. Regarding the hydrophobic properties, the addition of PDMS to the experimental products developed by the authors increased CA values to around 110°.

The previous synthesis was modified in order to achieve superhydrophobicity [25] by adding SiO_2 NPs in a similar approach than that previously developed by Manoudis et al. [44]. Fumed SiO_2 NPs of around 40 nm were added to the previously developed sol, and it was applied onto sandstone. Atomic force microscopy (AFM) and scanning electron microscopy (SEM) measurements demonstrated the formation of a coating composed of closely packed particles (Fig. 12.4a, b). The evaluation of wetting properties showed static CA values higher than 150° and CA hysteresis values below 7° (Fig. 12.4c). This effect is due to the combination of reducing surface energy (i.e., the presence of PDMS) and the roughness induced by SiO_2 NPs which creates air pockets between the water and the solid surface, promoting a Cassie–Baxter state [45].

The previous product was also applied on clay roof tiles and its effectiveness, and durability was evaluated [26]. The product conferred superhydrophobic properties (static CA of around 150° and hysteresis of around 7°) to the roof tiles, due to the combination of low surface energy and roughness, as previously explained. After being subjected to accelerated aging in a climatic chamber, the treated samples conserved high static CA values. However, a decrease in repellent properties was observed due to the loss of the Cassie–Baxter topography. In addition, all the treated samples showed color changes lower than 5.

Recently, an amphiphobic (superhydrophobic and oleophobic) coating was produced on sandstone, by means of a double-step process [46]. First, a sol containing a SiO_2 oligomer, 40-nm SiO_2 particles, and an aqueous solution of *n*-octylamine was applied on the selected stone. After the sol–gel transition took place, a SiO_2 nanocomposite of densely packed particles was produced, giving rise to a Cassie–Baxter state. Then, a hydrolyzed fluorinated alkoxysilane was applied onto the previously treated surface in order to reduce the surface energy. The treated surfaces
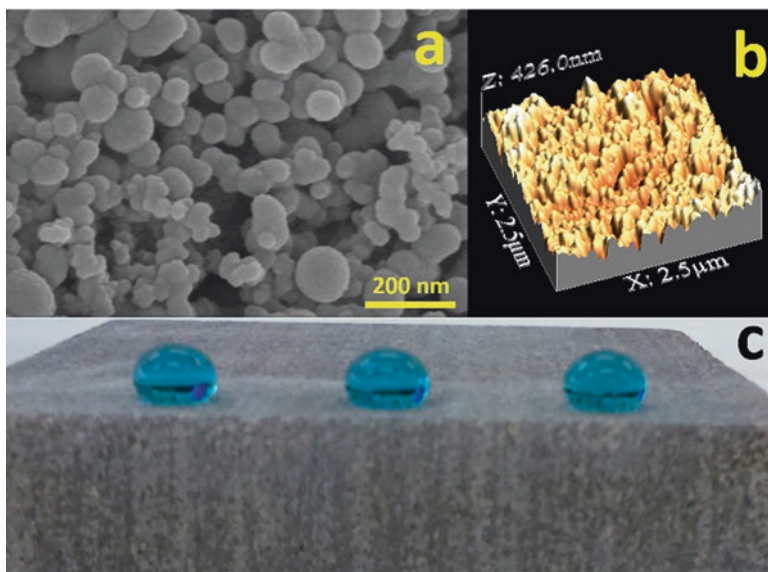
Fig. 12.4 (**a**) SEM, (**b**) 3D AFM images of superhydrophobic product on the sandstone under study, (**c**) water droplets on the superhydrophobic stone. "Reprinted with permission from Construction and Building Materials, Vol 76, I. De Rosario, F. Elhaddad, A. Pan, R. Benavides, T. Rivas, M.J. Mosquera "Effectiveness of a novel consolidant on granite: Laboratory and in situ results", pages 140–149, Copyright (2014), Elsevier"

showed superhydrophobic properties (static CA of around 160° and hysteresis of around 6°) with self-cleaning performance. Moreover, the application of a fluorinated compound allowed oleophobic surfaces (CA values with oil droplets of over 90°) to be obtained. Regarding the durability of this treatment, a peeling test was performed to test the adhesion of the coating to the stone. The surfaces demonstrated long-lasting properties due to the effective grafting between the SiO_2 nanocomposites with the stone surface.

## 12.5 Photocatalytic Consolidants with Self-Cleaning Properties

Since the photocatalytic effect of TiO_2 was discovered by Honda and Fujishima [47], it has been widely employed to produce building materials with self-cleaning and decontaminating properties [48]. A common strategy to achieve these photocatalytic materials is the application of TiO_2 NP dispersion on building substrates [49–54], but these types of coatings have an associated important drawback related to their durability. Commonly, the coatings constituted exclusively by NPs have low adherence and form cracked films, limiting their durability [55–58].

To resolve this problem, TiO_2 NPs were included in the sol–gel synthesis to produce TiO_2–SiO_2 xerogels that combine the TiO_2 photocatalytic properties with the great affinity and adhesion between the building substrate and the synthesized xerogels. The initial work conducted by the authors in this field consisted of the incorporation of commercial TiO_2 NPs in the sol–gel route (containing *n*-octylamine) to synthesize products containing different TiO_2 proportions [27]. These products were applied on a limestone for their evaluation and were compared with the treatment using an aqueous dispersion of TiO_2 NPs and other TiO_2/SiO_2 products prepared without *n*-octylamine. Both TiO_2 NPs and the product without *n*-octylamine produced cracked films on the stone, and these coatings were almost totally removed during an adhesion test, whereas the product containing *n*-octylamine produced a homogenous, crack-free coating with resistance to the adhesion test. The self-cleaning activity of the samples was evaluated by a methylene blue (MB) degradation test, with all samples containing TiO_2 showing a considerable MB decoloration (Fig. 12.5). Comparing the different treatments, it was found that for 800 h of UV illumination, the treatments with only TiO_2 NPs and the treatments containing *n*-octylamine showed similar MB degradations, whereas the treatments without *n*-octylamine showed the slowest degradations. Thus, *n*-octylamine also improves the self-cleaning activity due to the structure that it produces having a large pore volume that allows the diffusion of the reactant species into the photoactive centers. Later, this TiO_2/SiO_2 structure produced in the presence of *n*-octylamine was widely studied by transmission electron microscopy (TEM) [28]. This complete characterization study demonstrated that SiO_2 and TiO_2 are maintained as independent domains. The nanomaterial is composed of SiO_2 NPs of nearly uniform size, created by an inverse micelle mechanism due to the effect of *n*-octylamine. The preformed TiO_2 NPs are integrated into the SiO_2 aggregates. It was also demonstrated that some of the TiO_2 remains outside the SiO_2 matrix as individual NPs, which permits a direct photodegradation. These features favor the fast removal of MB due to the synergistic effect of its adsorption into the mesoporous SiO_2 structure and its photodegradation by TiO_2 NPs.

The TiO_2/SiO_2 product with the best performance (containing 2% w/v of commercial TiO_2NPs) was also compared with two commercial products, a consolidant (TV 100, Evonik) and a photocatalytic product (E503, Nanocer) [59]. The results of this study showed that the experimental product developed by the authors and the commercial photocatalytic had similar self-cleaning activities, with the experimental product demonstrating higher adhesion. The experimental product also produced a greater increase in the stone's resistance compared with the commercial consolidant, confirming its use as a multifunctional treatment for stone preservation, providing consolidant and self-cleaning properties.

The following study evaluated the influence of the type of TiO_2 NPs and their loading on the properties of the resultant TiO_2/SiO_2 materials [60]. Regarding the type of TiO_2 NPs, it was found that the best self-cleaning activity corresponded with the particles that had the larger size and the sharper shape. These particles with an initial average size of 20 μm were significantly reduced (at nanometric scale) after ultrasonic stirring during the synthesis. Their higher activity was attributed to the

Fig. 12.5 Evolution of MB stains during the self-cleaning test. Photographs for (**a**) untreated stone, (**b**) treated with TiO_2/SiO_2 product, and (**c**) evolution of MB degradation
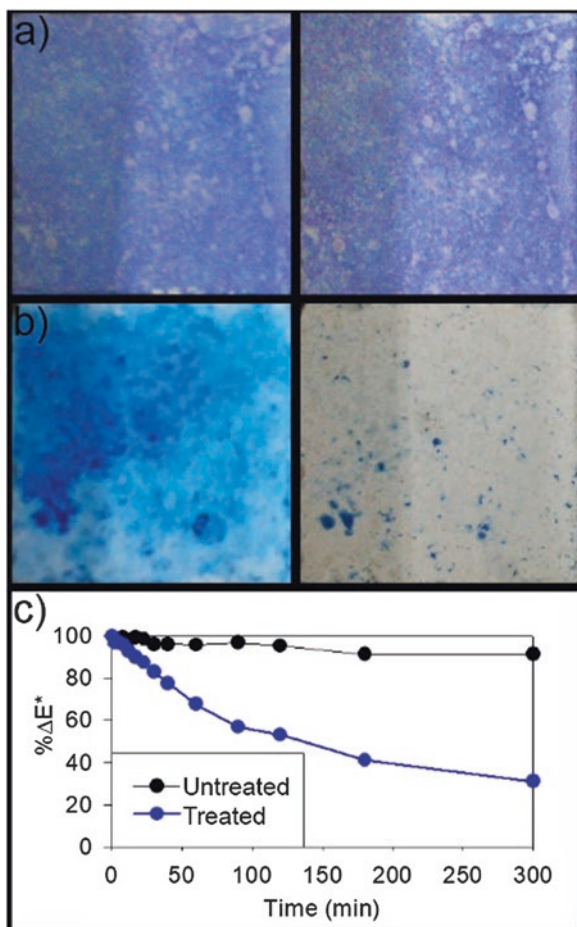
surface of the TiO_2 NPs being more available in the structure of the materials constituted by this type of NP. The sequence of TiO_2 loading showed an unexpected behavior, the TiO_2 increasing from 1 to 4% w/v improved the self-cleaning effectiveness considerably, but the treatments with 10% w/v exhibited the lowest photoactivity. It was correlated that this activity fell with a drastic pore volume reduction for the xerogels containing 10% w/v TiO_2. This behavior reconfirmed that the matrix where the particles are embedded needs a pore structure with good connectivity to achieve a correct photoactivity. Additionally, the use of 10% w/v TiO_2 presented other drawbacks such as low adherence and inhibition of the catalytic effect of *n*-octylamine during sol–gel transition, thus increasing the gel times.

The last goal of the study was to improve the efficiency of TiO_2 photoactivity for real applications or rather in the presence of visible light as the amount of UV light

from sunlight is limited. Silver doping was chosen as a strategy for improving the TiO_2 photoactivity due to two facts: (1) the noble metal NPs reduce the electron–hole recombination rate, and (2) their localized surface plasmon resonance extends the photocatalyst activation to visible light [61]. A silver precursor solution was added to the TiO_2/SiO_2 sol–gel synthesis, which was reduced in situ, giving rise to silver NPs dispersed in the xerogel structure [62]. The obtained materials had an important visible light absorption, and the treated stones showed greater self-cleaning activities compared with their counterparts without silver.

Currently, the use of gold NPs is being studied to improve the effectiveness of this product, and evaluation of the self-cleaning performance against real staining agents, such as soot, and the decontaminant activity is also being investigated by NO photodegradation.

12.6   Consolidant/Biocide Products

The biological growth on stones can be inhibited by the incorporation into the SiO_2 matrix of bioactive components such as organic biocides [63], photocatalytic materials based on TiO_2 [54, 64] and ZnO [65, 66], and products incorporating biocidal metals (Ag, Cu, etc.) in the form of their salts [67, 68] or as NPs [18, 69]. Multifunctional treatments (i.e., consolidant, hydrophobic, and biocide properties) have been developed by adding CuO or Ag NPs to the previously described synthesis route. Copper oxide and silver NPs show some promising advantages as an inexpensive alternative to other biocidal agents. Compared to organic biocides (e.g., benzalkonium chloride, quaternary ammonium salts, etc.), they are more stable against sunlight and oxidation. In addition, they are compatible with hydrophobic treatments, unlike the commonly used organic quaternary ammonium salts [70]. In contrast to TiO_2 and ZnO particles, they are equally effective in darkness and light conditions. Another advantage, related to their stability, is the ease of immobilizing them in a matrix which allows a controlled release of the biocide species [71].

In a recent study [29], it was reported the synthesis and characterization of multifunctional (consolidant and biocidal) CuO/SiO_2 nanocomposites for the conservation of stone building materials. The nanocomposites integrate commercial CuO NPs (0.00–0.35% w/v) in a SiO_2-based matrix prepared according to previous studies (TEM image in Fig. 12.6a) and were applied on a limestone. The biocidal activity of the nanocomposites was measured against two reference laboratory organisms: Gram-negative bacteria (*E. coli*) and a yeast (*S. cerevisiae*). The cell growth in the stones was inhibited by 87% for *E. coli* and 80% for *S. cerevisiae*, with respect to the control samples, with the products containing 0.15% w/v CuO (Fig. 12.6b). However, the stones treated with products containing a higher quantity of CuO (0.35% w/v) showed lower inhibition (37% and 20%, for *E. coli* and *S. cerevisiae*, respectively) due to the agglomeration and precipitation of CuO. The consolidation effectiveness was measured by the Vickers hardness test and drilling resistance. The surface of the stones treated with CuO/SiO_2 nanocomposites presented up to a 25%
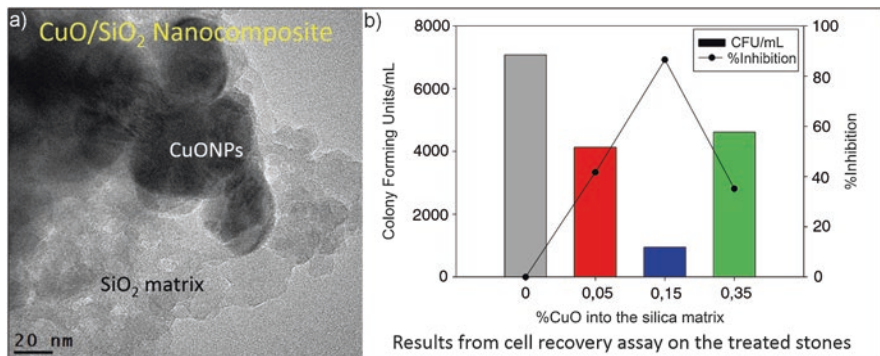
Fig. 12.6 (**a**) TEM image of the CuO/SiO$_2$ consolidant/biocide product (**b**): results from the biocide test against *E. coli*. "Reprinted with permission from Materials & Design, Vol 114, R. Zarzuela, M. Carbú, M.L.A. Gil, J.M. Cantoral, M.J. Mosquera, "CuO/SiO$_2$ nanocomposites: A multifunctional coating for application on building stone", pages 364–372, Copyright (2016), Elsevier"

increase in the Vickers hardness test. The drilling resistance values increased up to 45% for the treated stones. The hydrophobic properties were evaluated by measuring the static CA and water absorption by capillarity. For the treated stone samples, all static CA values were above 90°, and the total water uptake decreased over 95%. The hydrophobic nature was due to the presence of ethoxy groups, as confirmed by Fourier transform infrared spectroscopy (FTIR) measurements.

In a recent work conducted by the authors, the use of surface-modified SiO$_2$/Ag NPs for the production of treatments with combined superhydrophobic and biocide effects has been studied. The modification of the surface of the SiO$_2$NPs with an aminoalkyl-alkoxysilane increases the stability of the Ag NPs during the synthesis and promotes a more homogeneous distribution, leading to improved biocide effectiveness.

12.7 Conclusion

TEOS-based products are commonly employed for preserving cultural heritage stone structures. A well-known drawback of these conservation products is their tendency to crack during their drying into the stone structure. It is obvious that a cracking material cannot suitably preserve the treated substrate. A simple and low-cost route to obtain crack-free materials has been developed. Specifically, a silica precursor and a surfactant are mixed under ultrasonic agitation. The micelles created by the surfactant act as nanoreactors, producing a structure composed of nearly uniform silica nanoparticles. This mesoporous structure prevents material cracking because it reduces capillary pressure during gel drying. Due to their crack-free structure, these mesoporous materials show an improved consolidant performance

and better adherence to the stone substrates. Additionally, this surfactant-assisted sol–gel strategy provides the advantage of a high versatility. By simple chemical modifications (addition of PDMS, SiO_2 NPs, fluorinated compounds, TiO_2 NPs, CuO NPs, etc.) of the process, it is possible to obtain multifunctional products with a combination of consolidant and hydrophobic/superhydrophobic, oleophobic, photocatalytic, and biocide performance.

References

1. Chang D, Liu J. Review of the influence of freeze-thaw cycles on the physical and mechanical properties of soil. Sci Cold Arid Reg. 2013;5(4):457–60.
2. Hall K, Thorn CE. Thermal fatigue and thermal shock in bedrock: an attempt to unravel the geomorphic processes and products. Geomorphology. 2014;206:1–13.
3. Shi XJ, Shi XF. Numerical prediction on erosion damage caused by wind-blown sand movement. Eur J Environ Civ Eng. 2014;18:550–66.
4. El-Gohary MA. A holistic approach to the assessment of the groundwater destructive effects on stone decay in Edfu temple using AAS, SEM-EDX and XRD. Environ Earth Sci. 2016;75:13.
5. Dragovich D, Egan M. Salt weathering and experimental desalination treatment of building sandstone, Sydney (Australia). Environ Earth Sci. 2011;62:277–88.
6. Friedrich EWE. Solubilization, transport and deposition of mineral cations by microorganisms-efficient rock weathering agents. In: Drever JI, editor. The Chemistry of Weathering. 1st ed. Dordrecht: Springer Netherlands; 1985;161–173.
7. Tiano P. Biodegradation of cultural heritage: decay mechanisms and control methods. CNR-Centro di Stud Sulle Cause Deperimento e Metod Conserv Opere d'Arte. 2001;9:1–37.
8. Diakumaku E, Gorbushina AA, Krumbein WE, et al. Black fungi in marble and limestones—an aesthetical, chemical and physical problem for the conservation of monuments. Sci Total Environ. 1995;167:295–304.
9. Saiz-Jimenez C. Microbial melanins in stone monuments. Sci Total Environ. 1995;167:273–86.
10. Randazzo L, Montana G, Alduina R, et al. Flos Tectorii degradation of mortars: an example of synergistic action between soluble salts and biodeteriogens. J Cult Herit. 2015;16:838–47.
11. Zanardini E, Abbruscato P, Ghedini N, et al. Influence of atmospheric pollutants on the biodeterioration of stone. Int Biodeter Biodegr. 2000;46:8305.
12. Miller AZ, Sanmartín P, Pereira-Pardo L, et al. Bioreceptivity of building stones: a review. Sci Total Environ. 2012;426:1–12.
13. Doehne E, Price CA. Stone conservation: An Overwiew of Current Research. 2nd ed. Los Angeles: Getty Publications; 2010.
14. Sang YK, Man CS, Un YK, Hyung JK. Conservation study of stones by using acrylic monomer. Polymer. 2008;32:213–8.
15. Barberio M, Veltri S, Imbrogno A, Stranges F, Bonano A, Antici P. TiO_2 and SiO_2 nanoparticles film for cultural heritage: conservation and consolidation of ceramic artifacts. Surf Coat Technol. 2015;271:174–80.
16. Costa D, Rodrigues JD. Consolidation of a porous limestone with nanolime. 12th International Congress on the Deterioration and Conservation of Stone.

17. Ivask A, George S, Bondarenko O, Kahru A. Nano-antimicrobials. 1st ed. Berlin: Springer; 2012.
18. Carrillo-González R, Martínez-Gómez MA, González-Chávez MDCA, Mendoza Hernández JC. Inhibition of microorganisms involved in deterioration of an archaeological site by silver nanoparticles produced by a green synthesis method. Sci Total Environ. 2016;565:872–81.
19. Wheeler G. Alkoxysilanes and the consolidation of stone. 1st ed. Los Angeles: Getty Publications; 2005.
20. Pinto APF, Rodrigues JD. Stone consolidation: the role of treatment procedures. J Cult Herit. 2008;9:38–53.
21. Scherer GW. Recent progress in drying of gels. J Non Cryst Solids. 1992;147–148:363–74.
22. Mosquera MJ, de los Santos DM, Rivas T. Surfactant-synthesized ormosils with application to stone restoration. Langmuir. 2010;26:6737–45.
23. Illescas JF, Mosquera MJ. Surfactant-synthesized PDMS/silica nanomaterials improve robustness and stain resistance of carbonate stone. J Phys Chem C. 2011;115:14624–34.
24. Illescas JF, Mosquera MJ. Producing surfactant synthesized nanomaterials in situ on a building susbstrate, without volatile organic compounds. Appl Mater Interfaces. 2012;4:4259–69.
25. Facio DS, Mosquera MJ. Simple strategy for producing superhydrophobic nanocomposite coatings in situ on a building substrate. ACS Appl Mater Interfaces. 2013;5:7517–26.
26. Carrascosa LAM, Facio DS, Mosquera MJ. Producing superhydrophobic roof tiles. Nanotechnology. 2016;27:95604.
27. Pinho L, Mosquera MJ. Titania-silica nanocomposite photocatalysts with application in stone self-cleaning. J Phys Chem C. 2011;115:22851–62.
28. Pinho L, Hernández-Garrido JC, Calvino JJ, Mosquera MJ. 2D and 3D characterization of a surfactant-synthesized TiO_2–SiO_2 mesoporous photocatalyst obtained at ambient temperature. Phys Chem Chem Phys. 2013;15:2800–8.
29. Zarzuela R, Carbú M, Gil MLA, et al. CuO/SiO_2 nanocomposites: a multifunctional coating for application on building stone. Mater Des. 2017;114:364–72.
30. Mosquera MJ, de los Santos DM, Montes A, Valdez-Castro L. New nanomaterials for consolidating stone. Langmuir. 2008;24:2772–8.
31. Facio DS, Luna M, Mosquera MJ. Facile preparation of mesoporous silica monoliths by an inverse micelle mechanism. Microporous Mesoporous Mater. 2017;247:166–76.
32. Rodrigues JD, Grossi A. Indicators and ratings for the compatibility assessment of conservation actions. J Cult Herit. 2007;8:32–43.
33. De Rosario I, Elhaddad F, Pan A, et al. Effectiveness of a novel consolidant on granite: laboratory and in situ results. Construct Build Mater. 2015;76:140–9.
34. Figueiredo MO, Silva TP, Veiga JP. Analysis of degradation phenomena in ancient, traditional and improved building materials of historical monuments. Appl Phys A Mater Sci Process. 2008;92:151–4.
35. Charola AE. Acid rain effects on stone monuments. J Chem Educ. 1987;64:436.
36. Bravo AH, Soto AR, Sosa ER, et al. Effect of acid rain on building material of the El Tajín archaeological zone in Veracruz, Mexico. Environ Pollut. 2006;144:655–60.
37. Young T. An essay on the cohesion of fluids. Philos Trans R Soc Lond A. 1805;95:65–87.
38. Gao L, McCarthy TJ. A perfectly hydrophobic surface (θ(A)/θ(R) = 180°/180°). J Am Chem Soc. 2006;128:9052–3.
39. Gao L, McCarthy TJ. Wetting 101°. Langmuir. 2009;25:14105–15.
40. Lafuma A, Quéré D. Superhydrophobic states. Nat Mater. 2003;2:457–60.
41. Cassie ABD, Baxter S. Wettability of porous surfaces. Trans Faraday Soc. 1944;40:546–51.
42. Sun T, Feng L, Gao X, Jiang L. Bioinspired surfaces with special wettability. Acc Chem Res. 2005;38:644–52.
43. Wenzel RN. Resistance of solid surfaces to wetting by water. Ind Eng Chem. 1936;28:988–94.
44. Manoudis PN, Papadopoulou S, Karapanagiotis I, et al. Polymer-silica nanoparticles composite films as protective coatings for stone-based monuments. J Phys Conf Ser. 2007;61:1361–5.
45. Bhushan B, Her EK. Fabrication of superhydrophobic surfaces with high and low adhesion inspired from rose petal. Langmuir. 2010;26:8207–17.

46. Facio DS, Carrascosa LAM, Mosquera MJ. Producing lasting amphiphobic building surfaces with self-cleaning properties. Nanotechnology. 2017;28:265601.

47. Fujishima A, Honda K. Electrochemical photolisis of water at a semiconductor electrode. Nature. 1972;238:37–8.

48. Chen J, Poon CS. Photocatalytic construction and building materials: from fundamentals to applications. Build Environ. 2009;44:1899–906.

49. Gherardi F, Colombo A, D'Arienzo M, et al. Efficient self-cleaning treatments for built heritage based on highly photo-active and well-dispersible TiO_2 nanocrystals. Microchem J. 2016;126:54–62.

50. Liu Q, Liu Q, Zhu Z, et al. Application of TiO_2 photocatalyst to the stone conservation. Mater Res Innov. 2015;19:S8-51–4.

51. Bergamonti L, Alfieri I, Lorenzi A, et al. Nanocrystalline TiO_2 coatings by sol–gel: photocatalytic activity on Pietra di Noto biocalcarenite. J Sol-Gel Sci Technol. 2015;75:141–51.

52. Licciulli A, Calia A, Lettieri M, et al. Photocatalytic TiO_2 coatings on limestone. J Sol-Gel Sci Technol. 2011;60:437–44.

53. Quagliarini E, Bondioli F, Goffredo GB, et al. Smart surfaces for architectural heritage: preliminary results about the application of TiO_2-based coatings on travertine. J Cult Herit. 2012;13:204–9.

54. Quagliarini E, Bondioli F, Goffredo GB, et al. Self-cleaning and de-polluting stone surfaces: TiO_2 nanoparticles for limestone. Construct Build Mater. 2012;37:51–7.

55. Mendoza C, Valle A, Castellote M, et al. TiO_2 and TiO_2–SiO_2 coated cement: comparison of mechanic and photocatalytic properties. Appl Catal Environ. 2015;178:155–64.

56. Rao KVS, Subrahmanyam M, Boule P. Immobilized TiO_2 photocatalyst during long-term use: decrease of its activity. Appl Catal Environ. 2004;49:239–49.

57. Calia A, Lettieri M, Masieri M. Durability assessment of nanostructured TiO_2 coatings applied on limestones to enhance building surface with self-cleaning ability. Build Environ. 2016;110:1–10.

58. Borsoi G, Veiga R, Silva AS. Effect of nanostructured lime-based and silica-based products on the consolidation of historical renders. In: University of West Scotland, editors. Proceedings of the 3rd historic mortars conference. Glasgow; 2013.

59. Pinho L, Elhaddad F, Facio DS, Mosquera MJ. A novel TiO_2–SiO_2 nanocomposite converts a very friable stone into a self-cleaning building material. Appl Surf Sci. 2013;275:389–96.

60. Pinho L, Mosquera MJ. Photocatalytic activity of TiO_2-SiO_2 nanocomposites applied to buildings: influence of particle size and loading. Appl Catal Environ. 2013;134–135:205–21.

61. Zhou X, Liu G, Yu J, Fan W. Surface plasmon resonance-mediated photocatalysis by noble metal-based composites under visible light. J Mater Chem. 2012;22:21337–54.

62. Pinho L, Rojas M, Mosquera MJ. Ag-SiO_2-TiO_2 nanocomposite coatings with enhanced photoactivity for self-cleaning application on building materials. Appl Catal Environ. 2014;178:144–54.

63. Eyssautier-Chuine S, Gommeaux M, Moreau C, et al. Assessment of new protective treatments for porous limestone combining water-repellency and anti-colonization properties. Q J Eng Geol Hydrogeol. 2014;47:177–87.

64. Perkas N, Lipovsky A, Amirian G, et al. Biocidal properties of TiO_2 powder modified with Ag nanoparticles. J Mater Chem B. 2013;1:5309.

65. Ruffolo SA, La Russa MF, Malagodi M, et al. ZnO and $ZnTiO_3$ nanopowders for antimicrobial stone coating. Appl Phys A Mater Sci Process. 2010;100:829–34.

66. Ditaranto N, van der Werf ID, Picca RA, et al. Characterization and behaviour of ZnO-based nanocomposites designed for the control of biodeterioration of patrimonial stoneworks. New J Chem. 2015;39:6836–43.

67. Arreche R, Bellotti N, Blanco M, Vázquez P. Improved antimicrobial activity of silica–Cu using a heteropolyacid and different precursors by sol–gel: synthesis and characterization. J Sol-Gel Sci Technol. 2015;75:374–82.

68. Eyssautier-Chuine S, Vaillant-Gaveau N, Gommeaux M, et al. Efficacy of different chemical mixtures against green algal growth on limestone: a case study with Chlorella vulgaris. Int Biodeter Biodegr. 2015;103:59–68.
69. MacMullen J, Zhang Z, Dhakal HN, et al. Silver nanoparticulate enhanced aqueous silane/ siloxane exterior facade emulsions and their efficacy against algae and cyanobacteria biofouling. Int Biodeter Biodegr. 2014;93:54–62.
70. Moreau C, Vergès-Belmin V, Leroux L, et al. Water-repellent and biocide treatments: assessment of the potential combinations. J Cult Herit. 2008;9:394–400.
71. Young M, Santra S. Copper (cu)–silica nanocomposite containing valence-engineered Cu: a new strategy for improving the antimicrobial efficacy of Cu biocides. J Agric Food Chem. 2014;62:6043–52.

Anexo I†-Participación de congresos

HYDROPHOBE VII

7th International Conference on Water Repellent Treatment and Protective Surface Technology for Building Materials

Lisbon, LNEC, 11-12 September, 2014

⚫ LNEC LABORATÓRIO NACIONAL DE ENGENHARIA CIVIL

Certificate

The Organising Committee certifies that

LUIS ANTONIO MARTÍNEZ CARRASCOSA

has attended the Conference activities.

(Total 14 hours)

The Organising Committee

Joao-Manuel Mimoso

16

UNIVERSIDAD
DE MÁLAGA

TechnoHeritage
Red de Ciencia y Tecnología para la
Conservación del Patrimonio Cultural

CONGRESO NACIONAL: ESTUDIO Y CONSERVACIÓN DEL PATRIMONIO CULTURAL

(ECPC – 2015) Málaga, 16-19 Noviembre 2015

CERTIFICADO DE ASISTENCIA
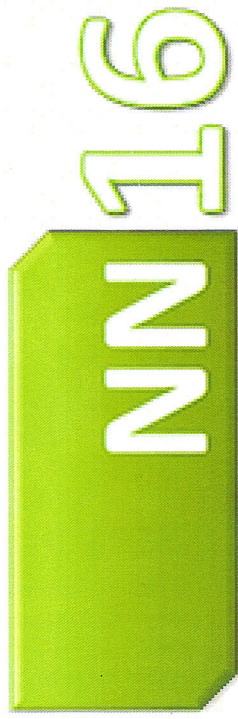
Luis Antonio Martínez Carrascosa

Universidad de Cádiz

Ha asistido al mencionado congreso nacional, presentando la siguiente comunicación oral:

- Un procedimiento simple para producir recubrimientos superhidrófobos con aplicación en la protección del Patrimonio. Luis A.M. Carrascosa, María J. Mosquera.

Víctor Hernández Jolín
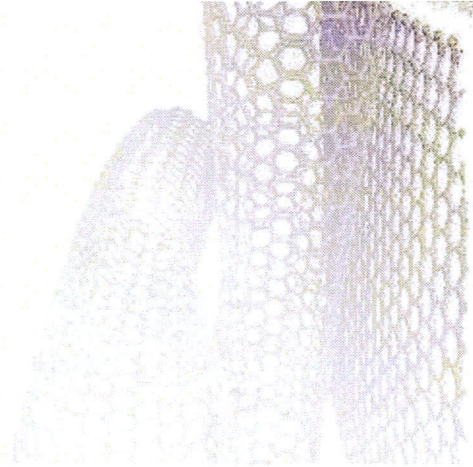
Presidente del Comité Organizador

13th International Conference on
Nanosciences & Nanotechnologies (NN16)
5-8 July 2016, Thessaloniki, Greece

NN 16

This is to certify that

Luis Antonio Martinez Carrascosa

has participated in the

13th International Conference on Nanosciences & Nanotechnologies (NN16)

held in *Thessaloniki, July 5-8, 2016*

Friday, July 8, 2016
Chair of NN16

Professor S. Logothetidis

CERTIFICATE

L.A.M. Carrascosa

Has attended to the Congress with an oral communication entitled

Long-lasting superhydrophobic coatings for stones

María Jesús Mosquera
Chair of Technoheritage 2017

TechnoHeritage **2.0.1.7** May 21-24 Cádiz, Spain